

**THE EFFECT OF STRUCTURAL ORDERING ON ACTIVE,
PASSIVE, AND LOCALIZED CORROSION IN SELECTED MODEL
ALLOY SYSTEMS**

A Dissertation

Presented to the Faculty of the School of Engineering and Applied Science
University of Virginia

In Partial Fulfillment of the
Requirements for the Degree of
Doctor of Philosophy (Materials Science and Engineering)

by

Derek John Horton
December 2011

APPROVAL SHEET

The dissertation is submitted in partial fulfillment of the
requirements for the degree of
Doctor of Philosophy (Materials Science and Engineering)

Derek J. Horton
(Author)

This dissertation has been read and approved by the examining Committee:

Dr. John R. Scully
(Dissertation Advisor)

Dr. James M. Fitz-Gerald
(Committee Chairmen)

Dr. S. Joseph Poon
(Committee Member)

Dr. William A. Soffa
(Committee Member)

Dr. Giovanni Zangari
(Committee Member)

Accepted for the School of Engineering and Applied Science:

Dean, School of Engineering and Applied
Science
December 2011

Abstract

Amorphous materials are often touted as having superior corrosion resistance due to the presence of a supersaturated solid solution and the absence of structural and chemical non-uniformities. However, the role of nanostructural changes on the corrosion properties of metallic solid solution alloys is unclear. The objective of this research is to utilize model binary and ternary solid solution alloys to investigate the effect of structural ordering on corrosion properties in the absence of an accompanying chemical partitioning. Two model alloy systems were selected for this study. The first was amorphous $\text{Cu}_{75}\text{Hf}_{20}\text{Dy}_{05}$ which undergoes single phase devitrification to a stoichiometrically equivalent crystalline solid solution. The second alloy was crystalline $\text{Fe}_{50}\text{Pd}_{50}$ which undergoes an order-disorder transformation and forms both ordered or disordered phases of the same composition. The nanoscale chemical and structural characteristics of these alloys were interrogated using a combination of x-ray diffraction, electron backscatter diffraction, scanning transmission electron microscopy and atom probe tomography. A broad survey of the global corrosion behavior of these alloys was conducted in the active, passive, and localized breakdown corrosion regimes. These studies identified specific conditions where the difference in nanostructure led to pronounced differences in corrosion behavior.

Because the amorphous $\text{Cu}_{75}\text{Hf}_{20}\text{Dy}_{05}$ alloy crystallizes to a single phase it is an ideal solid solution alloy for the study of effects of nanostructure on corrosion properties. Importantly, the alloy is a mixture of elements with substantially different electrochemical behavior involving a readily passivated refractory element (Hf) and a transition metal (Cu) that can be active or passive depending on conditions. The

amorphous structure is more susceptible to passive film breakdown and exhibits increased dissolution of Cu compared to the crystalline state. Both passivity and dissolution behavior strongly indicate that the role of nanostructure, in particular short range compositional variations, is significant. In the case of the amorphous alloy, the lack of a periodic structure with sufficient Hf concentration reduced the ability of the oxide to enrich in Hf and form a covering surface net. During active dissolution, Hf-Cu 1st and 2nd nearest neighbor bonds are speculated to restrict Cu dissolution. Hf lean regions are theorized to result from short and medium range order in the metallic glass and this promotes Cu dissolution under conditions where no oxide is formed.

The interplay of corrosion behavior of the constituent elements in $\text{Cu}_{75}\text{Hf}_{20}\text{Dy}_{05}$ is reversed in hydrofluoric acid solution. Preferential Hf dissolution resulted in a nanoporous Cu structure with a pore diameter of around 10 nm. Remaining copper reorganized by surface diffusion to form an fcc Cu nanostructure in both conditions. Dissolution and reorganization to form fcc Cu occurred more readily in the amorphous $\text{Cu}_{75}\text{Hf}_{20}\text{Dy}_{05}$ alloy compared to its crystalline counterpart resulting in a more uniform nanoporous structure. This was found to be likely due to faster surface diffusion in the amorphous structure.

Atom probe tomography and composition sensitive annular dark-field imaging characterization of the $\text{Cu}_{75}\text{Hf}_{20}\text{Dy}_{05}$ amorphous alloy was compared to experimental and modeling of clustering in similar Cu-Zr amorphous metals where significant short and medium range order in the form of clustering were found. The study of amorphous and crystalline $\text{Cu}_{75}\text{Hf}_{20}\text{Dy}_{05}$ indicates that the ordered crystal structure plays a dominant role in the corrosion behavior due to less clustering and the more periodic presence of

beneficial solute atoms at the atomic scale which can enhance oxide formation, impede dissolution and alter surface diffusion. These results suggest a negative impact due to random atomic clustering in the amorphous state.

Fe₅₀Pd₅₀ forms ordered (pT) and disordered (fcc) crystalline structures without compositional variation between the phases. These two structural states were studied in the passive, active, and passive-localized breakdown conditions through studies encompassing a wide range of pH and solution environments, including those with and without chloride. A sharp contrast between the two phases was observed during dissolution in acidic environments. The dissolution behavior of disordered Fe₅₀Pd₅₀ was found to strongly relate to the crystallographic orientation of specific grains. Similar dissolution behavior was not observed for the ordered structure, which dissolves more quickly than the disordered structure.

The susceptibility to dissolution of the disordered structure in this acidic environment was characterized for 300 grains forming a representative picture of the crystallographic nature of dissolution and surface roughness as a function of grain orientation. The {100} and {111} oriented grains had low surface roughness and showed the highest resistance to dissolution. Both surface roughness and dissolution were substantially increased for grain orientations near {110}. The orientations with the highest surface roughness and most dissolution had orientations between 10 and 20° from the {111} plane normal. Dissolution depth was found to linearly depend on the crystallographic angle from the {100} plane normal up to 40° and up to 10° from the {111} plane normal. However, the rate of increase in dissolution (per °) was higher near the {111} plane normal than the {100} plane normal. Highly dissolved orientations

exhibit structural faceting, and the overall dissolution rate of a given orientation is likely determined by the surface coverage of the slowly dissolving, low index, facets.

This study provides an unprecedented investigation of the link between nanostructural details and macroscopic corrosion properties in solid solution alloys. This work helps elucidate the role of nanostructure on corrosion properties which is fundamentally important to a wide range of commercial materials. In particular, it underscores the care that must be taken in using amorphous alloys in applications where corrosion resistance is required. While increased solubility limits are a definite benefit to the corrosion resistance of amorphous alloys, the amorphous structure can have detrimental effects with respect to both passivity and dissolution resistance. Controlling texture is often utilized for improving crystalline alloy properties. The corrosion resistance of polycrystalline materials could also be engineered by selecting specific corrosion resistant orientations as long as the relationship between orientation and corrosion resistance is well defined. This study was the first to define that relationship comprehensively for a solid solution alloy. Lastly, this study points to new routes for the synthesis of nanoporous Cu based materials with controlled porosity which may have applications as far-ranging as catalysis and super-antimicrobial efficacy.

Acknowledgements

I fully realize that it is not very often in the realm of science research that you have the opportunity to have an open ended project that allows the freedom to pursue in depth tangentially related topics. I feel very lucky to have had such a project. In particular would like to thank my Advisor, Dr. John Scully, for providing me with this opportunity and for all of his help and guidance throughout my dissertation. I'm very appreciative of the support of the NSF under grant numbers DMR-0504983 and DMR-0906663. I'd also like to thank my dissertation committee, Dr. Fitz-Gerald, Dr. Poon, Dr. Soffa, and Dr. Zangari, and my pseudo-advisor Dr. Jesser for their many helpful discussions.

This work grew into a hybrid project of many different branches within Materials Science and it would not have been possible without substantial help from my colleagues. My thanks to the following people in particular: Dr. John Perepezko (Case Western) for originally providing the Cu-Hf-Dy alloy, Dr. Soffa for providing the Fe-Pd alloys, and Dr. Poon and Dr. Shiflet for enabling the synthesis of my own amorphous alloys. My EBSD work would have proven much more difficult without the guidance and help of Vipul, Rupalee and James. Matt, Chris and Andrew C. selflessly helped me with my TEM work. Dr. Dan Schreiber (PNNL) and Dr. Sergio Perez (Oxford) really bent over backwards to help out with the atom probe tomography work. On the electrochemistry side of things, I appreciate the help of all of my colleagues within CESE and in particular from Tomo, Hongbo, Hung, and Andrew K.

Graduate school would not have been possible without the support of countless friends within the department. Last, and far from least, I'd like to thank Emily and my family for their steadfast support and encouragement.

Table of Contents

Abstract.....	i
Acknowledgements	v
Table of Contents	vi
List of Tables	xi
List of Figures.....	xiii
List of Symbols	xxxii
1 Introduction.....	1
1.1 Metallurgical Background	3
1.1.1 Amorphous Glass Relaxation	4
1.1.2 Amorphous Single Phase Devitrification.....	6
1.1.3 Order - Disorder Transformation	7
1.2 Previous Electrochemical Studies on Structural Change without Change in Composition.....	9
1.2.1 Relaxation of the Amorphous Structure	11
1.2.2 Partial Devitrification of the Amorphous Structure.....	12
1.2.3 Single Phase Crystallization	13
1.2.4 Order-Disorder Transformation in Crystalline Structure.....	14
1.2.5 Critical Unresolved Issues	16
1.3 Objectives of Research	16
1.4 Thesis Organization	17
1.5 References.....	19
2 Survey of Electrochemical Behavior of Cu₇₅Hf₂₀Dy₀₅ in the Active and Passive State.....	23
2.1 Abstract.....	23
2.2 Introduction.....	24
2.2.1 Cu ₇₅ Hf ₂₀ Dy ₀₅₀ Alloy Synthesis and Transformation Characteristics.....	24
2.2.2 Amorphous Structure	28
2.3 Electrochemical Characteristics of the Cu, Hf and Dy System	35
2.3.1 Cu.....	36

2.3.2 Hf and Dy.....	38
2.3.3 Previous Corrosion Studies on Cu-based Amorphous Materials	39
2.4 Critical Unresolved Issues	39
2.5 Experimental.....	39
2.6 Results.....	41
2.6.1 Characterization of Cu ₇₅ Hf ₂₀ Dy ₀₅	41
2.6.2 Electrochemical Behavior in the Passive State.....	46
2.6.3 Metastable Pitting Susceptibility during Localized Breakdown of the Passive State.....	48
2.6.4 Metastable Dissolution Behavior of Cu ₇₅ Hf ₂₀ Dy ₀₅ alloys in the Active Regime for Cu	52
2.7 Discussion.....	59
2.7.1 Effect of Nanostructure on Preferential Dissolution of Cu from the Matrix	59
2.7.2 Role of Nearest Neighbor Distance in Protective Film Formation.....	60
2.7.3 Hf as a Dissolution Moderator.....	64
2.8 Conclusion	66
2.9 References.....	67
3 Preferential Dissolution of Hf and Subsequent Surface Reconstruction Comparison between the Amorphous and Crystalline States of Cu₇₅Hf₂₀Dy₀₅.....	71
3.1 Abstract.....	71
3.2 Introduction.....	72
3.3 Critical Unresolved Issue.....	75
3.4 Experimental.....	75
3.4.1 Metallurgical Characterization.....	75
3.4.2 Corrosion Measurements	76
3.5 Results.....	78
3.5.1 Thermodynamics of F ⁻ -Hf/Cu-H ₂ O systems.....	78
3.5.2 Structural Characterization of the Amorphous and Crystalline States	83
3.5.3 Anodic Electrochemical Dissolution Behavior.....	83

3.5.4 Effect of Structure on Increase in Hydrogen Evolution with Concurrent Hafnium Dissolution.....	87
3.5.5 Effect of Structure on Cu Dissolution.....	89
3.5.6 Preferential Hf Dissolution in a Potential Regime dominated by Hf Dissolution.....	97
3.6 Discussion.....	113
3.6.1 Behavior During Preferential Hf dissolution.....	114
3.6.2 Dealloying Mechanism: The Role of Surface Diffusion	117
3.6.3 Behavior during Cu and Hf dissolution.....	121
3.7 Conclusions.....	123
3.8 References.....	124
4 The Role of Composition and Structure during Dissolution and Passivity/Breakdown in Fe_{1-x}Pd_x alloys.....	127
4.1 Abstract.....	127
4.2 Introduction.....	128
4.2.1 Fe _x Pd _{1-x} Alloy Production and Synthesis.....	129
4.3 Electrochemical Characteristics of the Fe/Pd - H ₂ O system and the Effect of Cl ⁻	132
4.3.1 Chloride Complexation and Absorption.....	135
4.4 Critical Unresolved Issues.....	137
4.5 Experimental.....	137
4.6 Results.....	139
4.6.1 Characterization of Fe _{1-x} Pd _x microstructures.....	139
4.6.2 Electrochemical Behavior in Cl ⁻ Containing Solutions.....	145
4.7 Discussion.....	167
4.7.1 Interpretation of the Critical Potential and the Effect of Pd content.....	167
4.7.2 Effect of Structure and Orientation: Dissolution Revealed Microstructure.....	170
4.8 Conclusion.....	171
4.9 References.....	172
5 Electrochemical Behavior of pT and fcc Fe₅₀Pd₅₀ during Active, Passive and Localized Corrosion.....	175

5.1 Abstract.....	175
5.2 Introduction.....	176
5.2.1 Fe ₅₀ Pd ₅₀ Alloy Synthesis and Phase Transformation Characteristics.....	176
5.3 Critical Unresolved Issues	179
5.4 Experimental.....	179
5.5 Results.....	180
5.5.1 Characterization of Fe ₅₀ Pd ₅₀ Microstructures.....	180
5.5.2 Electrochemical Behavior in the Active State	183
5.5.3 Electrochemical Behavior in Passive Environments and Localized Breakdown	196
5.6 Discussion.....	202
5.6.1 Benefit of Pd	202
5.6.2 Morphological Difference Due to Structure	203
5.7 Conclusion	204
5.8 Appendix 1. H Absorption on Pd and Fe ₅₀ Pd ₅₀	206
5.8.1 Pd as a Hydrogen Electrode.....	206
5.8.2 The Role of H absorption on Pd	213
5.8.3 Effect of Hydrogen during Open Circuit Behavior: Structure Dependence.....	215
5.8.4 Effect of Structural Change on the HER reaction.....	218
5.9 References.....	220
6 Dissolution Anisotropy in Fe₅₀Pd₅₀.....	222
6.1 Abstract.....	222
6.2 Introduction.....	224
6.2.1 Electron Backscatter Diffraction.....	226
6.2.2 Critical Unresolved Issues	230
6.3 Experimental.....	230
6.4 Results.....	235
6.4.1 Materials Characterization.....	235
6.4.2 Electrochemical Behavior in HCl Solution.....	237

6.4.3 Relationship between Dissolution Behavior and Crystallographic Orientation in Disordered fcc Fe ₅₀ Pd ₅₀	242
6.4.4 Surface Roughness: Faceted Grain Morphology and Correlation to Dissolution in Disordered fcc Fe ₅₀ Pd ₅₀	244
6.4.5 Morphological Evolution after Increased Dissolution in Disordered fcc Fe ₅₀ Pd ₅₀	245
6.4.6 Dissolution Behavior of Ordered pT Fe ₅₀ Pd ₅₀	261
6.4.7 Comparison between Dissolution Behavior of fcc and pT Fe ₅₀ Pd ₅₀	266
6.5 Discussion.....	269
6.5.1 Orientation Dependent Dissolution in Disordered fcc Fe ₅₀ Pd ₅₀	269
6.5.2 The Role of Crystal Structure during Dissolution of fcc and pT Fe ₅₀ Pd ₅₀	279
6.6 Conclusion	281
6.7 Appendix 1. Crystallographic Models of Selected Orientations	283
6.8 References.....	285
7 Conclusions and Future Work.....	288
7.1 Conclusions.....	288
7.2 Suggested Future Work.....	290
7.2.1 Role of the Amorphous Structure on Corrosion Properties in the Cu ₇₅ Hf ₂₀ Dy ₀₅ Alloy.....	290
7.2.2 Role of the Structure in the Fe ₅₀ Pd ₅₀ Alloys.....	291

List of Tables

Table 1.1. Literature survey of prior corrosion studies focusing on phase change without a change in composition.....	15
Table 2.1. Coordination number of Hf and Cu central atoms in the amorphous $\text{Cu}_{75}\text{Hf}_{20}\text{Dy}_{05}$ structure based on calculations of the dense random packing model. The assumed atomic radii are 0.128 nm for Cu and 0.159 nm for Hf. Calculations based on Equation 2.2[11]. Divergence from 12 close packed nearest neighbors is due to the η_{2D} approximation.	29
Table 2.2. Dominant coordination number of solute atoms in $\text{Ni}_{81}\text{B}_{19}$, $\text{Ni}_{80}\text{P}_{20}$, $\text{Zr}_{84}\text{Pt}_{16}$, $\text{Ni}_{63}\text{Nb}_{37}$ metallic glasses based on <i>ab initio</i> calculations, from [18].	30
Table 2.3. Annealing temperature, resulting phase and grain size of $\text{Fe}_{50}\text{Pd}_{50}$ alloy. Annealing at 600 °C devitrifies the amorphous alloy to a single phase $\text{Cu}_{51}\text{Hf}_{14}$.43	
Table 3.1. Calculated values for the pH, $[\text{F}^-]$, $[\text{HF}_2^-]$ and $[\text{HF}]$ of the 0.01, 0.1 and 1 M HF solution. Balance is H_2F_2	80
Table 3.2. Calculated charge density of amorphous and crystalline $\text{Cu}_{75}\text{Hf}_{20}\text{Dy}_{05}$ in 0.1 M HF solution under potentiostatic polarization at -150 mV _{SCE} for at least 6 replicate tests in each condition. The total anodic charge density has been used to calculate the approximate number of monolayers that has undergone preferential Hf dissolution and the dealloying penetration.	102
Table 4.1. Phase, composition and structure for $\text{Fe}_{1-x}\text{Pd}_x$ alloys.	132
Table 4.2. $\text{Fe}_{1-x}\text{Pd}_x$ alloy heat treatment table with resulting phase identification. Grain size measurements are based on optical micrographs and electron backscattered diffraction ($\text{Fe}_{50}\text{Pd}_{50}$).	139
Table 4.3. Calculated bct $\text{Fe}_{70}\text{Pd}_{30}$ peak positions assuming lattice parameters a and c are 0.296 and 0.300 nm from [14], respectively.....	142
Table 4.4. Total charge accumulated during potentiostatic polarization in deaerated 1 M HCl solution at 0.45 V _{SCE} . Faraday's Law was used to calculate the calculated dissolution depth.	156
Table 4.5. Surface area covered by pits after cyclic polarization (Figure 4.24) in 0.06 M NaCl solution. The apex potential was about 0.7 V _{SCE} for all compositions but the sustained current density was higher in the case of $\text{Fe}_{70}\text{Pd}_{30}$. The apex potential for $\text{Fe}_{70}\text{Pd}_{30}$ was -0.1 V _{SCE} . Average pit diameter ranged from 6-15 μm and no significant difference was measured at the different alloy compositions. Pd showed no events, and Fe showed uniform dissolution.....	161
Table 4.6. Pit diameter and pit surface coverage after cyclic polarization (Figure 4.25) in 0.6 M NaCl solution. The apex potential was about 0.6 V _{SCE} for all compositions but the sustained current density was higher in the case of $\text{Fe}_{70}\text{Pd}_{30}$. The calculated pit surface area is excluding the area of increased dissolution for $\text{Fe}_{70}\text{Pd}_{30}$. The value including this area is shown in parenthesis. Pd showed no events, and Fe showed uniform dissolution.....	162

Table 4.7. Table of critical potentials (V_{SCE}). Colored shading is indicates the operating corrosion mechanism. Blue shaded boxes are indicative of dealloying, Red indicates pitting, and Green indicates uniform-type dissolution showing grain specific morphological faceting. To convey the potential dependence of dissolution, the critical potential for the Fe-Pd alloys during active dissolution (e.g., see Figure 4.14) is defined as the potential at a current of 10^{-4} A/cm ²	168
Table 5.1. Annealing temperature, resulting phase and grain size of Fe ₅₀ Pd ₅₀ alloy.	181
Table 5.2. Table of critical potentials (V_{SCE}) in neutral and basic NaCl environments. In neutral environments both structural states of Fe ₅₀ Pd ₅₀ undergo pitting type breakdown of the passive film. In 2 M NaCl+NaOH solution a more uniform type of dissolution is observed.....	198
Table 5.3. Pd experimental open circuit potential in HCl solution at three concentrations. The open circuit potentials are constant with respect to time and they increase by 0.30 V per order of magnitude increase [H ⁺] The open circuit potentials are reproduced here from Figure 5.33.	208
Table 5.4. Pd charge density during H charging and discharging stages in deaerated 1 M HCl solution. Charging was performed using potentiostatic polarization at -0.35 V_{SCE} (under-potential of 0.15 V w.r.t. E_0) and discharge cycles at 0.35 V_{SCE} (over-potential 0.55 V w.r.t. E_0).....	209
Table 6.1. Total accumulated charge density during potentiostatic polarization at 0.45 V_{SCE} in deaerated 1 M HCl solution. At each measured interval, the total charge during polarization is significantly higher for the ordered pT structural state than the disordered fcc state.....	240
Table 6.2. Total accumulated charge during potentiostatic polarization of fcc Fe ₅₀ Pd ₅₀ at 0.45 V_{SCE} for 400 s in deaerated 1 M HCl solution. The total charge is used to calculate the average expected depth of dissolution using Faraday's Law. Each experiment had similar charge accumulation and correspondingly similar expected depth of dissolution.....	240
Table 6.3. Tabulated roughness, S_a , and relative dissolution depths for selected grains shown in Figures 6.11, 6.14, and 6.15, delimited by thick lines. All 3 β_i values are listed for each grain. The grey shaded β_i regions indicate orientations within 10° of a primary cube plane normal. Grains with the roughest surface and highest amount of dissolution have $\beta\{111\}$ between 10 and 20° (red shaded).....	247
Table 6.4. Slope and root-mean-square (RMS) error of linear fits of the charge vs. minimum, maximum and average depth of dissolution for disordered fcc and ordered pT Fe ₅₀ Pd ₅₀	267

List of Figures

- Figure 1.1. Binary A-B amorphous alloy structure with areas of increased free volume... 4
- Figure 1.2. Schematic free energy curves of devitrification of glass alloys showing devitrification paths of four different compositions of a metallic glass. Paths A, C and D are massive transformations. However, both A and C are metastable. Adapted from [25, 26]..... 7
- Figure 1.3. Schematic representation of the defect size and the detrimental effect on corrosion resistance..... 9
- Figure 1.4. Schematic representation of knowledge regarding solid solution alloy dissolution. 11
- Figure 1.5. Illustration of the thesis organization. A wide range of experiments establish the electrochemical properties of each alloy system. These experiments direct a more narrowly focused set of experiments to elucidate the role of structure on corrosion properties. A narrowly focused in depth study of specific corrosion regime provides a mechanistic understanding of the role of structure on the corrosion behavior. 18
- Figure 2.1. Cu-Hf binary phase diagram [6]. Amorphous $\text{Cu}_{75}\text{Hf}_{20}\text{Dy}_{05}$ crystallizes to the line compound $\text{Cu}_{51}\text{Hf}_{14}$ at 22 at% Hf on the phase diagram. 26
- Figure 2.2. Schematic model of the $\text{Cu}_{51}\text{Hf}_{14}$ crystal structure with Dy dissolved into Hf lattice sites. The unit cell is hexagonal P6/m (space group 175) with lattice parameters $a=1.118$ nm, $c=0.824$ nm. The density is 11.05 g/cm³. Model created using Diamond Crystallography Software [7]. 26
- Figure 2.3. Schematic representations of atomic radial distributions of lattice positions within the $\text{Cu}_{51}\text{Hf}_{14}$ perfect crystal lattice. The first three plots (top, lower left) show the distribution of Hf atoms around the 3 Hf atom lattice sites. The lower right plot shows the radial distribution of Cu and Hf atoms around a central Cu atom. Interatomic distances determined using Diamond Crystallography Software [7]. Radial lattice distances within ± 0.15 Å were considered as an equal distance the origin Cu atom. 27
- Figure 2.4. Partial coordination number (CN) as a function of composition in $\text{Cu}_{1-x}\text{Zr}_x$ amorphous metallic glasses determined experimentally by both x-ray and neutron diffraction. CN_{A-B} designates the coordination around central atom A by surrounding atom type B. The number of Cu-Zr bonds is greater than random packing would suggest indicating preferential dissimilar bonding of Cu and Zr. Recreated from [22]. 31
- Figure 2.5. Fraction of Voronoi cells around Cu (top) and Zr (bottom) as a function of composition molecular dynamic simulations of the amorphous structure. The Voronoi cells for selected Cu clusters are shown with orange atoms representing Cu and gray Zr. The CN for the most common cells is shown. Adapted from [15], with permission from Permagon. 34
- Figure 2.6. Distribution of atoms belonging to $\langle 0, 0, 12, 0 \rangle$ Cu centered clusters in $\text{Cu}_{65}\text{Zr}_{35}$ based on ab-initio molecular dynamics simulations. The green represent

- atoms belonging to the Cu-centered $\langle 0, 0, 12, 0 \rangle$ clusters and red balls represent atoms in the remaining part of the system, respectively. Adapted, with permission, from Li, M., C. Wang, S. Hao, M. Kramer, and K. Ho, *Physical Review B*, 2009. **80**(18). Copyright 2009 by the American Physical Society [26]. 35
- Figure 2.7. Combined Cu, Hf and Dy potential-pH equilibrium diagram for the Cu/Hf/Dy-H₂O system at 25°C with ion concentrations assumed to be 10⁻⁶ M [39]. 37
- Figure 2.8. Cu and Hf Oxide Stability Diagram at 25°C with ion concentrations assumed to be 10⁻⁶ M [39]. The assumed reaction is the chemical reaction of HfO²⁺ to form HfO₂. For Cu, at pH <9 the Cu²⁺ reacts to form CuO. At higher pH, the HfCuO₂⁻ anion reacts to form the oxide..... 37
- Figure 2.9. Calculated Cu-Cl⁻-H₂O E-pH diagrams at Cl⁻ concentrations of 1 M (left) and 0.1 M right. The ion concentrations are assumed to be 10⁻⁶ M. Calculated and plotted using Medusa [13]. 38
- Figure 2.10. X-ray diffraction spectra of Cu₇₅Hf₂₀Dy₀₅ melt spun ribbon as received (amorphous) and after annealing at 600°C for 30 minutes. The crystalline phase is identified as Cu₅₁Hf₁₄ [47] with a 0.6° phase shift. The small peak at 30.5° is likely due to surface layer HfO₂ formation..... 43
- Figure 2.11. High resolution TEM bright field micrograph of amorphous Cu₇₅Hf₂₀Dy₀₅ showing a fully amorphous structure. The inlaid diffraction pattern shows no crystallization (FFT). 44
- Figure 2.12. High-angle annular dark-field imaging (HAADF, left) The cloudy regions, about 20 nm, in the HAADF micrograph indicate Z contrast. The bright areas indicate regions of low Z and Cu enrichment. The line profile (on right) shows the relative intensity measured by the contrast (I_0 = white), after correction for sample thickness (subtraction of the linear background). The bright areas are 6.5-9 nm in diameter..... 44
- Figure 2.13. Atom probe tomography composition map (1 nm slice) of amorphous Cu₇₅Hf₂₀Dy₀₅ (top) and the corresponding pair distribution functions (bottom). Orange atoms are Hf and green atoms are Dy. Cu (blue) atoms are omitted for clarity. A uniform distribution of both Cu and Hf are seen. Some slight clustering of the Dy atoms is suggested. Work performed by Dan Schreiber and PNNL as part of their user facility (EMSL). 45
- Figure 2.14. Initial cycle during cyclic voltammetry for Cu and amorphous and crystalline Cu₇₅Hf₂₀Dy₀₅ in deaerated pH 8.4 at a scan rate of 1 mV/s. The Nernst potentials for Cu/Cu₂O and Cu₂O/CuO are shown for reference. 47
- Figure 2.15. Cyclic voltammetry for polycrystalline Cu in deaerated pH 8.4 at a scan rate of 1 mV/s. The Nernst potentials for Cu/Cu₂O and Cu₂O/CuO are shown for reference..... 47
- Figure 2.16. Cyclic voltammetry amorphous (left) and crystalline (right) Cu₇₅Hf₂₀Dy₀₅ in deaerated pH 8.4 at a scan rate of 1 mV/s. The Nernst potentials for Cu/Cu₂O and Cu₂O/CuO are shown for reference. The amorphous structural state shows a diminished second oxidation peak and minimal reduction peaks during the initial

- cycle. These peaks increase slightly with each cycle, but the overall current density is substantially lower for the amorphous compared to the crystalline structural state of $\text{Cu}_{75}\text{Hf}_{20}\text{Dy}_{05}$ 47
- Figure 2.17. E-log(i) behavior of high purity Cu showing the effect of increasing $[\text{SO}_4^{2-}]$ in deaerated pH 8.4 borate buffer. In 0.01 M Na_2SO_4 solution no breakdown potential is observed, while the increase in concentration to 0.1 M and 0.5 M shows a decrease in critical potential. These results are similar to behavior observed by Cong [4]. 50
- Figure 2.18. E-Log(i) behavior of Hf, Cu and $\text{Cu}_{75}\text{Hf}_{20}\text{Dy}_{05}$ in pH 8.4 borate buffer and 0.5 M Na_2SO_4 solution. Amorphous and crystalline $\text{Cu}_{75}\text{Hf}_{20}\text{Dy}_{05}$ show numerous metastable current transients. In this environment Hf shows only passive current, while Cu undergoes breakdown and sustained dissolution at $0.3 \text{ V}_{\text{SCE}}$ 51
- Figure 2.19. E-Log(i) behavior (left) and potentiostatic polarization at $0.41 \text{ V}_{\text{SCE}}$ indicated by the dashed line (right) of Hf, Cu and $\text{Cu}_{75}\text{Hf}_{20}\text{Dy}_{05}$ in pH 8.4 borate buffer and 0.1 M Na_2SO_4 solution. The total anodic current of the amorphous state is 0.17 C/cm^2 and for the crystalline state is 0.05 C/cm^2 51
- Figure 2.20. E-log*i* behavior of Hf, Cu and $\text{Cu}_{75}\text{Hf}_{20}\text{Dy}_{05}$ in deaerated 0.1 M (left) and 1 M (right) H_2SO_4 solution at pH 0.7 and -0.3, respectively. For reference, the oxidation potentials are listed assuming species concentrations of 10^{-3} M 56
- Figure 2.21. E-log*i* behavior of Hf, Cu and $\text{Cu}_{75}\text{Hf}_{20}\text{Dy}_{05}$ in deaerated 0.5 M H_2SO_4 solution. For reference, the oxidation potentials are listed assuming species concentrations of 10^{-3} M 56
- Figure 2.22. Cyclic voltammetry at 5 mV/s for amorphous and crystalline $\text{Cu}_{75}\text{Hf}_{20}\text{Dy}_{05}$ in deaerated 0.5 M H_2SO_4 solution (pH 0). The 1st cycle (top left) and 5th cycle (top right) show the amorphous structural state has larger current density in both oxidation peaks over all 5 cycles Both states show metastable breakdown of the passive film above the Cu oxidation peaks. 57
- Figure 2.23. Total charge in the first oxidation peak of amorphous and crystalline $\text{Cu}_{75}\text{Hf}_{20}\text{Dy}_{05}$ during rapid cyclic voltammetry at 20 mV/s from -0.5 to $0.6 \text{ V}_{\text{SCE}}$ in deaerated 0.5 M H_2SO_4 solution. The amorphous state shows higher sustained charge at 3.6 mC/cm^2 than the crystalline state which decays to 0.4 mC/cm^2 within 11 cycles. 57
- Figure 2.24. Potentiostatic polarization in deaerated 0.5 M H_2SO_4 at $0.15 \text{ V}_{\text{SCE}}$ (top) and XPS depth profiling after the potentiostatic exposure for 1200 s (bottom) of amorphous and crystalline $\text{Cu}_{75}\text{Hf}_{20}\text{Dy}_{05}$. The total accumulated charge in the amorphous state is 0.255 C/cm^2 compared to 0.076 C/cm^2 in the crystalline state. The XPS results show surface enrichment of Hf resulting from preferential dissolution of Cu up to 40 SiO_2 equivalent nm of depth. Despite the anodic charge difference (increases by a factor of 5 for the amorphous state) no corresponding increase in the dealloyed layer depth is seen. XPS results carried out at Institute for Critical Technology and Applied Science at Virginia Polytechnic Institute. . 58
- Figure 2.25. Schematic model of the HfO_2 crystal structure (left) and Hf atomic distribution (right). The unit cell is orthorhombic Pnam (space group 62) with

- lattice parameters $a = 0.554$ nm, $b = 0.646$ nm, and $c = 0.331$ nm. [51] Model created using Diamond Crystallography Software [7]..... 61
- Figure 2.26. Schematic model of 4x4 unit cells (left) of the hexagonal $\text{Cu}_{51}\text{Hf}_{14}$ crystal structure. Radius of the atoms was assumed to be 0.128 and 0.159 nm for Cu and Hf, respectively. In the model on right (Figure 2.6, adapted from [26]), the green balls designate atoms belonging to $\langle 0,0,12,0 \rangle$ clusters in the $\text{Cu}_{65}\text{Zr}_{35}$ metallic glass. These clusters, centered on Cu atoms, contain an above average proportion of the Zr atoms [22]. The outlined region (white) in the $\text{Cu}_{65}\text{Zr}_{35}$ model has approximately the same area as the $\text{Cu}_{51}\text{Hf}_{14}$ are schematic. The $\text{Cu}_{51}\text{Hf}_{14}$ model created using Diamond Crystallography Software [7]..... 63
- Figure 3.1. The working electrode specimen mounting configuration in epoxy with perpendicular mounting (left) and with a large ribbon section exposed (right). .. 77
- Figure 3.2. Calculated speciation diagram for F^- - H_2O for solutions containing 0.1 M F^- ions in solution at 25°C..... 80
- Figure 3.3. Calculated Cu- F^- - H_2O Pourbaix diagrams with F^- concentrations of 0 mM, 10 mM and 1 M at room temperature. 81
- Figure 3.4. Calculated Hf- F^- - H_2O Pourbaix diagrams with F^- concentrations of 0 mM, 10 mM and 1 M at room temperature. 81
- Figure 3.5. Calculated Dy- F^- - H_2O Pourbaix diagrams with F^- concentrations of 0 mM, 10 mM and 1 M at room temperature. 82
- Figure 3.6. Open circuit behavior (top) and the anodic polarization (bottom) behavior of amorphous and crystalline $\text{Cu}_{75}\text{Hf}_{20}\text{Dy}_{05}$ alloys compared to the high purity polycrystalline alloying elements at 1 mV/s in aerated 1 M HF solution..... 85
- Figure 3.7. Open circuit behavior (top) and the anodic polarization (bottom) behavior of amorphous and crystalline $\text{Cu}_{75}\text{Hf}_{20}\text{Dy}_{05}$ alloys compared to the high purity polycrystalline alloying elements at 1mV/s behavior in aerated 0.1 M HF solution. 86
- Figure 3.8. Cyclic voltammograms of $\text{Cu}_{75}\text{Hf}_{20}\text{Dy}_{05}$ amorphous (left) and crystalline (right) in aerated 0.1 M HF solution at a scan rate of 20 mV/s 88
- Figure 3.9. Hydrogen evolution current density at $-0.9 V_{\text{SCE}}$ during the upward scan of each cycle. Total potential range per cycle was $-1 V_{\text{SCE}}$ to $-0.1 V_{\text{SCE}}$ at a scan rate of 20 mV/s in aerated 0.1 M HF solution 88
- Figure 3.10. Cyclic voltammograms of Cu and Hf from $-0.25 V_{\text{SCE}}$ to $0.5 V_{\text{SCE}}$, scan rate 20 mV/s, in aerated 0.1 M HF solution. For Cu, every 5 cycles is plotted. The direction of solid arrow indicates increasing cycle number. For Hf, a single representative cycle is shown..... 89
- Figure 3.11. Cyclic voltammograms of amorphous and crystalline $\text{Cu}_{75}\text{Hf}_{20}\text{Dy}_{05}$ from $-0.25 V_{\text{SCE}}$ to $0.5 V_{\text{SCE}}$ at a scan rate of 20 mV/s in aerated 0.1 M HF solution. Cycles 1-4 are shown. Numbers indicate cycle number for amorphous $\text{Cu}_{75}\text{Hf}_{20}\text{Dy}_{05}$. The arrow indicates increasing cycle number for crystalline $\text{Cu}_{75}\text{Hf}_{20}\text{Dy}_{05}$ 93

- Figure 3.12. Cyclic voltammograms of amorphous and crystalline $\text{Cu}_{75}\text{Hf}_{20}\text{Dy}_{05}$ from $-0.25 V_{\text{SCE}}$ to $0.5 V_{\text{SCE}}$ at a scan rate of 20 mV/s in aerated 0.1 M HF solution. The final cycle, 40, is shown..... 93
- Figure 3.13. Cyclic voltammograms of crystalline $\text{Cu}_{75}\text{Hf}_{20}\text{Dy}_{05}$ from $-0.25 V_{\text{SCE}}$ to $0.5 V_{\text{SCE}}$ at a scan rate of 20 mV/s in aerated 0.1 M HF solution. Cycles plotted are 1-20 (top) and 16-40 (bottom). Arrows tracks the maximum current density during a given cycle and direction indicates increasing cycle number..... 94
- Figure 3.14. Cyclic voltammograms of amorphous $\text{Cu}_{75}\text{Hf}_{20}\text{Dy}_{05}$ from $-0.25 V_{\text{SCE}}$ to $0.5 V_{\text{SCE}}$, scan rate 20 mV/s, in aerated 0.1 M HF solution. Cycle 6-13, selected cycles represented, show the growth of peak at $250 \text{ mV}_{\text{SCE}}$ during the downward scan. Dashed lines indicate scan direction..... 95
- Figure 3.15. Cyclic voltammograms of amorphous $\text{Cu}_{75}\text{Hf}_{20}\text{Dy}_{05}$ from $-0.25 V_{\text{SCE}}$ to $0.5 V_{\text{SCE}}$, scan rate 20 mV/s, in aerated 0.1 M HF solution. Cycles 13-22 show a decrease in the $250 \text{ mV}_{\text{SCE}}$ peak highlighted by the solid arrow. Dashed lines indicate scan direction..... 95
- Figure 3.16. Cyclic voltammograms of amorphous $\text{Cu}_{75}\text{Hf}_{20}\text{Dy}_{05}$ from $-0.25 V_{\text{SCE}}$ to $0.5 V_{\text{SCE}}$, scan rate 20 mV/s, in aerated 0.1 M HF solution. Cycles 22-40, selected cycles represented, show a decrease in current density to the stable E-i behavior. Dashed lines indicate cycle direction..... 96
- Figure 3.17. Calculated charge density per cycle of amorphous and crystalline $\text{Cu}_{75}\text{Hf}_{20}\text{Dy}_{05}$ alloys during cyclic voltammetry from -0.25 to $0.5 V_{\text{SCE}}$ at 20 mV/s. High purity polycrystalline Cu and Hf are also shown. Dy is not shown because the charge density is less than 0.0001 C/cm^2 96
- Figure 3.18. Anodic current density vs. time behavior of amorphous and crystalline $\text{Cu}_{75}\text{Hf}_{20}\text{Dy}_{05}$ alloys and the high purity polycrystalline alloying elements subjected to potentiostatic polarization at $-150 \text{ mV}_{\text{SCE}}$ in aerated 0.1 M HF solution..... 103
- Figure 3.19. Anodic current density vs. time behavior measurements of analogous large ribbon samples large ribbon (surface area approximately $0.1\text{-}0.25 \text{ cm}^2$) specimens of amorphous and crystalline $\text{Cu}_{75}\text{Hf}_{20}\text{Dy}_{05}$ alloys subjected to potentiostatic polarization at $-150 \text{ mV}_{\text{SCE}}$ in aerated 0.1 M HF solution. 103
- Figure 3.20. Anodic current density vs. time behavior measurements of amorphous and crystalline $\text{Cu}_{75}\text{Hf}_{20}\text{Dy}_{05}$ alloy specimens subjected to potentiostatic polarization at $-150 \text{ mV}_{\text{SCE}}$ in aerated 0.1 M HF solution. The initial 7200 seconds are shown. Numbers identify exposure repetition..... 104
- Figure 3.21. Anodic current density vs. time behavior measurements of amorphous and crystalline $\text{Cu}_{75}\text{Hf}_{20}\text{Dy}_{05}$ alloy specimens subjected to potentiostatic polarization at $-150 \text{ mV}_{\text{SCE}}$ in aerated 0.1 M HF solution for up to 20,000 seconds. Numbers identify exposure repetition. 105
- Figure 3.22. Total accumulated anodic charge density of amorphous and crystalline $\text{Cu}_{75}\text{Hf}_{20}\text{Dy}_{05}$ during potentiostatic polarization at $-150 \text{ mV}_{\text{SCE}}$ in 0.1 M HF solution. Error bars represent 1 standard deviation. 106

- Figure 3.23. XRD spectra of the amorphous $\text{Cu}_{75}\text{Hf}_{20}\text{Dy}_{05}$ after potentiostatic polarization at $-150 \text{ mV}_{\text{SCE}}$ in 0.1 M HF solution. Spectra are shown with increasing total anodic charge. The peaks for polycrystalline Cu are shifted $+0.2^\circ$ are labeled. 107
- Figure 3.24. XRD spectra of the crystalline $\text{Cu}_{75}\text{Hf}_{20}\text{Dy}_{05}$ after potentiostatic polarization at $-150 \text{ mV}_{\text{SCE}}$ in 0.1 M HF solution shown in Figure 3.21. Spectra organized by the total anodic charge and time of exposure. The peaks for polycrystalline Cu (no shift) are also labeled. 107
- Figure 3.25. SEM micrograph of the post exposure surface of the amorphous $\text{Cu}_{75}\text{Hf}_{20}\text{Dy}_{05}$ specimen with 6.47 C/cm^2 of total accumulated charge during potentiostatic polarization at $-150 \text{ mV}_{\text{SCE}}$ in 0.1 M HF solution for 20 ks. 108
- Figure 3.26. SEM micrograph of the post exposure surface of the crystalline $\text{Cu}_{75}\text{Hf}_{20}\text{Dy}_{05}$ specimen with 3.05 C/cm^2 of total accumulated charge during potentiostatic polarization at $-150 \text{ mV}_{\text{SCE}}$ in 0.1 M HF solution for 20 ks. 108
- Figure 3.27. SEM micrographs of the crystalline $\text{Cu}_{75}\text{Hf}_{20}\text{Dy}_{05}$ dealloyed specimen cross section potentiostatically polarized at $-0.15 \text{ V}_{\text{SCE}}$ in 0.1 M HF solution. Duration and total accumulated charge was 4.2 ks - 0.007 C/cm^2 (a), 7.2 ks - 0.461 C/cm^2 (b), and 20 ks - 3.05 C/cm^2 (c). 109
- Figure 3.28. SEM micrographs of the amorphous $\text{Cu}_{75}\text{Hf}_{20}\text{Dy}_{05}$ dealloyed specimen cross section potentiostatically polarized at $-0.15 \text{ V}_{\text{SCE}}$ in 0.1 M HF solution. Duration and total accumulated charge was 7.2 ks - 1.15 C/cm^2 (d), 8.8 ks - 2.29 C/cm^2 (e), and 20 ks - 6.47 C/cm^2 (f). 110
- Figure 3.29. Dealloyed layer thickness as a function of the total anodic charge accumulated during potentiostatic polarization at $-0.15 \text{ V}_{\text{SCE}}$ in 0.1 M HF solution for amorphous (Figure 3.23) and crystalline (Figure 3.24) $\text{Cu}_{75}\text{Hf}_{20}\text{Dy}_{05}$. The dealloyed layer thickness is measured by ex-situ cross section SEM images of the dealloyed layer. Average dealloyed layer thickness is marked while error bars indicate the min and max measured values. The linear fit of the data has a slope of $2.04 \mu\text{m} / (\text{C/cm}^2)$ and a correlation coefficient of 0.9946. 111
- Figure 3.30. EDS line profiles through the two dealloyed regions of the amorphous $\text{Cu}_{75}\text{Hf}_{20}\text{Dy}_{05}$ ribbon potentiostatically polarized at $-0.15 \text{ V}_{\text{SCE}}$ in 0.1 M HF solution (point *f* - 6.05 C/cm^2 , 20ks). The indicated direction, left to right, on the SEM micrographs is followed in the EDS composition plots. Dashed lines indicate the composition of the parent ribbon established by area scans on the cross section of the middle region: Cu 73.4 at%, Hf 20.7 at %, and Dy 6.0 at %. EDS spectra of dealloyed regions of crystalline specimen *c*, not shown here, indicate enriched concentrations of Cu and Dy at 81.1 and 7.6 at%, respectively, while the Hf concentration is 0.7 at%. 112
- Figure 3.31. Distribution functions for mobile atom formation enthalpies on crystalline and amorphous materials under a given driving force (T, or in this case applied potential). Adapted from [34], with permission from Elsevier BV. 121
- Figure 4.1. Fe-Pd binary phase diagram. The solid line indicates the equiatomic $\text{Fe}_{50}\text{Pd}_{50}$ composition and the marked solid circles indicate, at 898 K (625°C), the ordered L1_0 structure and the high temperature austenite, γ , disordered fcc phase. Earlier

versions of the phase diagram show a slight variation in the eutectoid temperature at 878 K (605 °C) [12]. The dashed lines indicate the Fe₇₀Pd₃₀ and Fe₆₅Pd₃₅ compositions. The solid squares indicate the annealing temperature for the disordered fcc phase (Fe₆₅Pd₃₅) and the bct martensite (Fe₇₀Pd₃₀)..... 131

Figure 4.2. Combined Fe-Pd potential-pH equilibrium diagram for Fe/Pd -H₂O system at 25°C and ion concentrations assumed to be 10⁻⁶ [16]. For the Fe and Pd system non-hydroxides are considered. Note the Fe diagram is actually curved at the intersection between the Fe²⁺, Fe³⁺ and Fe₂O₃ species. 134

Figure 4.3. Fe Oxide Stability Diagram for Fe₂O₃ (red, right axis) and Fe(OH)₂ (black, left axis) at 25°C and considering only Fe-H₂O system [16]. The oxide stability shows that at low pH Fe₂O₃ is the dominant oxide but only at high potentials where Fe³⁺ is the stable species. At high pH the minimum concentration required for formation of the Fe(OH)₂ is at pH 11..... 134

Figure 4.4. Calculated potential-pH equilibrium diagram for the Pd/Cl⁻-H₂O system at 25°C. The series of regions (white, then shaded) indicate the thermodynamically stable region PdCl₄²⁻ at Cl⁻ concentrations of 1 M, 0.1 M and 0.01 M. The Pd²⁺ concentration assumed to be 10⁻⁶ M. Calculated using Medusa [17]. 136

Figure 4.5. Optical micrograph of the Fe₇₀Pd₃₀ microstructure after annealing at annealed at 1100 °C for 100 hours and water quenched. The microstructure was revealed by chemically etching using a mixture of 60 vol% concentrated hydrochloric acid (HCl) and 40% concentrated nitric acid (HNO₃)..... 141

Figure 4.6. X-ray diffraction spectrum of Fe₇₀Pd₃₀ after annealing at 1100 °C for 100 hours and water quenched. Indexed diffraction peaks correspond to a bcc structure with lattice parameter 0.298 nm and site occupancy factors of 0.7 for Fe and 0.3 for Pd. The calculated density based on the crystal structure is 8.912 g/cm³..... 142

Figure 4.7. X-ray diffraction spectrum for Fe₅₀Pd₅₀ and Fe₆₅Pd₃₅ after annealing at 950 °C for 10 hours and water quench. The spectra for both compositions index as the fcc γ structure with allowed lattice reflections marked. The peak intensity of the Fe₅₀Pd₅₀ sample is the expected trend based for a polycrystalline powder sample. The difference in intensity for the Fe₆₅Pd₃₅ sample implies a change texture (i.e., change in prevalence of grains and their size which is likely due to the Fe₆₅Pd₃₅ sample being smaller and having less interaction volume). The calculated density of Fe₆₅Pd₃₅ is 8.874 g/cm³ and for Fe₅₀Pd₅₀ is 9.790 g/cm³..... 143

Figure 4.8. Optical micrograph, with increased contrast, of the Fe₆₅Pd₃₅ sample after electrochemical etching by anodic polarization in 0.1 M HCl solution. The grain size ranged from 5 to 100 μ m with an average grain size of about 28 μ m..... 144

Figure 4.9. SEM micrograph of the Fe₅₀Pd₅₀ sample after electrochemical etching by polarization in 0.1 M HCl solution at 0.45 V_{SCE} for 400 s. An electron backscattered diffraction map (EBSD) of the grain orientations in the sample surface normal direction is also shown to better illuminate grains. The average grain size is 26 μ m. A detailed analysis of significance of the orientation on dissolution behavior in HCl solution will be discussed in detail in Chapter 6. .. 144

- Figure 4.10. E-log*i* behavior in 0.01 M HCl solution at a scan rate of 1 mV/s. For clarity only the anodic portion of the cyclic polarization curve is shown for all alloys except Fe₇₀Pd₃₀. The full scan is shown to show the post activation behavior. For reference, the potentials of various oxidation reactions are shown (solid lines) at pH 2 and species concentrations of 10⁻⁶ M. 148
- Figure 4.11 Optical micrographs for Fe₇₀Pd₃₀ (left), Fe₆₅Pd₃₅ (center) and Fe₅₀Pd₅₀ (right) after cyclic polarization (Figure 4.10) in deaerated 0.1 M HCl solution showing characteristic surface features. The Fe₇₀Pd₃₀ exhibits grain boundary dissolution and pits initiated along grain boundaries. Fe₆₅Pd₃₅ microstructure exhibits numerous pitting events. The Fe₅₀Pd₅₀ microstructure shows small pitting events. Note that while the Fe₇₀Pd₃₀ sample underwent dissolution at lower applied potentials, the total charge accumulated is less than the case of the Fe₆₅Pd₃₅ resulting in less overall dissolution..... 148
- Figure 4.12. Cyclic E-log*i* behavior in deaerated 0.1 M HCl solution at a scan rate of 1 mV/s (direction indicated by arrows). The current for high purity polycrystalline Fe is above the current cutoff threshold and is represented by a single point. A potentiostatic polarization at 0.3 V_{SCE}, indicated by the dashed line, is shown in Figure 4.15. For reference, the potentials of various oxidation reactions are shown (solid lines) at pH 1 and species concentrations of 10⁻⁶ M. Oxidation of Fe to aqueous Fe²⁺ cation occurs at -0.86 V_{SCE}..... 149
- Figure 4.13. Optical micrographs for Fe₇₀Pd₃₀ (left), Fe₆₅Pd₃₅ (center) and Fe₅₀Pd₅₀ (right) after cyclic polarization (Figure 4.12) in deaerated 0.1 M HCl solution showing characteristic surface features. The Fe₇₀Pd₃₀ surface shows cracking indicative of reduced volume during preferential dissolution of Fe. Fe₆₅Pd₃₅ shows crystallographically dependent dissolution while for the Fe₅₀Pd₅₀ alloy the dissolution is predominantly uniform. The dissolution behavior of Fe₅₀Pd₅₀ at higher HCl solution concentrations is similar to Fe₆₅Pd₃₅ seen here (See the next section, and Chapter 5 and 6)..... 149
- Figure 4.14. Cyclic E-log*i* behavior in deaerated 1 M HCl solution at a scan rate of 1 mV/s. The dashed line on the E-log*i* plot indicates the 0.45 V_{SCE} potential used for the potentiostatic polarization experiments. For reference, the potentials of various oxidation reactions are shown (solid lines) at pH 0 and species concentrations of 10⁻⁶ M. The corrosion induced surface morphology in 1 M HCl solution is highlighted in the next section..... 150
- Figure 4.15. Representative potentiostatic polarization behavior in aerated 0.1 M HCl solution at an applied potential of 0.3 V_{SCE} over the initial 600 s of exposure. The total charge for Fe₇₀Pd₃₀ is 26.15 C/cm² (600s exposure). The other two alloys were polarized for 1800s and for Fe₆₅Pd₃₅, the total charge 0.07 C/cm², and for Fe₅₀Pd₅₀ the total charge is 0.01 C/cm². 152
- Figure 4.16. XPS depth profiles for Fe₅₀Pd₅₀ and Fe₆₅Pd₃₅. Fe₅₀Pd₅₀ shows little if any Pd enrichment in the first 100 equivalent nm. Fe₆₅Pd₃₅ shows 5% Pd enrichment at the surface layer. There appears to be a shift between the measured concentrations and the bulk concentrations by -5% for Pd and +5% for Fe. For

- Fe₇₀Pd₃₀, Pd is enriched to a composition of about 60% Pd at an equivalent depths 1000 nm. 152
- Figure 4.17. SEM micrograph and EDS line (inset) of Fe₇₀Pd₃₀ scan after potentiostatic polarization in 0.1 M HCl solution at 0.3 V_{SCE}. The line scan is across the interface of the lacquered region (dotted line) which is protected from solution to the exposed area. The x-axis of the EDS line scan corresponds with position along the marked line scan indicated by the arrow. In the lacquered region the composition is Fe₆₈Pd₃₂ approximately the bulk composition. The initial dealloyed region between 50 and 100 μm followed an unexposed region due to coverage of the lacquer. Spikes in the composition values correspond to the cracked areas along the surface. A working distance of 15 mm and 15 kV accelerating voltage was utilized for both the image and EDS analysis..... 154
- Figure 4.18. XRD of the exposed Fe₇₀Pd₃₀ shows a mixture of the parent martensitic phase (indicated by the red pre-exposure pattern) and pure Pd (fcc). This spectrum indicates that significant preferential dissolution of iron has occurred and the remaining Pd atoms have reorganized to the form a fcc Pd structure within the first 5 μm of depth. There is a 0.6° phase shift to smaller 2θ after exposure indicating a shift more Pd in the martensitic structure. As the Pd alloying amount in bcc Fe increases from ferrite to Fe₉₇Pd₃ the bcc peaks shift to lower 2θ..... 154
- Figure 4.19. Representative potentiostatic polarization behavior in deaerated 1 M HCl solution at an applied potential of 0.45 V_{SCE} for 400 s for Fe₅₀Pd₅₀ and 200 s for Fe₇₀Pd₃₀ and Fe₆₅Pd₃₅. The total accumulated charge density is 66.36, 7.51, and 3.99 C/cm² for Fe₇₀Pd₃₀, Fe₆₅Pd₃₅, and Fe₅₀Pd₅₀, respectively. 156
- Figure 4.20. SEM micrograph (left) and EDS line (right) scan of Fe₇₀Pd₃₀ after potentiostatic polarization in 1 M HCl solution at 0.45 V_{SCE} for 200 s with total accumulated charge of 66.3 C/cm². The line scan, indicated by the arrow, is across the interface of the lacquered region (on the left) which is protected from solution. The Fe₆₅Pd₃₅ surface undergoes preferential dissolution of Fe. The accelerating voltage for both the image and EDS analysis is 15 kV and working distance of 15 mm. 157
- Figure 4.21. SEM micrograph (left) and EDS line (right) scan of Fe₆₅Pd₃₅ after potentiostatic polarization in 1 M HCl solution at 0.45 V_{SCE} for 200 s with total accumulated charge of 7.52 C/cm². The SEM micrograph indicates some grain specific faceted behavior after dissolution. The line scan, indicated by the arrow, is across the interface of the lacquered region (on the left) which is protected from solution. No significant qualitative compositional variations are observed between the protected and dissolved areas. The accelerating voltage for both the image and EDS analysis is 15 kV and working distance of 15 mm. 157
- Figure 4.22. SEM micrograph (left) and EDS line (right) scan of Fe₅₀Pd₅₀ after potentiostatic polarization in 1 M HCl solution at 0.45 V_{SCE} for 400 s with total accumulated charge of 3.99 C/cm². The SEM micrograph indicates grain specific faceted behavior after dissolution. The line scan, indicated by the arrow, is across the interface of the lacquered region (on the left) which is protected from solution. No significant qualitative compositional variations are observed between the

- protected and dissolved areas. The accelerating voltage for both the image and EDS analysis is 15 kV and working distance of 15 mm. 158
- Figure 4.23. SEM micrograph of Fe₆₅Pd₃₅ (top) and Fe₅₀Pd₅₀ (bottom) after potentiostatic polarization in 1 M HCl solution at 0.45 V_{SCE}. Fe₆₅Pd₃₅ was polarized for 200 s with 7.52 C/cm² total accumulated charge and Fe₅₀Pd₅₀ was polarized for 400 s with total accumulated charge of 3.99 C/cm². The Fe₅₀Pd₅₀ microstructure shows distinct dissolution induced grain faceted morphologies and lower dissolution than the Fe₆₅Pd₃₅. The Fe₆₅Pd₃₅ microstructure has similar grain dependent faceted morphology to the Fe₅₀Pd₅₀ but the differences in grain specific dissolution are less pronounced. 159
- Figure 4.24. Cyclic E-log*i* behavior in 0.06 M NaCl solution at pH 6 at a scan rate of 1 mV/s. For reference, the potentials of various oxidation reactions are shown (solid lines) at pH 6 and species concentrations of 10⁻⁶ M. The Fe oxidation reaction to Fe²⁺ reaction occurs at -0.86 V_{SCE}. 162
- Figure 4.25. Cyclic E-log*i* behavior in 0.6 M NaCl solution at pH 6 at a scan rate of 1 mV/s. For reference, the potentials of various oxidation reactions are shown (solid lines) at pH 6 and species concentrations of 10⁻⁶ M. Fe oxidation to Fe²⁺ occurs at -0.86 V_{SCE}. No Pd-Cl⁻ complex is formed at this pH. 163
- Figure 4.26. Optical micrographs for Fe₇₀Pd₃₀ (left), Fe₆₅Pd₃₅ (center) and Fe₅₀Pd₅₀ (right) after cyclic polarization in deaerated 0.6 M NaCl solution (Figure 4.12) showing characteristic surface features. The apex potentials were between 0.4 and 0.5 V_{SCE}. The Fe₇₀Pd₃₀ surface shows large pits (due, in part, to the large anodic charge due to lack of repassivation) and regions of increased corrosion damage. Fe₆₅Pd₃₅ and Fe₅₀Pd₅₀ show pitting corrosion but generally pitting events on Fe₅₀Pd₅₀ are smaller and have a lower density than Fe₅₀Pd₃₅. 163
- Figure 4.27. Cyclic E-log*i* behavior in 2 M NaCl at pH 11.0 with a scan rate of 1 mV/s. For reference, the potentials of various oxidation reactions are shown (solid lines) at pH 11 and species concentrations of 10⁻⁶ M. The Fe/Fe(OH)₂ reaction occurs at -0.94 V_{SCE}, Fe/Fe₃O₄ occurs at -0.98 V_{SCE}, and hydrogen evolution (H⁺/H₂) occurs at -0.90 V_{SCE}. 165
- Figure 4.28. Open circuit before and after cyclic before (left) and after (right) cyclic polarization 2 M NaCl pH 11.0. For reference, the potentials of various oxidation reactions are shown (solid lines) at pH 6 and species concentrations of 10⁻⁶ M. Prior to polarization the open circuit of the alloys increase with increasing Pd concentration. After the experiment, the open circuit potential of Pd, Fe₅₀Pd₅₀ and Fe₆₅Pd₃₅ follow a similar trend, while Fe and Fe₇₀Pd₃₀ exhibit similar behavior. 165
- Figure 4.29. Optical micrographs of Fe₇₀Pd₃₀ (top left), Fe₆₅Pd₃₅ (top right), Fe₅₀Pd₅₀ (bottom left and SEM, bottom right) surface after cyclic polarization in 2 M NaCl solution at pH 11. The Fe₆₅Pd₃₅ and Fe₇₀Pd₃₀ alloys show behavior dominated by pitting events. In the Fe₅₀Pd₅₀ alloy (SEM image, bottom right) the surface shows uniform dissolution type behavior with some grain dependent morphological features. Some pit-like regions of increased dissolution relative to the neighboring

- region (sub grain sized) is also present. The surface of the Fe₅₀Pd₅₀ alloy shows grain dependent dissolution characteristics typical of both Fe₆₅Pd₃₅ and Fe₅₀Pd₅₀ alloys in acidic Cl⁻ solutions. 166
- Figure 5.1. Schematic model Fe₅₀Pd₅₀ fcc disordered γ phase with representative random site occupancy shown. The fcc phase (Fm-3m) has lattice constant $a=0.3804$ nm and a site occupancy factor of 0.5, the atomic ratio. The density is 9.790 g/cm³. Model created using Diamond Crystallography Software [3]. 177
- Figure 5.2. Schematic model of Fe₅₀Pd₅₀ L1₀ structure. The L1₀ phase has symmetry P4/mmm with lattice constants $a=0.3852$ nm and $c=0.3723$ nm and a density of 9.755 g/cm³. Pd atoms lie at the $c=1/2$ lattice sites while Fe atoms occupy the vertices. Model created using Diamond Crystallography Software [3]. 177
- Figure 5.3. The number of atoms at a given distance from a given atom in the disordered fcc structure. Each atom site has an occupancy of 0.5 for Fe and Pd. Interatomic distances determined using Diamond Crystallography Software [3]. 178
- Figure 5.4. The number of Fe and Pd atoms from a given atom in the ordered pT structure. Interatomic distances determined using Diamond Crystallography Software [3]. 178
- Figure 5.5. X-ray diffraction spectrum of the disordered fcc Fe₅₀Pd₅₀ sample after annealing at 950 °C for 10 hours and water quenched. The 5 indexed peaks all corresponded to the fcc γ -phase structure with lattice parameter $a = .3804$ nm and site occupancy coefficient of 0.5 for both Fe and Pd. 181
- Figure 5.6. X-ray diffraction spectrum of the ordered pT Fe₅₀Pd₅₀ sample after annealing at 605 °C for 30 days and water quenched. The indexed peaks, indicated by vertical dashes and labeled, corresponded to the pT L1₀ phase which has space group P4/mmm with lattice constants $a=3.852$ Å and $c=3.723$ Å. [1]. In the L1₀ structure, Pd atoms occupy the $c=1/2$ lattice positions and Fe atoms at the unit cell corners. 182
- Figure 5.7. SEM micrographs of the polytwinned structure in pT Fe₅₀Pd₅₀ after potentiostatic polarization at 0.45 V_{SCE} for 400 s and a total accumulated charge density of 10.5 C/cm². 182
- Figure 5.8. Open circuit potential (top) and E-log*i* behavior (bottom) in deaerated 0.5 M H₂SO₄ solution at a scan rate of 1 mV/s. Dashed lines indicate the potential range for cyclic voltammetry potential sweep. For reference, the potentials of various oxidation reactions are shown (solid lines) at pH 1 and species concentrations of 10^{-6} M. Oxidation of Fe to aqueous Fe²⁺ cation occurs at -0.86 V_{SCE}. 185
- Figure 5.9. Total anodic charge during potential cycles from -0.59 to 0.31 V_{SCE} at a scan rate of 20 mV/s in deaerated 0.1 M (top-left), 0.5 M (top-right), 1 M (bottom-left) H₂SO₄ solution. The total anodic charge is similar for both structural states in all three solution concentration. A representative plot of the open circuit behavior in 0.5 M H₂SO₄ solution is shown (bottom-right). The OCP for both fcc and pT structural states increases in all concentrations. 186

- Figure 5.10. Potentiostatic polarization in deaerated 1 M H₂SO₄ at 0.31 V_{SCE}. Both structural states show initial current decay to very small current densities and slightly higher overall current in fcc Fe₅₀Pd₅₀. The high current density on Pd is likely due to an H oxidation current density. No surface damage was observed (see appendix). 186
- Figure 5.11. Open circuit (left) and Cyclic E-log*i* (right) behavior in deaerated 0.1 M HCl solution at a scan rate of 1 mV/s (direction indicated by arrows). Dashed lines indicate potentiostatic polarization potentials. The current for high purity polycrystalline Fe is above the current cutoff threshold and is represented by a single point. For reference, the potentials of various oxidation reactions are shown (solid lines) at pH 1 and species concentrations of 10⁻⁶ M. Oxidation of Fe to aqueous Fe²⁺ is at -0.86 V_{SCE} and HER is at -0.3 V_{SCE}. 190
- Figure 5.12. Open circuit (left) and Cyclic E-log*i* (right) behavior in deaerated 1 M HCl solution at a scan rate of 1 mV/s. The dashed line on the E-log*i* plot indicates the 0.45 V_{SCE} potential used for the potentiostatic polarization experiments. For reference, the potentials of various oxidation reactions are shown (solid lines) at pH 0 and species concentrations of 10⁻⁶ M. 190
- Figure 5.13. Total accumulated anodic charge for Fe₅₀Pd₅₀ fcc and pT during a 2 hour potentiostatic polarization in 0.1 M HCl solution. The structural state with the higher charge at each potential corresponds to the state with higher current density at that potential during cyclic polarization in Figure 4.12. 191
- Figure 5.14. Through focus optical micrographs of the Pd surface after polarization to 0.9 V_{SCE} in deaerated 1 M HCl solution (Figure 5.12) showing significant Pd dissolution. 192
- Figure 5.15. Potentiostatic polarization of Pd (left) in deaerated 1 M HCl solution at 0.45 V_{SCE} for 3600 s. The optical micrograph shows little corrosion of the surface. It is worth noting that the potential was applied immediately after contact with the solution (no OCP hold) and therefore limited H charging of the Pd, see Section 5.8. 192
- Figure 5.16. Optical micrographs of the surface of pT (left) and fcc (right) Fe₅₀Pd₅₀ after polarization in deaerated 1 M HCl solution to 0.6 V_{SCE} (Figure 5.12). The pT structural state generally uniform surface morphology with region of increased morphology. The fcc structure shows grain dependent etched-like morphology. 192
- Figure 5.17. SEM micrographs of the surface morphology of fcc Fe₅₀Pd₅₀ after a 1 hour open after open circuit potential and cyclic polarization in 1 M HCl solution. Grains (top, outlines added for illustration) show crystallographic dependent dissolution characteristics. The higher magnification micrographs show ‘etch-pit’ dissolution with four-fold symmetry (lower left, right grain) and three fold symmetry (lower right) in a different grain. 193
- Figure 5.18. Potentiostatic polarization of pT Fe₅₀Pd₅₀ at 0.45 V_{SCE} in deaerated 1 M HCl solution (left). The total charge during polarization is 11.1 C/cm². The SEM

- micrograph (right) shows the post corrosion surface morphology. Some faceting is seen, but at length scales smaller than the grain size. 194
- Figure 5.19. Potentiostatic polarization of fcc Fe₅₀Pd₅₀ at 0.45 V_{SCE} in deaerated 1 M HCl solution (left). The total charge during polarization is 2.2 C/cm². The SEM micrograph (right) shows the post corrosion surface morphology which indicates a strong grain dependence..... 194
- Figure 5.20. SEM micrograph (left) and EDS line (right) scan of fcc Fe₅₀Pd₅₀ after potentiostatic polarization in 1 M HCl solution at 0.45 V_{SCE} for 400 s with total accumulated charge of 3.99 C/cm². The SEM micrograph indicates grain specific faceted behavior after dissolution. The line scan, indicated by the arrow, is across the interface of the lacquered region (on the left) which is protected from solution. No significant qualitative compositional variations are observed between the protected and dissolved areas..... 195
- Figure 5.21. SEM micrograph (left) and EDS line (right) scan of pT Fe₅₀Pd₅₀ after potentiostatic polarization in 1 M HCl solution at 0.45 V_{SCE} for 400 s with total accumulated charge of 6.50 C/cm². The line scan, indicated by the arrow, is across the interface of the lacquered region (on the left) which is protected from solution. No significant qualitative compositional variations are observed between the protected and dissolved areas..... 195
- Figure 5.22. E-*logi* behavior in deaerated 1 mM NaOH (pH 11) at scan rate of 1mV/s. The full scan for fcc and pT Fe₅₀Pd₅₀ is expanded on the right. For reference, the potentials of various oxidation reactions are shown (solid lines) at pH 11 and species concentrations of 10⁻⁶ M. At this pH, Fe oxidization Fe/Fe₃O₄ is at -0.98 V_{SCE} and HER is at -0.89 V_{SCE}. 196
- Figure 5.23. Fe₅₀Pd₅₀ E-*logi* behavior in deaerated 2 M NaCl + 1 mM NaOH solution (pH 11) at 1mV/s. For reference, the potentials of various oxidation reactions are shown (solid lines) at pH 11 and species concentrations of 10⁻⁶ M. At this pH, Fe oxidization Fe/Fe₃O₄ occurs at -0.98 V_{SCE} and the reversible potential for HER occurs at -0.89 V_{SCE}. 198
- Figure 5.24. Optical micrographs (top) and SEM micrographs (bottom) of Fe₅₀Pd₅₀ fcc (left) and pT (right) surface after cyclic polarization in 2 M NaCl solution at pH 11 to a peak potential of about 0.65 V_{SCE} (Figure 5.23). In the fcc structure areas showing pit-like features, but is dominated by grain dependent dissolution characteristics typical of the fcc structure Cl⁻ solutions. The pT shows some grain dependence in its dissolution behavior but the morphology is predominantly more uniform type corrosion..... 199
- Figure 5.25. Cyclic E-*logi* behavior in 0.06 M NaCl solution at pH 6 at a scan rate of 1 mV/s. For reference, the potentials of various oxidation reactions are shown (solid lines) at pH 6 and species concentrations of 10⁻⁶ M. The Fe/Fe²⁺ (aq) reaction is at -0.86 V_{SCE} and hydrogen evolution (H⁺/H₂) reaction is at -0.60 V_{SCE}. No Pd-Cl⁻ complex is formed at this pH. 200
- Figure 5.26. SEM micrographs for fcc Fe₅₀Pd₅₀ (left) and pT Fe₅₀Pd₅₀ (right) after cyclic polarization in deaerated 0.6 M NaCl solution (Figure 4.24) showing

- characteristic surface features. The accelerating voltage is 15 kV and working distance is 15 mm..... 200
- Figure 5.27. Cyclic E-log*i* behavior in 0.6 M NaCl solution at pH 6 at a scan rate of 1 mV/s. For reference, the potentials of various oxidation reactions are shown (solid lines) at pH 6 and species concentrations of 10^{-6} M. Fe oxidation to Fe^{2+} occurs at $-0.86 \text{ V}_{\text{SCE}}$. No Pd-Cl⁻ complex is formed at this pH..... 201
- Figure 5.28. Optical micrographs for fcc Fe₅₀Pd₅₀ (left) and pT Fe₅₀Pd₅₀ (right) after cyclic polarization in deaerated 0.6 M NaCl solution (Figure 4.25) showing characteristic surface features. The apex potentials were between 0.4 and 0.5 V_{SCE}. Both structural states exhibit pitting behavior. 201
- Figure 5.29. Cyclic E-log*i* behavior in deaerated 1 M HCl solution at 1 mV/s. The sample was initially conditioned by charging at $0.2 \text{ V}_{\text{SCE}}$ for 8 hours to remove any absorbed H. The initial cycle began at $0.1 \text{ V}_{\text{SCE}}$, an over-potential to the H_{abs} reaction, and cycled to $0.4 \text{ V}_{\text{SCE}}$. The polarization behavior is non-Faradaic and is the capacitive current ($i = C \cdot dV/dt$) on Pd. The downward scan to $-0.5 \text{ V}_{\text{SCE}}$ induces H absorption ($\text{H}^+ + e^- \rightarrow \text{H}_{\text{abs}}$) and the subsequent cycle shows an increase in the current density due to the H_{abs} oxidation to H⁺ oxidation reaction..... 211
- Figure 5.30. Pd current vs. time behavior during alternating H charging and discharging cycles as a function of charging duration. H charging was performed using potentiostatic polarization at $-0.35 \text{ V}_{\text{SCE}}$ (under potential -0.15 V) and H discharge cycles at $0.2 \text{ V}_{\text{SCE}}$ (over potential $0.2 \text{ V}_{\text{SCE}}$). At 3600 s, the current during discharge decays to $6 \cdot 10^{-5}$, and at 18 ks (not shown) the current decays to steady state at $2.4 \cdot 10^{-5} \text{ A/cm}^2$. At 36 ks, the current showed limited decay to $1.28 \cdot 10^{-5} \text{ A/cm}^2$ 211
- Figure 5.31. Pd current- \sqrt{t} dependence during the discharge cycles at $0.2 \text{ V}_{\text{SCE}}$ in deaerated 1 M HCl solution. The current increases with respect to charging time. The slope of the discharging current is linear (with respect to \sqrt{t}) from 10 to 30 $\sqrt{\text{s}}$. The slopes of after both charging cycles is about $1 \cdot 10^{-5} \text{ A} \cdot \text{cm}^2/\text{s}^{1/2}$ 212
- Figure 5.32. E-log*i* behavior in in deaerated 1 M HCl solution with likely operating reactions illustrated. The Tafel slope of the HER assumed to be 118 mV/decade and corrosion current density is 10^{-5} A/cm^2 . The hypothetical Pd oxidation reaction (Pd/PdCl_4^{2-}) has a 59mV/decade Tafel slope and exchange current density of 10^{-7} A/cm^2 . The limiting current density, i_{lim} , is about $1 \cdot 10^{-3} \text{ A/cm}^2$. Based on the observed behavior, it is likely that the HER reaction has a very high exchange current density (10^{-4} A/cm^2 [8]) while the Pd oxidation reaction has a much lower exchange current density..... 214
- Figure 5.33. Open circuit behavior in 0.01, 0.1 and 1 M HCl solution for Fe₅₀Pd₅₀ fcc (upper left), Fe₅₀Pd₅₀ pT (upper right), and Pd (lower left). The τ - concentration plot (lower right) shows the time until a change in convexity of the potential rise during the open circuit exposures as a function of HCl solution concentration. The open circuit potential of the Fe₅₀Pd₅₀ pT structure rises more rapidly than the fcc structure..... 217

- Figure 6.1. The virtual sample chamber shows the specimen - microscope orientation configuration for EBSD characterization. The three coordinate systems are identified by their subscripts: m indicates the microscope orientation, 0 is the specimen primary orientation, and l is the orientation of EBSD acquisition. During EBSD acquisition, the specimen rotated about the y_m and y_0 axis to a tilt of 70° 228
- Figure 6.2. The Bunge Euler angle convention is depicted by the coincident axes (X_0, Y_0, Z_0) and the three rotations: ϕ_1, Φ, ϕ_2 . The angle between the surface normal direction (for Cubic crystals $\langle hkl \rangle$) and the $\{100\}$ plane normal is defined by Φ . Figure adapted from [18]. 229
- Figure 6.3. Inverse pole figure (IPF) coloring scheme to represent crystal orientations. 229
- Figure 6.4. Schematic representation of $\{hkl\}$ positions defined by the angular distance, β_i , from the 3 low index cubic planes: $\{100\}$, $\{110\}$ and $\{111\}$. α_i represents the angle between β_i and the linear lines between the $\{100\}$ and $\{110\}$ poles for $\alpha_{\{100\}}$ and $\alpha_{\{110\}}$ and between the $\{100\}$ and $\{111\}$ poles for $\alpha_{\{111\}}$. As in *Nicolas* [19]. 229
- Figure 6.5. X-ray diffraction spectrum of the disordered fcc $\text{Fe}_{50}\text{Pd}_{50}$ sample after annealing at 950°C for 10 hours and water quenched. The 5 indexed peaks all corresponded to the fcc γ -phase structure with lattice parameter $a = .3804\text{ nm}$ and site occupancy coefficient of 0.5 for both Fe and Pd. 236
- Figure 6.6. X-ray diffraction spectrum of the ordered pT $\text{Fe}_{50}\text{Pd}_{50}$ sample after annealing at 605°C for 30 days and water quenched. The indexed peaks, indicated by vertical dashes and labeled, corresponded to the pT $L1_0$ phase which has space group $P4/mmm$ with lattice constants $a=3.852\text{\AA}$ and $c=3.723\text{\AA}$. [22]. The transformation from fcc γ -phase to $L1_0$ involves Pd atoms occupying the $c=1/2$ lattice positions and Fe atoms at the vertices. 236
- Figure 6.7. Open circuit (left) and $E\text{-log } i$ (right) behavior in deaerated 1 M HCl solution at a scan rate of 1 mV/s. The dashed line on the $E\text{-log } i$ plot indicates the 0.45 V_{SCE} potential used for the potentiostatic polarization experiments. 241
- Figure 6.8. Representative $i - \text{time}$ behavior of ordered-fcc and disordered-pT during potentiostatic polarization at 0.45 V_{SCE} in deaerated 1 M HCl solution. 241
- Figure 6.9. CLSM topographical plot of disordered fcc $\text{Fe}_{50}\text{Pd}_{50}$, Region 1 after potentiostatic polarization at 0.45 V_{SCE} in deaerated 1 M HCl solution with total accumulated charge 3.29 C/cm^2 (Exposure 2, Table 6.2). Numbers indicate specific grains used to identify regions in micrographs, with properties listed in Table 6.3. 248
- Figure 6.10. EBSD mapping (left) and corresponding reduced IPF (right) of Region 1 in the sample normal direction with an EBSD step size of $1\text{ }\mu\text{m}$. Black points on the EBSD map indicate areas that failed to index to a grain orientation. 248
- Figure 6.11. SEM micrographs from Region 1 of disordered fcc $\text{Fe}_{50}\text{Pd}_{50}$, with 3.29 C/cm^2 of total anodic charge and select grains identified. Grains 1 and 7 are within 10° of the $\{100\}$ plane normal. Grain 6 is within 5° of the $\{111\}$, while

Grains 2 and 8 are about 15° from the $\{111\}$. Grains 4 and 10 are within 15° of the $\{110\}$ plane normal. Grain orientation approximate $\{hkl\}$: Grain 1 $\{610\}$, Grain 2 $\{533\}$, Grain 3 $\{310\}$, Grain 4 $\{430\}$, Grain 5 $\{621\}$, Grain 6 $\{665\}$, Grain 7 $\{611\}$, Grain 8 $\{533\}$, Grain 9 $\{520\}$, and Grain 10 $\{530\}$ 249

Figure 6.12. CLSM topographical plot of Region 2 of disordered fcc $\text{Fe}_{50}\text{Pd}_{50}$ after potentiostatic polarization at $0.45 V_{\text{SCE}}$ in deaerated 1 M HCl solution with total accumulated charge of 3.46 C/cm^2 (Exposure 1, Table 6.2). Numbers indicate specific grains used to identify regions in micrographs, with properties listed in Table 6.3. 250

Figure 6.13. EBSD mapping (left) and corresponding reduced IPF (right) of Region 2 in the sample normal direction. EBSD step size $1 \mu\text{m}$. Black points on the EBSD map indicate steps that failed to index. Grain 14, indicated by the dashed circle in the IPF, has orientation near $\{123\}$ and is white on the IPF. 250

Figure 6.14. SEM micrograph of Region 2 of disordered fcc $\text{Fe}_{50}\text{Pd}_{50}$ with 3.46 C/cm^2 of total anodic charge and grains 11-16 identified. Grain 11 is within 2° of the $\{100\}$ plane normal. Grain 12, 13, and 15 are 1° and 6° and 14° from the $\{111\}$ plane normal, respectively. Grain 14 and 16 are 20° and 10° from the $\{110\}$ plane normal, respectively. Grain orientation approximate $\{hkl\}$: Grain 11 $\{100\}$, Grain 12 $\{111\}$, Grain 13 $\{554\}$, Grain 14 $\{421\}$, Grain 15 $\{221\}$, Grain 16 $\{641\}$, Grain 7 $\{611\}$, Grain 8 $\{533\}$, Grain 9 $\{520\}$, and Grain 10 $\{530\}$ 251

Figure 6.15. SEM micrograph of disordered fcc $\text{Fe}_{50}\text{Pd}_{50}$ grains with orientations near $\{110\}$. Grains 20, 23 and 24 have orientations within 7° of the $\{110\}$ plane normal, while 17, 19 and 21 are within 15° . These grains are a subset of Region 3 which had a total charge during potentiostatic polarization of 4.00 C/cm^2 (Exposure 3, Table 6.2). Dashed lines indicate grain boundaries of limited contrast. CLSM topographical map and EBSD maps are not shown for this region. Grain orientation approximate $\{hkl\}$: Grain 17 $\{641\}$, Grain 18 $\{531\}$, Grain 19 $\{641\}$, Grain 20 $\{540\}$, Grain 21 $\{530\}$, Grain 22 $\{542\}$, Grain 23 $\{651\}$, and Grain 24 $\{110\}$ 252

Figure 6.16. Relative dissolution depth of disordered fcc $\text{Fe}_{50}\text{Pd}_{50}$ as a function of β_i for each grain in Region 1. Each grain has the three β_i associated with the primary cube zone axis. A linear fit of $\beta_{\{100\}}$ up to 40° has a slope of $-0.064 \mu\text{m} / ^\circ$ angular deviation from $\{100\}$ excluding $\beta_{\{111\}} < 10^\circ$. The root mean square error of this fit is 0.852. This plot includes grains adjacent to Region 1 which are not shown in the plots in Figure 6.9-6.11. 253

Figure 6.17. Relative dissolution depth is plotted as a function of β_i for each grain in Region 2 (Figure 6.12-6.14). Each grain has the three β_i associated with the primary cube zone axis. A linear fit of β_{100} up to 40° has a slope of $-0.060 \mu\text{m} / ^\circ$ angular deviation from $\{100\}$, excluding $\beta_{\{111\}} < 10^\circ$. The RMS error of the linear fit is 0.955 253

Figure 6.18. Relative dissolution depth of disordered fcc $\text{Fe}_{50}\text{Pd}_{50}$ as a function $\beta_{\{100\}}$. Regions within 10° of the $\{111\}$ and $\{110\}$ plane normals are indicated by open triangle and open circle symbols, respectively. A linear fit of the data over the

- first 40°, excluding data within 10° either {100} and {110} plane normal, has a slope of -0.071 $\mu\text{m}/^\circ$ and a RMS error of 0.33. 254
- Figure 6.19. Relative dissolution depth disordered fcc Fe₅₀Pd₅₀ as a function $\beta_{\{100\}}$ of plotted for $\alpha_{\{100\}} = 0 - 10^\circ$ (in the direction of the {110} plane normal) and 35 – 45° (in the direction of the {111} plane normal). The decrease at high $\beta_{\{100\}}$ for large $\alpha_{\{100\}}$ is due to proximity to the {111} orientation. 254
- Figure 6.20. Relative dissolution depth of disordered fcc Fe₅₀Pd₅₀ as a function $\beta_{\{111\}}$. A linear fit, solid line, of the first 10° (delimited by the dashed line) has a slope of -0.24 $\mu\text{m}/^\circ$ and an intercept -0.22 μm and RMS error of 1.56. 255
- Figure 6.21. Relative dissolution depth of disordered fcc Fe₅₀Pd₅₀ as a function $\beta_{\{110\}}$. No statistically significant trend at $\beta_{\{110\}} < 20^\circ$ is observed. 255
- Figure 6.22. Relative depth of dissolution of individual disordered fcc Fe₅₀Pd₅₀ grains as a function of crystallographic orientation plotted on an equal area inverse pole figure in the sample normal (z) direction. The region with highest dissolution is between 10 and 20° from the {111} plane normal. Dashed lines indicate 10° degree increments from the three low index cube plane normals: {100}, {110} and {111}. 256
- Figure 6.23. Calculated arithmetic mean deviation surface roughness, S_a , of disordered fcc Fe₅₀Pd₅₀ plotted on an equal area inverse pole figure. The smoothest grains less than 20° from the {100} and 10° from the {111} plane normals. The roughest region is between 10 and 20° from the {111} plane normal which corresponds to the region of most dissolution (Figure 6.22). 257
- Figure 6.24. Surface morphology of three disordered fcc Fe₅₀Pd₅₀ grains after potentiostatic polarization in deaerated 1 M HCl solution for 1000 s. During polarization the total accumulated charge was 10.8 C/cm² equivalent to a calculated average depth of dissolution of 3.75 μm . Both the {100} and {111} oriented grains, Grain 12 from Figure 6.14, show characteristic scalloped morphology. The {533} oriented grain has a $\beta_{\{111\}}$ of 16°, which is one of the highest dissolution susceptible orientations. The morphologically smooth, low corroding regions cover a small fraction of the exposed surface. The larger areas have significant morphological features indicative of dissolution. 258
- Figure 6.25. CLSM topographical image of a selected region of disordered fcc Fe₅₀Pd₅₀ after potentiostatic polarization at 0.45 V_{SCE} for 2500 s and a total accumulated charge density of 48.87 C/cm². 259
- Figure 6.26. SEM micrographs of the surface morphology of disordered fcc Fe₅₀Pd₅₀ after potentiostatic polarization at 0.45 V_{SCE} for 2500 s and a total accumulated charge density of 48.87 C/cm², shown in Figure 6.25. 259
- Figure 6.27. Surface morphology of a grain disordered fcc Fe₅₀Pd₅₀ after potentiostatic polarization in deaerated 1 M HCl solution for 2500 s and a total accumulated charge density of 48.87 C/cm². After increased dissolution grains remain distinct and show a terrace-ledge type structure with additional microscopic kinks on the ledges. 260

- Figure 6.28. Surface morphology of two grains after potentiostatic polarization in deaerated 1 M HCl solution for 2500 s and a total accumulated charge density of 48.87 C/cm^2 . The terrace shows the rectangular characteristic feature seen during dissolution of $\{100\}$ orientations..... 260
- Figure 6.29. CLSM topographical image of the optical region shown in Figure 6.30 of disordered fcc $\text{Fe}_{50}\text{Pd}_{50}$ after potentiostatic polarization at $0.45 \text{ V}_{\text{SCE}}$ for 400 s and a total accumulated charge density of 10.5 C/cm^2 . Grains exhibit anisotropic total depth of dissolution during the initial stages of dissolution. 262
- Figure 6.30. Optical micrographs reveal the polytwinned structure of ordered pT $\text{Fe}_{50}\text{Pd}_{50}$ after potentiostatic polarization at $0.45 \text{ V}_{\text{SCE}}$ for 400 s and a total accumulated charge density of 10.5 C/cm^2 . The expanded image, right, of area 1 shows that the twin boundaries are preferentially dissolving. 262
- Figure 6.31. SEM micrograph of the polytwinned structure in pT $\text{Fe}_{50}\text{Pd}_{50}$ shown in Area 1 of Figure 6.30 after potentiostatic polarization at $0.45 \text{ V}_{\text{SCE}}$ for 400 s s and a total accumulated charge density of 10.5 C/cm^2 263
- Figure 6.32. SEM micrograph of an additional polytwinned grain in pT $\text{Fe}_{50}\text{Pd}_{50}$. after potentiostatic polarization at $0.45 \text{ V}_{\text{SCE}}$ for 400 s s and a total accumulated charge density of 10.5 C/cm^2 263
- Figure 6.33. Optical micrograph of pits in ordered pT $\text{Fe}_{50}\text{Pd}_{50}$ after potentiostatic polarization at $0.45 \text{ V}_{\text{SCE}}$ for a total accumulated charge density of 7.1 C/cm^2 . 263
- Figure 6.34. CLSM topographical map (left) and Optical micrograph of ordered pT $\text{Fe}_{50}\text{Pd}_{50}$ after potentiostatic polarization at $0.45 \text{ V}_{\text{SCE}}$ for 1500 s and a total accumulated charge density of 54.5 C/cm^2 . The region indicated by the dashed box on the optical micrograph corresponds to the CLSM image. 264
- Figure 6.35. CLSM topographical map of an additional region of ordered pT $\text{Fe}_{50}\text{Pd}_{50}$ after potentiostatic polarization at $0.45 \text{ V}_{\text{SCE}}$ for 1500 s and a total accumulated charge density of 54.4 C/cm^2 . Some grains show anisotropic dissolution but the surface also has 5-10 μm pits..... 264
- Figure 6.36. CLSM topographical image of a selected region of ordered pT $\text{Fe}_{50}\text{Pd}_{50}$ after potentiostatic polarization at $0.45 \text{ V}_{\text{SCE}}$ for 2500 s and a total accumulated charge density of 94.6 C/cm^2 . Pits have increased in diameter to about 20 μm 265
- Figure 6.37. SEM micrograph of the surface morphology of ordered pT $\text{Fe}_{50}\text{Pd}_{50}$ after potentiostatic polarization at $0.45 \text{ V}_{\text{SCE}}$ for 2500 s and a total accumulated charge density of 94.6 C/cm^2 265
- Figure 6.38. Box plots showing the depth of dissolution during potentiostatic polarization at $0.45 \text{ V}_{\text{SCE}}$ in 1 M HCl solution for disordered-fcc (left) and ordered-pT (right) $\text{Fe}_{50}\text{Pd}_{50}$. The solid lines in the box indicate the 25th, 50th and 75th percentiles. The extended whisker shows the 5th and 95th percentile, and the crosses (x) indicate the 1st and 99th percentile. The open square is the set average and the horizontal dashes (—) are the set minimum and maximum. The data represents the depth of dissolution as an area average of the sample surface in all cases except the fcc 400 second condition which is normalized to each grain. 268

- Figure 6.39. Plot of the minimum, maximum and average depth of dissolution for disordered fcc (solid symbols) and ordered pT (open symbols) $\text{Fe}_{50}\text{Pd}_{50}$ as function of total accumulated charge density during potentiostatic polarization at $0.45 \text{ V}_{\text{SCE}}$ in 1 M HCl solution. 268
- Figure 6.40. Calculated surface energy, γ , of Pd on the IPF (top) and as a function of $\beta_{\{100\}}$ (bottom) at $\alpha = 0$ and 45° . There is a pronounced dependence of the surface energy on α . The highest surface energy occurs at orientations around $\beta_{\{100\}} 20 - 30^\circ$ and $\alpha = 0^\circ$ for Pd. The fcc orientation energy based on MEAM calculations from Zhang [29], the calculated surface energies for bcc Fe at 0 K and 1200 K (equilibrium) based on calculations from Grochola [30] (also by the MEAM method). 276
- Figure 6.41. Surface energy anisotropy for Cu at three different annealing temperatures, adapted from [34]. Reprinted from [33] with permission from Elsevier BV. 277
- Figure 6.42. Crystallographic models of the orientations near the $\{111\}$ plane normal. $\{544\}$ is 6° from the $\{111\}$ plane normal ($\beta_{\{111\}} = 6.2^\circ$). $\{432\}$ is 15° from the $\{111\}$ plane normal and lies in the region of orientations with the highest susceptibility to dissolution. Models created using Diamond Crystallography Software (<http://www.crystalimpact.com/>)..... 283
- Figure 6.43. Crystallographic models of orientations near the $\{100\}$ plane normal: $\{100\}$ top, $\{721\}$ middle and $\{732\}$ bottom. $\{721\}$ is 17° from the $\{100\}$ plane normal ($\beta_{\{100\}} = 17.7^\circ$). $\{732\}$ is 27° from the $\{111\}$ plane normal..... 284
- Figure 6.44. Crystallographic models of the orientations near the $\{110\}$ plane normal. $\{431\}$ is 14° from the $\{100\}$ plane normal ($\beta_{\{110\}} = 13.9^\circ$). 285

List of Symbols

a	lattice constant
c	lattice constant
C_H	concentration of hydrogen
CN	coordination number
D_H	hydrogen diffusivity
E_{app}	applied potential
E^0	equilibrium half-cell potential
F	Faraday's constant
G	Gibb's free energy
H_{abs}	absorbed hydrogen
i	current density
i_0	exchange current density
I	current
i_{lim}	limited current density
n	number of electrons transferred in a reaction
NN	nearest neighbor
R	atomic radius
R	universal gas constant
S_a	arithmetic mean deviation surface roughness
t	time
T	temperature
α_i	angle α between a $\{hkl\}$ and a linear edges of the inverse pole figure
β	symmetry factor
β_i	angular distance from a $\{100\}$, $\{110\}$ or $\{111\}$ plane normal
γ	surface energy
δ	diffusion layer thickness
η	over-potential
η_{2D}	two-dimensional packing fraction of atoms around a central atom
μ	chemical potential
ν	stoichiometric coefficient
ω	solid angle occupied by atoms surrounding a central atom

1 Introduction

Generally, most crystalline alloy systems have chemical gradients at homophase and heterophase interfaces, e.g. precipitate phases, phase boundaries. Grain boundaries in multi-component alloys often have a deficiency of preferential solute or segregation of elements. Multiphase alloys, particularly containing passivating element alloying additions have insoluble phases, such as dispersoids, and can have regions of phase formation and alloying element partitioning that often serve as initiation sites for localized corrosion. These combined chemical and structural inhomogeneities serve as weak sites that can prove detrimental to the corrosion resistance. It is difficult to determine what, if any, contributory detrimental effect exists due to structural change associated with these defects because there are both compositional and structural changes at the same time.

An outstanding question in understanding the corrosion of amorphous alloys is whether the amorphous structure per se offers good corrosion resistance. Amorphous alloy systems have historically had their superior corrosion resistance attributed to several mechanisms [1, 2]. Amorphous structure lacks grain boundaries, dislocations, and precipitate phases all of which are often detrimental to corrosion resistance. Structural and chemical homogeneity prevent non-uniformities, or defects, which can serve as initiation sites for localized corrosion. Alternatively, increased solubility of beneficial solute elements can lead to the formation of a more stable oxide or a solid solution with better dissolution resistance [3, 4]. Thirdly, minor alloying elements, traditionally added for other reasons, may act in a beneficial way [5-8]. In practice, these alloys often have desirable material properties in a partially devitrified state [9]. However, partial

devitrification often results in a degradation of corrosion performance [10]. Poor corrosion performance upon devitrification is generally blamed on loss of one or more of these conditions. The role of structural defects without chemical change on corrosion properties is unclear; few studies have been conducted and their results are either inconclusive or do not provide a systematic analysis of the role structure.

The purpose of this research is to systematically study the effect of strictly nano-structural differences on uniform, passive, and localized corrosion in the absence of chemical non-uniformities. This can be achieved by choosing model homogenous solid solution alloy systems that undergo structural change without the accompanying change in chemical composition. Structural changes can consist of minute changes in structure e.g., relaxation of an amorphous alloy from a high to a low free volume state [11]. Moreover, certain disordered or amorphous alloys can devitrify to form ordered grains of the same composition embedded in an amorphous matrix. Some disordered crystalline alloys can order via a nucleation and growth phase transformation to ordered crystalline alloys. Special cases of these structurally changing systems can form both phases with the same composition. These model alloys serve as the basis for this study.

This study focuses on an amorphous alloy, $\text{Cu}_{75}\text{Hf}_{20}\text{Dy}_{05}$, which devitrifies to form a single crystalline phase of the same composition. Additionally, an order-disorder transformation in crystalline $\text{Fe}_{50}\text{Pd}_{50}$ with no change in composition between the ordered and disordered phase is studied. The corrosion behavior of these systems was systematically studied during active, passive, and passive/pitting conditions.

1.1 Metallurgical Background

To adequately study amorphous alloy structure, the effect of structural change on corrosion properties the alloy systems and their phase transformations must be well characterized and understood. Amorphous alloys result from undercooling a liquid below a critical temperature where the alloy solidifies without forming a crystalline phase. As a result, amorphous alloys have no long range order (LRO). The atomic arrangement of atoms in metallic glasses has been described by the dense random packing (DRP) geometric model in which a random arrangement of hard spheres was used to describe the pair distribution functions of binary alloys with similar atomic radii [12]. Dissimilar atomic radii can be taken into account by considering the coordination number of atoms, e.g. an atom can have more small atoms around it than large ones. Short range order (SRO) arises from the thermodynamic preferential ordering of the atoms across short length scales. Also present in amorphous structures is vacant free volume, although not in the sense of crystalline vacancies. In the free volume model [13], the unoccupied volume is described as the freely mobile areas within the lattice, i.e. no activation energy is required for redistribution. Recently free volume has been described as a relative change in coordination number of atoms from the ideal state creating bond deficiencies [14, 15]. A schematic representation of an A-B binary alloy structure is shown in Figure 1.1 for elements with dissimilar radius.

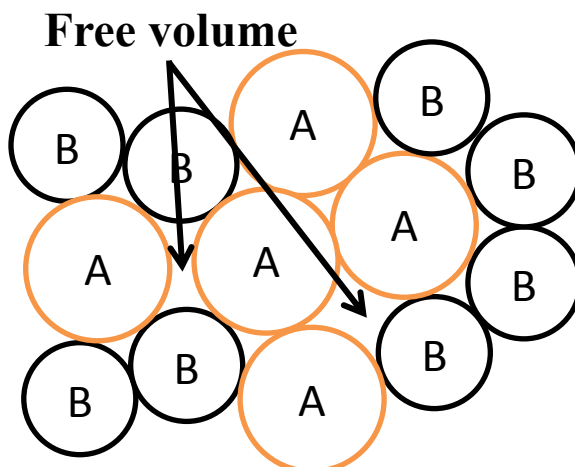


Figure 1.1. Binary A-B amorphous alloy structure with areas of increased free volume.

Structural change in amorphous alloys systems occurs during structural relaxation, and devitrification. Relaxation often involves a decrease in free volume, bond length interaction radius, or compositional rearrangement of atoms without radical changes in composition and alloying element partitioning [11, 16, 17]. Amorphous alloys can crystallize to a single phase via a massive transformation without changing composition between the disordered amorphous phase and the precipitated crystalline phase.

Crystalline alloys can also undergo a disordered to ordered crystalline phase transformation. In $\text{Fe}_{50}\text{Pd}_{50}$, both ordered ($L1_0$ structure) and disordered (fcc) phases have the same composition [18]. This system provides a good corollary system to the amorphous alloy system for the study of structure on corrosion properties.

1.1.1 Amorphous Glass Relaxation

In amorphous glasses, the atoms in the alloy are ‘frozen’ in position before the system has time to achieve an equilibrium crystal structure. Thus, amorphous alloys are disordered homogeneous solid solutions that lack the long range order present in their crystalline counterparts. Relaxation occurs when an amorphous alloy can achieve a lower

free energy through a thermally activated process without crystallization [19]. Annealing alloys below their crystallization temperature can cause diffusion of structural defects (e.g., free volume), topological short range ordering, or compositional short range ordering [16]. Topological SRO involves rearrangements of groups of atoms regardless of their chemical identities [20]. Chemical SRO occurs by short range diffusion as the atoms relax into equilibrium [16]. Relaxation can lead to pronounced changes in the Young's modulus, microhardness and other material properties [11]. Topological changes, i.e. changes in the distance between atoms, and compositional reordering are of particular interest from a corrosion standpoint. For example, a large variation in atomic distance between atoms could facilitate or inhibit dissolution, or compositional short range variations of a beneficial solute atom could affect bonding energies and, in turn, affect corrosion performance. In support of this notion is the well-known fact that a crystallographic orientation dependence on pitting corrosion has been found in Be, Zn, and Mg single crystals [21, 22]. The orientation dependence observed in these studies suggests that bond distance and coordination number is quite relevant for corrosion resistance.

The preceding discussion might lead to factors that are more prominent during active dissolution or pitting behavior as opposed to passive dissolution through an oxide film or passive film breakdown especially if the overlying passive oxide is amorphous (often the case for electrochemically grown oxides). In this case, subtle effects of relaxation might be masked by the behavior of the passive film. Thus, a systematic study of all corrosion regimes must all be considered before making statements about the role of structure.

1.1.2 Amorphous Single Phase Devitrification

Amorphous glasses can crystallize, or devitrify, to a single phase. When this phase transformation results in a change of structure without changing the composition between the parent phase and the new phase it is termed a massive transformation. Massive transformations are defined as having the following key characteristics: no chemical partitioning between phases, and occurs via a first order diffusional nucleation and growth mechanism [23, 24]. Growth of the massive phase occurs via short range atomic jumps across the parent-massive phase interface.

A schematic free energy diagram showing the driving force for compositionless transformation is shown in Figure 1.2. Devitrification from the glass along paths A, C and D can lead to transformations to a single phase. Often these phases are metastable with respect to the equilibrium phases. This is the case in devitrification path A, which produces a non-equilibrium phase of super saturated α . A lower free energy can be achieved by forming a mixture of crystalline phases α and β , e.g. metallic glass \rightarrow super saturated $\alpha \rightarrow$ equilibrium $\alpha+\beta$. In the case of devitrification path D, metallic glass $\rightarrow \beta$, the β phase is the thermodynamic equilibrium phase. Here, the phase transformation involves a structural change but no redistribution of alloying elements between the two phases and no chemical gradient. Thus, the opportunity exists to study a single phase β with the exact same composition as the parent glass phase (at composition D).

The $\text{Cu}_{75}\text{Hf}_{20}\text{Dy}_{05}$ will be shown to crystallize to a single phase and provides an opportunity to study the role of structure when there is no change in composition between the two phases.

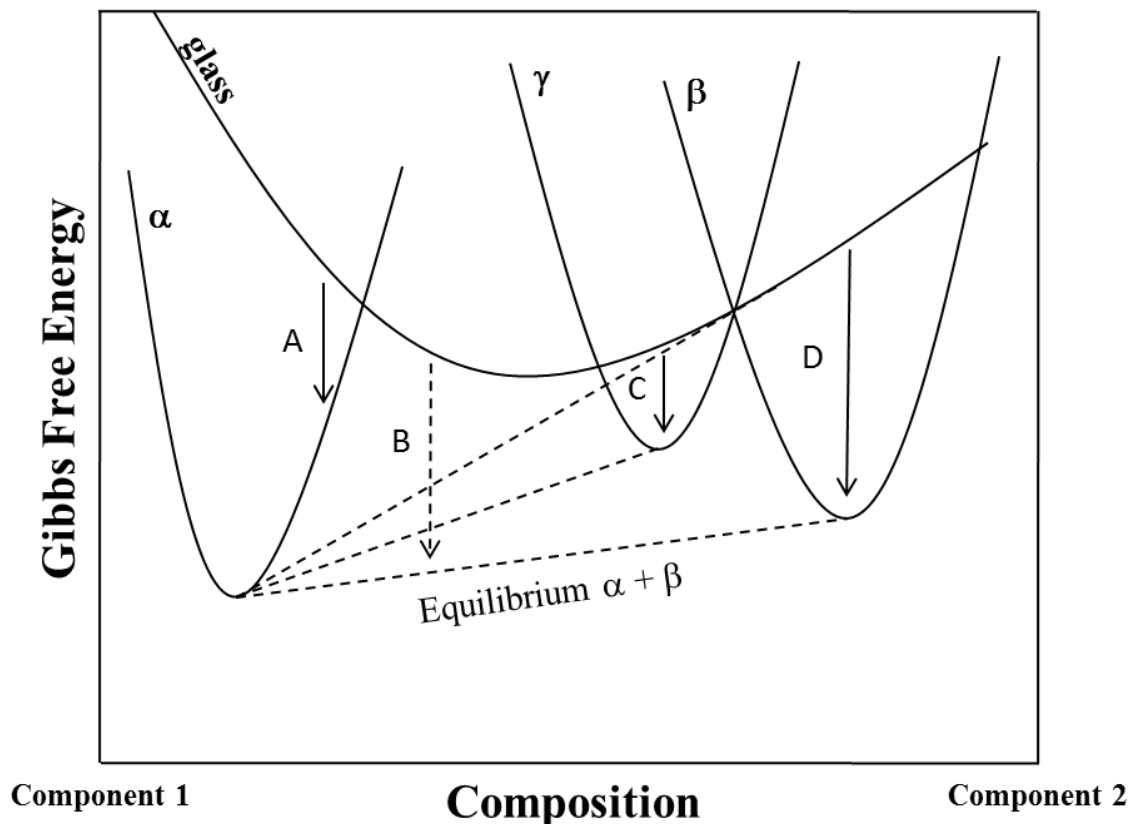


Figure 1.2. Schematic free energy curves of devitrification of glass alloys showing devitrification paths of four different compositions of a metallic glass. Paths A, C and D are massive transformations. However, both A and C are metastable. Adapted from [25, 26].

1.1.3 Order - Disorder Transformation

Order-disorder transformations typically consist of a high temperature disordered crystalline phase transforming upon cooling to an ordered crystalline state. In the disordered state the atoms occupy lattice sites at random. When cooled, the atoms then rearrange into a periodic ordered structure. Order-disorder transformations have been studied since the 1930s due to their interesting effect on physical properties and in particular magnetic properties [27]. Early alloy systems include Cu-Au, and ternary systems: Cu-Mn-Al (a Heusler alloy) and Fe-Ni-Al. These transformations can be first,

second or higher order and can occur by a nucleation and growth mechanism or by spinodal decomposition and can be either homogeneous or heterogeneous [28].

$\text{Fe}_{50}\text{Pd}_{50}$ transforms from a disordered fcc phase to an ordered pT phase of the same composition. This phase transformation is 1st order and occurs by a nucleation and growth mechanism [28]. This alloy provides an ideal opportunity to study the role of nano-structural change on corrosion properties.

1.2 Previous Electrochemical Studies on Structural Change without Change in Composition

In general, as the size of a material defect and the chemical differences between the defect zone and the matrix (alloy solid solution) increases the detrimental effect on localized corrosion increases as illustrated in Figure 1.3. For example, an alloy with large two-phase regions could give rise to detrimental galvanic corrosion. On a smaller scale, grain boundary segregation and the localized solute lean or depleted regions at the grain boundaries can give rise to intergranular corrosion.

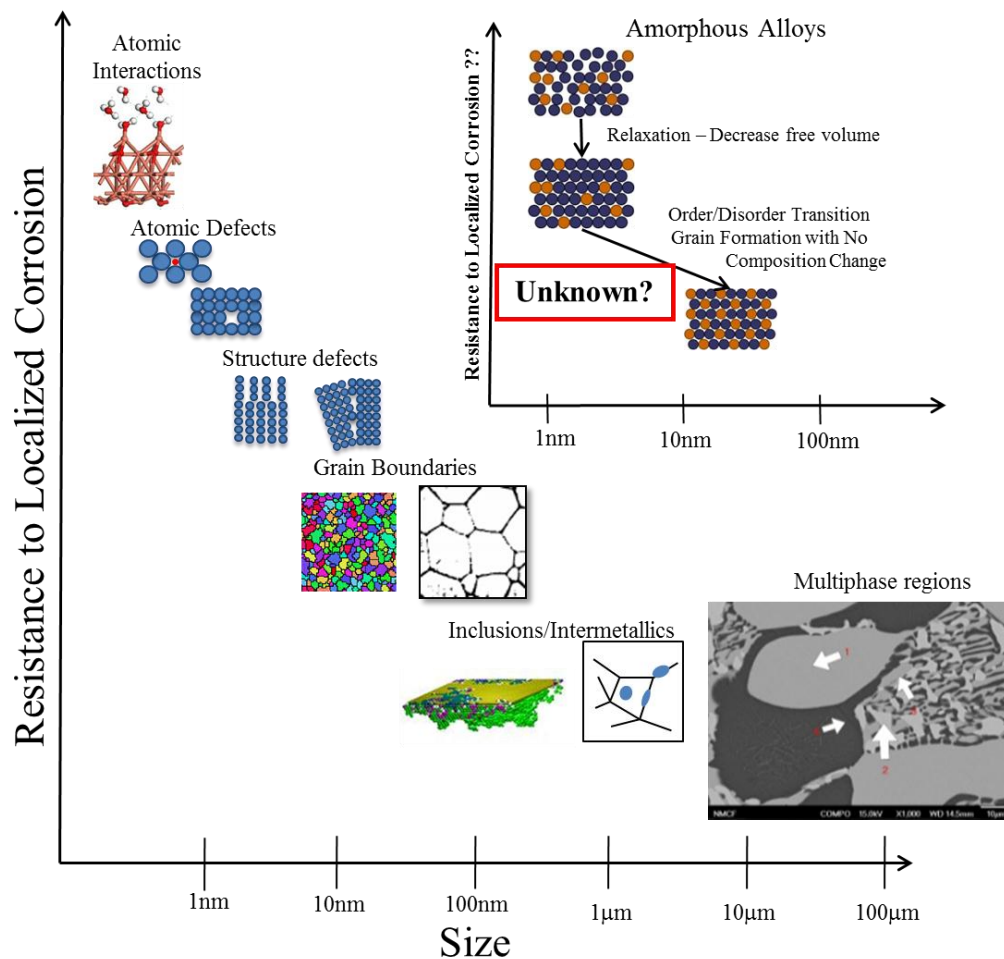


Figure 1.3. Schematic representation of the defect size and the detrimental effect on corrosion resistance.

An unresolved issue is the effect of nanostructure on solid solution alloys. Dissolution of materials is widely studied but gaps in terms of structure and composition exist, see Figure 1.4. A crystallographic orientation dependence on pitting corrosion has been observed in Be, Zn, and Mg single crystals [21, 22]. Etch pits develop crystallographic facets when corrosion is charge transfer controlled [29]. An example of a structural defect leading to increased dissolution susceptibility occurs during etching when the surface often shows closely spaced pits aligned perpendicular to grain boundaries corresponding to arrays of dislocations (stacks of edge dislocations in the simplest case) [30]. The energy at grain boundaries increases as the mismatch angle increases until a maximum energy is reached. Work by Metzger [31] on high purity Al presumably free of chemical segregation issues demonstrated that high angle-higher energy grain boundaries were susceptible to significant attack. Lower energy grain and sub-grain boundaries are significantly more resistant to intergranular corrosion under conditions where no impurity segregation (to the grain boundaries) occurs. A slower cooling rate allows for the segregation of impurities at the sub-grain boundaries making them susceptible to etching for additional reasons. These results suggest that impurities that concentrate at defects and boundaries play a large role on the corrosion properties. At shorter length scales (1-10 nm) the role of structure is unclear.

The role of structural change in amorphous alloys is still unclear. The results of published studies highlighting compositional and structural change and the resulting effect on corrosion properties will be explored in this section and are summarized in Table 1.1. In general, past studies on the corrosion of amorphous alloy have focused on: relaxation as a precursor to crystallization [10, 32], the effect of partial devitrification in

systems with large and small compositional difference between primary crystallization and the amorphous matrix [33-36], fully devitrified multi-phase systems (e.g. [32]), and devitrification to a single phase [37-43]. Additionally, studies have analyzed the role of order-disorder phase changes on corrosion [44].

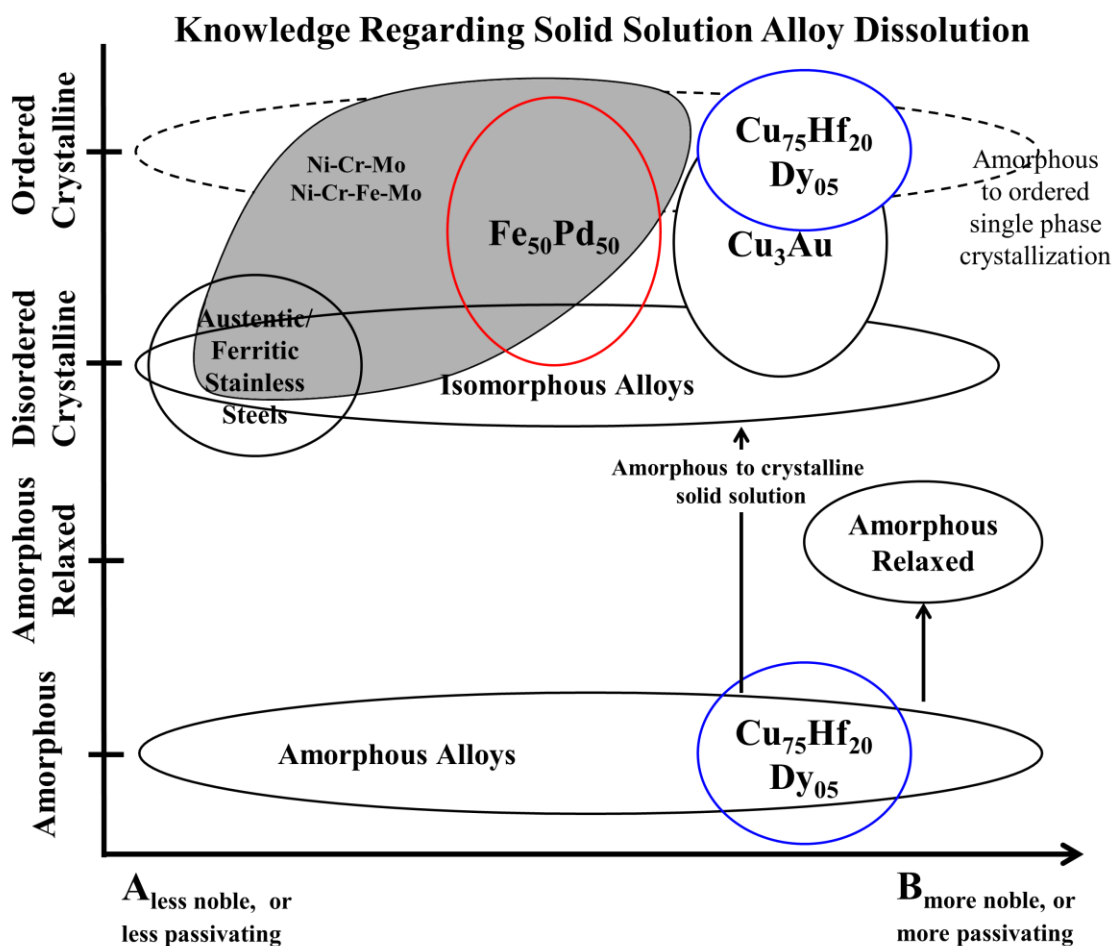


Figure 1.4. Schematic representation of knowledge regarding solid solution alloy dissolution.

1.2.1 Relaxation of the Amorphous Structure

Relaxation of an amorphous structure can have a large effect on its material properties including corrosion. The effect of relaxation was studied in an F-B-Si amorphous alloy [10]. It was found that heat treatments below the glass crystallization temperature reduced the corrosion current density. Additionally, impedance

measurements showed an increase in the charge transfer resistance as the amorphous alloy became more relaxed. The x-ray diffraction pattern for the as spun alloy shows what appear to be small crystalline peaks indicating the system studied could be a multiphase system. If true, the reduction in corrosion current density could be due to factors beyond structural relaxation. Relaxation of an amorphous $\text{Al}_{87}\text{Co}_7\text{Ce}_6$ alloy was shown to improve resistance during dissolution in NaOH solution compared to the as-quenched state. The quenched state was characterized to show a higher coordination number and reduced free volume than the as-quenched state [32].

1.2.2 Partial Devitrification of the Amorphous Structure

Due to the improved mechanical properties of partially devitrified amorphous alloys, numerous studies have looked at the roll of partial devitrification on the corrosion performance. These systems provide an interesting look at how the initial stages of crystallization changes the corrosion behavior of the amorphous alloy. The crystallization of these alloys involves changes in structure as well as chemical composition, but this is a material system where the structural difference between the amorphous and devitrified states is likely an important determinant for the resulting corrosion behavior. Aluminum based systems in particular have received significant attention from a mechanical perspective because the alloys partially devitrify by forming fcc Al nanocrystals depleted in the TM and RE elements which significantly enhance the mechanical properties [45, 46]. In Al-Fe-Gd, Al-Co-Ce and Al-Ni-Gd amorphous alloys, precipitation of Al nanocrystals, up to approximately 40% of the matrix and with size up to 100 nm, increased pitting resistance compared to both fully amorphous and pure aluminum [33]. Complete devitrification to equilibrium phases, consisting of solute rich intermetallics

and solute lean Al-rich regions, lead to corrosion performance similar to that of pure aluminum. Similarly, in Al-Ni-La amorphous alloys, partial devitrification lead to limited change in [35] or improved [36] corrosion behavior, whereas full crystallization caused a drastic reduction in corrosion resistance. These studies indicate that partial crystallization can have a beneficial effect on corrosion resistance. Possible mechanisms [33] causing this behavior relate to some factor compensating or offsetting the normally detrimental role of solute lean nanocrystals, e.g. solute buildup at nanocrystals [47]. Alternatively, perhaps the critical size necessary for pitting is larger than the physical size of the precipitated phase [48].

1.2.3 Single Phase Crystallization

Amorphous alloys that crystallize to a single phase are an interesting class of materials because they will not have compositional differences between the phases. These studies have focused on trying to understand the corrosion performance of amorphous alloys through comparison to their crystalline counterparts. Amorphous $\text{Cu}_{50}\text{Zr}_{50}$ was studied in amorphous and single phase states in 1M HCl and 1M HNO_3 , and the mass loss of the fully amorphous alloy was lower than after crystallization [39]. In contrast, $\text{Cu}_{60}\text{Zr}_{40}$ no significant difference were found between behavior of amorphous compared to single phase crystalline phases during anodic polarization in 0.5M H_2SO_4 [42]. The dissolution rate of amorphous $\text{Co}_{75}\text{B}_{25}$ decreased when the glass was crystallized to Co_3B in 0.5M Na_2SO_4 during active corrosion behavior [38]. In a multi-component $\text{Ni}_{52}\text{Cr}_{16}$ based alloy, the amorphous alloy devitrifies to form a single phase solid solution and little effect of devitrification on the anodic polarization behavior in 0.5 M H_2SO_4 +5% NaCl solution was found [41]. $\text{Ni}_{50}\text{Nb}_{50}$ crystallized to a single phase alloy and showed

limited difference in passive behavior in 1M HCl, but the amorphous Ni₅₀Nb₅₀ showed 30-40% fewer transients during a potential hold in 1M HCl than crystalline [49].

All of these results, summarized in Table 1.1, give conflicting indications; the structural change improves, diminishes or has no effect on corrosion performance. Unfortunately, these studies were typically done only in a single aqueous solution [38, 41, 42, 49] often primarily in acidic solutions [39]. Measurement techniques often interrogated average global properties and lacked the ability to assess local behavior.

1.2.4 Order-Disorder Transformation in Crystalline Structure

Crystalline order-disorder phase transformations often result in significantly different electrochemical behavior. Ordered single phase Cu₃Au exhibits passivity at higher potentials and has a higher dealloying potential than disordered Cu₃Au in 0.1M Na₂SO₄ +0.05M H₂SO₄ [44]. However, in off stoichiometric Cu₈₂Au₁₈ this effect was minimized. The single phase disordered matrix is outside of the ordered Cu₃Au phase range indicated on the phase diagram and likely transformed to a multi-phase ordered matrix. With an ordered distribution of atoms, the formation of a continuous oxide network is more easily achieved. The idea of a critical beneficial solute element to form a passive layer is discussed in detail in the graph theory and percolation models of oxides [50, 51]. The ordered Cu₃Au could lead to a stronger more protective oxide which is responsible for the increased pitting resistance. In contrast, the disordered Cu₃Au might have surface regions where it is lean in protective Au on a local atomic scale. These regions could serve as the initial dealloying sites.

Table 1.1. Literature survey of prior corrosion studies focusing on phase change without a change in composition.

Transformation	Alloy	Experiment	Solution	Regime	Findings	Ref.
Relaxation	Fe-B-Si	Exposure test, Icorr	0.1 M H ₂ SO ₄	Active	Relaxation decreases I _{corr} (30 mA) and reduced mass loss during exposure tests	[10]
Relaxation	Al ₈₇ Co ₇ Ce ₆	Polarization, EIS	NaOH, NaCl	Active/Passive	Relaxation decreased mass loss, also characterized as reduced free volume and high CN	[32]
Amorphous - Single Phase Crystallization	Co ₇₅ B ₂₅	Polarization	0.5 M Na ₂ SO ₄	Passive	Dissolution rate decreases with formation of crystallized Co ₃ B	[38]
Amorphous - Single Phase Crystallization	Cu ₆₀ Zr ₄₀	Polarization	0.5 M H ₂ SO ₄	Passive	No significant difference after crystallization to a single phase	[42]
Amorphous - Single Phase Crystallization	Fe-Cr-P-C, Fe-Ni-Cr-P-B	Polarization vs. incremental annealing time	1 M HCl	Active/Pitting	Solid solution worse than amorphous	[40]
Amorphous - Single Phase Crystallization	Cu ₅₀ Ti ₅₀ , Cu ₅₀ Zr ₅₀	Polarization, Mass Loss	1 M HCl, 1 M HNO ₃	Active/Oxidizing	Amorphous better than Crystalline. Cu ₅₀ Ti ₅₀ double phase, Cu ₅₀ Zr ₅₀ single	[39]
Amorphous - Single Phase Crystallization	Ni-based	Polarization	0.5M H ₂ SO ₄ +5% NaCl	Active	Behavior showed little difference between solid solution and amorphous phase	[41]
Amorphous - Single Phase Crystallization	Ni-B-Sn	Polarization	1M NaCl	Passive/Pitting	Little difference between phases	[37]
Amorphous Single Phase Crystallization	Ni ₅₀ Nb ₅₀	Polarization/ Potential Hold	1M HCL	Passive	Polarization shows little difference. During potentiostatic polarization amorphous shows fewer current transients than crystallized	[49]
Amorphous - Multi-Phase Crystallization	Al-Ni-La	Polarization	0.001-0.1 M NaCl + 0.05 M Na ₂ SO ₄	Passive/Pitting	Crystallization with limited composition change resulted in limited change in corrosion resistance	[35]
Order-Disorder	Cu ₃ Au	Polarization	1N Na ₂ SO ₄ + 0.01N H ₂ SO ₄	Dealloying	Ordered Cu ₃ Au exhibited more passivity and higher pitting potential	[44]

1.2.5 Critical Unresolved Issues

Understanding the role of nano-structure on the corrosion properties at the nm-range length scales is an important fundamental question especially as engineering materials become more advanced. The lack of structural defects is a contributing mechanism that is often thought, without proof, to be one of the main underlying benefits of corrosion resistant amorphous alloys.

Previous studies focusing on the role of structure on corrosion properties have been limited in terms of scope (utilizing a single or only acidic solution, poorly characterized phase transformation, or lack of a well-defined structural change). Moreover, these studies typically utilized a single method and lacked modern electrochemical techniques. Overall no consistent effect of structure on corrosion performance has been established.

1.3 Objectives of Research

The primary objective of this research is to utilize well understood and characterized phase transformations in model alloy solid solution materials free of large heterogeneities to study the role of structure on the corrosion behavior in situations where the compositional changes between phases are nonexistent. Two model alloy systems were chosen for this research and synthesized using high purity materials. Amorphous $\text{Cu}_{75}\text{Hf}_{20}\text{Dy}_{05}$ devitrifies to form a single phase. Crystalline $\text{Fe}_{50}\text{Pd}_{50}$ undergoes an order-disorder phase transformation forming both structural states of the same composition.

A comprehensive set of electrochemical techniques, surface analysis and microscopy will be employed to establish the corrosion behavior of each structural state

in the active, passive and localized corrosion regimes. These studies will utilize differences in electrochemical behavior of the constituent alloying elements to emphasize particular roles within the corrosion regimes (e.g. active dissolution of 1 alloying element while passive layer formation of the other alloying element). A modern suite of techniques capable of analyzing surface structure, surface chemistry, electrochemical properties on a small length scale, and global electrochemical properties will be used.

1.4 Thesis Organization

For each alloy system, a broad survey of the electrochemical behavior is presented. The purpose of the survey is two-fold. It provides a comprehensive analysis of the behavior of the different structural states in a wide breadth of conditions. Secondly, this survey identifies electrochemical regimes where the difference in behavior between the structural states is significant and directs a more narrow survey of corrosion properties within a corrosion regime. Within the conditions where differences are significant, a highly focused set of experiments including high resolution microscopy were made to determine a mechanistic understanding of the role of structure on specific corrosion properties. An illustration of this process is shown in Figure 1.5. This thesis is organized by alloy system: Chapter 2-3 presents the $\text{Cu}_{75}\text{Hf}_{20}\text{Dy}_{05}$ alloy and Chapters 4-6 focuses on the Fe-Pd alloy system. The primary purpose of Chapters 4 and 5, which are a survey of the electrochemical properties of the Fe-Pd alloy system, is to establish the conditions investigated in Chapter 6. Each chapter is prefaced by an introduction including previous work relevant to that series of investigations.

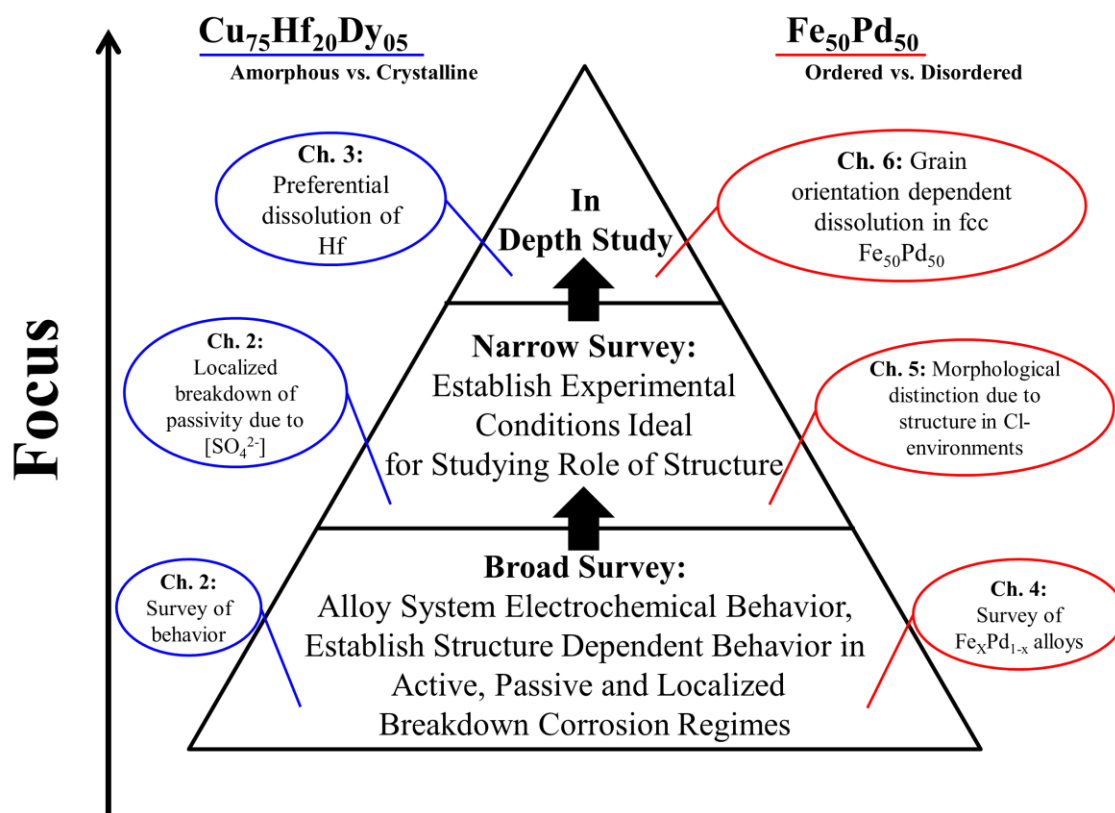


Figure 1.5. Illustration of the thesis organization. A wide range of experiments establish the electrochemical properties of each alloy system. These experiments direct a more narrowly focused set of experiments to elucidate the role of structure on corrosion properties. A narrowly focused in depth study of specific corrosion regime provides a mechanistic understanding of the role of structure on the corrosion behavior.

Chapter 2 presents the introduction to the $\text{Cu}_{75}\text{Hf}_{20}\text{Dy}_{05}$ alloy system and its transformation to a crystalline single phase alloy. Results of a wide range of environmental and experimental conditions are presented. The role of amorphous vs. crystalline structure is elucidated under conditions of passivity and local breakdown of the passive film due to SO_4^{2-} .

Chapter 3 focuses on the behavior of the amorphous vs. crystalline $\text{Cu}_{75}\text{Hf}_{20}\text{Dy}_{05}$ alloy under conditions of preferential dissolution of Hf from the matrix leading to a nanoporous dealloyed structure. The structural state was found to greatly affect the rate of dealloying and the resulting morphology.

Chapter 4 introduces the Fe-Pd alloy system and presents the effect of Pd alloying through a comparison of the three compositions: martensitic Fe₇₀Pd₃₀, and fcc Fe₆₅Pd₃₅/Fe₅₀Pd₅₀ which are both disordered phases.

Chapter 5 presents the behavior the ordered (pT) and disordered (fcc) Fe₅₀Pd₅₀. These provide a wide-ranging survey of behavior of the two structural states of Fe₅₀Pd₅₀ and highlight the dissolution induced grain dependent morphological characteristics of the disordered, fcc phase.

Chapter 6 elucidates the grain orientation dependent dissolution behavior of the disordered (fcc) Fe₅₀Pd₅₀ phase. The amount of dissolution is correlated to the disordered (fcc) Fe₅₀Pd₅₀ grain orientation and the surface roughness. The dissolution behavior is compared in detail to the ordered (pT) Fe₅₀Pd₅₀ phase. The underlying characteristics of these dissolution processes are discussed.

Chapter 7 presents the conclusions of this work. Situations where the local atomic structure is an important consideration for the overall corrosion behavior are summarized. Remaining questions and suggested future work are also detailed.

1.5 References

1. Hashimoto, K., 2002 *W.R. Whitney Award Lecture: In pursuit of new corrosion-resistant alloys*. Corrosion, 2002. **58**(9): p. 715-722.
2. Scully, J.R. and A.M. Lucente, *Corrosion of Amorphous Metals*, in *ASM handbook*, C. S.D. and J. Covino, B.S., Editors. 2005, ASM International: Materials Park, OH. p. 476-489.
3. Farmer, J., J.S. Choi, C. Saw, J. Haslam, D. Day, P. Hailey, T.G. Lian, R. Rebak, J. Perepezko, J. Payer, D. Branagan, B. Beardsley, A. D'amato, and L. Aprigliano, *Iron-Based Amorphous Metals: High-Performance Corrosion-Resistant Material Development*. Metallurgical and Materials Transactions a-Physical Metallurgy and Materials Science, 2009. **40A**(6): p. 1289-1305.
4. Scully, J.R., A. Gebert, and J.H. Payer, *Corrosion and related mechanical properties of bulk metallic glasses*. Journal of Materials Research, 2007. **22**(2): p. 302-313.

5. Aburada, T., N. Unlu, J.M. Fitz-Gerald, G.J. Shiflet, and J.R. Scully, *Effect of Ni as a minority alloying element on the corrosion behavior in Al-Cu-Mg-(Ni) metallic glasses*. Scripta Materialia, 2008. **58**(8): p. 623-626.
6. Aburada, T., J.M. Fitz-Gerald, and J.R. Scully, *Synthesis of nanoporous copper by dealloying of Al-Cu-Mg amorphous alloys in acidic solution: The effect of nickel*. Corrosion Science, 2011. **53**(5): p. 1627-1632.
7. Aburada, T., *Effects of Minor Solute on Corrosion*, in *Materials Science and Engineering*. 2011, University of Virginia: Charlottesville, VA.
8. Jayaraj, J., K.B. Kim, H.S. Ahn, and E. Fleury, *Corrosion mechanism of N-containing Fe-Cr-Mo-Y-C-B bulk amorphous alloys in highly concentrated HCl solution*. Materials Science and Engineering a-Structural Materials Properties Microstructure and Processing, 2007. **449**: p. 517-520.
9. Greer, A.L., *Partially or fully devitrified alloys for mechanical properties*. Materials Science and Engineering a-Structural Materials Properties Microstructure and Processing, 2001. **304**: p. 68-72.
10. Souza, C.A.C., F.S. Politi, and C.S. Kiminami, *Influence of structural relaxation and partial devitrification on the corrosion resistance of Fe₇₈B₁₃Si₉ amorphous alloy*. Scripta Materialia, 1998. **39**(3): p. 329-334.
11. Chen, H.S., *Influence of Structural Relaxation on Density and Young Modulus of Metallic Glasses*. Journal of Applied Physics, 1978. **49**(6): p. 3289-3291.
12. Cargill, G.S., *Dense Random Packing of Hard Spheres as a Structural Model for Noncrystalline Metallic Solids*. Journal of Applied Physics, 1970. **41**(5): p. 2248-&.
13. Turnbull, D. and M.H. Cohen, *On Free-Volume Model of Liquid-Glass Transition*. Journal of Chemical Physics, 1970. **52**(6): p. 3038-&.
14. Lass, E.A., *Statistical thermodynamics and atomic structure of metallic glasses in Materials Science and Engineering*. 2008, University of Virginia: Charlottesville, VA.
15. Zhu, A., G.J. Shiflet, and S.J. Poon, *Diffusion in metallic glasses: Analysis from the atomic bond defect perspective*. Acta Materialia, 2008. **56**(14): p. 3550-3557.
16. Egami, T., *Structural Relaxation in Amorphous Alloys - Compositional Short-Range Ordering*. Materials Research Bulletin, 1978. **13**(6): p. 557-562.
17. Egami, T., *Structural relaxation in amorphous alloys - compositional short range ordering*. Materials Research Bulletin, 1978. **13**(6): p. 557-562.
18. Burton, B.P., *Fe-Pd (Iron-Palladium)*, in *Binary alloy phase diagrams*, T.B. Massalski, Editor. 1990, ASM International: Materials Park, Ohio. p. p 1749-1751.
19. Cahn, R.W. and A.L. Greer, *Chapter 19 - Metastable States of Alloys*, in *Physical Metallurgy (Fourth Edition)*, W.C. Robert and H. Peter, Editors. 1996, North-Holland: Oxford. p. 1723-1830.
20. Egami, T. and T. Ichikawa, *Kinetics of Structural Relaxation in Amorphous Alloy Observed by X-Ray-Diffraction*. Materials Science and Engineering, 1978. **32**(3): p. 293-295.

21. Lillard, R.S., *Relationships between metal-metal bonding and crystallographic pitting in hcp metals*. Electrochemical and Solid State Letters, 2003. **6**(8): p. B29-B31.
22. Lillard, R.S., G.F. Wang, and M.I. Baskes, *The role of metallic bonding in the crystallographic pitting of magnesium*. Journal of the Electrochemical Society, 2006. **153**(9): p. B358-B364.
23. Aaronson, H.I., *Mechanisms of the massive transformation*. Metallurgical and Materials Transactions a-Physical Metallurgy and Materials Science, 2002. **33**(8): p. 2285-2297.
24. Massalski, T.B., *Massive transformations revisited*. Metallurgical and Materials Transactions a-Physical Metallurgy and Materials Science, 2002. **33**(8): p. 2277-2283.
25. Cahn, R.W. and A.L. Greer, *Metastable States of Alloys*, in *Physical metallurgy*, R.W. Cahn and P. Haasen, Editors. 1996, North-Holland: Amsterdam ; New York. p. 1723-1830.
26. Koster, U. and P. Weiss, *Crystallization and Decomposition of Amorphous Silicon-Aluminum Films*. Journal of Non-Crystalline Solids, 1975. **17**(3): p. 359-368.
27. Bragg, W.L., C. Sykes, and A.J. Bradley. *A study of the order-disorder transformation*. in *The Conduction of Electricity in Solids*. 1937. Bristol: Proceedings of the Physical Society.
28. Soffa, W.A. and D.E. Laughlin, *Decomposition and Ordering Processes Involving Thermodynamically 1st-Order Order-Disorder Transformations*. Acta Metallurgica, 1989. **37**(11): p. 3019-3028.
29. Ives, M.B., *Localized corrosion*, in *International corrosion conference series*, U.R. Evans, et al., Editors. 1974, National Association of Corrosion Engineers: Houston, Tex. p. 78-103.
30. Gilman, J.J. and W.G. Johnston, *Dislocations and mechanical properties of crystals*. 1957, New York: J. Wiley.
31. Metzger, M. and J. Intrater, *Sub-Grain Boundary Corrosion in High-Purity Aluminium*. Nature, 1954. **174**(4429): p. 547-549.
32. Tailleart, N., R. Huang, T. Aburada, D.J. Horton, and J.R. Scully, *Effect of Thermally-Induced Relaxation on Passivity and Corrosion of an Amorphous Al-Co-Ce alloy*. Corrosion Science, 2011. **{accepted}**.
33. Lucente, A.M. and J.R. Scully, *Pitting of Al-based amorphous-nanocrystalline alloys with solute-lean nanocrystals*. Electrochemical and Solid State Letters, 2007. **10**(5): p. C39-C43.
34. Lucente, A.M. and J.R. Scully, *Pitting and alkaline dissolution of an amorphous-nanocrystalline alloy with solute-lean nanocrystals*. Corrosion Science, 2007. **49**(5): p. 2351-2361.
35. Roy, A., K.L. Sahoo, and I. Chatteraj, *Electrochemical response of AlNiLa amorphous and devitrified alloys*. Corrosion Science, 2007. **49**(6): p. 2486-2496.
36. Wu, X.Q., M. Ma, C.G. Tan, X.B. Liu, and J.G. Lin, *Corrosion behavior of amorphous and crystalline ribbons of Al₈₆Ni₆La₆*. Rare Metal Materials and Engineering, 2007. **36**(9): p. 1668-1671.

37. Alvarez, M.G., S.M. Vazquez, F. Audebert, and H. Sirkin, *Corrosion behaviour of Ni-B-Sn amorphous alloys*. Scripta Materialia, 1998. **39**(6): p. 661-668.
38. Huerta, D. and K.E. Heusler, *Influence of Crystallization of Glassy Co75b25 on Its Dissolution Rates in Acid Sulfate-Solution*. Journal of Non-Crystalline Solids, 1983. **56**(1-3): p. 261-266.
39. Naka, M., K. Hashimoto, and T. Masumoto, *Corrosion Behavior of Amorphous and Crystalline Cu50ti50 and Cu50zr50 Alloys*. Journal of Non-Crystalline Solids, 1978. **30**(1): p. 29-36.
40. Naka, M., K. Hashimoto, and T. Masumoto, *Effect of Heat-Treatment on Corrosion Behavior of Amorphous Fe-Cr-P-C and Fe-Ni-Cr-P-B Alloys in In Hcl*. Corrosion, 1980. **36**(12): p. 679-686.
41. Tong, H.S., *The Corrosion Behavior of a Ni Based Amorphous Alloy - the Effect of Devitrification*. Corrosion, 1985. **41**(1): p. 10-12.
42. Turn, J.C. and R.M. Latanision, *The Influence of Structure on the Corrosion of Glassy Copper-Zirconium Alloys*. Corrosion, 1983. **39**(7): p. 271-279.
43. Wang, Z.M., J. Zhang, X.C. Chang, W.L. Hou, and J.Q. Wang, *Structure inhibited pit initiation in a Ni-Nb metallic glass*. Corrosion Science, 2010. **52**(4): p. 1342-1350.
44. Parks, B.W., J.D. Fritz, and H.W. Pickering, *The Difference in the Electrochemical-Behavior of the Ordered and Disordered Phases of Cu3au*. Scripta Metallurgica, 1989. **23**(6): p. 951-956.
45. Chen, H., Y. He, G.J. Shiflet, and S.J. Poon, *Mechanical-Properties of Partially Crystallized Aluminum Based Metallic Glasses*. Scripta Metallurgica Et Materialia, 1991. **25**(6): p. 1421-1424.
46. Choi, G.S., Y.H. Kim, H.K. Cho, A. Inoue, and T. Masumoto, *Ultrahigh Tensile-Strength of Amorphous Al-Ni-(Nd,Gd)-Fe Alloys Containing Nanocrystalline Al Particles*. Scripta Metallurgica Et Materialia, 1995. **33**(8): p. 1301-1306.
47. Johnson, W.C., P. Zhou, A.M. Lucente, and J.R. Scully, *Composition Profiles around Solute-Lean, Spherical Nanocrystalline Precipitates in an Amorphous Matrix: Implications for Corrosion Resistance*. Metallurgical and Materials Transactions a-Physical Metallurgy and Materials Science, 2009. **40A**(4): p. 757-767.
48. Burstein, G.T. and G.O. Ilevbare, *The effect of specimen size on the measured pitting potential of stainless steel*. Corrosion Science, 1996. **38**(12): p. 2257-2265.
49. Wang, Z.M., J. Zhang, X.C. Chang, W.L. Hou, and J.Q. Wang, *Structure inhibited pit initiation in a Ni-Nb metallic glass* Corrosion Science, 2010. **52**(4): p. 1342-1350.
50. McCafferty, E., *Graph theory and the passivity of binary alloys*. Corrosion Science, 2000. **42**(11): p. 1993-2011.
51. Sieradzki, K. and R.C. Newman, *A Percolation Model for Passivation in Stainless-Steels*. Journal of the Electrochemical Society, 1986. **133**(9): p. 1979-1980.

2 Survey of Electrochemical Behavior of $\text{Cu}_{75}\text{Hf}_{20}\text{Dy}_{05}$ in the Active and Passive State

2.1 Abstract

The $\text{Cu}_{75}\text{Hf}_{20}\text{Dy}_{05}$ alloy is an ideal solid solution alloy for the study of effects of nano-structure on corrosion properties. The alloy can be produced in the fully amorphous state and annealing leads to single phase crystallization to the $\text{Cu}_{51}\text{Hf}_{14}$ structural state. Importantly, the alloy is a mixture of elements with substantially different electrochemical behavior involving a readily passivated refractory element (Hf) and a transition metal (Cu) that can be active or passive depending on conditions. This chapter introduces the alloy and the expected electrochemical properties of the alloy system. A survey of electrochemical behavior in the active, passive and localized corrosion states is presented. In these environments, Hf is typically shown to be a corrosion resistant alloying element that readily forms passive layers, while Cu and Dy are typically active.

The alloying of Hf into $\text{Cu}_{75}\text{Hf}_{20}\text{Dy}_{05}$ reduces the dissolution rate and highlights the role of Hf as a dissolution moderator in acidic SO_4^{2-} environments. The amorphous structure is more susceptible to passive film breakdown than the crystalline state in neutral SO_4^{2-} containing solution conditions. The amorphous structure exhibited increased dissolution of Cu at lower applied potentials compared to the crystalline structure. Both passivity and dissolution behavior strongly indicate that the role of nanostructure, in particular short range compositional variations is significant. In the case of the amorphous structure, the lack of a periodic structure reduces the efficacy of the oxide. Hf lean regions are theorized to result from short and medium range order in the metallic glass and promote Cu dissolution under conditions where no oxide is formed.

2.2 Introduction

2.2.1 $\text{Cu}_{75}\text{Hf}_{20}\text{Dy}_{05}$ Alloy Synthesis and Transformation Characteristics

Metastable amorphous metals are formed when a critical cooling rate is achieved and prevent crystallization during cooling of molten metallic alloys. Often the material characteristic cooling rate is extremely high requiring special processes to rapidly cool the material. One common method to achieve extremely high cooling rates is the melt spinning technique. The cooling rates are achieved by ejecting a molten metal onto a rapidly spinning wheel (typically Cu) to form metallic ribbon. Cooling rates achieved by this technique are 10^{4-7} K/s (see [1] for a summary of amorphous alloy formation techniques and schematics).

The amorphous $\text{Cu}_{75}\text{Hf}_{20}\text{Dy}_{05}$ alloy can be produced by the melt spinning technique. Differential scanning calorimetry of the amorphous ribbon at $40^\circ\text{C}/\text{min}$ showed a glass transition, T_g , at 518°C and a single crystallization peak at about 555°C [2]. Notably, amorphous $\text{Cu}_{75}\text{Hf}_{20}\text{Dy}_{05}$ melt spun ribbon devitrifies to a single phase, $\text{Cu}_{51}\text{Hf}_{14}$ and maintains the Cu to Hf ratio of approximately 4:1. The phase diagram for the Cu-Hf system is shown in Figure 2.1. $\text{Cu}_{51}\text{Hf}_{14}$ is a line compound at a Cu:Hf ratio of 78:22 atomic percent. The ratio of line compound suggests that Dy is accommodated in this crystal structure by occupying Hf lattice sites. Atomic distributions in the perfect $\text{Cu}_{51}\text{Hf}_{14}$ lattice are shown in Figure 2.2. The Hf-Hf atomic distribution plots show that there are 1 to 3 Hf atoms within 0.4 nm of each Hf atom and an additional 10 - 13 Hf atoms are between 0.4 and 0.6 nm from each Hf atom. The distribution of Cu and Hf atoms about a Cu atom show 20 Cu atoms and 3 Hf atoms within 0.4 nm of the Cu atom.

The ratio of Cu to Hf atoms within 0.4 nm of the Cu ‘origin’ atom varies between 2.8 and 6.7.

This phase transformation provides an ideal opportunity to study the effect of nano-structural change on corrosion properties in the absence of an accompanying chemical partitioning and precipitate formation. Another advantage to this alloy system is that Cu is a well understood electrochemical system due to its prevalence in engineering applications such as potable water systems [3-5].

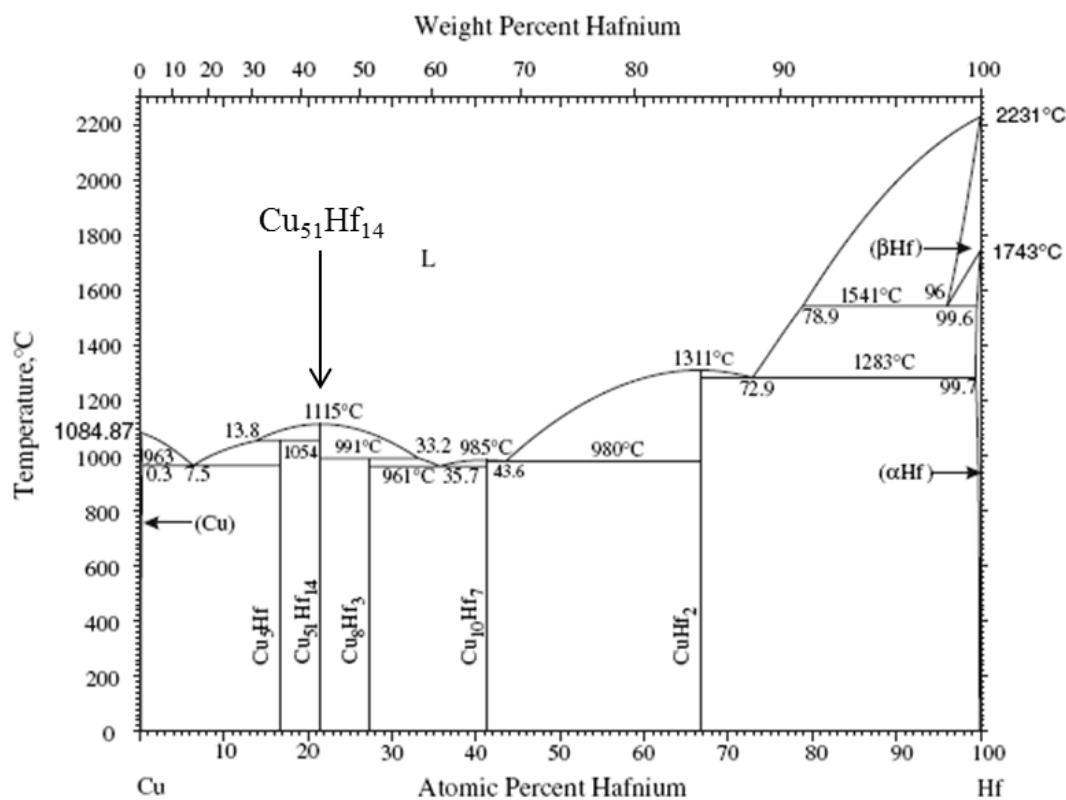


Figure 2.1. Cu-Hf binary phase diagram [6]. Amorphous $\text{Cu}_{75}\text{Hf}_{20}\text{Dy}_{05}$ crystallizes to the line compound $\text{Cu}_{51}\text{Hf}_{14}$ at 22 at% Hf on the phase diagram.

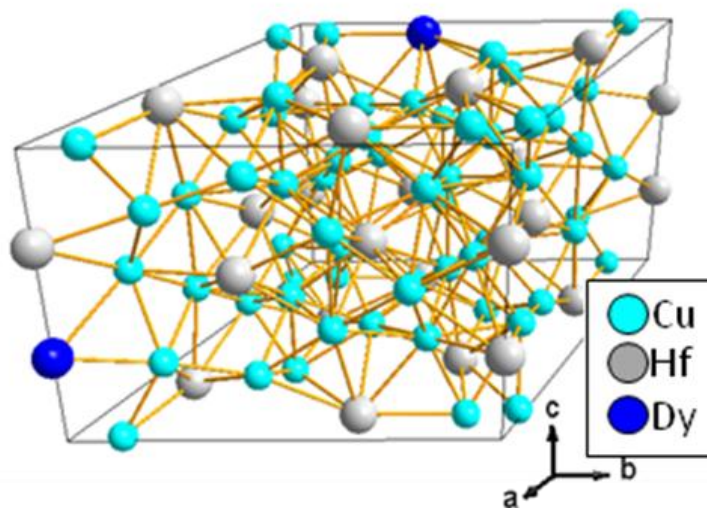


Figure 2.2. Schematic model of the $\text{Cu}_{51}\text{Hf}_{14}$ crystal structure with Dy dissolved into Hf lattice sites. The unit cell is hexagonal P6/m (space group 175) with lattice parameters $a = 1.118 \text{ nm}$, $c = 0.824 \text{ nm}$. The density is 11.05 g/cm^3 . Model created using Diamond Crystallography Software [7].

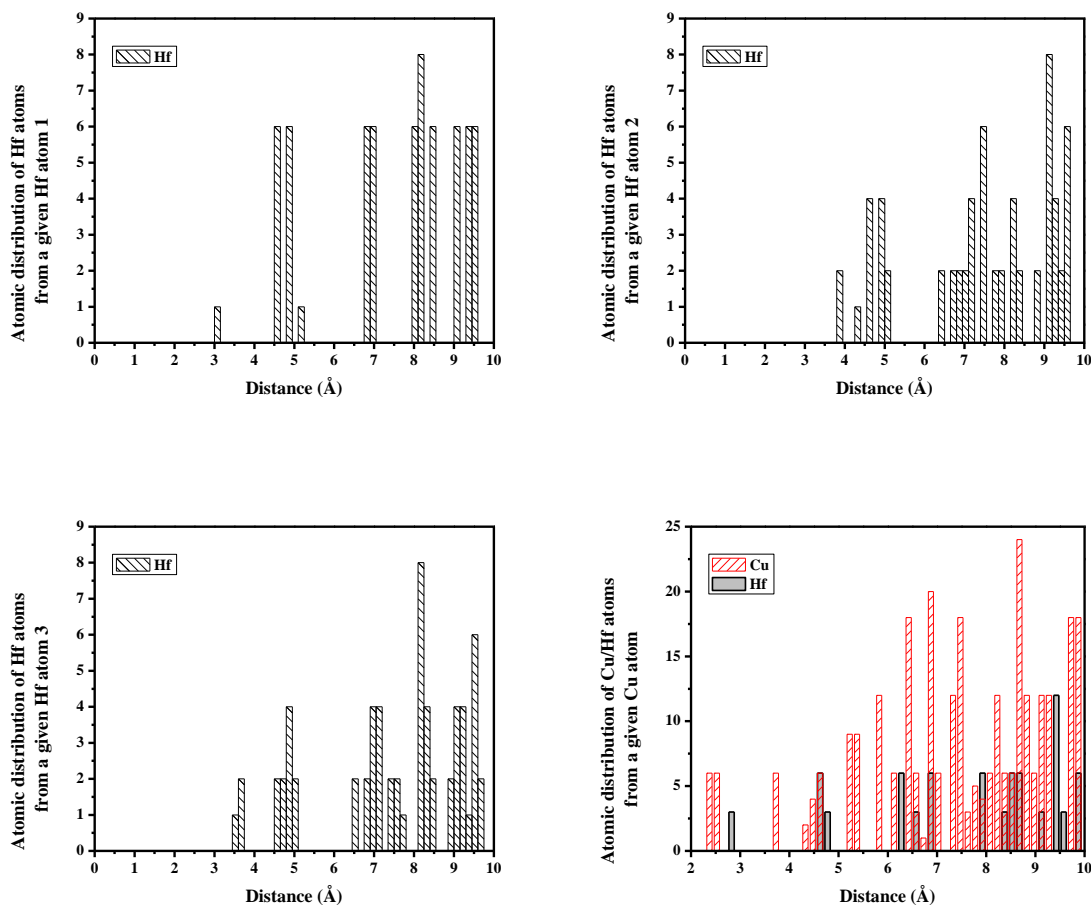


Figure 2.3. Schematic representations of atomic radial distributions of lattice positions within the $\text{Cu}_{51}\text{Hf}_{14}$ perfect crystal lattice. The first three plots (top, lower left) show the distribution of Hf atoms around the 3 Hf atom lattice sites. The lower right plot shows the radial distribution of Cu and Hf atoms around a central Cu atom. Interatomic distances determined using Diamond Crystallography Software [7]. Radial lattice distances within ± 0.15 Å were considered as an equal distance the origin Cu atom.

2.2.2 Amorphous Structure

The bond length, coordination number, nearest neighbor arrangements and free volume all may affect the corrosion tendencies of a solid solution alloy. It is important to compare these arrangements to the crystalline alloy described in 2.2.1. Therefore, it is of interest in amorphous solids to consider the arrangement of Cu and Hf atoms. Dense random packing of hard spheres was initially used to describe liquids [8, 9] and has been applied to model atoms within an amorphous metallic solid [10]. The dense random packing model can be used to calculate the coordination spheres of constituent atoms within an amorphous solid [11]. Egami presents a simple geometric calculation based on the solid angle (Equation 2.1) occupied by B atoms of radius R_B surrounding a central A atom of radius R_A . The solid angle can be used to calculate, Equation 2.2, the coordination number (CN) or number of B atoms surrounding a central A atom. The two-dimensional packing fraction on the surface of an atom, η_{2D} , is typically assumed to be 0.842 unless $R_A \gg R_B$. The CN of central Hf and Cu atoms calculated using this formula is shown in Table 2.1.

$$\omega_{A-B} = 2\pi \left[1 - \frac{\sqrt{R_A(R_A+2R_B)}}{R_A+R_B} \right] \quad 2.1$$

$$CN = \frac{4\pi}{\omega_{A-B}} \eta_{2D} \quad 2.2$$

Table 2.1. Coordination number of Hf and Cu central atoms in the amorphous $\text{Cu}_{75}\text{Hf}_{20}\text{Dy}_{05}$ structure based on calculations of the dense random packing model. The assumed atomic radii are 0.128 nm for Cu and 0.159 nm for Hf. Calculations based on Equation 2.2[11]. Divergence from 12 close packed nearest neighbors is due to the η_{2D} approximation.

Atom Type Surrounding a Central Atom	Coordination Number of a Central Hf atom	Coordination Number of a Central Cu atom
All Cu atoms	16.04	12.56
All Hf atoms	12.56	10.05
Cu and Hf atoms	15.14 [†]	11.88 [†]

[†] Using 0.135 nm as the radius of surrounding atoms. This value is the average radius of Cu and Hf atoms based on the atomic ratios in $\text{Cu}_{75}\text{Hf}_{20}\text{Dy}_{05}$.

Experimental determinations of the coordination sphere and the pair distribution functions (PDF) about a central atom are typically performed using high energy synchrotron X-rays. The experimentally determined coordination numbers often show values different than DRP model predictions, e.g. in Al-based alloys [12-14]. Other determinations of the packing structure of amorphous structures uses soft-sphere constructions and potential energy driven packing, e.g. the Leonard-Jones potential [15].

Models of amorphous alloys with binary compositions of dissimilar atomic radii have suggested short range ordering about the smaller elements [16]. Short range order (SRO) is defined as a non-random prevalence of specific coordination clusters surrounding atoms without causing any long range order. In $\text{Al}_{90}\text{Fe}_x\text{Ce}_{10-x}$ ($x=5,7$) the experimentally determined PDF indicates that short range ordering exists around both the Fe and Ce atoms [17]. Ab initio molecular dynamics simulations have been used to calculate the coordination number of a series of binary amorphous glasses [18]. It was found that, for three metal-metalloid glasses and a transition metal – transition metal glass, more than 75% of the solute atoms had 2 specific coordination numbers, see Table 2.2. These calculations show that specific coordination polyhedra are dominant for each alloy, and the type depends on solute element (Ni-B vs. Ni-P) and glass composition.

Metallic glasses of different types likely have very different short range structures and it is important to consider glass studies on alloys with compositions similar to $\text{Cu}_{75}\text{Hf}_{20}\text{Dy}_{05}$.

Table 2.2. Dominant coordination number of solute atoms in $\text{Ni}_{81}\text{B}_{19}$, $\text{Ni}_{80}\text{P}_{20}$, $\text{Zr}_{84}\text{Pt}_{16}$, $\text{Ni}_{63}\text{Nb}_{37}$ metallic glasses based on *ab initio* calculations, from [18].

Metallic Glass	Dominant Coordination Numbers
$\text{Ni}_{81}\text{B}_{19}$	9, 10
$\text{Ni}_{80}\text{P}_{20}$	10, 11
$\text{Zr}_{84}\text{Pt}_{16}$	11, 12
$\text{Ni}_{63}\text{Nb}_{37}$	14, 15

The binary Cu-Zr system has been studied in great detail due to the wide range of glass forming compositions (30% to 70 at% Zr) and as the prototype alloy for the TM-TM metallic glasses, see summary in [15]. This section will be presented in detail due to its likely applicability to the $\text{Cu}_{75}\text{Hf}_{20}\text{Dy}_{05}$ alloy which is predominantly a TM-TM amorphous alloy. Additionally, Zr and Hf share a wide range of general materials properties.

The density of the metallic glass Cu-Zr alloys is less than the interpolated density of crystalline Zr and Hf at all compositions [19]. This implies an increase in free volume relative to the crystalline state. The bonding type of the Cu-Zr amorphous alloys is likely metallic as the measured interatomic distances is nearly the sum of the atomic radii [20]. This suggests some reasonable applicability of the dense random packing of hard sphere models, see Table 2.1.

The SRO of this alloy system has been studied experimentally [20-22] and modeled using ab-initio molecular dynamic simulations [22-24]. The partial coordination

number (Cu-Cu, Cu-Zr, Zr-Zr, and Zr-Cu) was experimentally determined using x-ray neutron scattering and found to depend on the composition [20, 22]. Figure 2.4 shows that the partial coordination number as a function of composition [22]. At each composition studied, the central atom is surrounded by both Cu and Zr atoms. This is a key point and shows some SRO effect due to preferential bonding as the number of Zr atoms surrounding a central Cu atom is higher than statistical predictions based on a random packing model.¹ Thus, the dissimilar Cu-Zr bonds are more favored than the similar Cu-Cu bond types.

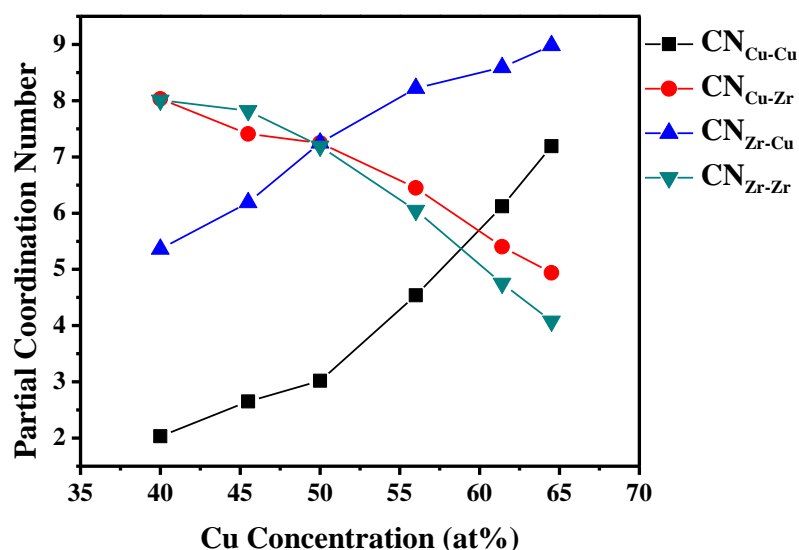


Figure 2.4. Partial coordination number (CN) as a function of composition in $\text{Cu}_{1-x}\text{Zr}_x$ amorphous metallic glasses determined experimentally by both x-ray and neutron diffraction. $\text{CN}_{\text{A-B}}$ designates the coordination around central atom A by surrounding atom type B. The number of Cu-Zr bonds is greater than random packing would suggest indicating preferential dissimilar bonding of Cu and Zr. Recreated from [22].

¹ The hard packing coordination numbers of Cu-Cu/Zr and Zr-Cu/Zr are similar to those calculated for Cu-Hf alloys, Table 2.1. The radius of Zr is 0.160 nm is nearly the same as Hf, 0.159 nm. A first order approximation of a random packing model for $\text{Cu}_{50}\text{Zr}_{50}$ alloy would entail 50% of the nearest neighbors of Cu (12 for similar atoms) be Zr, but each Zr atoms, owing to its larger radius, reduces the CN.

Molecular dynamic simulations of the Cu-Zr system show that the structure of the amorphous metallic glasses is dominated by a few specific structures, summarized in [15]. These structures are typically defined by Voronoi polyhedral cells about a central atom, for examples of this formulation see [9, 25]. The Voronoi cell notation describes a polyhedral cell by the number, n_i , of i -edged faces of the polyhedron that surrounds a central atom. These numbers are represented by the index $\langle n_3, n_4, n_5, n_6 \rangle$, meaning number of 3 edge faces, 4 edge faces, etc. The sum of the Voronoi indexes is the CN. For example, a perfect tetrahedron has the index $\langle 4, 0, 0, 0 \rangle$, and has 4 faces each with 3 edges and a CN of 4.

Results of simulations by Cheng calculate (Figure 2.5) the fraction of polyhedral cells around both Cu and Zr atom as a function of the Cu-Zr metallic glass composition [23, 24, 26]. The atomic arrangements about Cu and Zr are dominated by a few specific structures. In the case of the 70 at% Cu composition, 30% of the Cu centered cells are of the $\langle 0, 0, 12, 0 \rangle$ (CN 12)² type. 65% of the cells are only 4 different polyhedral types with CN of 12, 12, 11 and 13 in decreasing frequency. In contrast, the Zr centered cells have no cell-type fraction more dominant than 10% and therefore does not show any dominant cluster type. Moreover, it has been shown that the dominant $\langle 0, 0, 12, 0 \rangle$ Cu centered cluster type is not completely random in $\text{Cu}_{65}\text{Zr}_{35}$ and $\text{Cu}_{50}\text{Zr}_{50}$ metallic glass. These clusters are indicated by the green atoms in Figure 2.6, and they form string-like chains and networks leading to medium range order [26]. Preferential bonding of Zr to

² It's important to reiterate that the 12 NN Cu copper polyhedral contains both Cu and Zr atoms surrounding it (see diagrams in Figure 2.5 and also experimental results shown in Figure 2.4.

Cu (as seen in Figure 2.4), would result in the Cu centered $\langle 0, 0, 12, 0 \rangle$ cluster atoms having an above average concentration of Zr atoms.

In summary, the high Cu content Cu-Zr metallic glass studies form the string-like interconnected $\langle 0, 0, 12, 0 \rangle$ clusters (green atoms in Figure 2.6) are Cu centered and have a higher than statistically random number of Zr atoms. Therefore, it is likely that the interconnected regions within the amorphous structure are Zr rich. Short and medium range order is likely present in the amorphous $\text{Cu}_{75}\text{Hf}_{20}\text{Dy}_{05}$ structure based on its similarities to the high Cu content Cu-Zr amorphous glasses. The amorphous glass structure has important ramifications for the corrosion behavior $\text{Cu}_{75}\text{Hf}_{20}\text{Dy}_{05}$.

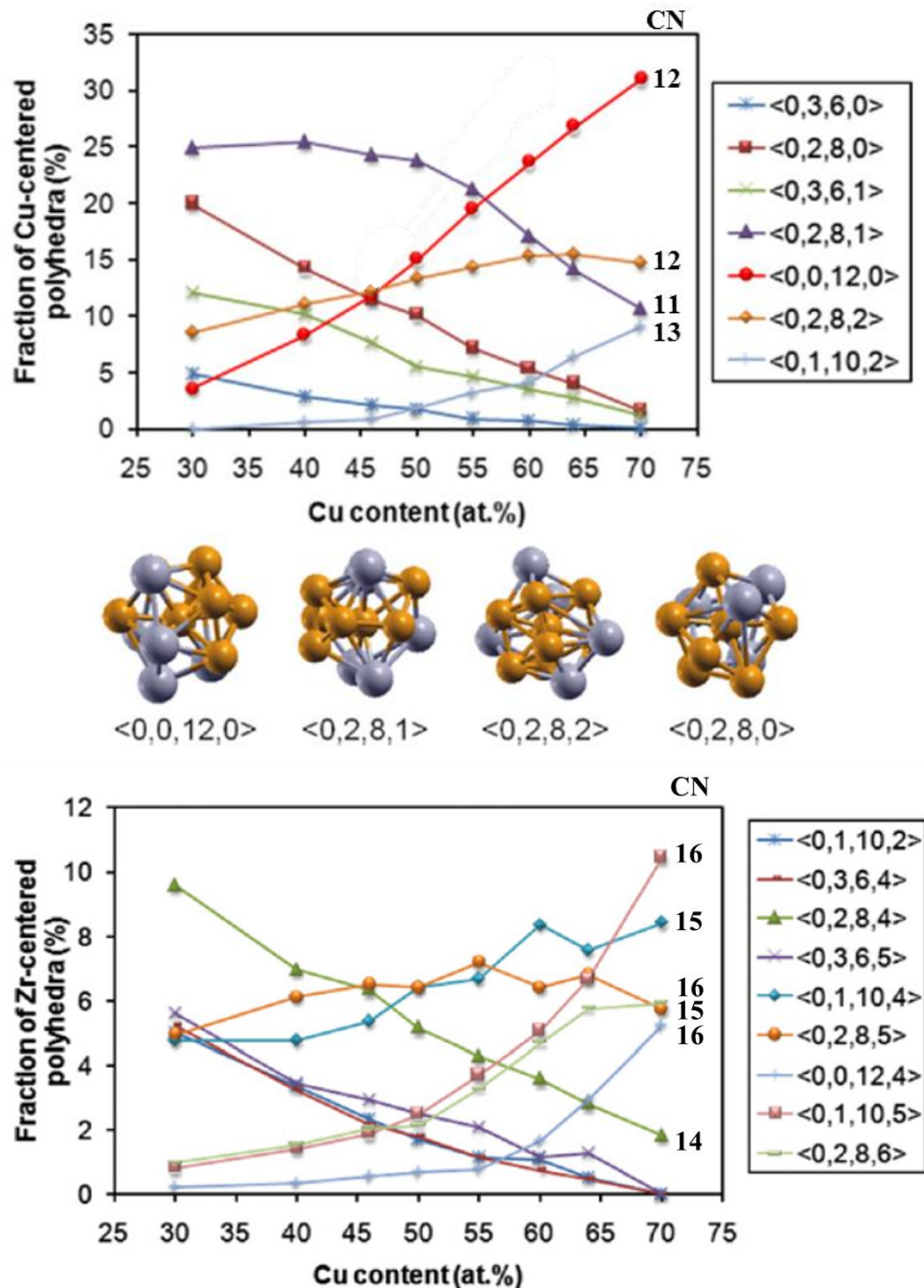


Figure 2.5. Fraction of Voronoi cells around Cu (top) and Zr (bottom) as a function of composition molecular dynamic simulations of the amorphous structure. The Voronoi cells for selected Cu clusters are shown with orange atoms representing Cu and gray Zr. The CN for the most common cells is shown. Adapted from [15], with permission from Permagon.

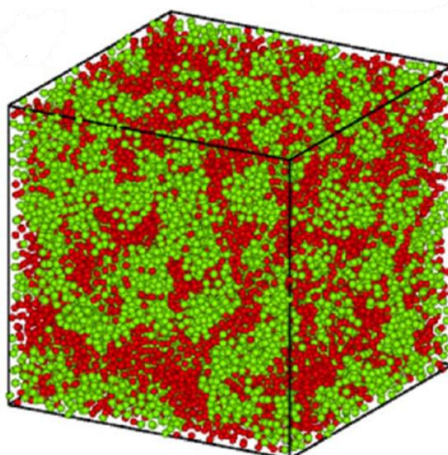


Figure 2.6. Distribution of atoms belonging to $\langle 0, 0, 12, 0 \rangle$ Cu centered clusters in $\text{Cu}_{65}\text{Zr}_{35}$ based on ab-initio molecular dynamics simulations. The green represent atoms belonging to the Cu-centered $\langle 0, 0, 12, 0 \rangle$ clusters and red balls represent atoms in the remaining part of the system, respectively. Adapted, with permission, from Li, M., C. Wang, S. Hao, M. Kramer, and K. Ho, *Physical Review B*, 2009. **80**(18). Copyright 2009 by the American Physical Society [26].

2.3 Electrochemical Characteristics of the Cu, Hf and Dy System

The thermodynamic predictions for stability, passivity and dissolution are shown in the equilibrium potential – pH diagrams, in Figure 2.7. The E-pH diagrams of Cu, Hf and Dy in H_2O at room temperature are presented superimposed to give some indication of the alloy behavior in terms of which alloying element is likely to be active, passive or noble in specific solution environments. In acidic environments, thermodynamics indicates that all 3 elements undergo active dissolution and there is no oxide formation. The Cu oxidation potential to the Cu^{2+} cation (assuming 10^{-6} M species concentration) is $-0.1 \text{ V}_{\text{SCE}}$ while both Hf and Dy are 2 V and 2.5 V lower. At intermediate pH, Cu is active and it is indicated that Hf likely forms a passive layer. Dy is generally active except at high pH where hydroxide formation is possible. Thermodynamically, there are 3 distinct regions: low pH where all elements are active, intermediate pH where Hf is passive while Cu is active and high pH where Cu and Hf are both passive. The oxide

stability diagram for Cu and Hf, shown in Figure 2.8, indicates that the most favorable pH for Cu oxide formation is around pH 10.

2.3.1 Cu

The Cu passive film formation in aqueous environments has been studied in detail and consists of an inner layer of Cu_2O and an outer layer of CuO [27, 28]. Anions, Cl^- and SO_4^{2-} , in solution do not affect the type or property of the oxide layer [29]. These anions are important because Cl^- [4, 30-32] and SO_4^{2-} [4, 33-35] both induce localized breakdown of the passive film. The absorption of the Cl^- anions into the oxide changed the character of the oxide leading to pit nucleation with higher Cl^- being more favorable for dissolution [36]. The thermodynamic stability considering 1 M and 0.1 M Cl^- anion concentrations in solution is shown in Figure 2.9. The formation of the CuCl_2^- complex reduces the thermodynamically stable passive region of the Cu_2O and Cl^- absorption into the oxide is predicted at high applied potential at intermediate pH. The dissolution kinetics in Cl^- indicates the CuCl_2^- complex movement is a mass transport rate limiting process [37]. The SO_4^{2-} anion increases the uniform dissolution rate of Cu [34, 38].

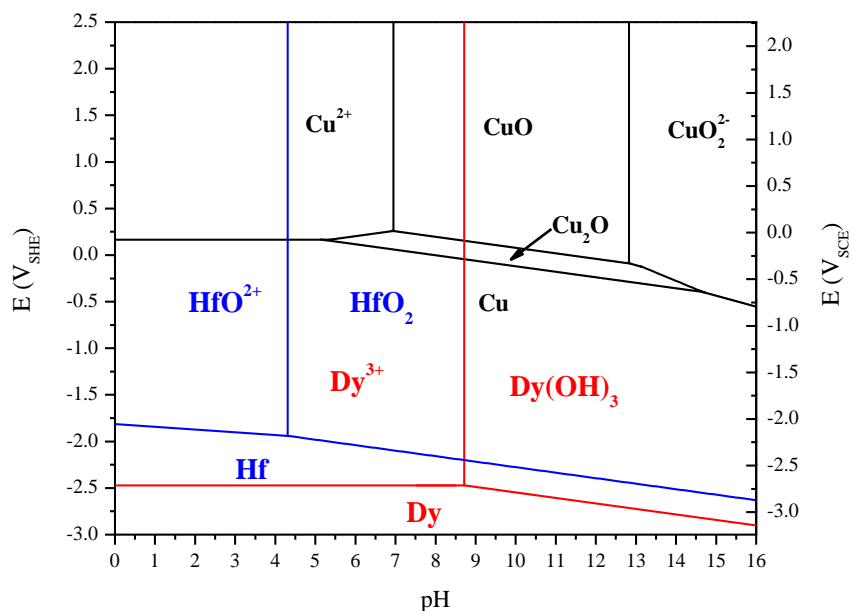


Figure 2.7. Combined Cu, Hf and Dy potential-pH equilibrium diagram for the Cu/Hf/Dy-H₂O system at 25°C with ion concentrations assumed to be 10⁻⁶ M [39].

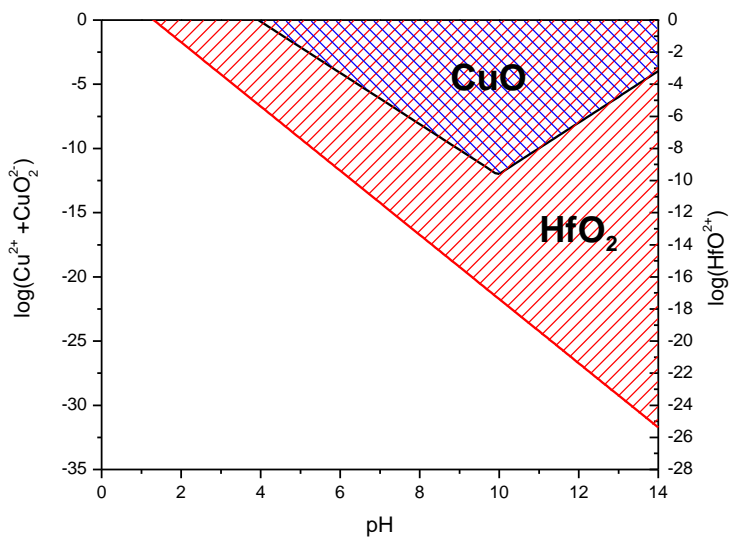


Figure 2.8. Cu and Hf Oxide Stability Diagram at 25°C with ion concentrations assumed to be 10⁻⁶ M [39]. The assumed reaction is the chemical reaction of HfO²⁺ to form HfO₂. For Cu, at pH < 9 the Cu²⁺ reacts to form CuO. At higher pH, the HfCuO₂⁻ anion reacts to form the oxide.

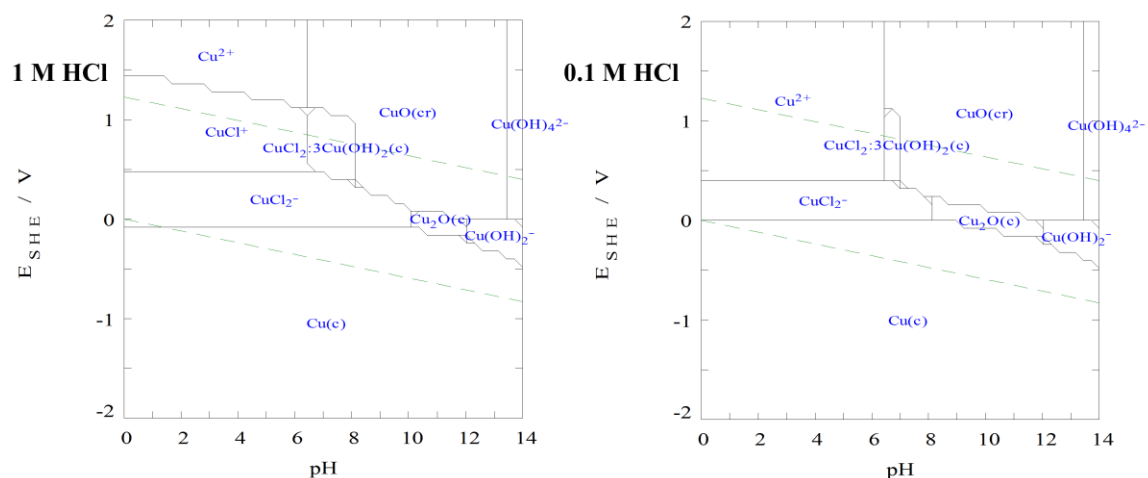


Figure 2.9. Calculated Cu-Cl-H₂O E-pH diagrams at Cl⁻ concentrations of 1 M (left) and 0.1 M right. The ion concentrations are assumed to be 10⁻⁶ M. Calculated and plotted using Medusa [13].

2.3.2 Hf and Dy

Hf shows similar corrosion behavior to Zr and is very corrosion resistant in mineral acids: Hf undergoes limited corrosion in H₂SO₄ solution, HNO₃, HCl and in strong basic environments, such as potassium hydroxide [40]. Hf corrodes in HF solution, by oxidation of Hf to HfF₄ by molecular HF (also producing H₂) [41]. Similar behavior was seen for Zr which oxidizes to ZrF₄ in HF solution [42]. Likely due to its active nature and limited use as an alloying element in engineering applications, the corrosion behavior of Dy has not been previously investigated in any detail.

This chapter will focus on environments where Hf shows very corrosion resistant behavior and either forms a stable passive film or exhibits kinetic passivity. Cu, Dy, or both elements will serve as detrimental solutes and lower the corrosion resistance. Experiments investigating the localized breakdown of passive films will utilize SO₄²⁻ as the detrimental anion due to its aggressiveness relative to Cl⁻ and to avoid precipitate insoluble complex phases present in Cl⁻ environments (CuCl is formed as part of the

oxidation process, see [43]). Additionally, dissolution in acidic SO_4^{2-} is likely not influenced by complexation [44]. Chapter 3 will focus on the preferential dissolution of Hf from the $\text{Cu}_{75}\text{Hf}_{20}\text{Dy}_{05}$ matrix under conditions where both Cu and Dy show noble behavior.

2.3.3 Previous Corrosion Studies on Cu-based Amorphous Materials

The effect of structural change in amorphous alloys to a single phase has been examined in the case of two Cu based amorphous alloys: $\text{Cu}_{50}\text{Ti}_{50}$ [45] and $\text{Cu}_{60}\text{Zr}_{40}$ [46]. Devitrification of the amorphous alloys to a structure with the same composition was found to lower corrosion resistance of $\text{Cu}_{50}\text{Ti}_{50}$ in 1 M HCl and 1 M HNO_3 , and was shown to have limited effect on $\text{Cu}_{60}\text{Zr}_{40}$ in 0.5 M H_2SO_4 . For $\text{Cu}_{60}\text{Zr}_{40}$, determination of corrosion current was made using only the Tafel extrapolation method and a superficial comparison of polarization behavior. However, both studies were performed with the alloy in an active state and did not address pitting or passivity.

2.4 Critical Unresolved Issues

The goal of this chapter is to explore the effect of the structural change from amorphous to crystalline $\text{Cu}_{75}\text{Hf}_{20}\text{Dy}_{05}$ on active, passive and localized corrosion. Is there a difference in corrosion behavior during passive and local dissolution in SO_4^{2-} solution? What is the underlying structural mechanism that changes the dissolution susceptibility and pitting resistance in SO_4^{2-} solution?

2.5 Experimental

Amorphous $\text{Cu}_{75}\text{Hf}_{20}\text{Dy}_{05}$ was produced by the melt spinning technique. High purity elements (Cu 99.999%, Hf 99.9% excluding Zr (nominally 2%), and Dy 99.9%)

were made into an ingot by arc melting under an argon atmosphere. The ingot was then inductively melted under argon and rapidly cooled on a Cu wheel of radius 10 mm with a rotation speed of 40 m/s. Prior to heat treatments, samples were first encapsulated in quartz tubes under argon. To fully crystallize the amorphous ribbon, encapsulated samples were annealed at 600°C for 30 minutes and then water quenched. The as-spun and annealed samples were characterized by XRD and TEM. X-ray diffraction (XRD) was performed using a Scintag XDS-2000 diffractometer with a Cu-K α source ($\lambda = 1.541\text{\AA}$). XRD spectra measurements were conducted in the $\theta/2\theta$ configuration. Transmission electron microscopy, TEM, analysis was performed using a FEI Titan 80-300 STEM operated at 300 kV. TEM specimens were prepared by cryogenic ion milling at 5 kV for 40 minutes. X-ray photoelectron spectroscopy (XPS) composition depth profiling was performed using a PHI Quantera SXM at the Institute for Critical Technology and Applied Science at Virginia Polytechnic Institute. Atom probe tomography measurements were performed on a field emission microscope, LEAP 4000, at 30K and a laser mode pulse at 200kHz with energy of 20 pJ. The total reconstruction volume was approximately $80 \times 80 \times 50 \text{ nm}^3$. The detector efficiency was about 37%. Experiment and analysis were performed by Dr. Daniel K. Schreiber, part of the Environmental Molecular Sciences Laboratory User Facility at the Pacific Northwest National Lab.

High purity element samples, used in comparative electrochemistry experiments, were polycrystalline Hf wire (99.7%, excluding Zr which is nominally 2%) and high purity polycrystalline Cu wire (>99.99%) with surface areas roughly equivalent to the $\text{Cu}_{75}\text{Hf}_{20}\text{Dy}_{05}$ ribbons. Electrochemistry experiments utilized a 3-electrode setup with an

exposed electrically isolated working electrode, reference electrode and platinum mesh counter electrode. The reference electrode used was a Saturated Calomel Electrode, hereafter referred to as SCE. In Cl^- free environments, a saturated $\text{Hg}/\text{Hg}_2\text{SO}_4$ (MSE) electrode was used, but potentials are converted to the SCE scale. Experimental measurements conducted include cyclic polarization, potentiostatic polarization, and cyclic voltammetry (CV). Scan rates were typically 1 mV/s in cyclic polarization experiments. In CV experiments a faster scan rate of 5 mV/s or 20 mV/s was used. The solution was deaerated through vigorous sparging using N_2 for at least 1 hour prior to electrochemical experiments. Chemical solutions were produced using reagent grade chemicals and pure water (resistivity 18.2 $\text{M}\Omega/\text{cm}$) produced by an Academic MilliQ filtration system (MilliPore).

2.6 Results

2.6.1 Characterization of $\text{Cu}_{75}\text{Hf}_{20}\text{Dy}_{05}$

The thermal processing conditions of amorphous and crystalline $\text{Cu}_{75}\text{Hf}_{20}\text{Dy}_{05}$ are summarized in Table 2.3. The amorphous structure of the as-quenched melt spun ribbon was verified using XRD, Figure 2.10. The amorphous structure was confirmed using high resolution TEM imaging, Figure 2.11. The diffraction pattern (FFT of the micrograph) confirms the amorphous structure. Compositional analysis using high-angle annular dark-field imaging (Figure 2.12) indicates compositional fluctuations on the order of 6-8 nm that are rich in higher-Z Hf/Dy. The alloy was fully crystallized to $\text{Cu}_{51}\text{Hf}_{14}$ structure by annealing at 600°C for 30 minutes followed by a water quench. XRD of the crystalline phase, Figure 2.10, shows a single phase of the $\text{Cu}_{51}\text{Hf}_{14}$ type with a 0.6 ° shift likely due

to dissolved Dy into the Hf lattice sites resulting in a slight lattice expansion and shift to higher 2θ .

The XRD spectra for the annealed specimen indicates single phase crystallization to a polycrystalline $\text{Cu}_{51}\text{Hf}_{14}$ phase, with a 0.6 degree phase shift likely due to Dy solid solution substitution on the Hf lattice sites. According to the phase diagram, $\text{Cu}_{51}\text{Hf}_{14}$ is a line compound [6]. Amorphous $\text{Cu}_{75}\text{Hf}_{20}\text{Dy}_{05}$ devitrifies to a single phase, $\text{Cu}_{51}\text{Hf}_{14}$, while maintaining a Cu to Hf ratio of approximately 4:1.

Atom probe tomography was used to determine the short range compositional variation present in the amorphous $\text{Cu}_{75}\text{Hf}_{20}\text{Dy}_{05}$ structural state, Figure 2.13. The pair distribution functions indicate a completely random distribution of Cu and Hf atoms. A slight clustering of Dy atoms is seen. The atom probe reconstruction also exhibits some low-density pockets. The measured composition is $\text{Cu}_{74}\text{Hf}_{20}\text{Dy}_{05}\text{Zr}_{0.5}$ (at%). This measured composition is very close to the target composition (with the 0.5 at% Zr due to contamination of 'pure' Hf³).

³ It is difficult to completely isolate Hf from Zr. Zr is nominally 2% of the Hf alloying addition. 2% Zr of the 20 at% Hf alloying addition is 0.4% of the total alloying concentration

Table 2.3. Annealing temperature, resulting phase and grain size of $\text{Fe}_{50}\text{Pd}_{50}$ alloy. Annealing at 600°C devitrifies the amorphous alloy to a single phase $\text{Cu}_{51}\text{Hf}_{14}$.

Sample	Heat Treatment	Phase
$\text{Cu}_{75}\text{Hf}_{20}\text{Dy}_{05}$	Melt-spun	amorphous
$\text{Cu}_{75}\text{Hf}_{20}\text{Dy}_{05}$	600°C 30 min, water quenched	$\text{Cu}_{51}\text{Hf}_{14}$ -type

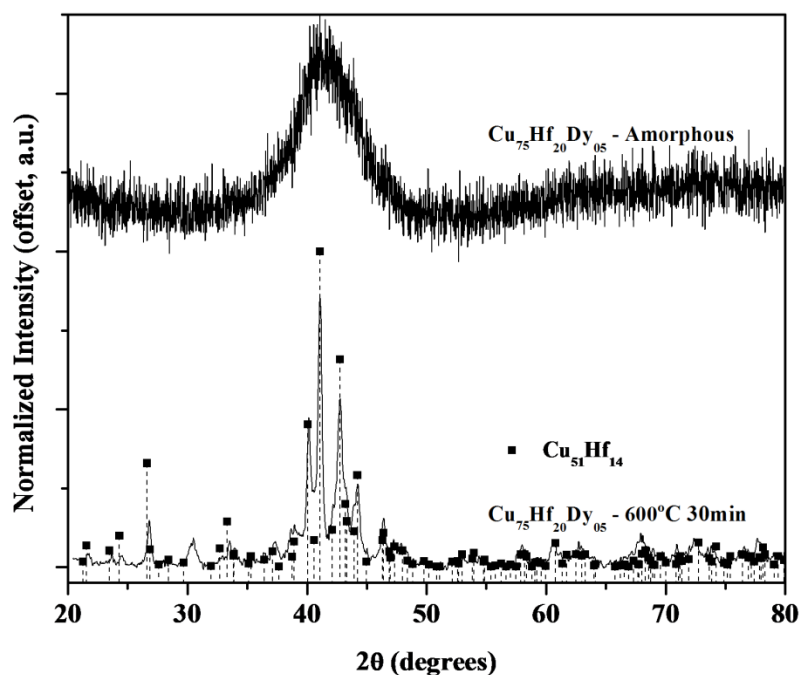


Figure 2.10. X-ray diffraction spectra of $\text{Cu}_{75}\text{Hf}_{20}\text{Dy}_{05}$ melt spun ribbon as received (amorphous) and after annealing at 600°C for 30 minutes. The crystalline phase is identified as $\text{Cu}_{51}\text{Hf}_{14}$ [47] with a 0.6° phase shift⁴. The small peak at 30.5° is likely due to surface layer HfO_2 formation.

⁴ The increase due to substitution of Dy atoms amounts to a 40% increase in the volume of the unit cell due to the increase in the Dy atomic radius. If 20% of the Hf atoms are replaced by Dy, then the volume of the unit cell would expand by roughly 0.3%. This equates to a 1% increase in the lattice parameters (assuming equal expansion in the c and a lattice direction). This expansion shifts all of the hexagonal diffraction peaks to lower 2θ by 0.4° .

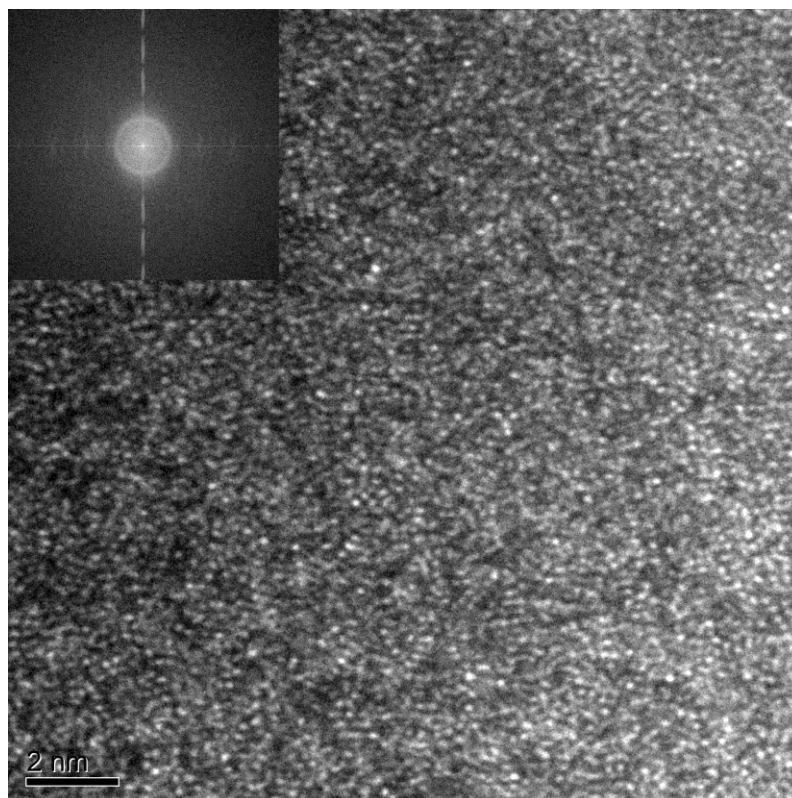


Figure 2.11. High resolution TEM bright field micrograph of amorphous $\text{Cu}_{75}\text{Hf}_{20}\text{Dy}_{05}$ showing a fully amorphous structure. The inlaid diffraction pattern shows no crystallization (FFT).

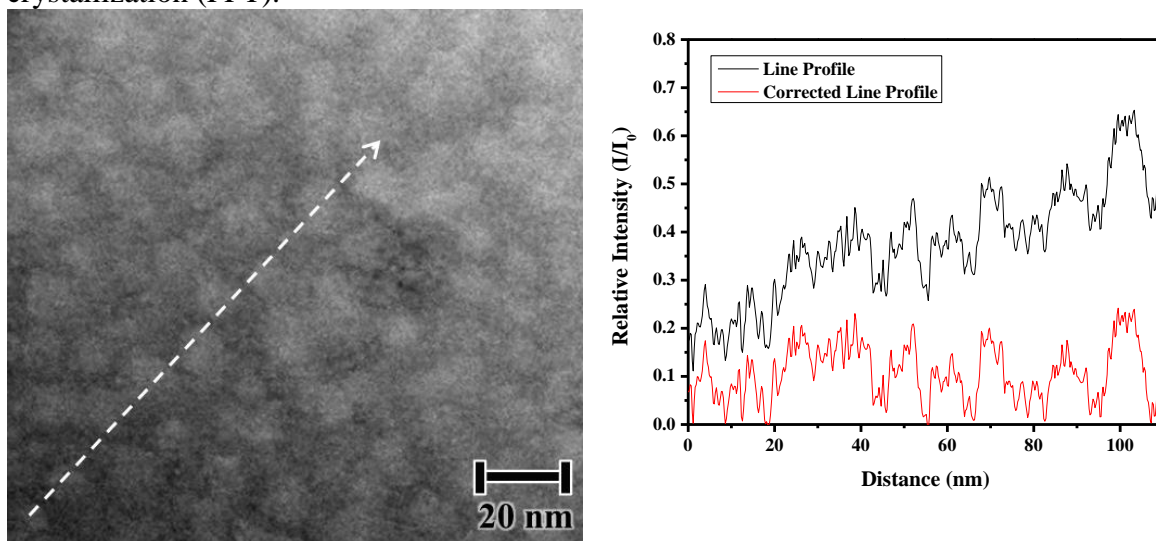


Figure 2.12. High-angle annular dark-field imaging (HAADF, left) The cloudy regions, about 20 nm, in the HAADF micrograph indicate Z contrast. The bright areas indicate regions of low Z and Cu enrichment. The line profile (on right) shows the relative intensity measured by the contrast ($I_0 = \text{white}$), after correction for sample thickness (subtraction of the linear background). The bright areas are 6.5-9 nm in diameter.

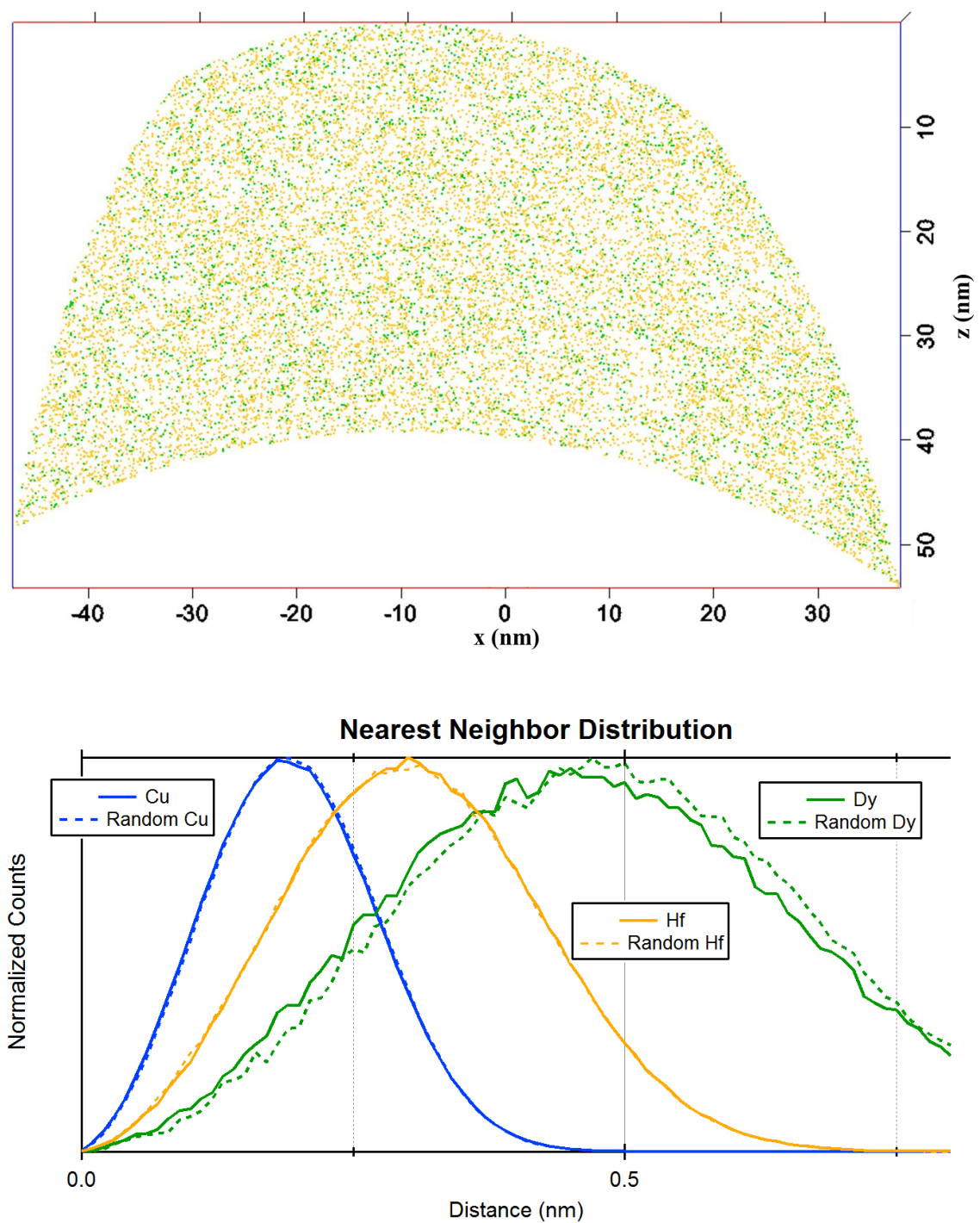


Figure 2.13. Atom probe tomography composition map (1 nm slice) of amorphous $\text{Cu}_{75}\text{Hf}_{20}\text{Dy}_{05}$ (top) and the corresponding pair distribution functions (bottom). Orange atoms are Hf and green atoms are Dy. Cu (blue) atoms are omitted for clarity. A uniform distribution of both Cu and Hf are seen. Some slight clustering of the Dy atoms is suggested. Work performed by Dan Schreiber and PNNL as part of their user facility (EMSL).

2.6.2 Electrochemical Behavior in the Passive State

Passive behavior was explored in pH 8.4 solution containing borate buffer using cyclic voltammetry to give some indication of oxide growth as a function of cycle. Figure 2.14 depicts the first cycle for both amorphous and crystalline $\text{Cu}_{75}\text{Hf}_{20}\text{Dy}_{05}$ compared to high purity Cu. Hf (not shown here) in this condition exhibits a high current during the first cycle indicative of passive film growth. Subsequent cycles, during film growth, have very low current density. No Hf oxide reduction is expected at these potentials (Figure 2.7). The scans of the Cu containing alloys scans indicate two oxidization peaks. During the reverse scan, there are double reduction peaks confirming reduction of the Cu^{1+} and Cu^{2+} oxides, which suggest the presence of a bi-layer oxide. Overall both structural states, amorphous and crystalline, exhibit passive behavior, but the overall current density is lower in the case of the amorphous state. The behavior during the first three cycles is shown for Cu compared to amorphous and crystalline $\text{Cu}_{75}\text{Hf}_{20}\text{Dy}_{05}$ in Figure 2.15 and the addition cycle behavior for each $\text{Cu}_{75}\text{Hf}_{20}\text{Dy}_{05}$ state, independently, in Figure 2.16. The oxidation and reduction peaks remain more pronounced during subsequent cycles in the case of Cu than for either alloy. This behavior suggests either oxide formation or oxide reduction is inhibited by Hf alloying and possible competing Hf oxide formation. In this case of the amorphous $\text{Cu}_{75}\text{Hf}_{20}\text{Dy}_{05}$, the current density of the oxidation peaks during the initial cycle is low, with minimal reduction peaks suggesting very thin oxides. Both oxidation and reduction peak magnitudes increase during each additional cycle. Overall the current magnitude in the amorphous structural state is lower than the crystalline case. The overall lower current density magnitudes and different cyclic behavior suggest that some aspects of the oxide are fundamentally different between the

amorphous and structural state of the $\text{Cu}_{75}\text{Hf}_{20}\text{Dy}_{05}$ alloy. The possible fundamental difference in the oxide as a result of the underlying structural state of the alloy will be explored under conditions of oxide breakdown.

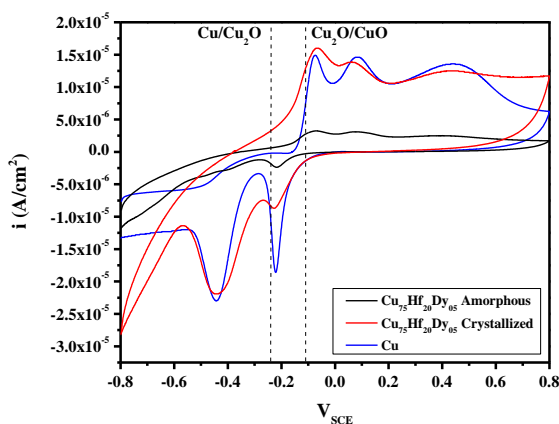


Figure 2.14. Initial cycle during cyclic voltammetry for Cu and amorphous and crystalline $\text{Cu}_{75}\text{Hf}_{20}\text{Dy}_{05}$ in deaerated pH 8.4 at a scan rate of 1 mV/s. The Nernst potentials for $\text{Cu}/\text{Cu}_2\text{O}$ and $\text{Cu}_2\text{O}/\text{CuO}$ are shown for reference.

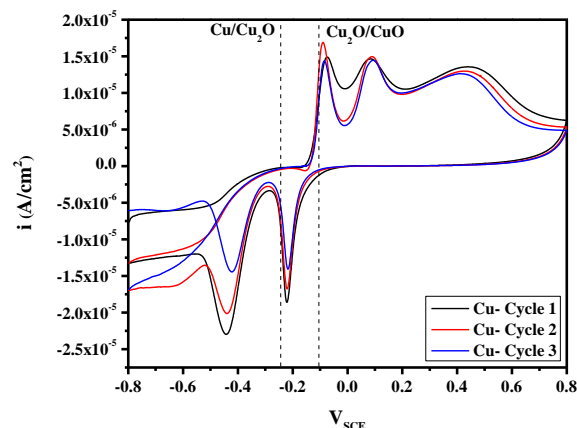


Figure 2.15. Cyclic voltammetry for polycrystalline Cu in deaerated pH 8.4 at a scan rate of 1 mV/s. The Nernst potentials for $\text{Cu}/\text{Cu}_2\text{O}$ and $\text{Cu}_2\text{O}/\text{CuO}$ are shown for reference.

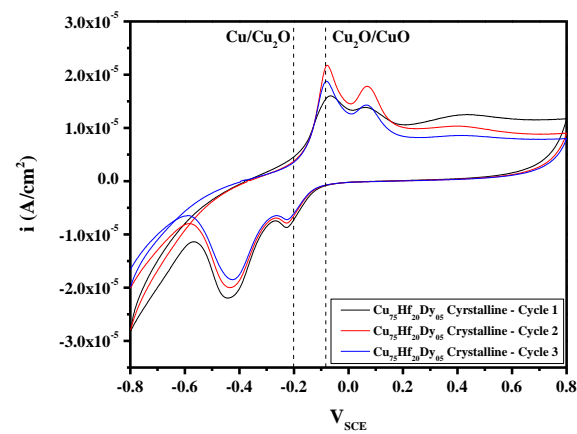
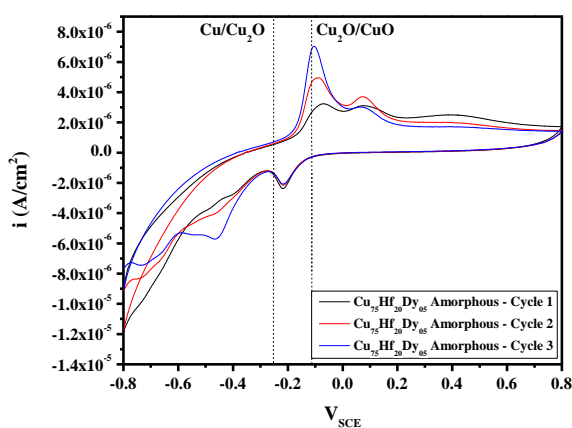


Figure 2.16. Cyclic voltammetry amorphous (left) and crystalline (right) $\text{Cu}_{75}\text{Hf}_{20}\text{Dy}_{05}$ in deaerated pH 8.4 at a scan rate of 1 mV/s. The Nernst potentials for $\text{Cu}/\text{Cu}_2\text{O}$ and $\text{Cu}_2\text{O}/\text{CuO}$ are shown for reference. The amorphous structural state shows a diminished second oxidation peak and minimal reduction peaks during the initial cycle. These peaks increase slightly with each cycle, but the overall current density is substantially lower for the amorphous compared to the crystalline structural state of $\text{Cu}_{75}\text{Hf}_{20}\text{Dy}_{05}$.

2.6.3 Metastable Pitting Susceptibility during Localized Breakdown of the Passive State

The presence of a Cu passive film at pH 8.4, predicted thermodynamically (Figure 2.7), was shown in the previous section. In this section, SO_4^{2-} anions will be used to induce breakdown of the passive film. The effect of increasing $[\text{SO}_4^{2-}]$ on Cu passivity in pH 8.4 borate buffer solution is shown in Figure 2.17. Increasing $[\text{SO}_4^{2-}]$ decreases the pitting potential of polycrystalline Cu from fully passive in 0.01M $[\text{SO}_4^{2-}]$ to approximately 0.3 V_{SCE} in 0.5 M $[\text{SO}_4^{2-}]$ in pH 8.4 borate buffer. Some metastable pitting is also indicated

The behavior of the $\text{Cu}_{75}\text{Hf}_{20}\text{Dy}_{05}$ alloys in pH 8.4 borate buffer and 0.5 M Na_2SO_4 is shown in Figure 2.18. In this environment Hf exhibits passivity without breakdown at all potentials. Cu undergoes breakdown and sustained dissolution at 0.3 V_{SCE} . Amorphous and crystalline $\text{Cu}_{75}\text{Hf}_{20}\text{Dy}_{05}$ show numerous metastable pit current transients but never exhibit the sustained dissolution seen for high purity Cu even during an upward scan to 1 V_{SCE} . There is a qualitative indication that the current transients are larger in the amorphous state compared to the crystalline condition. The large transients are followed by periods of lower current density with few transients. In contrast, the crystalline $\text{Cu}_{75}\text{Hf}_{20}\text{Dy}_{05}$ has more numerous, but smaller current transients. Similar behavior is seen in the less aggressive 0.1 M Na_2SO_4 solution, Figure 2.19. In this solution, the breakdown potential indicative of pit stabilization is elevated to around 1 V_{SCE} . The E-Log(i) behavior of the amorphous and crystalline $\text{Cu}_{75}\text{Hf}_{20}\text{Dy}_{05}$ both show numerous pit current transients at potentials below Cu breakdown. This is indicative of a more protective oxide in the case of high purity polycrystalline Cu.

These current transients were further explored using potentiostatic polarization, Figure 2.19 (right), at a potential within the metastable breakdown regime. Oxide breakdown transients are observed for both amorphous and crystalline $\text{Cu}_{75}\text{Hf}_{20}\text{Dy}_{05}$. The amorphous state undergoes more breakdown events. The total anodic charge for the amorphous structural state is 0.17 C/cm^2 over 3600 s, while the charge in the crystalline structural state is only 0.05 C/cm^2 .

These results indicate that there is a structure dependence on the ease of oxide breakdown and metastable pit formation Cu dissolution at local corrosion sites when the alloys are in the passive state. These results show strong evidence that the protective nature of the passive film and/or the dissolution from within pit initiated sites depends on the underlying structure of the alloy. The role of early stage pit growth is likely an underlying cause of the larger current transients. The passive film and underlying structure of amorphous $\text{Cu}_{75}\text{Hf}_{20}\text{Dy}_{05}$ facilitates local dissolution of largely Cu compared to the more protective film on the crystalline state.

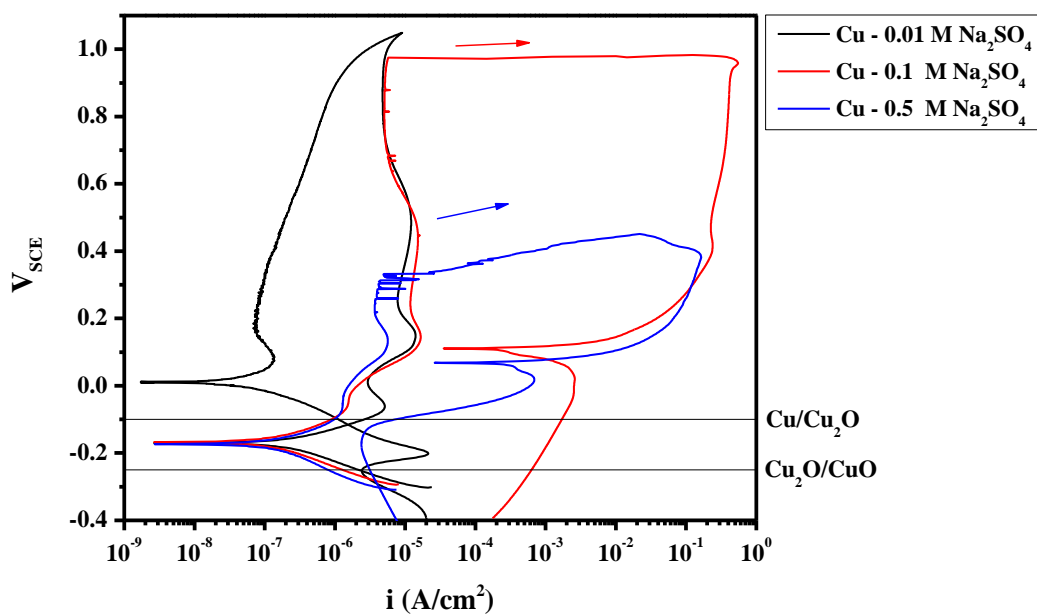


Figure 2.17. E-log(i) behavior of high purity Cu showing the effect of increasing $[\text{SO}_4^{2-}]$ in deaerated pH 8.4 borate buffer. In 0.01 M Na_2SO_4 solution no breakdown potential is observed, while the increase in concentration to 0.1 M and 0.5 M shows a decrease in critical potential. These results are similar to behavior observed by Cong [4].

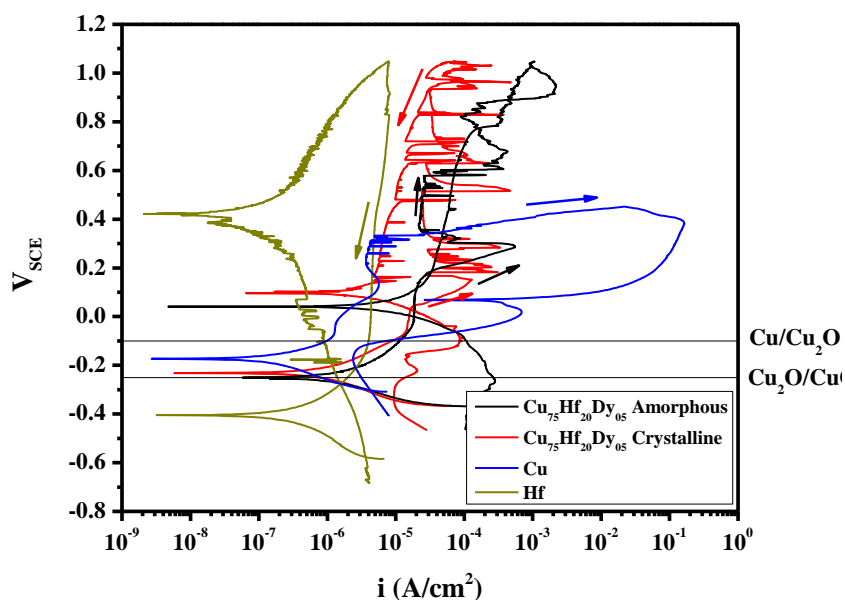


Figure 2.18. E-Log(i) behavior of Hf, Cu and $\text{Cu}_{75}\text{Hf}_{20}\text{Dy}_{05}$ in pH 8.4 borate buffer and 0.5 M Na_2SO_4 solution. Amorphous and crystalline $\text{Cu}_{75}\text{Hf}_{20}\text{Dy}_{05}$ show numerous metastable current transients. In this environment Hf shows only passive current, while Cu undergoes breakdown and sustained dissolution at 0.3 V_{SCE} .

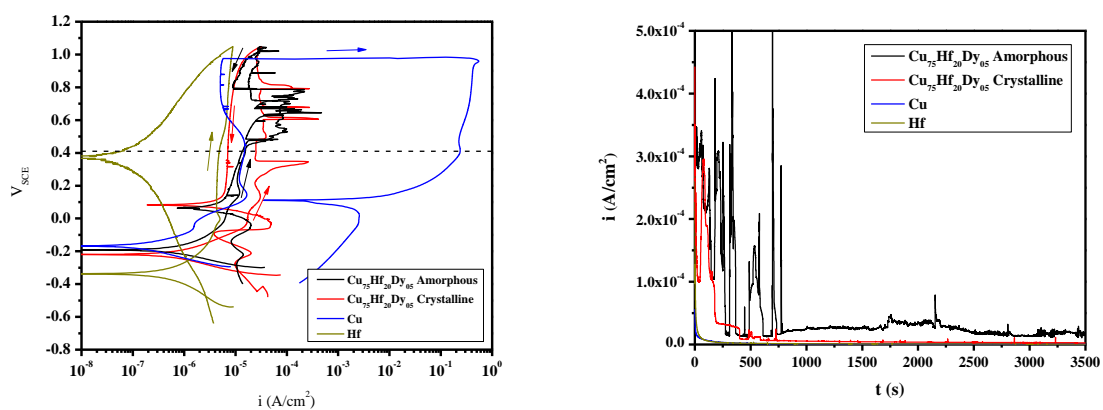


Figure 2.19. E-Log(i) behavior (left) and potentiostatic polarization at $0.41 V_{\text{SCE}}$ indicated by the dashed line (right) of Hf, Cu and $\text{Cu}_{75}\text{Hf}_{20}\text{Dy}_{05}$ in pH 8.4 borate buffer and 0.1 M Na_2SO_4 solution. The total anodic current of the amorphous state is 0.17 C/cm^2 and for the crystalline state is 0.05 C/cm^2 .

2.6.4 Metastable Dissolution Behavior of $\text{Cu}_{75}\text{Hf}_{20}\text{Dy}_{05}$ alloys in the Active Regime for Cu

In the previous two corrosion regimes, passive film formation and localized breakdown of the passive films/early stages of pit growth, the underlying structure affected dissolution. This section focuses on the behavior of $\text{Cu}_{75}\text{Hf}_{20}\text{Dy}_{05}$ in acidic SO_4^{2-} environments where no passive film formation is expected on Cu. A Hf passive film is not thermodynamically expected at this pH (Figure 2.7). However, Hf does not undergo dissolution in H_2SO_4 [40]. The lack of dissolution is due to kinetic passivity of Hf^{5+} . In contrast, Cu readily dissolves in acidic H_2SO_4 environments. This environment probes the effect of structure on the active dissolution of Cu under conditions where Hf is stable.

The behavior of the $\text{Cu}_{75}\text{Hf}_{20}\text{Dy}_{05}$ alloys was investigated at three concentrations of H_2SO_4 solution. The E- $\log i$ behavior in 1 and 0.1 M H_2SO_4 solution is shown in Figure 2.20 and in 0.5 M H_2SO_4 solution in Figure 2.21. The Hf current density does not vary significantly with potential and remains less than 10^{-5} A/cm² indicative of passivity. Similar Hf E- $\log i$ is observed at all three solution concentrations. Cu shows nearly charge transfer controlled dissolution behavior at all solution concentrations. The amorphous and crystalline $\text{Cu}_{75}\text{Hf}_{20}\text{Dy}_{05}$ show some measure of resistance due to the Hf in solid solution. The increase in current density over that of high purity Hf is within 1 order of magnitude in 0.1 M H_2SO_4 solution. In the higher concentration solutions the difference increases by 2-3 orders of magnitude. The alloying of Hf impedes the dissolution of Cu but this was

⁵ Formation of the HfO_2 oxide forms more quickly than the dissolution to the thermodynamically stable HfO^{2+} cation. This is a well-known effect in stainless steel where Cr alloying leads to protection at low pH despite that the Cr_2O_3 is not expected at this pH thermodynamically.

dependent on the aggressiveness of the solution. In more aggressive solution, the overall current density increases and the current transients become more substantial.

The amorphous and crystalline structures both show an active-passive transition consisting of the two oxidation peaks, likely Cu/Cu^{1+} and Cu/Cu^{2+} . The upper potential coincides with the main anodic process on high purity Cu. This peak in anodic current density is readily apparent in both structural states in 0.1 M H_2SO_4 solution. However, the current decreases at higher potentials, above the Cu-dissolution peak, and clearly indicates passivity. In the passive regime, current transients are observed in both states similar to the behavior of the $\text{Cu}_{75}\text{Hf}_{20}\text{Dy}_{05}$ alloys seen in the basic environments. The passive anodic current density of the amorphous state is higher than the crystalline state in 0.1 M H_2SO_4 solution, and is $6 \cdot 10^{-5} \text{ A/cm}^2$ and $2.5 \cdot 10^{-5} \text{ A/cm}^2$ for the two conditions, respectively (at $0.5V_{\text{SCE}}$ in the passive regime).

In the more aggressive 0.5 M H_2SO_4 solution, the Cu dissolution active-passive transition is more pronounced in both alloys. This is especially true in the case of the amorphous alloy where a substantial increase in dissolution occurs compared to the crystalline case. Above the active nose at $0 V_{\text{SCE}}$, the crystalline structure exhibits numerous metastable current transients while the amorphous condition shows only a few such events. Both the number and size of current transients in the crystalline state are increased in 1 M H_2SO_4 solution. In this solution the Cu active-passive nose of the amorphous alloy has increased compared to the lower solution concentrations. No active-passive nose is apparent⁶ in the case of the crystalline $\text{Cu}_{75}\text{Hf}_{20}\text{Dy}_{05}$ alloy; instead more

⁶ The active-passive nose size in the crystalline case is likely diminished due to the higher open circuit potential and the offsetting HER.

spontaneous passivity, with numerous high current density transients is observed. These events often persist which is indicative of pit growth prior to passivation as confirmed by optical examinations. Rapid cyclic scans were run across the Cu-dissolution nose to further elucidate this behavior. The potential range is indicated by the dashed line in Figure 2.21

Cyclic voltammetry experiments (at 5 mV/s) in the 0.5 M H₂SO₄ solution environment are shown in Figure 2.22 both as a comparison between the two structural states (top) and the cyclic trends for each alloy independently (bottom). Both oxidation peaks, the first oxidation peak at -0.1 V_{SCE} and the second at 0 V_{SCE}, are observed during the initial cycle for the amorphous and crystalline states. The reverse scans do not show Cu/Cu⁺ and Cu/Cu²⁺ reduction peaks. This indicates ejection of Cu cations into solution. The current density of the first oxidation peak (at -0.1 V_{SCE}) is substantially higher in the case of the amorphous structural state than the crystalline state. During subsequent cycles of the amorphous state, only a single distinct peak is seen at -0.5 V_{SCE}. In the crystalline state, both peaks remain distinct over all 5 cycles. Both conditions also show abrupt current spikes.⁷ The lowering of the Cu/Cu¹⁺ and Cu/Cu²⁺ peak height from the 1st to 5th cycle and the low passive current at high potentials suggests that Cu removed and ejected into solution through a passivating layer of HfO₂.

The structural state dependence of decay in the oxidation current density of the first oxidation peak was investigated using CV at 20 mV/s. The total charge density accumulated in the first oxidation peak for each structural state is shown in Figure 2.23.

⁷ The sustained appearance and number of transients in the amorphous case is likely due to limited overall dissolution due to the fast scan rate compared to the E-log*i* behavior in Figure 2.21.

The amorphous state shows sustained charge density for each cycle after the first of approximately 3.6 mC/cm^2 . The charge for the crystalline state decayed substantially each cycle to a final value of 0.4 mC/cm^2 .

The change in surface composition was determined using potentiostatic polarization at $0.15 V_{\text{SCE}}$, a potential just about the active-passive transition. The composition depth profile was determined by XPS after polarization. These results are shown in Figure 2.24. During polarization, the current density of the amorphous state is higher than crystalline state. The total charge was 0.255 and 0.076 C/cm^2 for the amorphous and crystalline states, respectively. The total expected depth of dissolution, based on the accumulated anodic charge during polarization and Faraday's Law, of the amorphous alloy was about 210 nm , while for the crystalline alloy it was 63 nm ⁸. The composition depth profile shows a dealloyed layer that is enriched in Hf, consistent with HFO passivation and direct ejection of Cu^{1+} and Cu^{2+} into solution. However, the dealloyed layer thickness is on the order of 30 SiO_2 equivalent nm. This result is significantly less than the expected depth from the dissolution charge assuming 100% preferential dissolution of Cu. Moreover, the composition depth profile is essentially the same for each structural state despite the difference in accumulated charge. It is likely that the dealloyed layer is on the order of the first 30 nm of the surface layer.

⁸ For the Faraday's law calculations, total preferential dissolution of the Cu from the matrix was assumed. Cu oxidation to the +2 valence state was assumed. The average density of pure Cu was used to calculate the depth. The preferential dissolution depth was calculated by using the Cu atomic ratio and assuming Under these assumptions the dissolution depth per charge density is $0.823 \text{ }\mu\text{m/C}\cdot\text{cm}^{-2}$. In the case of congruent dissolution, the dissolution depth per charge density is $0.46 \text{ }\mu\text{m/C}\cdot\text{cm}^{-2}$. In this case Hf oxidation to Hf^{1+} and the $\text{Cu}_{51}\text{Hf}_{14}$ crystal density were used.

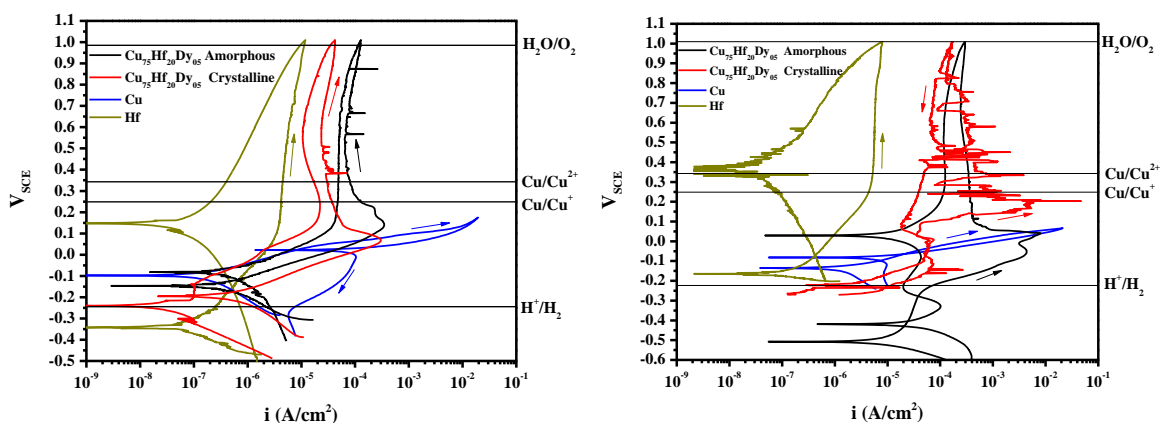


Figure 2.20. E-log*i* behavior of Hf, Cu and Cu₇₅Hf₂₀Dy₀₅ in deaerated 0.1 M (left) and 1 M (right) H₂SO₄ solution at pH 0.7 and -0.3, respectively. For reference, the oxidation potentials are listed assuming species concentrations of 10⁻³ M.

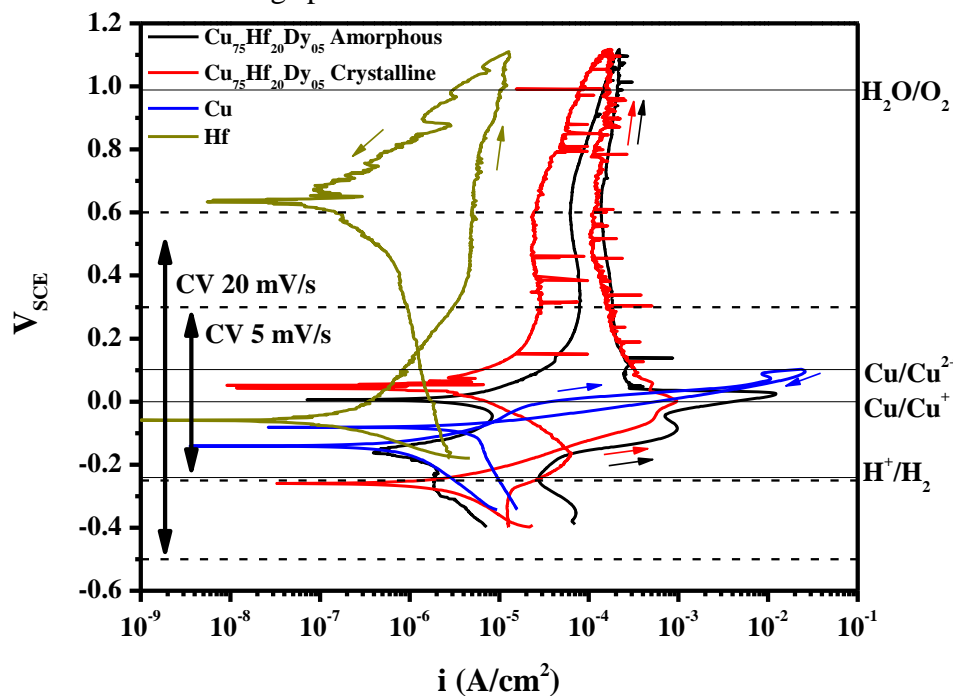


Figure 2.21. E-log*i* behavior of Hf, Cu and Cu₇₅Hf₂₀Dy₀₅ in deaerated 0.5 M H₂SO₄ solution. For reference, the oxidation potentials are listed assuming species concentrations of 10⁻³ M.

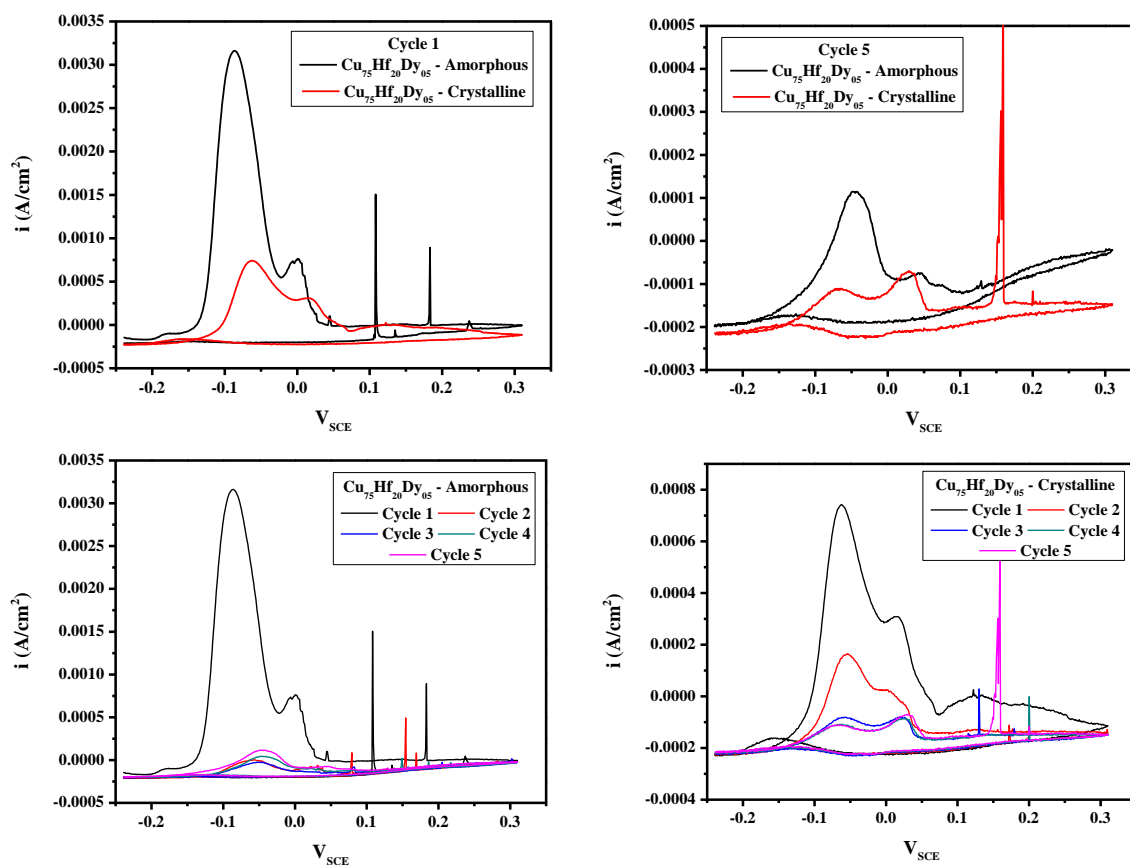


Figure 2.22. Cyclic voltammetry at 5mV/s for amorphous and crystalline $\text{Cu}_{75}\text{Hf}_{20}\text{Dy}_{05}$ in deaerated 0.5 M H_2SO_4 solution (pH 0). The 1st cycle (top left) and 5th cycle (top right) show the amorphous structural state has larger current density in both oxidation peaks over all 5 cycles. Both states show metastable breakdown of the passive film above the Cu oxidation peaks.

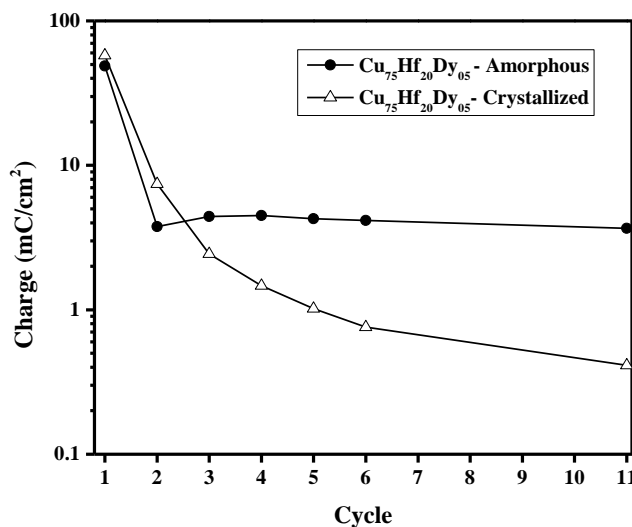


Figure 2.23. Total charge in the first oxidation peak of amorphous and crystalline $\text{Cu}_{75}\text{Hf}_{20}\text{Dy}_{05}$ during rapid cyclic voltammetry at 20 mV/s from -0.5 to 0.6 V_{SCE} in deaerated 0.5 M H_2SO_4 solution. The amorphous state shows higher sustained charge at 3.6 mC/cm^2 than the crystalline state which decays to 0.4 mC/cm^2 within 11 cycles.

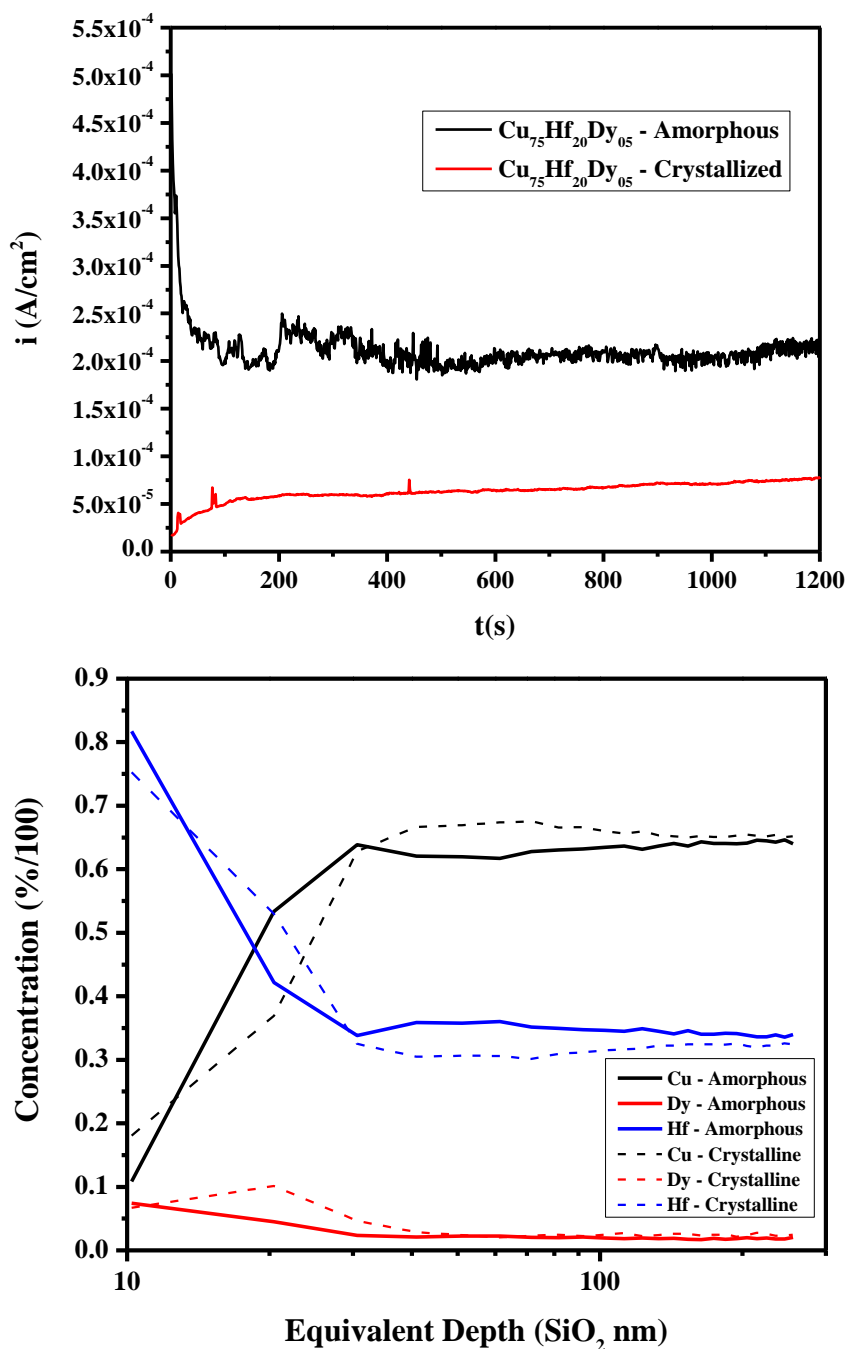


Figure 2.24. Potentiostatic polarization in deaerated 0.5 M H₂SO₄ at 0.15 V_{SCE} (top) and XPS depth profiling after the potentiostatic exposure for 1200 s (bottom) of amorphous and crystalline Cu₇₅Hf₂₀Dy₀₅. The total accumulated charge in the amorphous state is 0.255 C/cm² compared to 0.076 C/cm² in the crystalline state. The XPS results show surface enrichment of Hf resulting from preferential dissolution of Cu up to 40 SiO₂ equivalent nm of depth. Despite the anodic charge difference (increases by a factor of 5 for the amorphous state) no corresponding increase in the dealloyed layer depth is seen. XPS results carried out at Institute for Critical Technology and Applied Science at Virginia Polytechnic Institute.

2.7 Discussion

2.7.1 Effect of Nanostructure on Preferential Dissolution of Cu from the Matrix

In acidic environments, Cu actively dissolves while Hf is passive due to kinetic passivity (Figure 2.21). The contrast in nobility is a likely scenario leading to preferential dissolution. Moreover, the lowering of the Cu/Cu^{1+} and Cu/Cu^{2+} peak height from the 1st to 5th cycle (Figure 2.22) and the low passive current at high potentials suggests that Cu is removed through an increasingly perfect passivating layer of HfO_2 and that less near surface Cu is available after each cycle.

The composition depth profile indicates no difference in the composition profile between the amorphous and crystalline states of $\text{Cu}_{75}\text{Hf}_{20}\text{Dy}_{05}$ despite the difference in total dissolution (Figure 2.24). Therefore alloy dissolution involves both Hf and Cu dissolution and in a moving dissolution front with surface layer Hf enrichment and preferential Cu dissolution. The dissolution mechanism is some form of congruent dissolution and preferential dissolution which makes sense because Hf passivity is not thermodynamically assured.

This result corroborates the idea that the active/passive transition and oxidation peaks, within the active nose, is in fact Cu dissolution from the matrix instead of a reaction involving Hf or complexation of Cu. Within the detection limit of the XPS analysis, which is averaging roughly a 5 μm spot size, the dealloyed layer of the amorphous and crystalline state is very similar. X-ray diffraction (not shown) of the amorphous ribbon after a 1000 s potential hold at 0.4 V_{SCE} in aerated 0.5 M H_2SO_4 showed that the ribbon retained the amorphous structure after exposure. This result

indicates that was no X-ray detectable reorganization of remaining Hf in a crystalline state.

2.7.2 Role of Nearest Neighbor Distance in Protective Film Formation

A continuous network of passivating atoms is required for formation and complete coverage of a passive film [48-50]. The critical density of atoms has been theoretically calculated for binary alloys and compared the critical alloying concentration well established by experiments [48, 50]. In the Fe-Cr system, below 12 % Cr the corrosion resistance is poor because a continuous oxide is unable to form [50]. In this case, Sieradski showed that a critical separation distance of 0.418 nm is required for oxide bridging based on the distance between Cr clusters based on the ionic radii. Using this simple model, Cr atoms must be within the 2nd nearest neighbor (NN) distance of another Cr atom. Calculating the probability of this occurring agrees with the experimental values. McCafferty considers M-O-M interactions and a Graph Theory based analysis to calculate the critical solute volume within the passive film to form a passive layer [48]. In both these approaches, the distance between atoms is a significant parameter at a local scale.

The ordered $\text{Cu}_{75}\text{Hf}_{20}\text{Dy}_{05}$ structure has a periodic array of atoms (see Figure 2.2 and Figure 2.26), and the distance between Hf atoms is crystallographically well defined. The average distance between passivating Hf atoms is described for each of three Hf atoms based on the crystallographic radial distance of separation in Figure 2.3. These figures give some idea about the radial distance of Hf atoms from one another, i.e. the number of atoms within 0.4 nm, for instance. For comparison, the crystal structure of the

HfO₂ oxide is shown in Figure 2.25. In the oxide, 12 Hf atoms are required within 0.4 nm of each Hf atom. This criterion is higher than the distribution in the crystalline alloy. Therefore, dissolution, surface diffusion of Hf and some surface enrichment Hf is likely required for passive layer formation. These features make this alloy system in regimes where Hf passivity dominates the corrosion behavior (as is the case in acidic environments) to study the effect of the underlying structure.

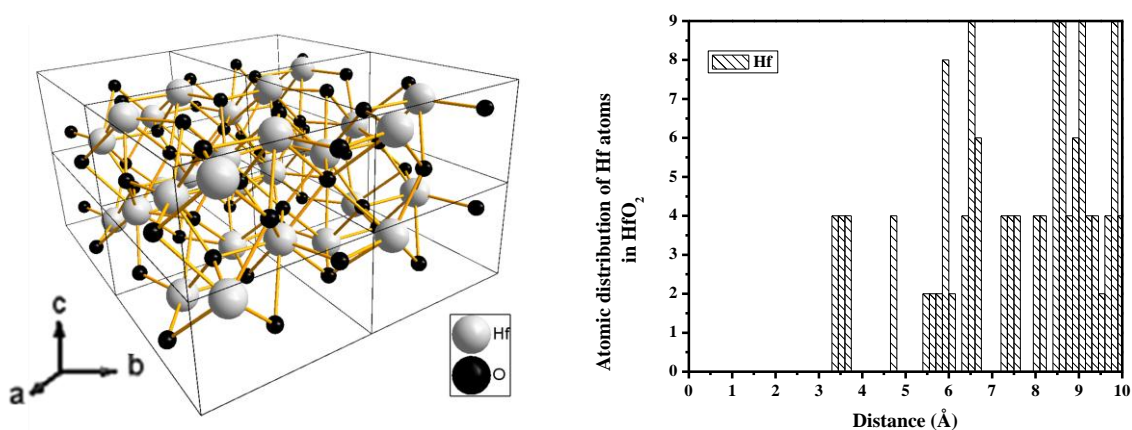


Figure 2.25. Schematic model of the HfO₂ crystal structure (left) and Hf atomic distribution (right). The unit cell is orthorhombic Pnam (space group 62) with lattice parameters $a = 0.554$ nm, $b = 0.646$ nm, and $c = 0.331$ nm. [51] Model created using Diamond Crystallography Software [7].

The disordered, amorphous Cu₇₅Hf₂₀Dy₀₅ structure does not have a well-defined atomic distribution. It is likely that there are fluctuations in composition leading to SRO and MRO. Compositional fluctuations are seen in STEM HAADF imaging (Figure 2.12). The Hf/Zr-rich regions were 6-9 nm in diameter and were separated by Cu-rich regions between 1 and 3 nm in width. The three-dimensional composition map, determined using atom probe tomography, showed a random distribution of Cu and Hf and a slight tendency for Dy clustering. Atom probe tomography is unable to resolve nearest neighbor atoms due to the finite detection efficiency. Ideally a complete elemental map of the NN

and second NN is needed to measure the clustering effect. Some low atomic density pockets were resolved, however, and these could be areas of increased dissolution susceptibility due to reduced bond strength and solute (Hf) lean regions.

It is likely that the Cu-Zr amorphous structure shares some similarities to the $\text{Cu}_{75}\text{Hf}_{20}\text{Dy}_{05}$ due to Cu being primarily alloyed with such similar metals (Hf and Zr). Experiments and models of the local structure in amorphous Cu-Zr alloys (Summarized in Section 2.2.2) showed that a few specific coordination polyhedral cells dominate the structure. For example, in the $\text{Cu}_{60}\text{Zr}_{40}$ alloy both Cu and Zr atoms around surrounded by both atom types (Figure 2.4) and Cu atoms have an above random concentration of Zr atoms as nearest neighbors [22]. Simulations of $\text{Cu}_{65}\text{Zr}_{35}$ structure showed that a specific Cu-centered $\langle 0, 0, 12, 0 \rangle$ polyhedral formed connected chains within the amorphous structure [26]. The Cu centered polyhedral cells have an above random concentration of Zr atoms leading to regions enriched in Zr (marked in green). The length scale of the MRO, $\langle 0, 0, 12, 0 \rangle$ member atoms (likely Hf-enriched regions) are between 10 and 20 atoms (between 2 and 6 nm).

A comparison of the periodic crystalline $\text{Cu}_{51}\text{Hf}_{14}$ structure and the simulated $\text{Cu}_{65}\text{Zr}_{35}$ amorphous structure with Cu centered $\langle 0,0,12,0 \rangle$ atoms marked is shown in Figure 2.26. In the crystalline structure, the distribution of Hf atoms is periodic. If indeed Hf-solute lean regions of the amorphous structure exist, as is the case in Cu-Zr, then the ability to form a uniform passive layer is impaired. Solute lean regions lead to a loss of passivity due to difficulty in ‘oxide bridging’ the solute lean region. There will be regions where the oxide does not have complete surface coverage. This leads to a loss of passivating ability in the amorphous state compared to the crystalline state as seen in

Figure 2.18, Figure 2.20 and Figure 2.21. Similar arguments can be made for the Cu based oxide formation: there will be regions where the oxide has a difficult time achieving complete surface coverage. In either case, the disordered structure would be detrimental to the overall localized corrosion resistance because of greater atomic scale fluctuations in composition. This adverse effect is seen in Figure 2.19, 2.21, and 2.22.

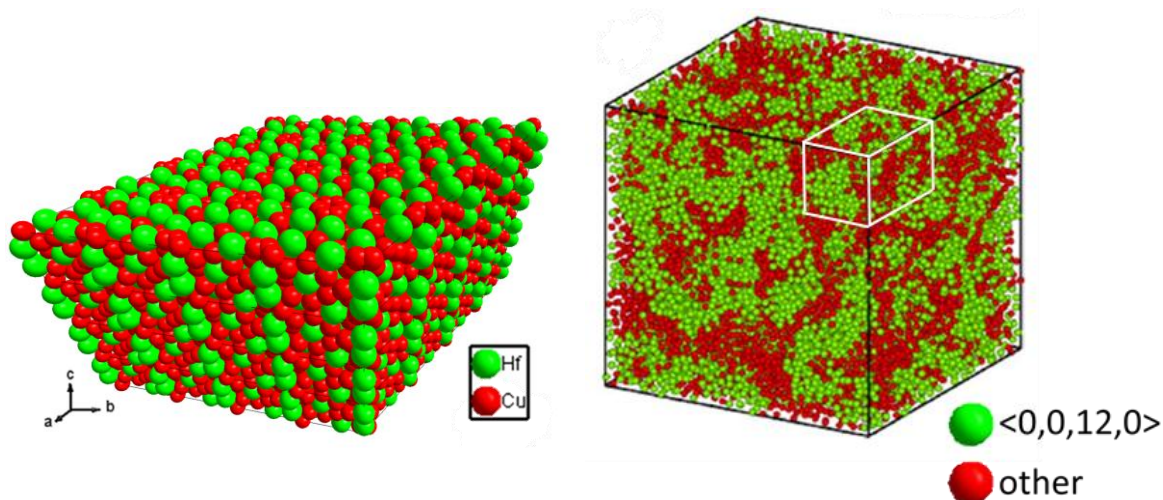


Figure 2.26. Schematic model of 4x4 unit cells (left) of the hexagonal $\text{Cu}_{51}\text{Hf}_{14}$ crystal structure. Radius of the atoms was assumed to be 0.128 and 0.159 nm for Cu and Hf, respectively. In the model on right (Figure 2.6, adapted from [26]), the green balls designate atoms belonging to $\langle 0,0,12,0 \rangle$ clusters in the $\text{Cu}_{65}\text{Zr}_{35}$ metallic glass. These clusters, centered on Cu atoms, contain an above average proportion of the Zr atoms [22]. The outlined region (white) in the $\text{Cu}_{65}\text{Zr}_{35}$ model has approximately the same area as the $\text{Cu}_{51}\text{Hf}_{14}$ are schematic. The $\text{Cu}_{51}\text{Hf}_{14}$ model created using Diamond Crystallography Software [7].

In the results section, it was observed that there are subtle differences in the passive layer formation in pH 8.4 borate buffer solution (Figure 2.14 and Figure 2.16). The crystalline structure shows Cu oxide formation similar in characteristic features (2 oxidation and reduction peaks) and magnitude to the polycrystalline high purity Cu sample. The disordered amorphous state shows much lower current density ($6.0 \cdot 10^{-6}$ compared to $1.5 \cdot 10^{-6} \text{ A/cm}^2$ in the first oxidation peak, Figure 2.14) indicative of less Cu-

based oxide formation. One hypothesis stemming from these results is that the oxide formation is less extensive due to the distribution of Cu atoms and local composition fluctuations on the order of the second NN distance which results in a less effective oxide

A corresponding decrease in the localized corrosion resistance was observed for the disordered amorphous structural state in Hf/Cu passive environments (Figure 2.18) and Cu active/Hf passive environments (Figure 2.21). In the metastable pitting experiments, more numerous events of higher overall charge were observed for the amorphous case than for the crystalline structure (Figure 2.19).

In the acidic environments, there are two stages of behavior. Low over-potentials (up to about $0.0V_{SCE}$, Figure 2.21) corresponds dissolution of surface Cu. Cu dissolution occurs more easily from the amorphous than crystalline state. The second stage, at higher applied potentials, is the metastable localized breakdown of the passive film, represented by the current transients (Figure 2.21).

The behavior of the crystalline state is dominated by metastable breakdown behavior at potentials higher than the Cu dissolution peak in the more aggressive 1 M H_2SO_4 solution (Figure 2.20). The results show that the protective capacity of the Hf-based oxide films is decreased due to the amorphous structure. These observations support the hypothesis of a more spatially defective imperfect oxide affiliated with the amorphous structure.

2.7.3 Hf as a Dissolution Moderator

In acidic H_2SO_4 solution, the amorphous structure undergoes significant Cu dissolution compared to the crystalline state (Figure 2.23). In this regime, the dissolution

moderating effect of the Hf is apparent. Dissolution requires the rupture of the atomic bonds surrounding the dissolving atom as it is oxidized. After all the bonds holding the atom to the surface cleave, the atom loses electrons and dissolves into solution forming a solvation sheath. The class of alloying additions that result in stronger bond formation are known as dissolution moderators [52]. These beneficial solute atoms must remain in solid solution to bestow uniform dissolution resistance to the alloy. One of the big advantages of the amorphous structure is the ability to dissolve alloying elements in high concentrations that provide dissolution moderation effect into solid solution with precipitate phase formation [13].

It was shown that Hf alloying greatly slows Cu dissolution from the alloy matrix (acidic environments, Figure 2.21 for instance). It is likely that Hf is acting as a dissolution moderator. With Hf dissolved into the matrix enough more dissolution resistant bonds are formed. A simplified example is the case where more Hf-Hf and Cu-Hf bonds are formed which are more resistant to bond cleavage than Cu-Cu bonds. In reality, the interplay of all NN and 2nd NN is important for determining the bond strength [53]. Dissolution of Cu from the amorphous alloy occurs more readily from the amorphous structure than the crystalline structure. A similar argument to the one made for passivity can be made here.

The disordered structure lacks the regular arrangement of Hf atoms that exists in the periodic structure. Evidence for compositional ‘clusters’ of solute lean regions is seen in the cloud like regions of Cu-rich areas in the TEM HAADF image in Figure 2.11. Thus, the concentration of solute is non-uniform and the corresponding moderating effect the solute-lean Hf atoms is diminished. The three-dimensional composition analysis

shows regions of decreased density in the amorphous state Figure 2.13. Within these regions atoms, it is likely that atoms would be less strongly bound to other atoms providing regions of increased dissolution susceptibility.

In Figure 2.21, the large peak of Cu dissolution from the amorphous structure is not observed is not seen in the crystalline structure. The increase in dissolution susceptibility is likely due to the regions that are Hf-solute lean which would more easily dissolve. This dissolution would continue until a surface meeting the characteristic threshold Hf concentration to forestall dissolution is revealed. After this point, the surface of the amorphous structure is less susceptible to dissolution transients than the crystalline structure, although the overall dissolution rate is very similar between the two structures.

2.8 Conclusion

In this chapter it was shown that the amorphous structure affects both the formation tendency of the passive film and the dissolution resistance. The passive film formed on the amorphous $\text{Cu}_{75}\text{Hf}_{20}\text{Dy}_{05}$ alloy was rationalized to be spatially less uniform and therefore more difficult to form a homogeneous uniform surface coverage than in the case of the crystalline $\text{Cu}_{75}\text{Hf}_{20}\text{Dy}_{05}$. During dissolution, the amorphous structure exhibited more Cu dissolution than the crystalline structure.

Determinations the amorphous structure using atom probe tomography did not detect any local atomic clustering. However, clustering observed in Cu-Zr alloys involves NN and 2NN ordering is below the detection limit of this technique. It was determined that no significant medium range ordering was detected. Local fluctuations in the free volume of the material were observed.

Atomic composition and free volume fluctuations at the local scale contribute to the overall corrosion behavior. The lack of a periodic distribution of the beneficial solute in the amorphous structure is thought to play a significant and detrimental role in this behavior.

2.9 References

1. Cahn, R.W. and A.L. Greer, *Chapter 19 - Metastable States of Alloys*, in *Physical Metallurgy (Fourth Edition)*, W.C. Robert and H. Peter, Editors. 1996, North-Holland: Oxford. p. 1723-1830.
2. Perepezko, J.H., *Material and characterization for Cu₇₅Hf₂₀Dy₀₅ graciously provided by J. Perepezko at Case Western Reserve University*. 1997.
3. Cong, H.B., *Understanding the interplay between water chemistry and electrochemical properties of copper*, in *Materials Science and Engineering*. 2009, University of Virginia: Charlottesville, VA.
4. Cong, H.B., H.T. Michels, and J.R. Scully, *Passivity and Pit Stability Behavior of Copper as a Function of Selected Water Chemistry Variables*. Journal of the Electrochemical Society, 2009. **156**(1): p. C16-C27.
5. Cong, H.B. and J.R. Scully, *Use of Coupled Multielectrode Arrays to Elucidate the pH Dependence of Copper Pitting in Potable Water*. Journal of the Electrochemical Society, 2010. **157**(1): p. C36-C46.
6. Okamoto, H., *Cu-Hf (Copper-Hafnium)*. Journal of Phase Equilibria and Diffusion, 2007. **28**(6): p. 583-584.
7. Brandenburg, K., *Modelling performed using Diamond Crystallography Software (<http://www.crystalimpact.com/>)*.
8. Bernal, J., *Geometry of the structure of monatomic liquids*. Nature, 1960. **185**(4706): p. 68-70.
9. Finney, J., *Random packings and the structure of simple liquids. I. The geometry of random close packing*. Proceedings of the Royal Society of London. A. Mathematical and Physical Sciences, 1970. **319**(1539): p. 479.
10. Cargill, G.S., *Dense Random Packing of Hard Spheres as a Structural Model for Noncrystalline Metallic Solids*. Journal of Applied Physics, 1970. **41**(5): p. 2248-&.
11. Egami, T., *Universal criterion for metallic glass formation*. Materials Science and Engineering a-Structural Materials Properties Microstructure and Processing, 1997. **226**: p. 261-267.
12. Aburada, T., *Effects of Minor Solute on Corrosion*, in *Materials Science and Engineering*. 2011, University of Virginia: Charlottesville, VA.
13. Aburada, T., J.M. Fitz-Gerald, and J.R. Scully, *Pitting and Dealloying of Solute-Rich Al-Cu-Mg-based Amorphous Alloys: Effect of Alloying with Minor Concentrations of Nickel*. Journal of the Electrochemical Society, 2011. **158**(9): p. C253-C265.

14. Hsieh, H.Y., B.H. Toby, T. Egami, Y. He, S.J. Poon, and G.J. Shiflet, *Atomic-Structure of Amorphous Al₉₀Fe_xCe_{10-x}*. Journal of Materials Research, 1990. **5**(12): p. 2807-2812.
15. Cheng, Y.Q. and E. Ma, *Atomic-level structure and structure–property relationship in metallic glasses*. Progress in Materials Science, 2011. **56**(4): p. 379-473.
16. Sadoc, J.F., J. Dixmier, and A. Guinier, *Theoretical calculation of dense random packings of equal and non-equal sized hard spheres applications to amorphous metallic alloys*. Journal of Non-Crystalline Solids, 1973. **12**(1): p. 46-60.
17. Hsieh, H.Y., T. Egami, Y. He, S.J. Poon, and G.J. Shiflet, *Short-Range Ordering in Amorphous Al₉₀Fe_xCe_{10-x}*. Journal of Non-Crystalline Solids, 1991. **135**(2-3): p. 248-254.
18. Sheng, H.W., W.K. Luo, F.M. Alamgir, J.M. Bai, and E. Ma, *Atomic packing and short-to-medium-range order in metallic glasses*. Nature, 2006. **439**(7075): p. 419-425.
19. Li, Y., Q. Guo, J.A. Kalb, and C.V. Thompson, *Matching Glass-Forming Ability with the Density of the Amorphous Phase*. Science, 2008. **322**(5909): p. 1816-1819.
20. Mattern, N., A. Schöps, U. Kühn, J. Acker, O. Khvostikova, and J. Eckert, *Structural behavior of Cu_xZr_{100-x} metallic glass (x= 35-70)*. Journal of Non-Crystalline Solids, 2008. **354**(10-11): p. 1054-1060.
21. Ma, D., A.D. Stoica, and X.L. Wang, *Power-law scaling and fractal nature of medium-range order in metallic glasses*. Nature Materials, 2008. **8**(1): p. 30-34.
22. Ma, D., A.D. Stoica, X.L. Wang, Z. Lu, M. Xu, and M. Kramer, *Efficient local atomic packing in metallic glasses and its correlation with glass-forming ability*. Physical Review B, 2009. **80**(1): p. 014202.
23. Cheng, Y., A.J. Cao, H. Sheng, and E. Ma, *Local order influences initiation of plastic flow in metallic glass: Effects of alloy composition and sample cooling history*. Acta Materialia, 2008. **56**(18): p. 5263-5275.
24. Cheng, Y., H. Sheng, and E. Ma, *Relationship between structure, dynamics, and mechanical properties in metallic glass-forming alloys*. Physical Review B, 2008. **78**(1): p. 014207.
25. Finney, J.L., *Modelling the structures of amorphous metals and alloys*. Nature, 1977. **266**(5600): p. 309-314.
26. Li, M., C. Wang, S. Hao, M. Kramer, and K. Ho, *Structural heterogeneity and medium-range order in Zr_{-x}Cu_{-{100-x}} metallic glasses*. Physical Review B, 2009. **80**(18): p. 184201.
27. Deutscher, R. and R. Woods, *Characterization of oxide layers on copper by linear potential sweep voltammetry*. Journal of applied electrochemistry, 1986. **16**(3): p. 413-421.
28. Strehblow, H.H. and B. Titze, *The investigation of the passive behaviour of copper in weakly acid and alkaline solutions and the examination of the passive film by ESCA and ISS*. Electrochimica Acta, 1980. **25**(6): p. 839-850.

29. Drogowska, M., L. Brossard, and H. Ménard, *Influence of anions on the passivity behavior of copper in alkaline solutions*. Surface and Coatings Technology, 1988. **34**(4): p. 383-400.
30. de Chialvo, M.R.G., R.C. Salvarezza, D. Vasquez Moll, and A.J. Arvia, *Kinetics of passivation and pitting corrosion of polycrystalline copper in borate buffer solutions containing sodium chloride*. Electrochimica Acta, 1985. **30**(11): p. 1501-1511.
31. Lee, S.-W., M.-Y. Huh, E. Fleury, and J.-C. Lee, *Crystallization-induced plasticity of Cu-Zr containing bulk amorphous alloys*. Acta Materialia, 2006. **54**(2): p. 349-355.
32. Milošev, I. and M. Metikoš-huković, *Effect of chloride concentration range on the corrosion resistance of Cu-xNi alloys*. Journal of applied electrochemistry, 1999. **29**(3): p. 393-402.
33. Souto, R.M., S. González, R.C. Salvarezza, and A.J. Arvia, *Kinetics of copper passivation and pitting corrosion in Na₂SO₄ containing dilute NaOH aqueous solution*. Electrochimica Acta, 1994. **39**(17): p. 2619-2628.
34. Reda, M.R. and J.N. Alhajji, *Role of solution chemistry on corrosion of copper in tap water: Effect of sulfate ion concentration on uniform and localized attack*. Corrosion, 1996. **52**(3): p. 232-239.
35. Qafsaoui, W., C. Blanc, J. Roques, N. Pébère, A. Shiri, C. Mijoule, and G. Mankowski, *Pitting corrosion of copper in sulphate solutions: inhibitive effect of different triazole derivative inhibitors*. Journal of applied electrochemistry, 2001. **31**(2): p. 223-231.
36. Milosev, I. and M. Metikos-Hukovic, *Passive Films on 90Cu-10Ni Alloy: The Mechanism of Breakdown in Chloride Containing Solutions*. Journal of the Electrochemical Society, 1991. **138**(1): p. 61-67.
37. Kear, G., B. Barker, and F. Walsh, *Electrochemical corrosion of unalloyed copper in chloride media--a critical review*. Corrosion Science, 2004. **46**(1): p. 109-135.
38. Jardy, A., A. Legal Lasalle-Molin, M. Keddou, and H. Takenouti, *Copper dissolution in acidic sulphate media studied by QCM and rrde under ac signal*. Electrochimica Acta, 1992. **37**(12): p. 2195-2201.
39. Pourbaix, M., *Atlas of electrochemical equilibria in aqueous solutions*. 1974, National Association of Corrosion Engineers: Houston, Tex. p. 183-197, 230-233, 384-392.
40. Holmes, D.R., *ASM handbook*, in *Corrosion: Materials*, S.D. Cramer, S. Bernard, and C. Jr., Editors. 1990, ASM International: Materials Park, OH.
41. James, W.J., J.W. Johnson, and M.E. Straumanis, *The difference effect and anodic behavior of hafnium dissolving in hydrofluoric acid*. Corrosion Science, 1963. **3**(4): p. 273-279.
42. James, W.J., W.G. Custead, and M.E. Straumanis, *Dissolution rates, electrochemical and passivation properties of alpha Zr---O solid solutions in HF*. Corrosion Science, 1962. **2**(4): p. 237-254.

43. Walsh, F.C., G. Kear, and B.D. Barker, *Electrochemical corrosion of unalloyed copper in chloride media - a critical review*. Corrosion Science, 2004. **46**(1): p. 109-135.
44. Mattsson, E., *Corrosion of Copper and Brass - Practical Experience in Relation to Basic Data*. British Corrosion Journal, 1980. **15**(1): p. 6-13.
45. Naka, M., K. Hashimoto, and T. Masumoto, *Corrosion Behavior of Amorphous and Crystalline Cu50ti50 and Cu50zr50 Alloys*. Journal of Non-Crystalline Solids, 1978. **30**(1): p. 29-36.
46. Turn, J.C. and R.M. Latanision, *The Influence of Structure on the Corrosion of Glassy Copper-Zirconium Alloys*. Corrosion, 1983. **39**(7): p. 271-279.
47. Gabathuler, J.P., P. White, and E. Parthe, *Zr14cu51 and Hf14cu51 with Gdag3.6 Structure Type*. Acta Crystallographica Section B-Structural Science, 1975. **B 31**(Feb15): p. 608-610.
48. McCafferty, E., *Graph theory and the passivity of binary alloys*. Corrosion Science, 2000. **42**(11): p. 1993-2011.
49. McCafferty, E., *Relationship between graph theory and percolation approaches in the passivity of Fe-Cr binary alloys*. Journal of the Electrochemical Society, 2008. **155**(10): p. C501-C505.
50. Sieradzki, K. and R.C. Newman, *A Percolation Model for Passivation in Stainless-Steels*. Journal of the Electrochemical Society, 1986. **133**(9): p. 1979-1980.
51. Haines, J., J.M. Léger, S. Hull, J.P. Petitet, A.S. Pereira, C.A. Perottoni, and J.A.H. da Jornada, *Characterization of the Cotunnite-Type Phases of Zirconia and Hafnia by Neutron Diffraction and Raman Spectroscopy*. Journal of the American Ceramic Society, 1997. **80**(7): p. 1910-1914.
52. Marcus, P., *On some fundamental factors in the effect of alloying elements on passivation of alloys*. Corrosion Science, 1994. **36**(12): p. 2155-2158.
53. Soffa, W.A., D.E. Laughlin, and N. Singh, *Interplay of ordering and spinodal decomposition in the formation of ordered precipitates in binary fcc alloys: Role of second nearest-neighbor interactions*. Philosophical Magazine, 2010. **90**(1-4): p. 287-304.

3 Preferential Dissolution of Hf and Subsequent Surface Reconstruction Comparison between the Amorphous and Crystalline States of $\text{Cu}_{75}\text{Hf}_{20}\text{Dy}_{05}$

3.1 Abstract

An amorphous solid solution alloy that undergoes devitrification without changing composition either locally or globally was utilized to examine the effects of structural ordering on corrosion properties in the absence of any accompanying chemical partitioning. Melt spun amorphous $\text{Cu}_{75}\text{Hf}_{20}\text{Dy}_{05}$ undergoes single phase devitrification to a $\text{Cu}_{51}\text{Hf}_{14}$ phase. The difference in corrosion behavior between these two structures was explored in hydrofluoric acid solutions where preferential dissolution of Hf occurred. Preferential Hf dissolution occurred more readily in the amorphous alloy specimens compared to its crystalline counterpart. Remaining Cu reorganized to form an fcc nanostructure in both conditions. This process occurred quickly in the amorphous state and more slowly in the case of the crystalline variant. A uniform nanoporous Cu sponge structure formed, with a pore diameter around 10 nm, after dissolution in the amorphous state. A less uniform nanoporous structure formed more slowly when occurring from the crystalline state. These differences were traced to the effects of ordering on both dissolution and surface diffusion.

3.2 Introduction

The role of atomic scale structure (nanostructure) on corrosion properties of metals remains unclear. This is in large part due to the presence and nature of structural and chemical defects which typically result in regions of structural and chemical inhomogeneity. These sites often dominate the corrosion behavior [1-3]. For amorphous alloy systems the lack of long range order, grain boundaries and defects is thought to be one of the key beneficial characteristics leading to the concept that amorphous alloys possess superior corrosion resistance compared to their crystalline counterparts [4]. However, it is becoming increasingly clear that corrosion resistance of amorphous alloys benefit from accommodating a large concentration of passivating or dissolution inhibiting elements in solid solution [5], lack of defects with chemical or structural non-uniformities [6], and complex roles of minor alloying elements often added for other reasons [7]. In contrast, the role of nanostructured atomic arrangements on the corrosion behavior of amorphous and crystalline alloys has been elusive and is not well understood (Ch. 2) [8-14].

Transformation of disordered amorphous alloys to ordered single phase crystalline alloys provides an ideal forum to study the role of structural ordering on the corrosion behavior without the accompanying complication of long range chemical partitioning. However, previous studies have led to contradictory conclusions regarding the effects of ordering without compositional change on the corrosion behavior of amorphous alloys increases [8, 9, 11], decreases [10, 14], and minimal effect [12, 13].

This study focuses on corrosion of an amorphous solid solution alloy compared to a stoichiometrically equivalent crystalline structure lacking other micrometer scale

defects. Preferential dissolution of one element from the matrix provides an ideal opportunity to use electrochemical techniques to explore the effect of ordering on this process. The role of ordering on preferential dissolution has been studied in the Cu_3Au system, which undergoes a transformation from a disordered crystalline solid solution to an ordered crystalline state. The ordered single phase exhibits passivity at higher potentials and has a higher critical dealloying potential than disordered crystalline Cu_3Au [15]. The crystallographic orientation of the initial dealloying of (111) Cu_3Au in sulfuric acid solution was carefully studied and low over-potential dealloying led to the formation of strained Au regions while higher over-potential dealloying caused the formation of relaxed Au islands with FCC structure [16].

Two issues are how structure affects the behavior of passive materials and how it affects dissolution in the active state. In the case of active dissolution, dealloying, or preferential dissolution of a less noble element, often occurs. Dealloying to form nanoporosity has been widely studied for catalyst production and other applications [17, 18]. In particular, significant research has been performed with the goal of producing nanoporous Cu using both crystalline and amorphous precursor alloys in a variety of solution environments. Nanoporous Cu was dealloyed from a single phase Mn-Cu alloy in hydrochloric and sulfuric acid solutions [19, 20]. Dissolution of Cu-based amorphous materials has also been studied. Dissolution of Al and Mg from an Al-Cu-Mg precursor alloy produced nanoporous Cu [21]. Amorphous $\text{Cu}_{60}\text{Zr}_{30}\text{Ti}_{10}$ ribbons were dealloyed by full immersion in varying low, 0.05 M – 1.0 M, concentrations of hydrofluoric acid solution under free corrosion conditions, where Zr and Ti were found to selectively dissolve forming nanoporous Cu [22]. Similar to Zr, it is expected that Hf would undergo

preferential dissolution in hydrofluoric acid solution [23]. In contrast, in alloy systems such as $\text{Cu}_{60}\text{Zr}_{30}\text{Ti}_{10}$ and $\text{Cu}_{75}\text{Hf}_{20}\text{Dy}_{05}$, where Cu is alloyed with primarily refractory elements, dealloying in mineral acids favors Cu dissolution.

Hydrofluoric (HF) acid is often used in electrochemistry because of its ability to preferentially dissolve elements (Nb, Zr, Ta [24], and Hf [23]) that normally are not very susceptible to dissolution in strong mineral acids, e.g., hydrochloric and sulfuric acid. Conversely, elements that typically dissolve in strong acids (A prime example is Mg which forms a fluoride based protective film [24]) are resistant to corrosion in HF acid solution. The difference in nobility between alloying elements creates situations ideal for studying the effect of structural ordering on dealloying. Preferential dissolution of less noble elements in HF acid solution occurs by selective dissolution of Hf without Cu oxidation. The comparative behavior of the disordered amorphous and crystalline $\text{Cu}_{75}\text{Hf}_{20}\text{Dy}_{05}$ is explored in hydrofluoric acid solution during Hf dissolution and Cu reorganization in this chapter. A separate chapter (2) compares the behavior of disordered amorphous and crystalline states on passivity and local corrosion. An additional study addresses the effect of structure in mineral acids where Hf is a strong passivator and Cu can dissolve preferentially.

In this work, amorphous and crystalline structures, with no change in composition, were studied using HF acid solution at concentrations of 0.1 and 1 M using potentiodynamic polarization, potentiostatic polarization methods and subsequent surface analysis. Controlled selective dissolution of Hf from the matrix was observed. After exposure to the solution environment, the structure was characterized using x-ray diffraction (XRD), the surface morphology using scanning electron microscopy (SEM)

and surface composition using energy dispersive spectroscopy attached to the SEM (SEM-EDS). We found that crystalline $\text{Cu}_{75}\text{Hf}_{20}\text{Dy}_{05}$ exhibits increased resistance to dissolution in HF solution compared to the amorphous $\text{Cu}_{75}\text{Hf}_{20}\text{Dy}_{05}$ of the same composition. The effect of ordering on dissolution of Hf and surface diffusion of Cu are discussed.

3.3 Critical Unresolved Issue

What is the effect of amorphous vs. crystalline $\text{Cu}_{75}\text{Hf}_{20}\text{Dy}_{05}$ structure on corrosion under conditions where Hf dissolves preferentially from the matrix and Cu reorganizes? This is in contrast to the previous chapter where Hf was a beneficial solute in the sulphate environments studied.

3.4 Experimental

3.4.1 Metallurgical Characterization

Amorphous $\text{Cu}_{75}\text{Hf}_{20}\text{Dy}_{05}$ was produced by the melt spinning technique. High purity elements (Cu 99.999%, Hf 99.9% excluding Zr (nominal 2%), and Dy 99.9%) were made into an ingot by arc melting under an argon atmosphere. The ingot was then inductively melted under argon and rapidly cooled on a Cu wheel of radius 10 mm with a rotation speed of 40 m/s. Prior to heat treatments, samples were first encapsulated in quartz tubes under argon. To fully crystallize the amorphous ribbon, encapsulated samples were annealed at 600°C for 30 minutes and then water quenched.

High purity element samples, used in comparative electrochemistry experiments, were polycrystalline Hf wire (99.7% Zr nominal 3%) and high purity polycrystalline Cu wire (>99.99%) with surface areas roughly equivalent to the $\text{Cu}_{75}\text{Hf}_{20}\text{Dy}_{05}$ ribbons.

3.4.2 Corrosion Measurements

The corrosion measurements were conducted using two different working electrode specimen mounting procedures with different exposed areas. Schematics of both are shown in Figure 3.1. The first involved ribbon samples which were mounted perpendicular to their long axis in epoxy with an exposed area of roughly $80\ \mu\text{m} \times 300\ \mu\text{m}$ and an approximate surface area of $10^{-4}\ \text{cm}^2$. The epoxy mounted samples were ground using successively finer grits, 400-600-800-1200, of SiC paper.

The epoxy and the associated small exposed area limit the post exposure characterization techniques including XRD, SEM and EDS. To alleviate these issues an alternative specimen mounting procedure, also shown in Figure 3.1, was used to expose a much larger surface area, about $0.1\ \text{cm}^2$, without using epoxy. In this setup, an unpolished ribbon was electrically connected to an Al-mounting pole using adhesive Cu tape. The area beneath the exposed ribbon had been previously electrically isolated from the solution by painting with a lacquer. The Al – Cu tape – specimen electrically connection was then lacquered to electrically isolate it from the solution. After exposure, the lacquer was easily removed and the Cu tape connection was severed to remove the specimen for XRD and SEM analysis. Ribbon cross sections were created by attaching the exposed ribbon to carbon tape and then slicing them with a razor blade. Surface morphological, dealloyed layer thickness and semi-quantitative compositional analysis was performed using a field emission gun JEOL 6700F SEM with an attached EDS detector.

Both setups utilized a traditional 3-electrode setup with an exposed electrically isolated working electrode, reference electrode and platinum counter electrode. An all

PTFE electrochemical cell was used due to the ability of the HF solution to dissolve borosilicate type glass. The reference electrode used was a Saturated Calomel Electrode, hereafter referred to as SCE, electrode with a plastic body and a ceramic ion junction. Chemical solutions were produced using reagent grade chemicals and pure water (resistivity $18.2 \text{ M } \Omega / \text{cm}$) produced by an Academic MilliQ filtration system (MilliPore). The solution was left aerated. Polarization experiments were conducted using a Gamry FAS2 Femtostat low current potentiostat.

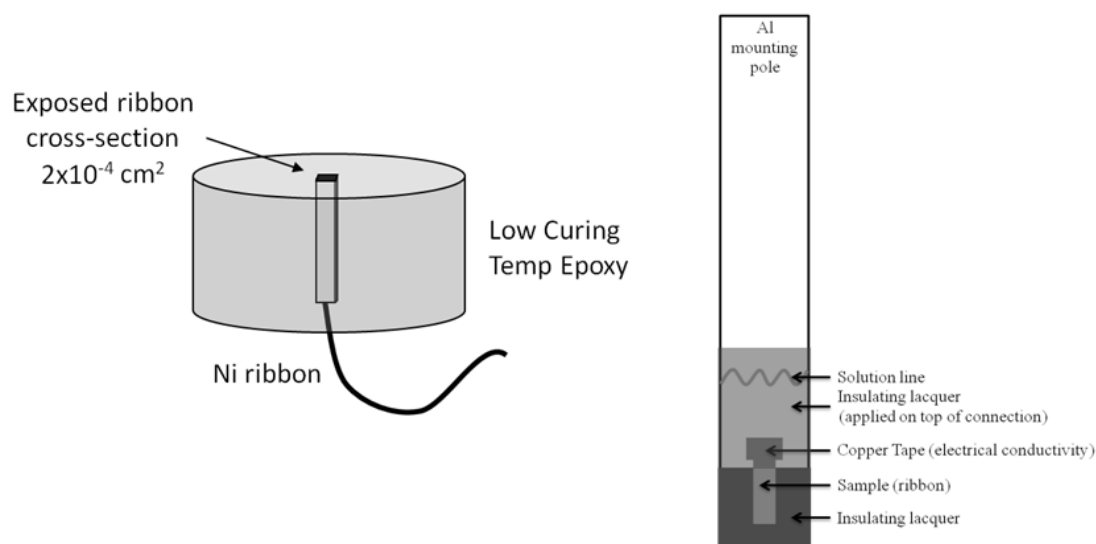


Figure 3.1. The working electrode specimen mounting configuration in epoxy with perpendicular mounting (left) and with a large ribbon section exposed (right).

The amorphous and annealed crystalline specimens were characterized by XRD and TEM prior to exposure. These specimens were subsequently mounted for electrochemical experiments using the two different mounting methods. Experimental measurements conducted include cyclic polarization, potentiostatic polarization, and cyclic voltammetry (CV) below the Cu open circuit potential (OCP) and through the Cu OCP to anodic potentials. Cyclic polarization behavior was measured at a scan rate of 1 mV/s with scans starting and ending at a potential 200 mV below the open circuit

potential with an apex potential of 1000 mV_{SCE}. Cyclic CV experiments had a scan rate of 20 mV/s.

Several assumptions and approximations were used to calculate the depth of penetration of preferentially dissolving Hf. The conversion from charge density to the quantity of monolayers removed was estimated using Faraday's Law. The total number of atoms in a given monolayer was assumed to be approximately 10^{15} atoms/cm². For the Cu₇₅Hf₂₀Dy₀₅ alloy, Hf atoms comprise 20 at %. Thus, the total number of Hf atoms is $0.2 \cdot 10^{15}$ atoms/cm². Assuming that Hf oxidizes to the +4 valence state, the total number of monolayers through which preferential Hf dissolution has occurred can be estimated assuming uniform dealloying. Additionally, an approximate depth of preferential dissolution penetration into the Cu₇₅Hf₂₀Dy₀₅ alloy was calculated from Faraday's Law using the average density of Hf. The uniform depth was converted to a dealloying depth by a factor of 5 to account for the fact that only 20 at % Hf was dissolving.

3.5 Results

3.5.1 Thermodynamics of F⁻-Hf/Cu-H₂O systems

HF is a weak acid with a dissociation constant, pK_a, of 3.20 [25]. The pH of the HF solution concentrations used in this study was calculated based on the weak acid approximation. For a 0.1 M HF solution, the speciation diagram, Figure 3.2, was calculated [26]. For HF solution concentrations of 0.01, 0.1 and 1 M, the pH and the anion concentrations determined by the speciation diagram are tabulated in Table 3.1. According to the speciation diagram, 0.01 M is approximately the concentration of F⁻ and HF₂⁻ anions in 0.1 M HF solution. With the rest present as HF or H₂F₂ dimer.

E-pH diagrams, Cu (Figure 3.3), Hf (Figure 3.4) and Dy (Figure 3.5), were calculated for a series of F^- concentrations for each constituent element [26]. The F^- concentrations plotted are 0.01M, the expected concentration present in 0.1 M HF solution, and 1 M. To compare, the Pourbaix diagram without any F^- (0 M) ions is also shown. The Pourbaix diagrams show that for low F^- concentrations, no Cu complexation is expected. However, at higher F^- concentrations (1 M F^-), a stable CuF^+ complex forms above pH 2.5. The horizontal Cu oxidation line at 0.18 V_{SHE} (-0.06 V_{SCE}) is unchanged from the water system except at higher concentrations of F^- and even then only at less acidic pH (above 4.5). For hafnium, the Pourbaix diagram remains unchanged even at high F^- concentrations indicating that F^- has no effect on the thermodynamic stability of Hf. At 10 mM F^- concentration, Dy forms 2 complexes, DyF^{2-} and DyF_2^{1-} , and a stable DyF_3 at a pH above a pH of about 2.8. At higher F^- concentrations, the region where DyF_3 is the stable species enlarges to include lower pH ranges. In 1 M F^- solution, DyF_3 is stable to nearly a pH of 1.

It has been observed that hafnium indeed corrodes in HF solution, and the likely electrochemical reaction, Equation 3.1, is oxidation of Hf to HfF_4 by molecular HF (also producing H_2) [23]. Similar behavior was seen for Zr which oxidizes to ZrF_4 in HF solution [27]. It is likely that HfF_4 is a thermodynamically unstable precipitate possibly forming a hydrate [28] or some other reaction with water, and thus not appearing on the Pourbaix diagram. The solubility of ZrF_4 has been determined and has some solubility, 1.5 g/100 mL, in water [25].



Table 3.1. Calculated values for the pH, $[F^-]$, $[HF_2^-]$ and $[HF]$ of the 0.01, 0.1 and 1 M HF solution. Balance is H_2F_2 .

$[HF]$	pH	$[F^-]$	$[HF_2^-]$	$[HF]$
1 M	1.61	8 mM	17 mM	350 mM
0.1 M	2.12	6 mM	2 mM	68 mM
0.01 M	2.65	2 mM	-	8 mM

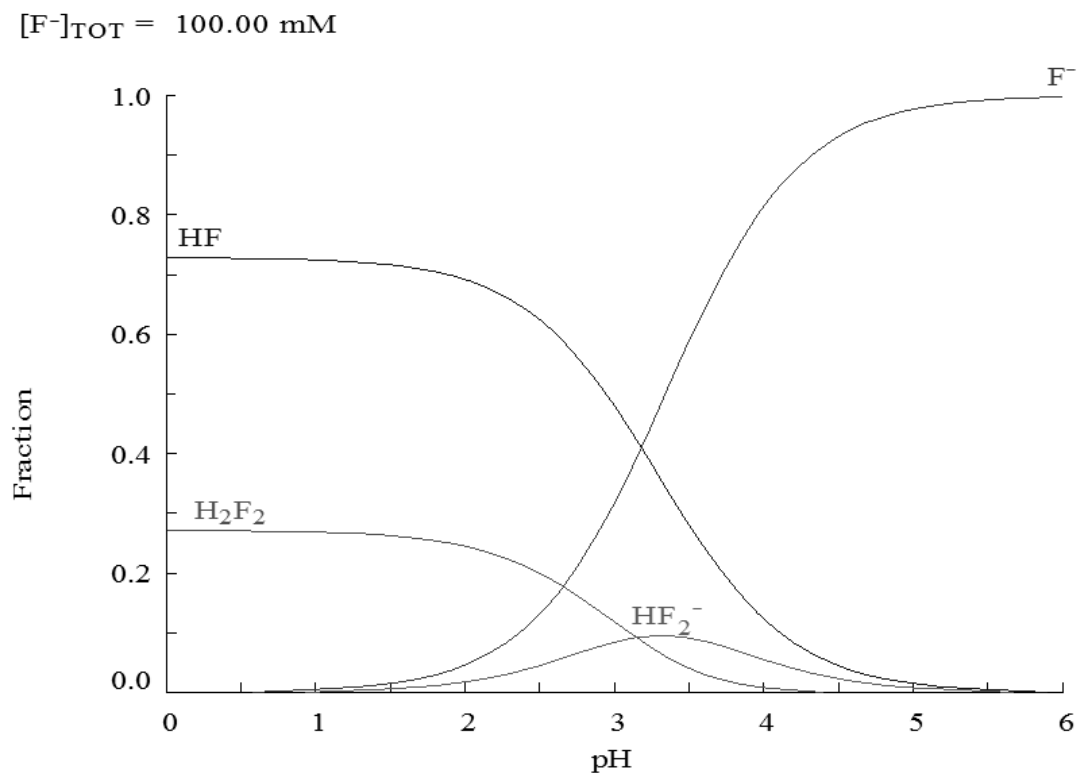


Figure 3.2. Calculated speciation diagram for F^- - H_2O for solutions containing 0.1 M F^- ions in solution at 25°C.

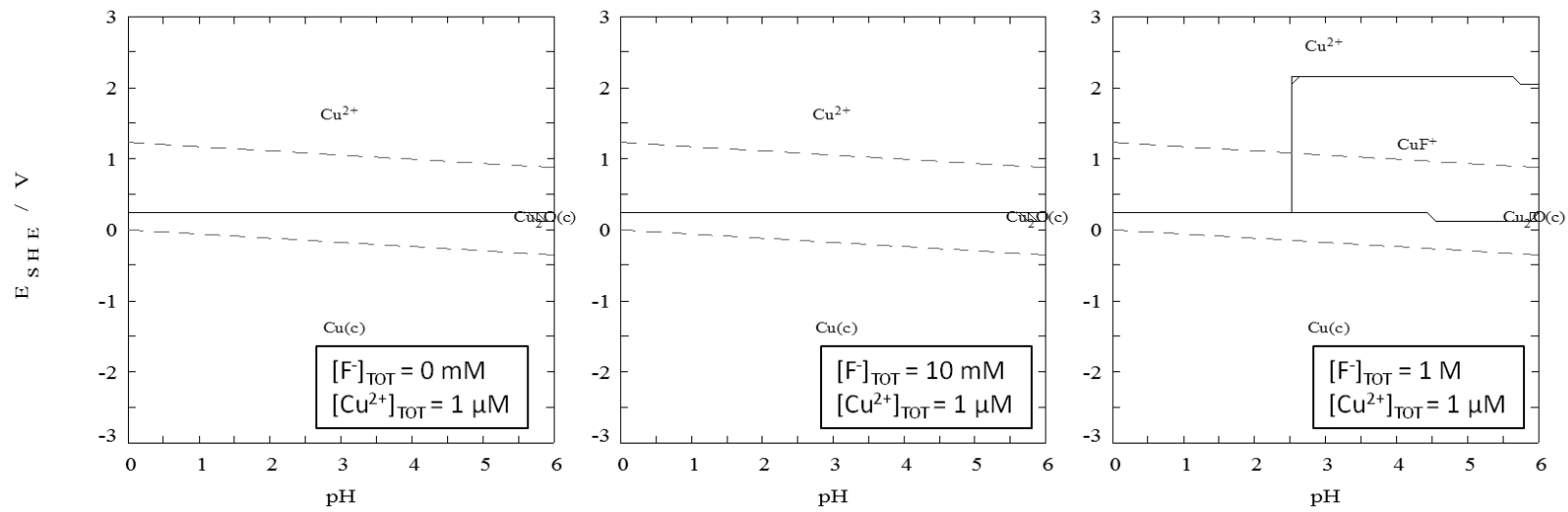


Figure 3.3. Calculated Cu-F-H₂O Pourbaix diagrams with F⁻ concentrations of 0 mM, 10 mM and 1 M at room temperature.

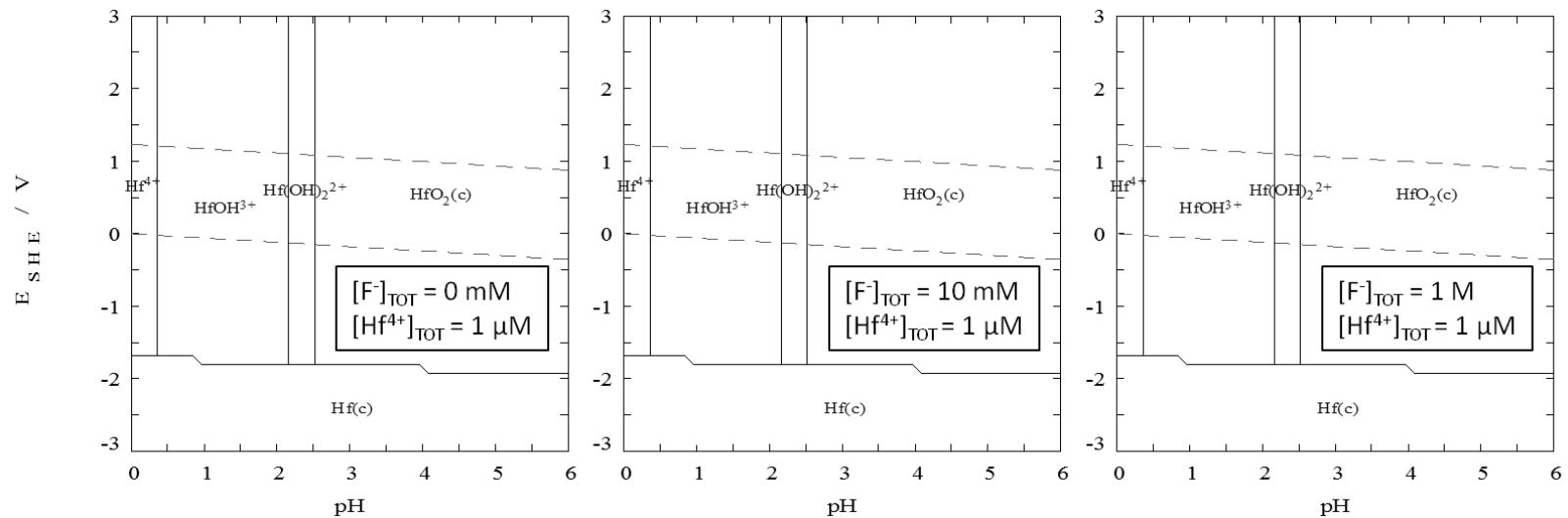


Figure 3.4. Calculated Hf-F-H₂O Pourbaix diagrams with F⁻ concentrations of 0 mM, 10 mM and 1 M at room temperature.

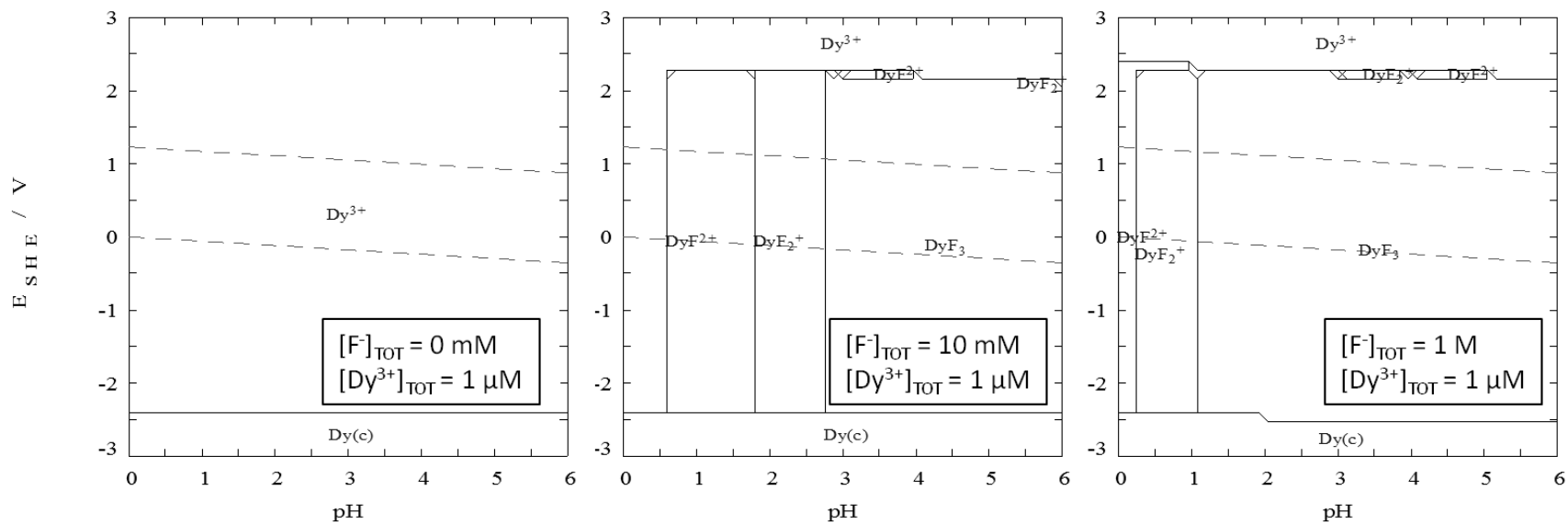


Figure 3.5. Calculated Dy-F⁻-H₂O Pourbaix diagrams with F⁻ concentrations of 0 mM, 10 mM and 1 M at room temperature.

3.5.2 Structural Characterization of the Amorphous and Crystalline States

The characterization of the amorphous and crystalline states were shown in Chapter 2. The amorphous ribbon crystallizes to a single $\text{Cu}_{51}\text{Hf}_{14}$ phase [29], with a 0.6 degree phase shift likely due to Dy solid solution substitution on the Hf lattice sites. The amorphous structure was confirmed by TEM. The compositional fluctuations at the nm scale were studied using both STEM (HAADF) and atom probe tomography.

3.5.3 Anodic Electrochemical Dissolution Behavior

The anodic polarization behavior of the amorphous and crystalline $\text{Cu}_{75}\text{Hf}_{20}\text{Dy}_{05}$ is compared to their primary alloying elements in 1 M (Figure 3.6) and 0.1 M (Figure 3.7) aerated HF solution. The polarization was preceded by a 600 second open circuit hold. Some important conclusions can be drawn from the OCP behavior. At both HF solution concentrations, Hf and Dy have a much lower OCP than Cu indicating coupled anodic and cathodic reactions at potentials where Cu is immune. Moreover, the OCP of both the amorphous and crystalline $\text{Cu}_{75}\text{Hf}_{20}\text{Dy}_{05}$ alloy is intermediate, between the potentials of high purity Cu and Hf/Dy. The alloy's open circuit potential increases with time suggests that Hf dissolution from the surface layers giving rise to a more Cu rich surface and associated nobility. At the higher 1 M HF solution concentration, both the amorphous and crystalline alloys undergo sharp decreases in potential. Likely, these potential decreases are due to newly exposed regions rich in Hf leading to a temporary increase in rate of Hf dissolution and an associated decrease in the open circuit potential. In the lower concentration 0.1 M HF solution, the OCP of the crystalline $\text{Cu}_{75}\text{Hf}_{20}\text{Dy}_{05}$

remains stable over time while the amorphous state shows the sharp potential drops seen in the higher HF concentration solution.

The polarization behavior in both solutions shows no passivity for either Cu or Hf, but distinctly different behavior. In 1 M HF solution, Hf corrodes above its OCP, $-1000 \text{ mV}_{\text{SCE}}$, at 10 mA/cm^2 of which is likely the anodic mass transport limited current density for Hf because there is no increase in current density as potential increases. Cu dissolution occurs above its open circuit at $-100 \text{ mV}_{\text{SCE}}$, but a form of weak salt-film based passivation occurs. This behavior is also seen for both states of the $\text{Cu}_{75}\text{Hf}_{20}\text{Dy}_{05}$ alloy. After the open circuit delay, the amorphous and crystalline $\text{Cu}_{75}\text{Hf}_{20}\text{Dy}_{05}$ both exhibit very similar E-log*i* behavior (Figure 3.6) to high purity Cu including breakdown events at potentials above $200 \text{ mV}_{\text{SCE}}$. Similar behavior is observed in lower concentration 0.1 M HF solution shown in Figure 3.7, but the apparent limiting current density for Hf dissolution is 1 mA/cm^2 . In 0.1 M HF solution, the crystalline state has a lower open circuit potential than the amorphous state but similar behavior at anodic overpotentials. In both solution concentrations, the amorphous and crystalline alloys have lower open circuit potentials than high purity Cu and dissolve at slightly lower potentials. The key result of these experiments is that Hf dissolves at significantly lower potentials than Cu. Testing within this region, where high purity Cu is immune, will dissolve Hf preferentially and enable the residual uncorroded Cu to reorganize.

Optical micrographs after the polarization experiment showed the surface of both amorphous and crystalline $\text{Cu}_{75}\text{Hf}_{20}\text{Dy}_{05}$ had changed from an initial Ag metallic color to an orange color indicating the surface layer had likely become Cu rich. This will be

explored in more detail using the larger exposure area mounted ribbon specimens and is discussed in the later sections.

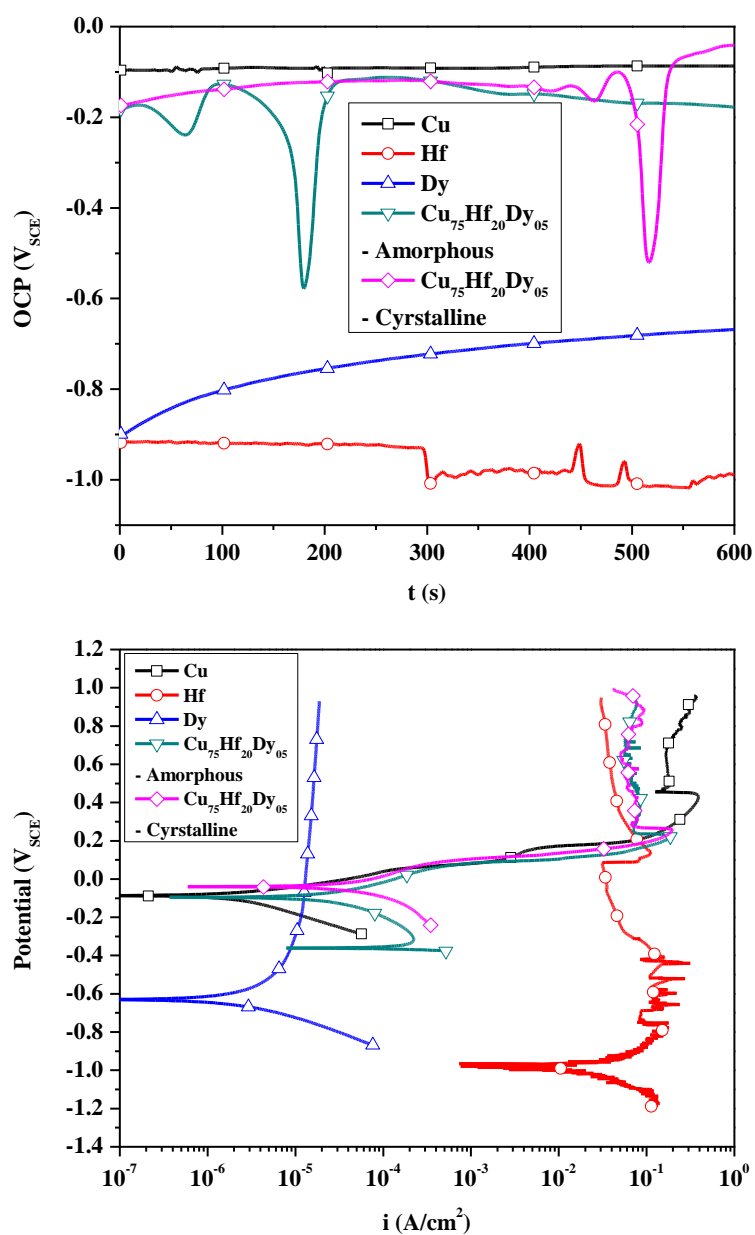


Figure 3.6. Open circuit behavior (top) and the anodic polarization (bottom) behavior of amorphous and crystalline Cu₇₅Hf₂₀Dy₀₅ alloys compared to the high purity polycrystalline alloying elements at 1 mV/s in aerated 1 M HF solution.

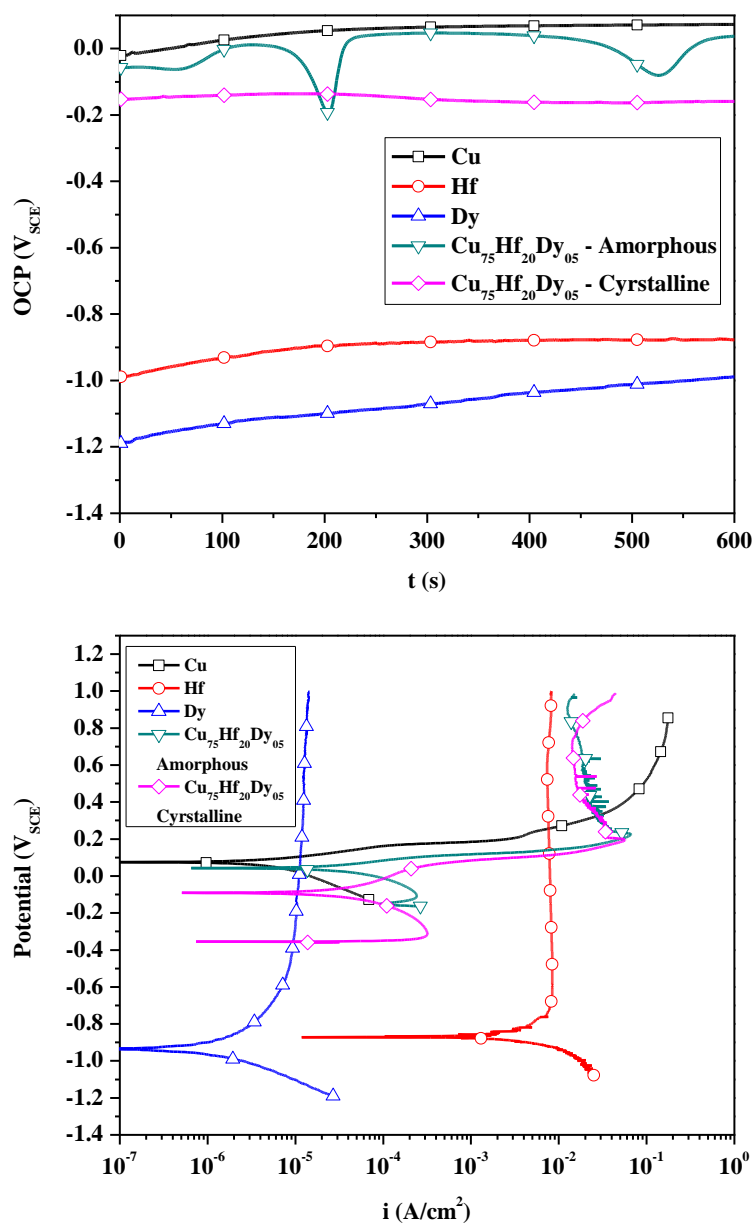


Figure 3.7. Open circuit behavior (top) and the anodic polarization (bottom) behavior of amorphous and crystalline $Cu_{75}Hf_{20}Dy_{05}$ alloys compared to the high purity polycrystalline alloying elements at 1mV/s behavior in aerated 0.1 M HF solution.

3.5.4 Effect of Structure on Increase in Hydrogen Evolution with Concurrent Hafnium Dissolution

Rapid CV experiments performed on the amorphous and crystalline $\text{Cu}_{75}\text{Hf}_{20}\text{Dy}_{05}$ samples to explore differences in Hf dissolution behavior in aerated 0.1 M HF solution without mass transport effects. The experiments were cycled (-1 to -0.1 V_{SCE}) over the potential range where Hf dissolution is expected while Cu remains stable. The cyclic voltammogram ranged from near the Hf OCP at -1 V_{SCE} to just below the Cu OCP at -0.1 V_{SCE} . The cyclic voltammograms (Figure 3.8) of the amorphous and crystalline $\text{Cu}_{75}\text{Hf}_{20}\text{Dy}_{05}$ show an increase in cathodic current density as the cycle number increases. This increasing cathodic half-cell reaction is likely HER with a Nernst potential of -0.341 V_{SCE} in 0.1 M HF solution.

The cathodic current densities are greater for the amorphous case than for the crystalline case. This behavior is readily apparent in Figure 3.9 which shows the current density at a potential of, -0.9 V_{SCE} , during the upward scan of each cycle. This plot also shows increase in magnitude of the cathodic current density for both the amorphous and crystalline samples. The increase in cathodic current density is attributed to enhanced hydrogen evolution on Cu [30]. By cycle 20, the amorphous sample stabilizes at higher cathodic current densities, -0.22 A/cm^2 , than the crystalline sample, -0.16 A/cm^2 . The interpretation of this data is that Cu enrichment and associated Hf dissolution occurs more readily in the case of the amorphous alloy.

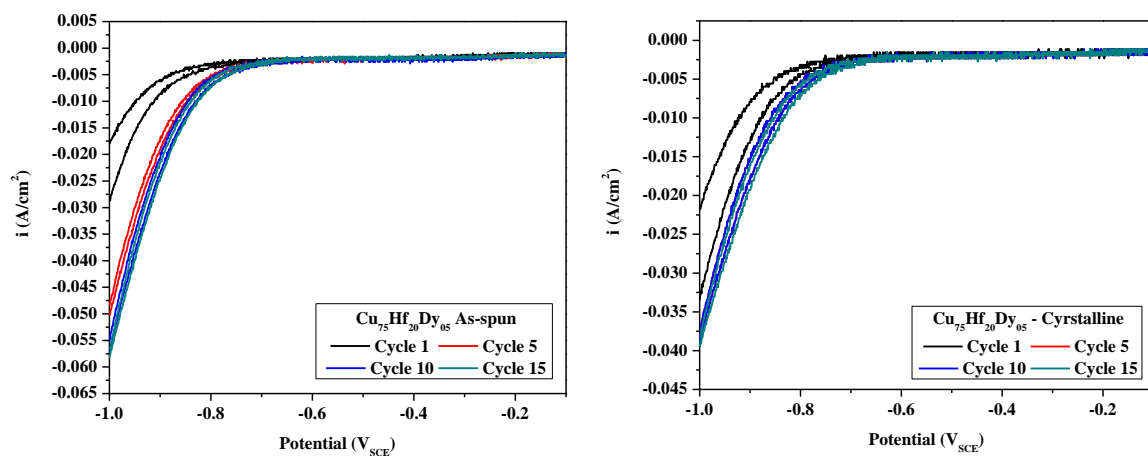


Figure 3.8. Cyclic voltammograms of $\text{Cu}_{75}\text{Hf}_{20}\text{Dy}_{05}$ amorphous (left) and crystalline (right) in aerated 0.1 M HF solution at a scan rate of 20 mV/s.

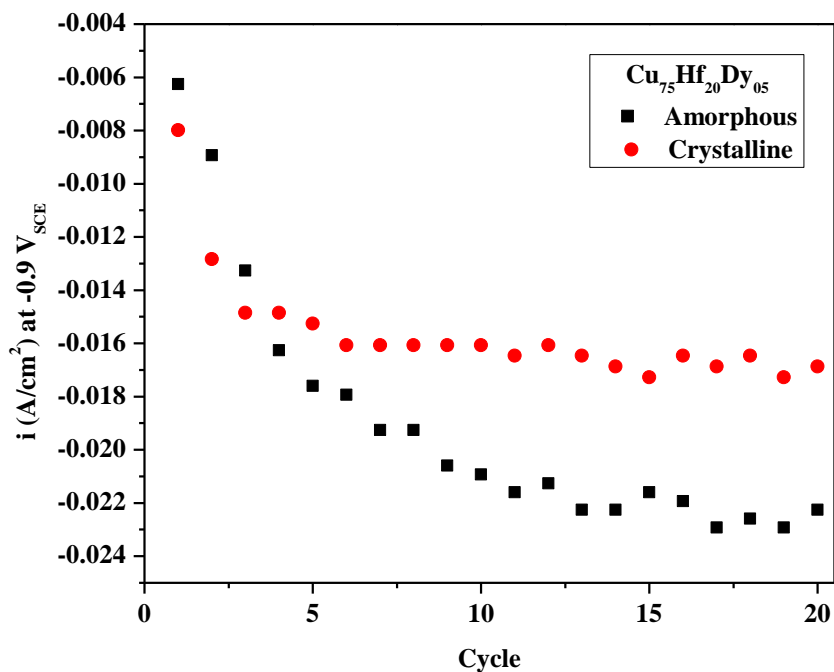


Figure 3.9. Hydrogen evolution current density at $-0.9 \text{ V}_{\text{SCE}}$ during the upward scan of each cycle. Total potential range per cycle was $-1 \text{ V}_{\text{SCE}}$ to $-0.1 \text{ V}_{\text{SCE}}$ at a scan rate of 20 mV/s in aerated 0.1 M HF solution.

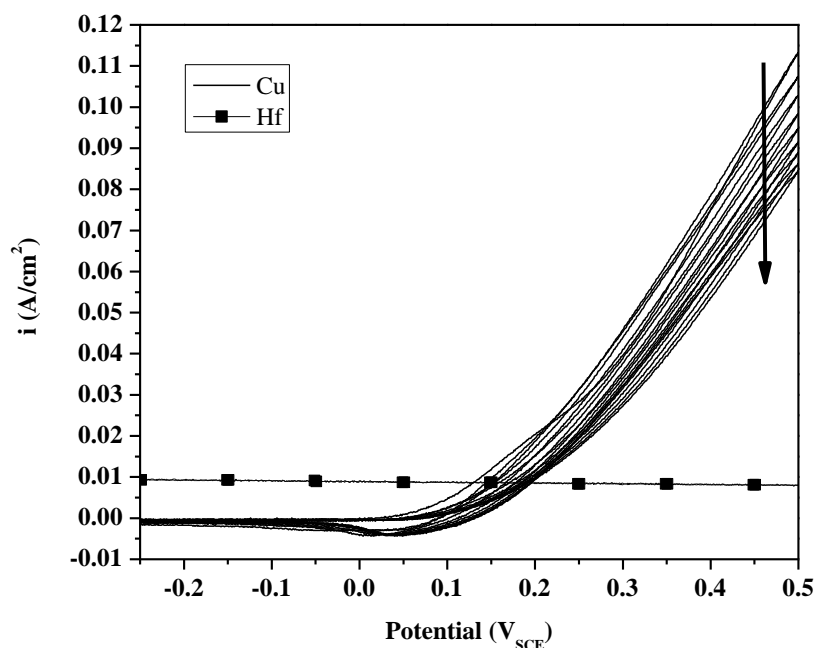


Figure 3.10. Cyclic voltammograms of Cu and Hf from $-0.25 V_{SCE}$ to $0.5 V_{SCE}$, scan rate 20 mV/s , in aerated 0.1 M HF solution. For Cu, every 5 cycles is plotted. The direction of solid arrow indicates increasing cycle number. For Hf, a single representative cycle is shown.

3.5.5 Effect of Structure on Cu Dissolution

Rapid CV experiments were also performed to highlight the Cu dissolution behavior as a function of structure. This was performed in aerated 0.1 M HF solution in a potential regime where Cu dissolution is faster than Hf dissolution (Figure 3.7). The initial potential was $-0.250 V_{SCE}$ and the apex potential was $0.5 V_{SCE}$. A total of 40 consecutive cycles were run at 20 mV/s in aerated 0.1 M HF . The polarization behavior indicates that over this entire potential range Hf dissolution and Dy oxidation is expected. Above 100 mV , Cu is expected to dissolve as well.

Figure 3.10 shows the CV behavior of the primary constituent elements, Cu and Hf. Figure 3.11-Figure 3.16 detail CV results for amorphous and crystalline $\text{Cu}_{75}\text{Hf}_{20}\text{Dy}_{05}$. Figure 3.11 and Figure 3.12 focus on comparisons of the Cu dissolution

behavior of the amorphous and crystalline structure. Trends in the cyclic behavior are shown for crystalline $\text{Cu}_{75}\text{Hf}_{20}\text{Dy}_{05}$, Figure 3.13, and for amorphous $\text{Cu}_{75}\text{Hf}_{20}\text{Dy}_{05}$, Figure 3.14 -Figure 3.16.

Figure 3.10 shows the cyclic voltammogram for Cu and Hf. For all 40 cycles, Cu is active above $0.1 V_{\text{SCE}}$. The peak anodic current density slightly as the cycle number increases. Hf also undergoes dissolution at its mass transport limiting current density over the entire potential range. Only a single representative Hf CV is shown. The measured current density correlates with the limiting current density measured by cyclic polarization. Dy, not shown in the figure, has constant initial current density during the first cycle of $90 \mu\text{A}/\text{cm}^2$. For the subsequent cycles, the Dy specimen had a constant cathodic current density around $-200 \mu\text{A}/\text{cm}^2$.

The first 4 cycles of the CV experiments are shown in Figure 3.11 comparing both amorphous and crystalline $\text{Cu}_{75}\text{Hf}_{20}\text{Dy}_{05}$ states. During each cycle the anodic current density for the amorphous state is much higher than the crystalline state. Additionally, at potentials higher than the active nose, the current density for both cases decreases. In addition for the amorphous case there are numerous large anodic transient events at increased potentials. The charge during the large current density transients during the first few cycles of the amorphous alloy is $1\text{-}2 \text{ mC}/\text{cm}^2$ which is roughly equal to 6 - 12 monolayers of uniform dissolution. In contrast, the transient events are far fewer in number and significantly smaller in magnitude ($0.5 \text{ mC}/\text{cm}^2$ and ~ 3 monolayers) in the case of the crystalline state.

Figure 3.12 shows the final, typically stable for the last 5-10 cycles, current density for each state. In the amorphous state, there are two oxidation peaks, one around $50 \text{ mV}_{\text{SCE}}$ and a second around $150 \text{ mV}_{\text{SCE}}$. There is a large reduction peak at $-50 \text{ mV}_{\text{SCE}}$ likely due to redeposition of Cu ions from solution. In the crystalline specimen, the initial lower potential oxidation peak is not present but the specimen does exhibit the higher potential oxidation peak. The corresponding reduction peak is much smaller in the crystalline specimen compared to the amorphous one.

Figure 3.13 shows the trend for all 40 CV cycles for crystalline $\text{Cu}_{75}\text{Hf}_{20}\text{Dy}_{05}$. The first 20 cycles show the decrease in the oxidation peak with initial apex at about $275 \text{ mV}_{\text{SCE}}$. As the cycles increase the peak diminishes in magnitude and shifts to higher potentials. At cycle 20, the nose of the oxidation peak has shifted to approximately $430 \text{ mV}_{\text{SCE}}$. Cycles 20-40 show a further increase in the potential of the apex current density and a continued decrease until the steady state behavior, described in Figure 3.12, is reached.

The behavior of the amorphous specimen is significantly different and can be described as having different stages. Cycles 1-4, Figure 3.11, show the reduction of the initial oxidation peak, with apex current density at $250 \text{ mV}_{\text{SCE}}$, and a decrease in accompanying transient events. Cycles 5-6 show a shift in the oxidation peak, during the upward scan, to a broad peak between 300 and $450 \text{ mV}_{\text{SCE}}$. Over the next 7 cycles, the oxidation peak during the upward scan decreases in magnitude but remains at the same potential. On the downward scan, from high potential to low, a peak grows at about $230 \text{ mV}_{\text{SCE}}$. The growth of this peak is shown in Figure 3.14 for select cycles. For cycles 13-

22, Figure 3.15, the peak present during the downward scan peak diminishes until the steady state is reached by about cycle 35, Figure 3.16.

The total charge density was calculated for each cycle for the constituent elements, except Dy which has a negligible charge, and the amorphous and crystalline $\text{Cu}_{75}\text{Hf}_{20}\text{Dy}_{05}$. The charge vs. cycle is plotted in Figure 3.17. Cu has a comparatively high charge density per cycle while Hf is constant at much lower value corresponding to its limiting current density. The crystalline $\text{Cu}_{75}\text{Hf}_{20}\text{Dy}_{05}$ very quickly decreases to low current densities crossing below 0.6 C/cm^2 by cycle 12; whereas for amorphous $\text{Cu}_{75}\text{Hf}_{20}\text{Dy}_{05}$ the decrease in charge is much slower, matching the Cu dissolution rate for a number of cycles, and does not cross below 0.6 C/cm^2 until cycle 23. The final charge density for both the crystalline and amorphous state is somewhat similar in magnitude, with the crystalline specimen slightly lower, and is lower than the current density for the Hf dissolution reaction. The lower charge density arises possibly due to the beneficial role of passivation brought on by Dy forming DyF_3 or possibly some other form of dissolution inhibition. In summary, the findings of these experiments indicate that in a regime where Cu dissolves faster than Hf, more Cu dissolves from the amorphous alloy than the crystalline alloy.

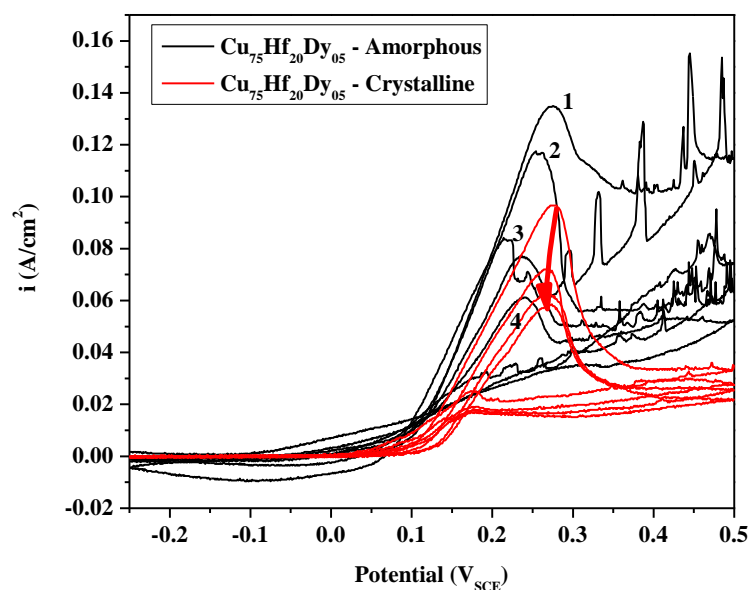


Figure 3.11. Cyclic voltammograms of amorphous and crystalline $\text{Cu}_{75}\text{Hf}_{20}\text{Dy}_{05}$ from $-0.25 V_{\text{SCE}}$ to $0.5 V_{\text{SCE}}$ at a scan rate of 20 mV/s in aerated 0.1 M HF solution. Cycles 1-4 are shown. Numbers indicate cycle number for amorphous $\text{Cu}_{75}\text{Hf}_{20}\text{Dy}_{05}$. The arrow indicates increasing cycle number for crystalline $\text{Cu}_{75}\text{Hf}_{20}\text{Dy}_{05}$.

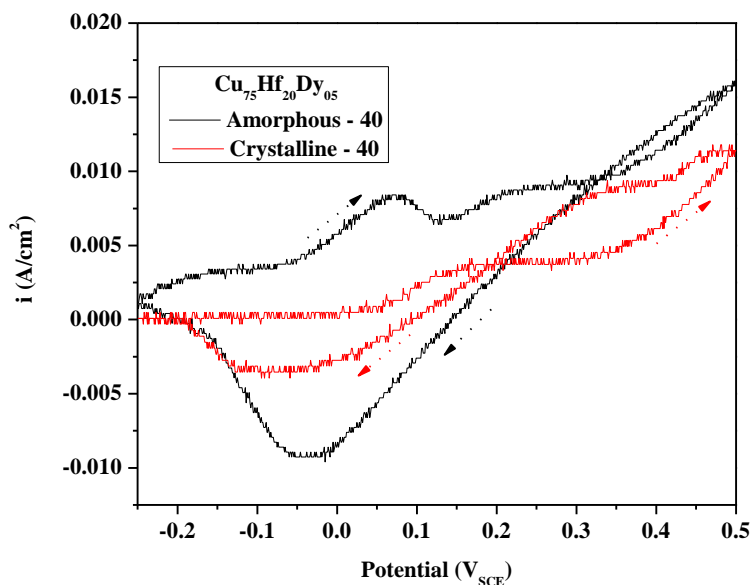


Figure 3.12. Cyclic voltammograms of amorphous and crystalline $\text{Cu}_{75}\text{Hf}_{20}\text{Dy}_{05}$ from $-0.25 V_{\text{SCE}}$ to $0.5 V_{\text{SCE}}$ at a scan rate of 20 mV/s in aerated 0.1 M HF solution. The final cycle, 40, is shown.

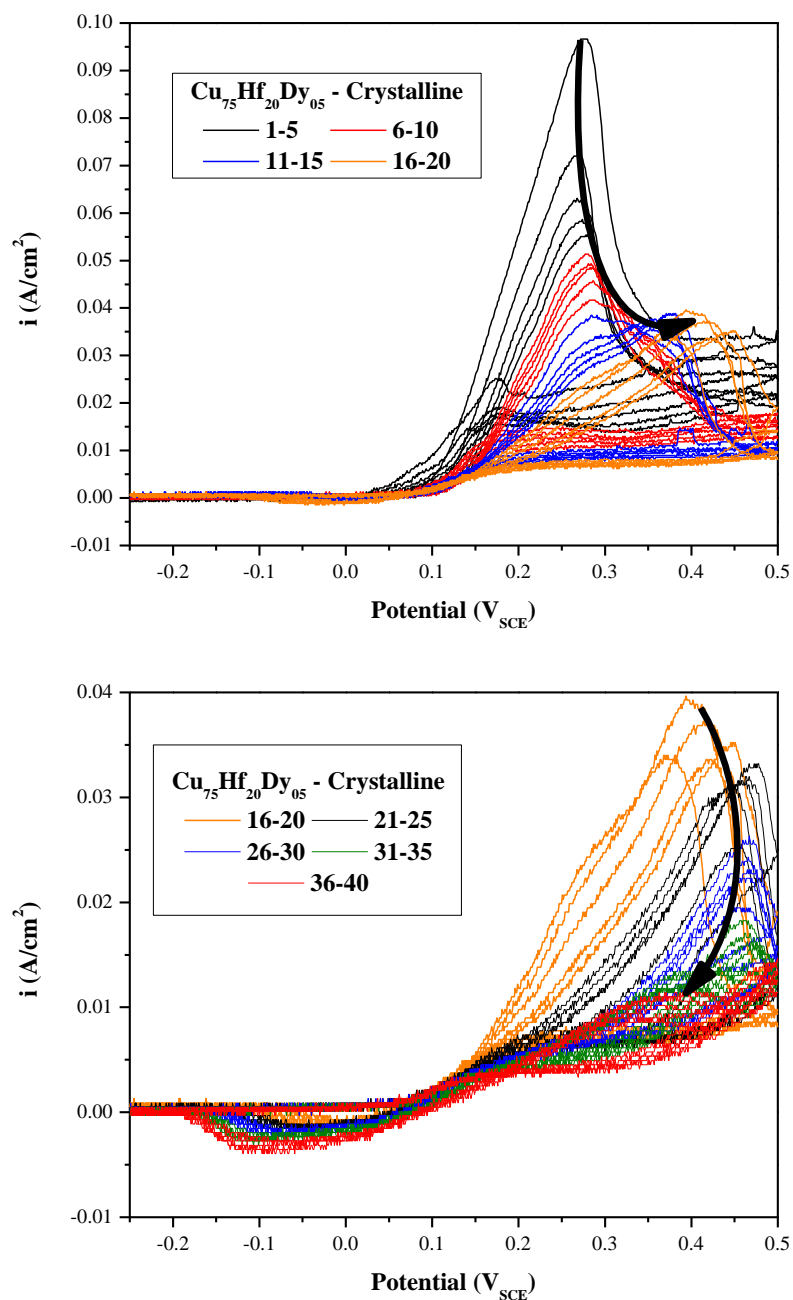


Figure 3.13. Cyclic voltammograms of crystalline $\text{Cu}_{75}\text{Hf}_{20}\text{Dy}_{05}$ from $-0.25 \text{ V}_{\text{SCE}}$ to $0.5 \text{ V}_{\text{SCE}}$ at a scan rate of 20 mV/s in aerated 0.1 M HF solution. Cycles plotted are 1-20 (top) and 16-40 (bottom). Arrows tracks the maximum current density during a given cycle and direction indicates increasing cycle number.

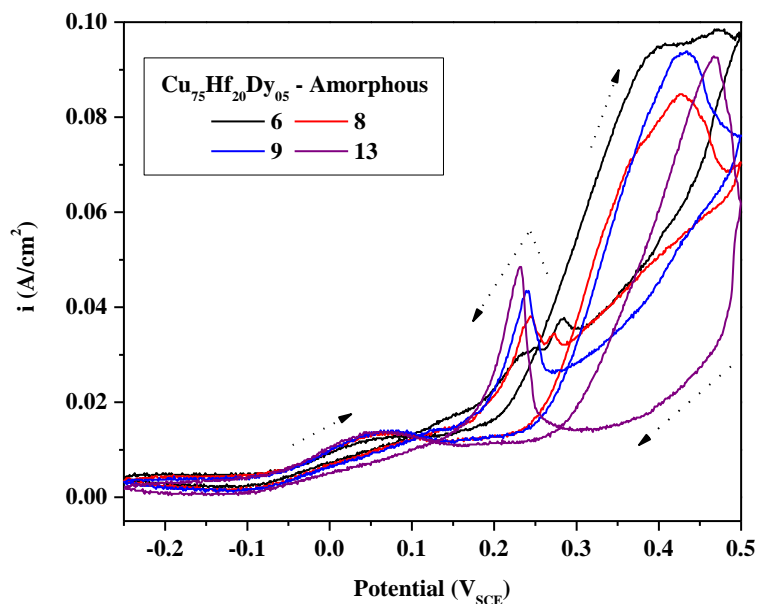


Figure 3.14. Cyclic voltammograms of amorphous Cu₇₅Hf₂₀Dy₀₅ from -0.25 V_{SCE} to 0.5 V_{SCE}, scan rate 20 mV/s, in aerated 0.1 M HF solution. Cycle 6-13, selected cycles represented, show the growth of peak at 250 mV_{SCE} during the downward scan. Dashed lines indicate scan direction.

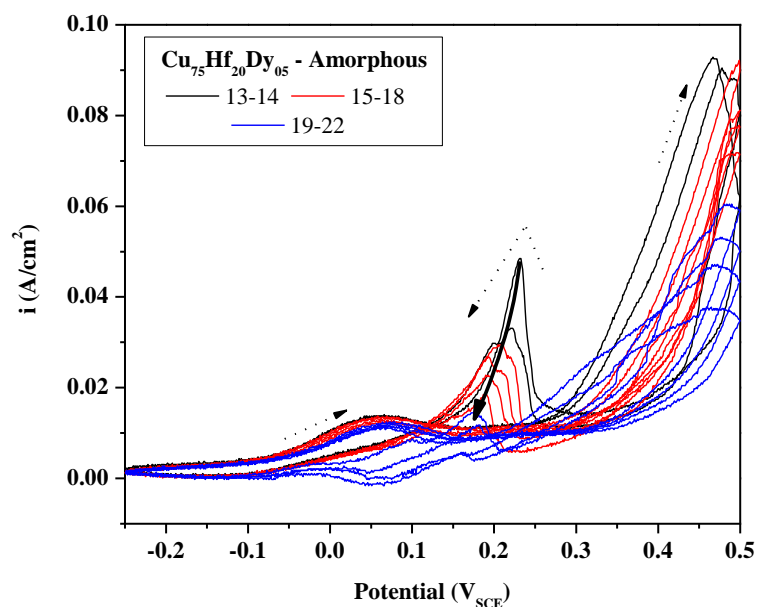


Figure 3.15. Cyclic voltammograms of amorphous Cu₇₅Hf₂₀Dy₀₅ from -0.25 V_{SCE} to 0.5 V_{SCE}, scan rate 20 mV/s, in aerated 0.1 M HF solution. Cycles 13-22 show a decrease in the 250 mV_{SCE} peak highlighted by the solid arrow. Dashed lines indicate scan direction.

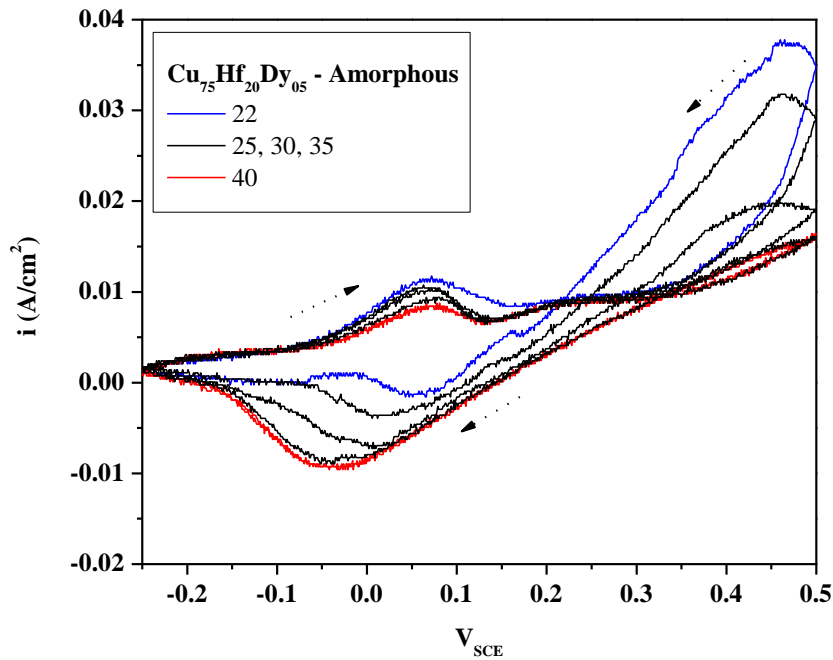


Figure 3.16. Cyclic voltammograms of amorphous $\text{Cu}_{75}\text{Hf}_{20}\text{Dy}_{05}$ from $-0.25 \text{ V}_{\text{SCE}}$ to $0.5 \text{ V}_{\text{SCE}}$, scan rate 20 mV/s , in aerated 0.1 M HF solution. Cycles 22-40, selected cycles represented, show a decrease in current density to the stable E-i behavior. Dashed lines indicate cycle direction.

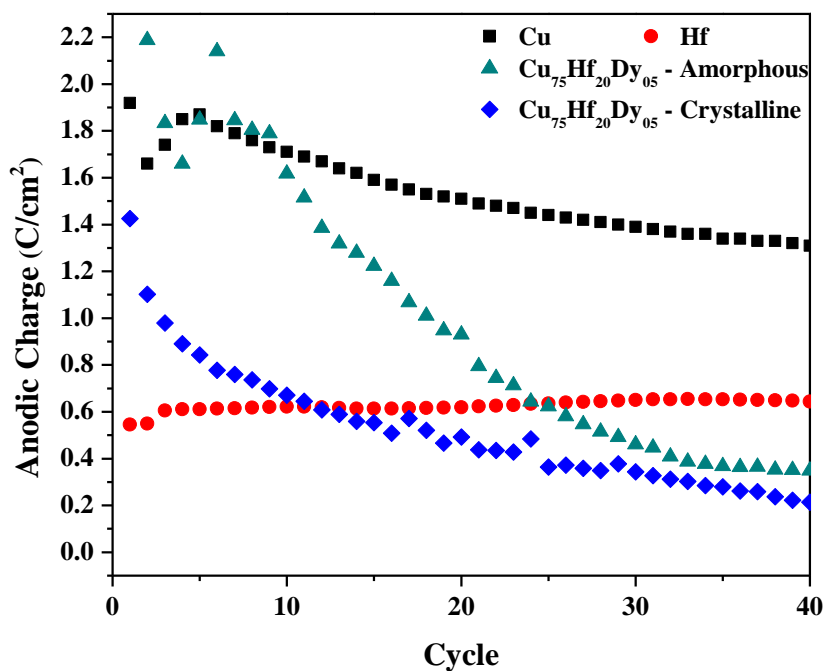


Figure 3.17. Calculated charge density per cycle of amorphous and crystalline $\text{Cu}_{75}\text{Hf}_{20}\text{Dy}_{05}$ alloys during cyclic voltammetry from -0.25 to $0.5 \text{ V}_{\text{SCE}}$ at 20 mV/s . High purity polycrystalline Cu and Hf are also shown. Dy is not shown because the charge density is less than 0.0001 C/cm^2 .

3.5.6 Preferential Hf Dissolution in a Potential Regime dominated by Hf Dissolution

Potentiostatic polarization was performed, Figure 3.18, at a potential below the Cu OCP where preferential Hf dissolution is expected. As expected, the electrochemical current density on high purity Cu remains cathodic, while Hf has a high anodic current density, approximately 0.01 A/cm^2 , indicative of Hf dissolution. The amorphous $\text{Cu}_{75}\text{Hf}_{20}\text{Dy}_{05}$ remains cathodic for the initial 1800 s before sharp peaks of anodic current density persist until the end of the experiment at 5400 s. In contrast, the crystalline $\text{Cu}_{75}\text{Hf}_{20}\text{Dy}_{05}$ has a brief period of initially anodic current and then remains cathodic. The total anodic charge sustained during the brief anodic current in the crystalline state is 3.3 mC/cm^2 while the total anodic current in the amorphous state is 2.15 C/cm^2 . These results indicate that the crystalline structure is less susceptible to Hf dissolution than the amorphous structure. The contrast between the amorphous and crystalline structures is further explored by XRD and SEM characterization as a function of exposure time.

For both amorphous and crystalline $\text{Cu}_{75}\text{Hf}_{20}\text{Dy}_{05}$, a series of potentiostatic polarization experiments were performed with durations ranging from 3600 s to 20 ks to achieve statistically significant observations regarding the i vs. time behavior and to perform ex-situ post corrosion characterization. Representative i vs. time behavior for the amorphous and crystalline specimens is shown in Figure 3.19. Figure 3.20 shows the i vs. time behavior of the amorphous and crystalline $\text{Cu}_{75}\text{Hf}_{20}\text{Dy}_{05}$ conditions. The first 7200s of exposure duration is shown for each independent experiment, replicate experiments are labeled by test number. In Figure 3.21, the i vs. time behavior for the entire experimental duration, up to 20 ks, is shown. During the first 7200 s of exposure, the crystalline

specimens typically have a very high initial current density which rapidly decays over the first 100 s and becomes cathodic. Over the exposure time, the net current then increases over time first becoming less cathodic then increasingly anodic. This increase in current density is due to increasing Hf dissolution. Additionally, there are characteristic events where the current density rapidly decreases to or towards cathodic currents and stabilizes. Also seen in some crystalline specimens are large current density transients followed by periods of lower current density. For the amorphous state, the initial current density spike decays similarly to the crystalline condition although fewer specimens transition from anodic to cathodic currents. Following the initial potential drop, the current density very quickly rises to high anodic currents, average of 1 mA/cm^2 at 3600 s and 2 mA/cm^2 at 7200 s. These values are significantly higher than those observed in the crystalline specimens which have an average current density of less than 0.5 mA/cm^2 and less than 1 A/cm^2 at 3600 s and 7200 s, respectively.

The amorphous state does not show the reductions in current density seen in the crystalline state. Instead the amorphous specimens follow a general trend to higher current densities were seen with time. The average charge density of all of the replicates is plotted in Figure 3.22. At 3600 s the total accumulated charge in the crystalline condition is 0.07 C/cm^2 which is significantly lower than that for the amorphous condition, 0.357 C/cm^2 . The charge corresponds to an average of approximately 500 monolayers of preferential Hf dissolution for the crystalline case. In contrast 3,000 monolayers dissolved for the amorphous case. At 7200 s, the total charge difference

between the amorphous and crystalline states increases to 0.7 C/cm^2 . The data from each separate potentiostatic polarization is summarized in Table 3.2.

XRD spectra are shown as a function of increasing charge, with HF solution exposure times listed, for the amorphous, and crystalline, specimens (Figure 3.23 and Figure 3.24). Both alloys undergo surface layer recrystallization to FCC Cu as the surface layer dealloys. The amorphous alloy, with its overall significantly higher i vs. time behavior, undergoes surface reorganization to FCC Cu at 7.6 ks of polarization and 1.15 C/cm^2 of accumulated charge. Initially, both the broad amorphous peak and the FCC Cu peaks are detected. At higher accumulated charge, the Cu peaks become better defined. For the crystalline case, surface reorganization is not indicated by the XRD spectra at polarization times less than the 20 ks during which 3.05 C/cm^2 (calculated approximations: 24 k monolayers, $7 \mu\text{m}$) of charge accumulated. Both the characteristic $\text{Cu}_{51}\text{Hf}_{14}$ and the FCC Cu patterns are detected. At an intermediate charge accumulation of 0.461 C/cm^2 (4 k monolayers, $1.2 \mu\text{m}$) the Cu FCC peaks are not yet apparent.

SEM microscopy was used to determine the surface morphology after exposure. Figure 3.25 shows the surface morphology of the amorphous specimen after the 20 ks potentiostatic polarization with 6.5 C/cm^2 of total anodic charge. The surface morphology indicates a uniform distribution of pores with an approximate 10 nm diameter and nodules. In contrast, the surface morphology of the crystalline specimen, Figure 3.26, does not show the same uniform porous structure seen in the amorphous samples. The pores are smaller than those observed in the amorphous samples. The through thickness morphology, Figure 3.27 and Figure 3.28, was analyzed using ribbon cross sections.

These figures show the growth of the dealloyed region as a function of increasing charge at the exposure duration and charge accumulation of the XRD spectra (a, b and c for crystalline $\text{Cu}_{75}\text{Hf}_{20}\text{Dy}_{05}$ and d, e and f for amorphous $\text{Cu}_{75}\text{Hf}_{20}\text{Dy}_{05}$). The higher resolution cross-section morphology of crystalline specimen *c* (Figure 3.27) and amorphous specimen *f* (Figure 3.28) show increased surface roughness in the crystalline state.

The dealloyed layer thickness, measured by these SEM micrographs, is plotted as a function of charge in Figure 3.29. The plot shows the average dealloyed layer thickness as the sum of the dealloyed thickness for both directions of exposure. At shorter exposure times the amorphous alloy has a significantly larger dealloyed layer. Both the crystalline and amorphous specimens dealloyed layer thickness as a function of charge fall on the same linear fitted line with a slope of $2.04 \mu\text{m} / (\text{C}/\text{cm}^2)$. From Faraday's Law, the charge is linearly proportional to the dealloying thickness. The dealloyed layer thickness approximation (shown in Table 3.2) assumed all of the charge resulted in Hf dissolution to Hf^{4+} . The calculated value of the dealloyed layer the thickness for the amorphous case with $6.49 \text{ C}/\text{cm}^2$ of anodic charge, point *f*, is $15.2 \mu\text{m}$. The experimentally measured value is $13.6 \mu\text{m}$. For the crystalline specimen, *c*, the calculated dealloying thickness was $7.1 \mu\text{m}$ and the experimentally determined thickness was $6.8 \mu\text{m}$. In both cases there is reasonable agreement. Since both the amorphous and crystalline specimens fall on the same linear line, the charge efficiency, or charge required to dissolve an Hf atom, is the same. The key difference between the amorphous and crystalline alloys is that the

amorphous alloy undergoes preferential dissolution much more quickly than the crystalline alloy and, thus, these thicknesses occur after different exposure periods

Semi-quantitative EDS analysis showed preferential dissolution of Hf within the dealloyed region and enrichment of both Cu and Dy. Line scans across the two dealloyed region cross sections of amorphous specimen f (6.05 C/cm^2) are shown in Figure 3.30. The measured Hf concentration, measured values in at%, were less than 5 % across the dealloyed region while the Cu and Dy concentration were enriched to 85-90 % and 10-12 %, respectively. Using the EDS spectrum generated by the parent amorphous matrix (middle region) the composition was determined to be Cu 73 %, Hf 21 % and Dy 6%, which is close to the nominal composition of $\text{Cu}_{75}\text{Hf}_{20}\text{Dy}_{05}$. The measured concentrations across the dealloyed region were fairly uniform and there were no substantial through thickness concentration gradients. Similar behavior was seen in the crystalline specimens. The EDS results show that preferential dissolution of Hf occurred during the potentiostatic exposure in HF solution within the dealloyed region while the parent matrix retained the nominal alloy concentration for both the amorphous and crystalline conditions. There was not, however, a statistically significant difference between the measured compositions in the fully dealloyed regions of the amorphous and crystalline states.

Table 3.2. Calculated charge density of amorphous and crystalline Cu₇₅Hf₂₀Dy₀₅ in 0.1 M HF solution under potentiostatic polarization at -150 mV_{SCE} for at least 6 replicate tests in each condition. The total anodic charge density has been used to calculate the approximate number of monolayers that has undergone preferential Hf dissolution and the dealloying penetration.

Cu ₇₅ Hf ₂₀ Dy ₀₅ Specimen	Exposure Time (s)	Total Charge (C/cm ²)	Tot. Anodic Ch. 3600 s (C/cm ²)	Tot. Anodic Ch. 7200 s (C/cm ²)	Tot. Anodic Ch. (C/cm ²)	Monolayers Removed	Depth of Penetration (μm)	Test Number
Amorphous	9380	0.23	0.30	1.214	1.67	13 k	3.9	1
Amorphous	9600	0.66	0.30	0.692	0.96	7.5 k	2.3	2
Amorphous	7700	0.98	0.29	1.053	1.16	9.0 k	2.7	3
Amorphous	8800	2.30	0.69	1.764	2.30	17.9 k	5.4	4
Amorphous	20000	6.47	0.29	.846	6.49	50.7 k	15.2	5
Amorphous	15200	3.20	0.32	1.038	3.20	25.0 k	7.5	6
Average			0.357	1.101				
Crystalline	4200	-0.05	0.007	-	0.01	55	0.02	1
Crystalline	7300	0.48	0.12	0.49	0.50	11.6 k	1.2	2
Crystalline	9600	0.09	0.004	0.05	0.13	1.0 k	0.3	3
Crystalline	7300	0.38	0.09	0.39	0.40	3.1 k	0.9	4
Crystalline	6200	-0.06	0.001	-	0.003	70	0.01	5
Crystalline	3700	0.23	0.23	-	0.23	5.4 k	0.5	6
Crystalline	20000	0.75	0.05	0.10	0.76	17.8 k	1.8	7
Crystalline	20000	3.03	0.08	0.45	3.05	71.5 k	7.1	8
Average			0.071	0.295				

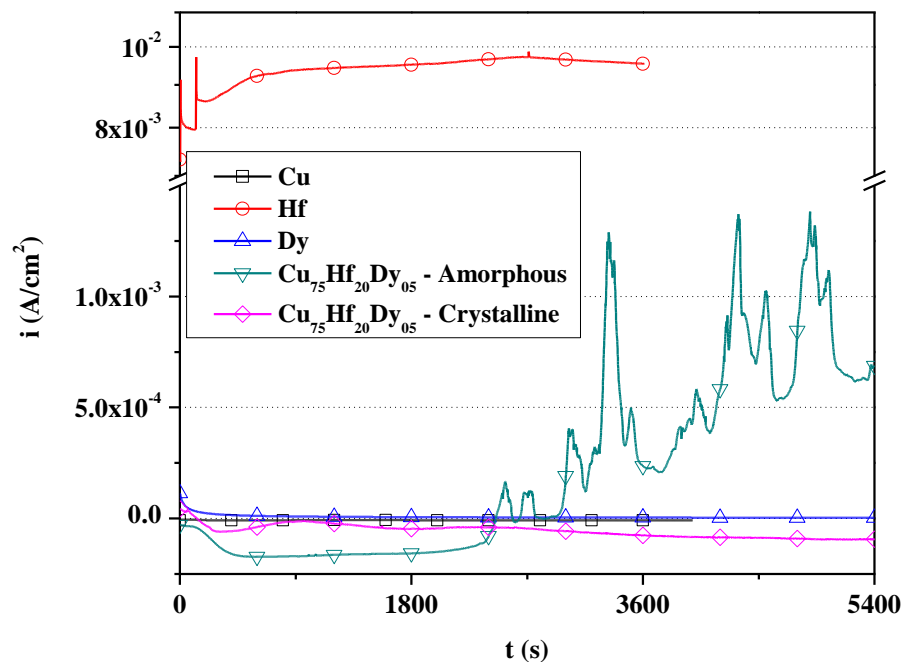


Figure 3.18. Anodic current density vs. time behavior of amorphous and crystalline $\text{Cu}_{75}\text{Hf}_{20}\text{Dy}_{05}$ alloys and the high purity polycrystalline alloying elements subjected to potentiostatic polarization at $-150 \text{ mV}_{\text{SCE}}$ in aerated 0.1 M HF solution.

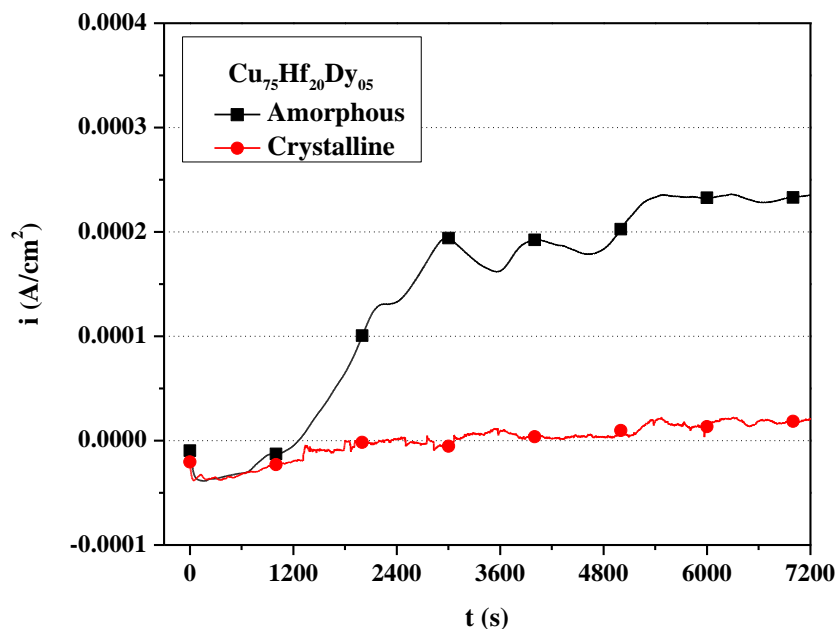


Figure 3.19. Anodic current density vs. time behavior measurements of analogous large ribbon samples large ribbon (surface area approximately $0.1\text{-}0.25 \text{ cm}^2$) specimens of amorphous and crystalline $\text{Cu}_{75}\text{Hf}_{20}\text{Dy}_{05}$ alloys subjected to potentiostatic polarization at $-150 \text{ mV}_{\text{SCE}}$ in aerated 0.1 M HF solution.

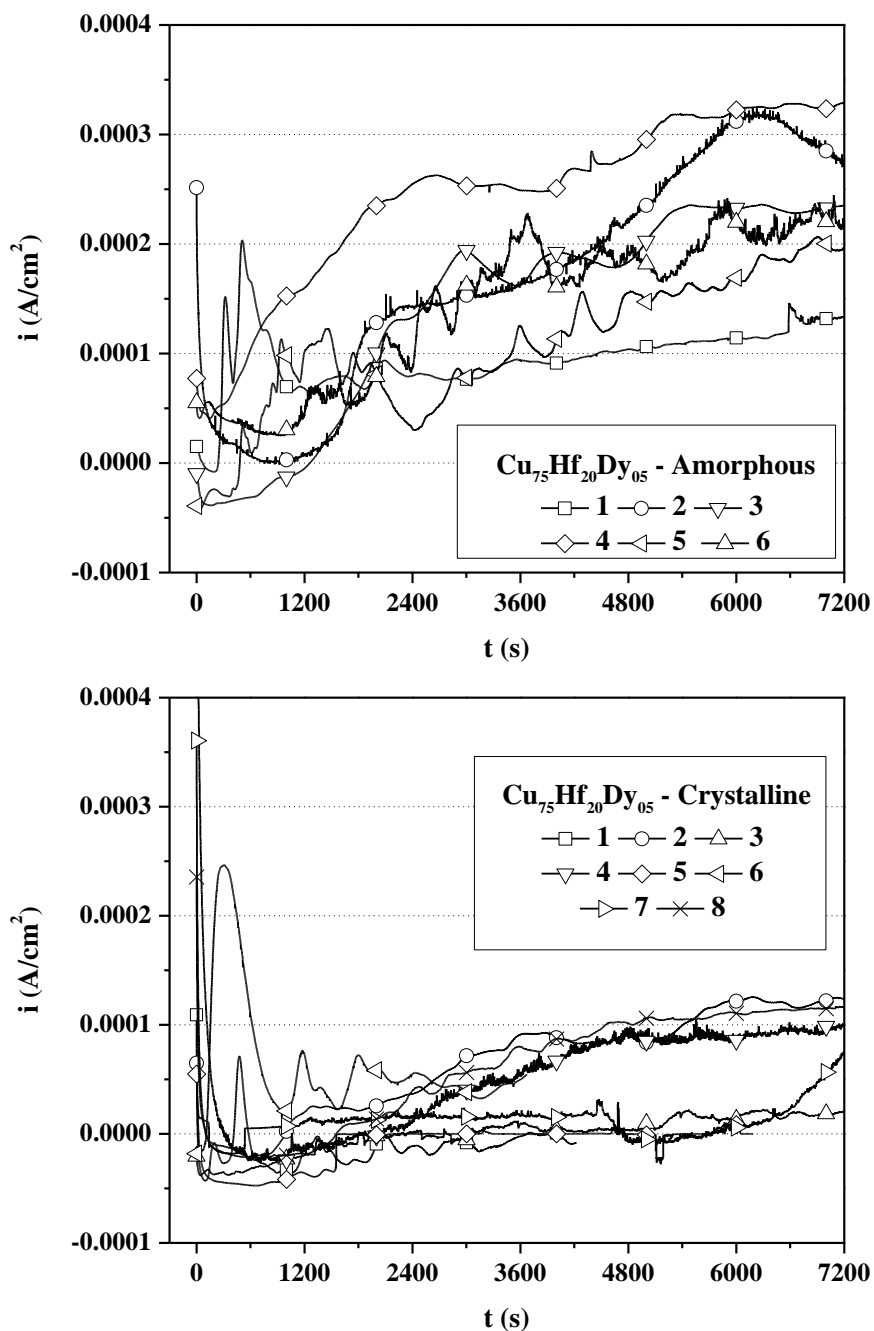


Figure 3.20. Anodic current density vs. time behavior measurements of amorphous and crystalline $\text{Cu}_{75}\text{Hf}_{20}\text{Dy}_{05}$ alloy specimens subjected to potentiostatic polarization at $-150 \text{ mV}_{\text{SCE}}$ in aerated 0.1 M HF solution. The initial 7200 seconds are shown. Numbers identify exposure repetition.

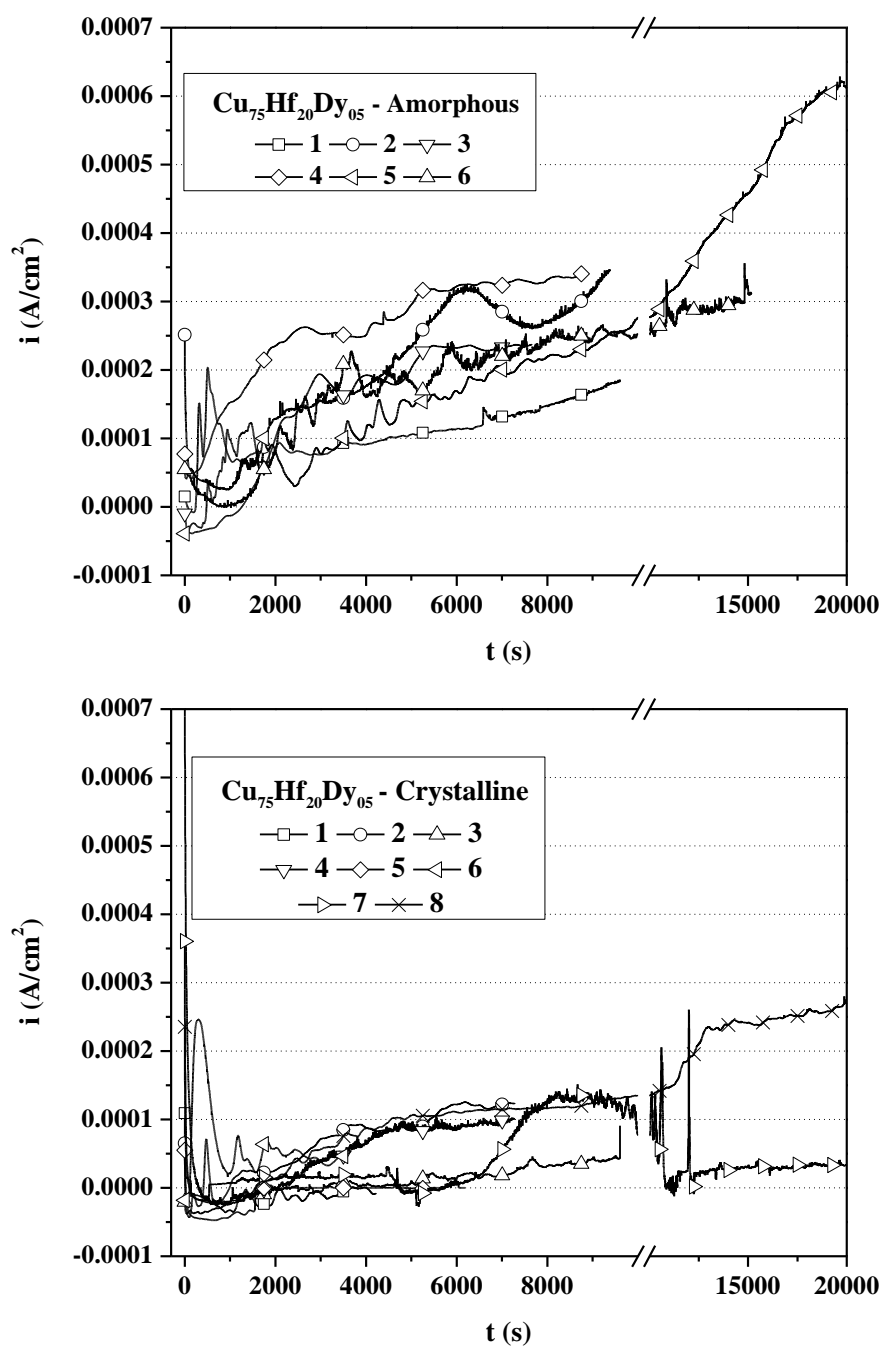


Figure 3.21. Anodic current density vs. time behavior measurements of amorphous and crystalline $\text{Cu}_{75}\text{Hf}_{20}\text{Dy}_{05}$ alloy specimens subjected to potentiostatic polarization at $-150 \text{ mV}_{\text{SCE}}$ in aerated 0.1 M HF solution for up to 20,000 seconds. Numbers identify exposure repetition.

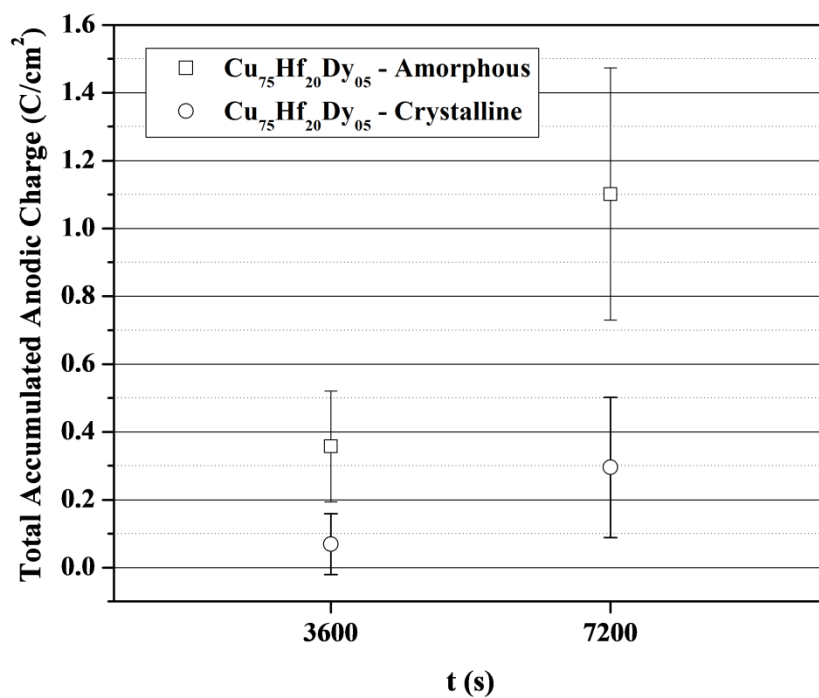


Figure 3.22. Total accumulated anodic charge density of amorphous and crystalline $\text{Cu}_{75}\text{Hf}_{20}\text{Dy}_{05}$ during potentiostatic polarization at $-150 \text{ mV}_{\text{SCE}}$ in 0.1 M HF solution. Error bars represent 1 standard deviation.

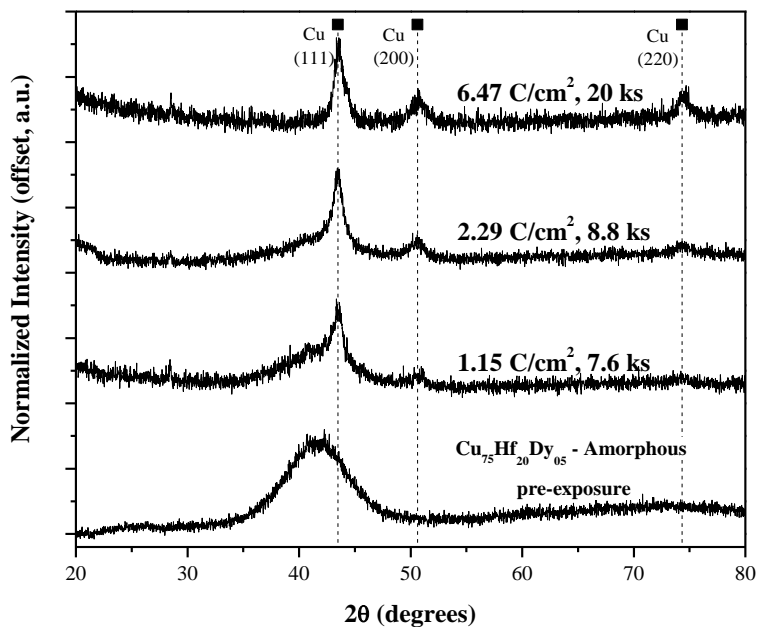


Figure 3.23. XRD spectra of the amorphous $\text{Cu}_{75}\text{Hf}_{20}\text{Dy}_{05}$ after potentiostatic polarization at $-150 \text{ mV}_{\text{SCE}}$ in 0.1 M HF solution. Spectra are shown with increasing total anodic charge. The peaks for polycrystalline Cu are shifted $+0.2^\circ$ are labeled.

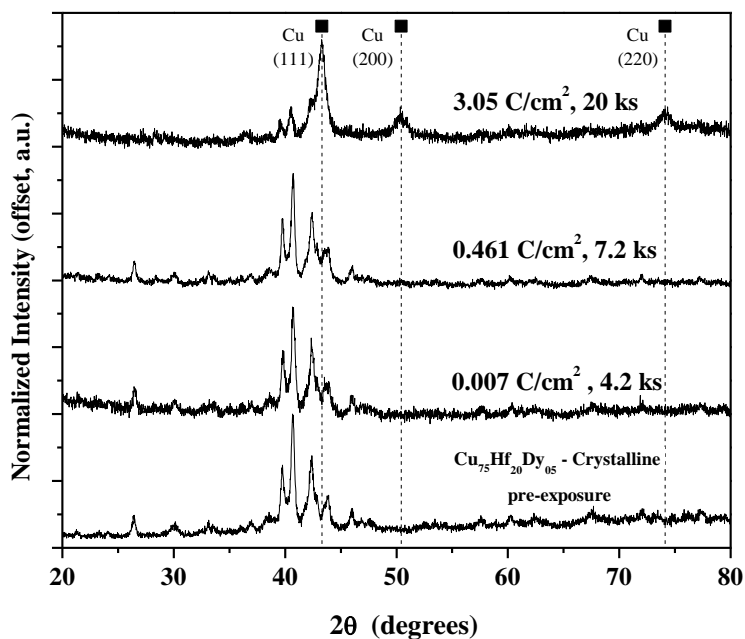


Figure 3.24. XRD spectra of the crystalline $\text{Cu}_{75}\text{Hf}_{20}\text{Dy}_{05}$ after potentiostatic polarization at $-150 \text{ mV}_{\text{SCE}}$ in 0.1 M HF solution shown in Figure 3.21. Spectra organized by the total anodic charge and time of exposure. The peaks for polycrystalline Cu (no shift) are also labeled.

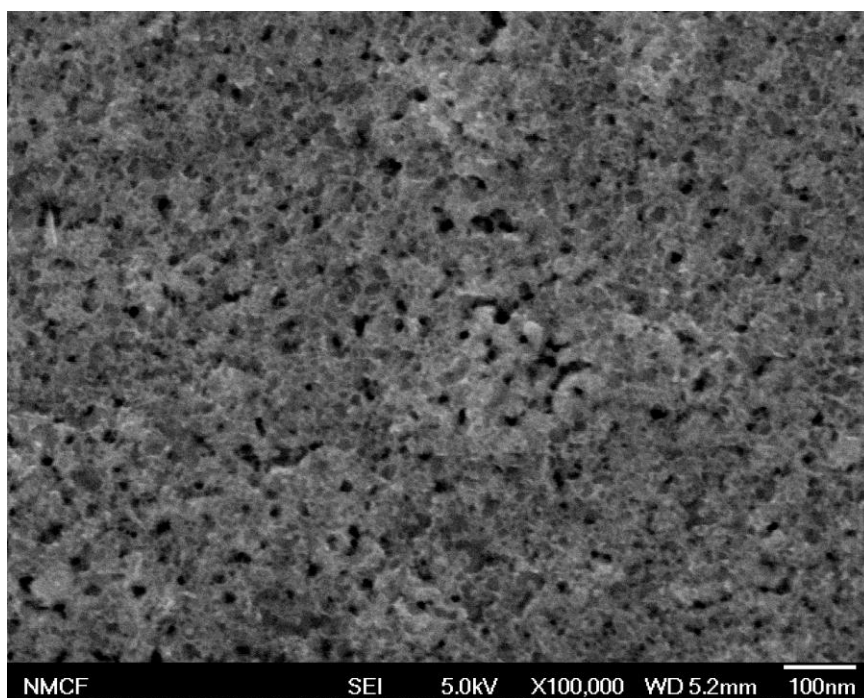


Figure 3.25. SEM micrograph of the post exposure surface of the amorphous $\text{Cu}_{75}\text{Hf}_{20}\text{Dy}_{05}$ specimen with 6.47 C/cm^2 of total accumulated charge during potentiostatic polarization at $-150 \text{ mV}_{\text{SCE}}$ in 0.1 M HF solution for 20 ks.

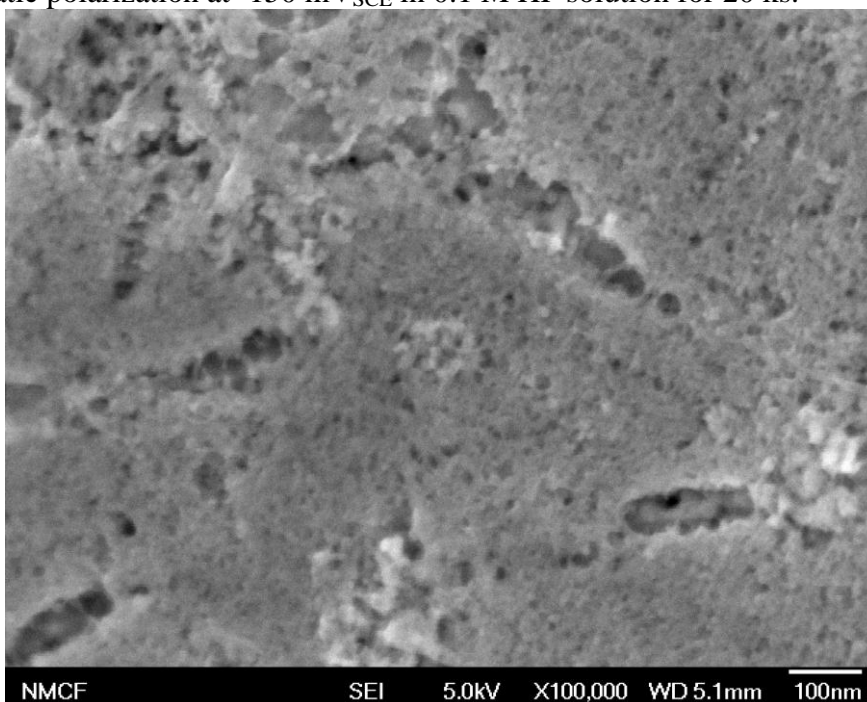


Figure 3.26. SEM micrograph of the post exposure surface of the crystalline $\text{Cu}_{75}\text{Hf}_{20}\text{Dy}_{05}$ specimen with 3.05 C/cm^2 of total accumulated charge during potentiostatic polarization at $-150 \text{ mV}_{\text{SCE}}$ in 0.1 M HF solution for 20 ks.

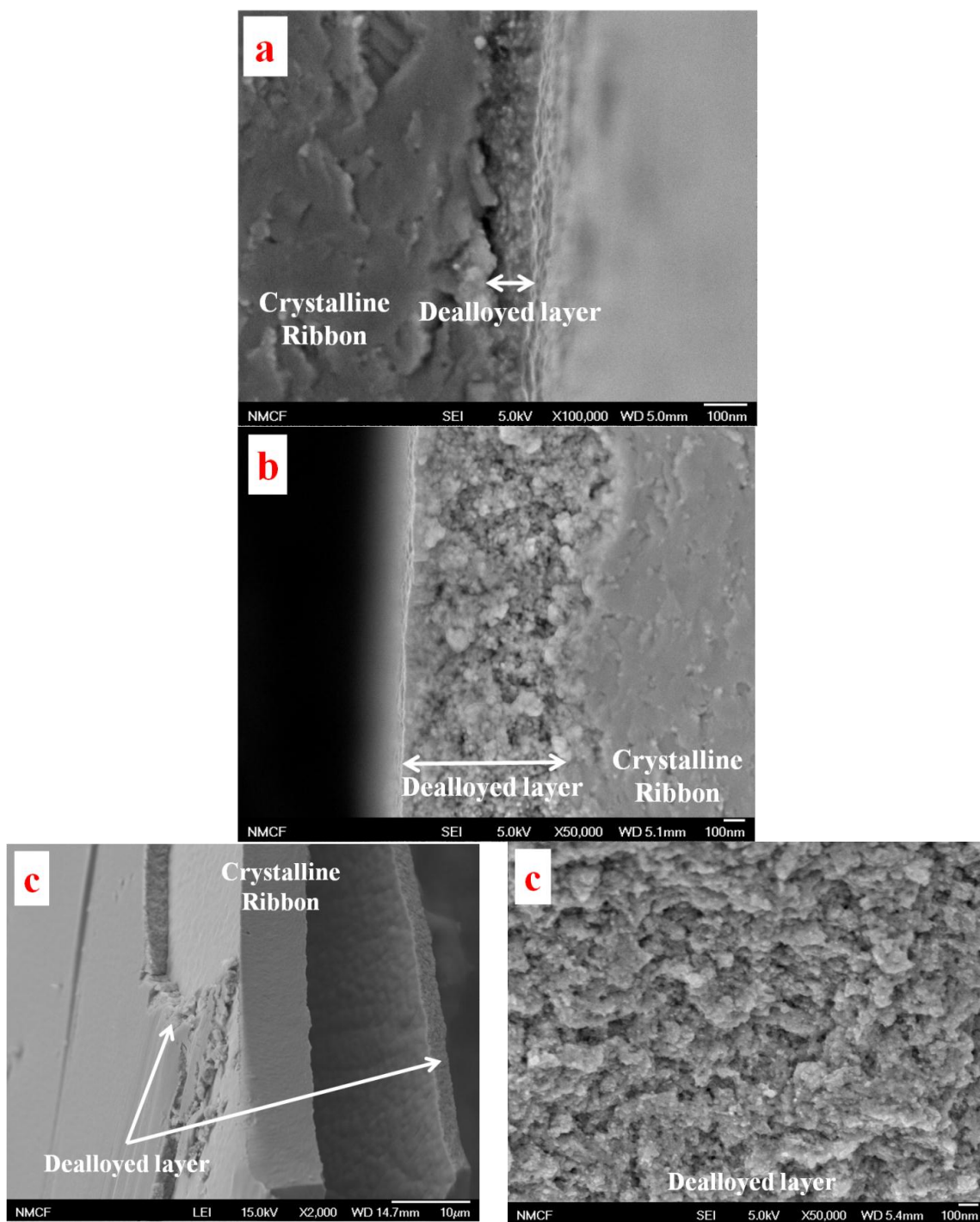


Figure 3.27. SEM micrographs of the crystalline $\text{Cu}_{75}\text{Hf}_{20}\text{Dy}_{05}$ dealloyed specimen cross section potentiostatically polarized at $-0.15 \text{ V}_{\text{SCE}}$ in 0.1 M HF solution. Duration and total accumulated charge was 4.2 ks - 0.007 C/cm^2 (a), 7.2 ks - 0.461 C/cm^2 (b), and 20 ks - 3.05 C/cm^2 (c).

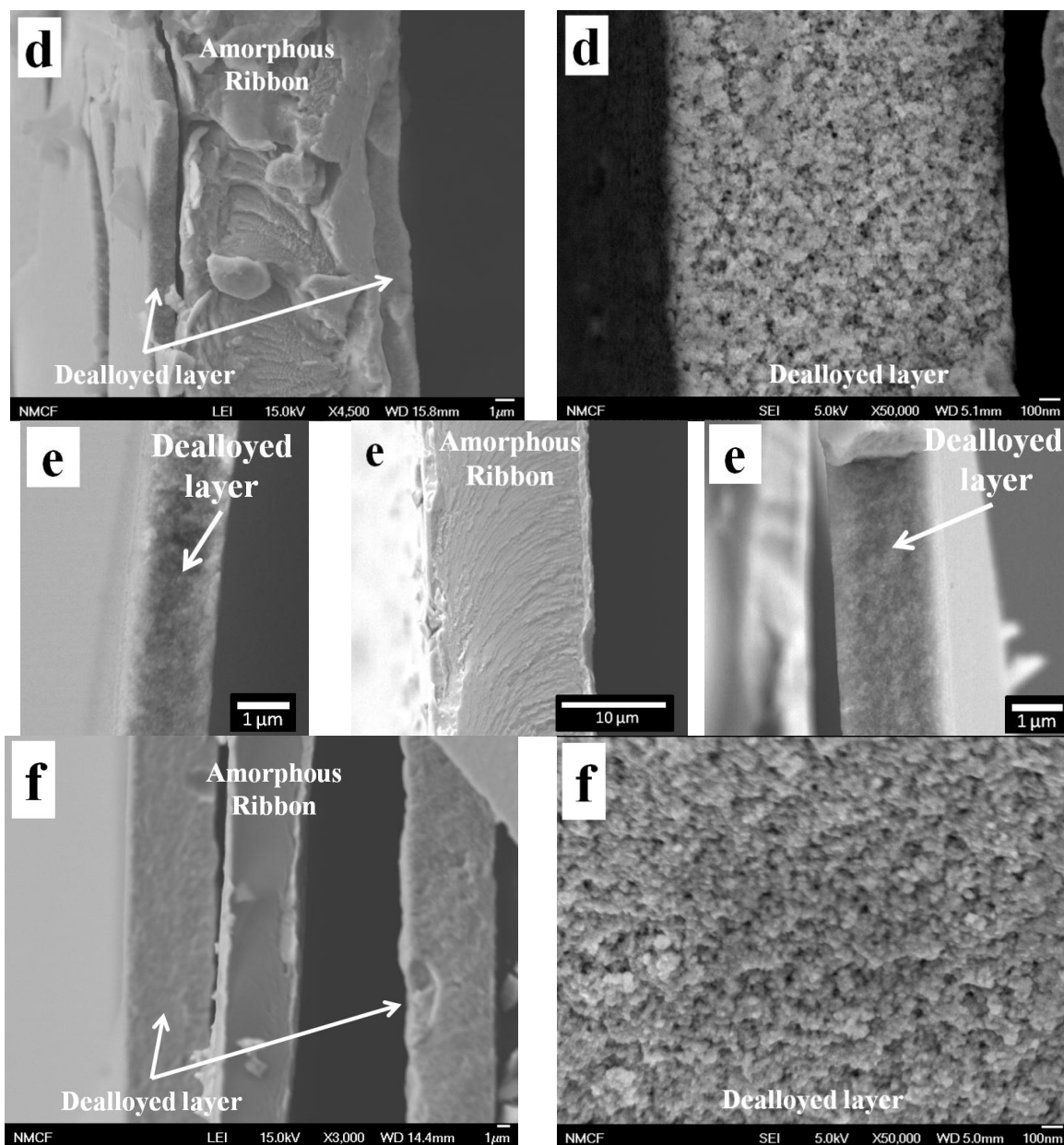


Figure 3.28. SEM micrographs of the amorphous $\text{Cu}_{75}\text{Hf}_{20}\text{Dy}_{05}$ dealloyed specimen cross section potentiostatically polarized at $-0.15 V_{\text{SCE}}$ in 0.1 M HF solution. Duration and total accumulated charge was 7.2 ks – 1.15 C/cm^2 (d), 8.8 ks – 2.29 C/cm^2 (e), and 20 ks – 6.47 C/cm^2 (f).

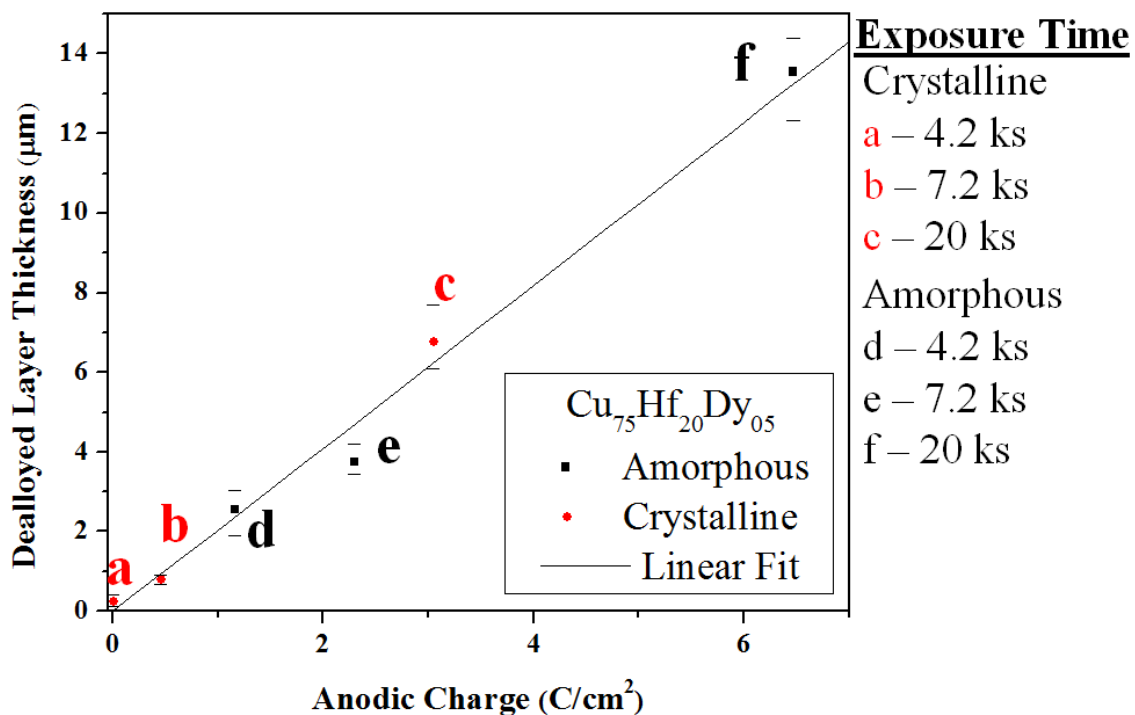


Figure 3.29. Dealloyed layer thickness as a function of the total anodic charge accumulated during potentiostatic polarization at $-0.15 V_{SCE}$ in 0.1 M HF solution for amorphous (Figure 3.23) and crystalline (Figure 3.24) $Cu_{75}Hf_{20}Dy_{05}$. The dealloyed layer thickness is measured by ex-situ cross section SEM images of the dealloyed layer. Average dealloyed layer thickness is marked while error bars indicate the min and max measured values. The linear fit of the data has a slope of $2.04 \mu m / (C/cm^2)$ and a correlation coefficient of 0.9946.

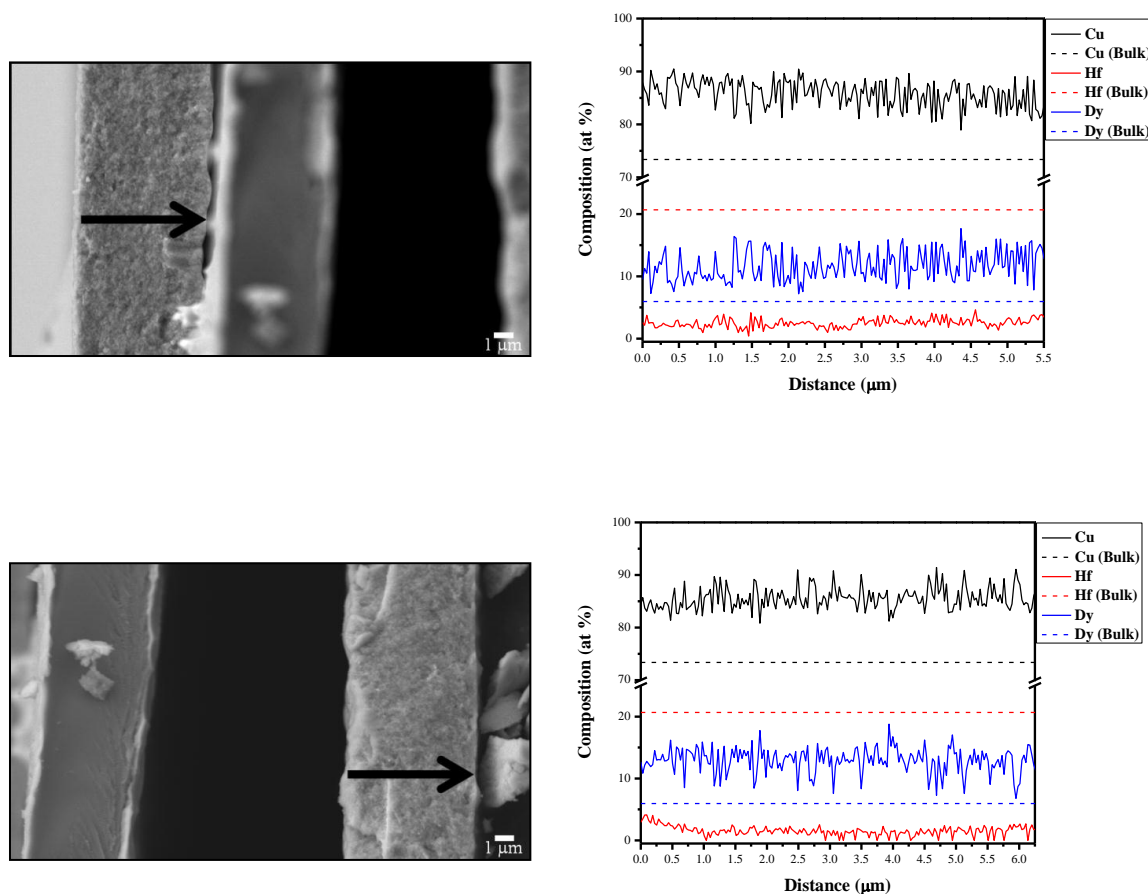


Figure 3.30. EDS line profiles through the two dealloyed regions of the amorphous $\text{Cu}_{75}\text{Hf}_{20}\text{Dy}_{05}$ ribbon potentiostatically polarized at $-0.15 \text{ V}_{\text{SCE}}$ in 0.1 M HF solution (point $f - 6.05 \text{ C/cm}^2$, 20ks). The indicated direction, left to right, on the SEM micrographs is followed in the EDS composition plots. Dashed lines indicate the composition of the parent ribbon established by area scans on the cross section of the middle region: Cu 73.4 at%, Hf 20.7 at %, and Dy 6.0 at %. EDS spectra of dealloyed regions of crystalline specimen c , not shown here, indicate enriched concentrations of Cu and Dy at 81.1 and 7.6 at%, respectively, while the Hf concentration is 0.7 at%.

3.6 Discussion

Amorphous $\text{Cu}_{75}\text{Hf}_{20}\text{Dy}_{05}$ was produced by melt spinning as verified by both XRD and TEM diffraction. The amorphous melt spun ribbon was shown to devitrify to a single crystalline phase of structure type $\text{Cu}_{51}\text{Hf}_{14}$. The two $\text{Cu}_{75}\text{Hf}_{20}\text{Dy}_{05}$ alloy conditions, amorphous and crystalline, were then compared using a variety of electrochemical techniques to explore the effect of the structure change, from disordered amorphous to ordered crystalline, on the corrosion properties in HF solution in a situation where neither material was passive.

The cyclic polarization behavior indicates and the potentiostatic polarization results further substantiate that Hf undergoes preferential dissolution from the $\text{Cu}_{75}\text{Hf}_{20}\text{Dy}_{05}$ matrix at potentials below the Cu OCP. Dy is fully passive over the measured potentials and is thermodynamically likely to form a DyF_3 species at a slightly less acidic pH than in the bulk 0.1 M HF solution. Post corrosion SEM analysis by EDS found surface particles consisting of Dy and F. The cyclic polarization of Cu in 1 M HF solution, Figure 3.6, shows limited Cu passivation brought about by a salt film at anodic potentials. Similar behavior is seen in amorphous and crystalline $\text{Cu}_{75}\text{Hf}_{20}\text{Dy}_{05}$ although at a suppressed potential.

The limiting current density of Hf dissolution determined the polarization scans is much lower than its mass transport limited current density. In 0.1 M HF solution, the limited current density is 0.01 A/cm^2 while in 1 M HF solution it is higher at 0.1 A/cm^2 and is considerably less stable undergoing current density transients. The current instability gives evidence for a current that is limited by a dissolving film, likely HfF_4 ,

instead of more typical mass transport limiting current density. In the 1 M HF solution the concentration of HF species in solution is a factor of 5 times higher than in 0.1 M HF solution. According to the HF oxidation reaction shown in Equation 3.1, an increase in HF concentration increases the concentration of molecular HF in solution and would increase the rate of the reaction. One plausible corrosion mechanism limiting the Hf dissolution rate would be the Hf oxidizing to the HfF_4 phase which likely has only limited solubility. The dissolution of this film is then the rate limiting mechanism. Optical micrographs after the cyclic polarization measurements of the high purity polycrystalline Hf specimen, not shown here, support this view and show evidence of a pitting-like corrosion mechanism.

3.6.1 Behavior During Preferential Hf dissolution

At potentials below the Cu OCP, The total current can be broken down into the negative cathodic HER on Cu and the two positive oxidation reactions: Hf dissolution and Dy passivation. As the cathodic current density increases, the surface becomes enriched in Cu. Thus the surface layer has a higher proportion of Cu atoms increasing the number of available Cu cathodic reaction sites. The oxidation reactions would then occur over less surface area and the overall reaction becomes more cathodic. The increased cathodic current densities were seen in the cyclic voltammetry experiments below the Cu oxidation potential (Figure 3.8).

In the case of the cyclic voltammetry experiments below the Cu OCP, summarized in Figure 3.9, the current density for both amorphous and crystalline $\text{Cu}_{75}\text{Hf}_{20}\text{Dy}_{05}$ becomes increasingly cathodic, dominated by HER on Cu [30], as the

cycles increase indicating Hf dissolution and Cu enrichment. The increase in cathodic current densities exhibited by the amorphous structure indicates more complete Cu enrichment in the surface compared to the crystalline structure. The difference in the steady current density values, reached between cycle 15 and 20, likely arises due to more complete dissolution of the surface layer in the amorphous structure; whereas for the crystalline structure if the Hf dissolution is significantly slower, the Hf anodic reaction can still occur leading to the less cathodic current density. During the OCP hold prior to polarization in 0.1 M and 0.1 M HF solution, there were stronger spikes to more negative potentials in the amorphous specimen in 0.1 M HF solution. In the higher concentration HF solution the more pronounced negative potential spikes occurred in both the amorphous and crystalline state.

Similar behavior was seen in the potentiostatic polarization experiments at $-150 \text{ mV}_{\text{SCE}}$. In Figure 3.18, the amorphous and crystalline states are initially cathodic over the first 2000 s with the amorphous specimen having a higher cathodic current density. After the initial period of cathodic current density, the amorphous alloy undergoes large transient current spikes to anodic current densities. These current spikes are most likely due to sustained Hf dissolution from the matrix. In the larger exposure area experiments, a cathodic current region was observed for both amorphous and crystalline states, Figure 3.19. In the case of the amorphous states, the current density very rapidly increased to anodic currents, while for the crystalline specimens the cathodic current region had longer duration and the anodic current rise was slower. The total anodic accumulated

charge was substantially less for the crystalline state than for the amorphous state, shown at 3600 s and 7200 s in Figure 3.22.

SEM micrographs show no coarsening of the pores as exposure time, and charge, increases in the amorphous state. In the crystalline condition, at much slower comparative time scales, a porous structure is also formed. The surface, in the crystalline state (Figure 3.26), is significantly less uniform and shows smaller pore size. The post exposure XRD spectra show that structural reorganization occurs in both amorphous and crystalline $\text{Cu}_{75}\text{Hf}_{20}\text{Dy}_{05}$. It takes the crystalline state significantly longer duration exposures to significantly selectively dissolve Hf enough to enable structural reorganization to FCC Cu than for the amorphous state.

Analysis of the dealloyed cross sections confirmed that the dealloyed layer thickness was proportional to the measured charge during the potentiostatic polarization experiments. Both the amorphous and crystalline states have the same charge efficiency, 2.04 μm of Hf dealloyed by 1 C/cm^2 . The dealloyed layer thickness is reasonably well predicted by calculations using Faraday's Law, shown in Table 3.2, which assumes 4 electron oxidation of Hf and uses basic assumptions about the density. As was indicated by the charge calculations from the exposure experiment and the XRD spectra, the dealloyed layer growth was substantially slower for the amorphous solid solution alloy than the crystalline alloy. Figure 3.25 and 3.26 confirmed that through thickness porosity was present in the dealloyed layer for both the amorphous and crystalline structures. The cross section morphology of the dealloyed layers indicates that a less uniform porous structure forms in the crystalline specimen than in the amorphous specimens.

3.6.2 Dealloying Mechanism: The Role of Surface Diffusion

Dealloying to form nanoporous structures is typically controlled by diffusion processes. In a binary solution of more noble, MN, and less noble, LN, atoms, as the surface LN atoms dissolve the surface reorganizes via surface diffusion to islands of the equilibrium MN structure [31]. Meanwhile bulk diffusion of LN atoms from the matrix to the dealloyed layer interface also occurs. Typically, under STP conditions, dealloying is controlled by the rate of surface diffusion of the MN atoms during island formation as bulk diffusion is typically much too slow to be a dominant factor [32]. The influence of minor alloying elements on the surface diffusion has been shown to have a measurable effect on the porosity formation during dealloying [21].

In the $\text{Cu}_{75}\text{Hf}_{20}\text{Dy}_{05}$ -HF solution system, Hf is preferentially dissolved. As dissolution of the LN Hf atoms occurs, the MN Cu atoms reorganize to the equilibrium FCC structure (Figure 3.23-3.24). It is likely under these conditions that bulk diffusion is not a significant factor. Indeed, EDS spectra of the dealloyed layer cross sections did not indicate a gradient in species concentration (Figure 3.30). As the surface reorganizes to FCC Cu, porosity develops in the dealloyed layer allowing solution penetration through the dealloyed layer thickness to the dealloyed layer-matrix interface. It is likely that this process is controlled by the surface diffusion of the Cu atoms and the mechanistic reasoning underlying the behavior of the crystalline structure compared to the amorphous solid solution structure lies in the difference between the surface diffusion rates of the two alloys. The resulting morphology indicates that the pore size is larger and more

uniformly distributed in the case of the amorphous solid solution initial structure and that the dealloying process occurs more quickly.

The preferential dissolution can be divided into two stages: initial dealloying, surface reorganization of the MN atoms to form FCC Cu and propagation of the dealloying front through the thickness of the parent ribbon. In each stage, the effect of the structural difference between the amorphous solid solution alloy and the crystalline alloy will be discussed.

Dissolution of an atom from a surface involves the cleaving of bonds, which in this case is the removal of the Hf atoms from its neighboring atoms. In an amorphous structure there exists a distribution of nearest neighbor atoms and a corresponding distribution of binding energies of Hf atoms, while in a crystalline structure there is a periodic arrangement of atoms leading to discrete binding energies of Hf atoms. In Figure 3.31, discrete activation energy for surface mobility from kinks and terraces compared to a continuum of activation energy is illustrated. It is likely that regions in the amorphous alloy have Hf atoms that are more weakly bonded than the weakest bond in the crystalline structure. These regions would include a higher density of weaker bonds, e.g., Hf atoms with numerous nearest neighbor Hf atoms, would be more likely to dissolve, while a reduced density of stronger bonds such as atoms surrounded mostly by Cu and Dy. would be less likely to dissolve under these electrochemical conditions. In an amorphous disordered solid solution, the bond types and the associated energies for each Hf atom will be less uniform than a crystalline alloy with the same composition.

Therefore, there should be local regions where dissolution of Hf should be increased in the amorphous alloy compared to the crystalline structure.

As the Hf atoms dissolve from the matrix, Cu and Dy are enriched and the Cu atoms reorganize into FCC Cu and the volume reduction leads to porosity. The formation of the MN Cu equilibrium structure requires surface diffusion of the Cu atoms. It is reasonable to conclude that the surface diffusion is faster on the amorphous matrix than the crystalline matrix. Several experimental observations substantiate this claim. The regular spacing of larger pores developed in the amorphous solid solution alloy during dealloying indicates that an equilibrium distribution is more easily achieved in the amorphous structure compared to the crystalline structure. The larger pore size enhances the solution penetration through the porosity further increasing the dissolution rate of Hf from the matrix. However, there is no evidence of the pore size increasing during the exposure time in the crystalline alloy which should happen if a uniform distribution of larger pores is a low energy state (Figure 3.27). Thus, some feature of the crystalline structure is impeding the surface diffusion of Cu atoms. Likely the effect of the more regular spacing of the Dy atoms in the crystalline structure (substituted on Hf lattice sites in the $\text{Cu}_{51}\text{Hf}_{14}$ structure) leads to impediments to surface diffusion of Cu. There is no Dy solubility in Cu [32], however there is no indication of secondary phases in the XRD, although that is not necessarily expected even with enriched Dy to 5-10 at% in the dealloyed region due to the large x-ray penetration depth.

Surface diffusion of adatoms on amorphous alloys has not been studied in any detail except on amorphous silicon due to its use in microelectronic and catalytic

functions [33, 34]. Surface defects on crystalline surface have characteristic activation energy for surface diffusion such as steps, kinks or islands [35]. The surface diffusion of Si was analyzed theoretically by assuming various effective activation barriers with distance resulting in increased short range surface diffusion [36]. A continuum activation energy model was also used to describe the formation of mobile species (Figure 3.31) calculations were made that show a 2 order magnitude decrease in the surface mass self-diffusion pre-factor and an activation energy approximately in line with the lower bound expected mass transfer the highest measured for crystalline silicon [33]. More recent work used simulations to determine the underlying diffusion mechanism in amorphous Si consisting of many atoms diffusing a comparatively short distance, 2-3 pm, at shorter time scales compared at short time scales compared to crystalline diffusion [37]. The amorphous Si, despite being covalently bonded, provides a compelling argument that amorphous surface diffusion is fundamentally different than on crystalline surfaces. In the present context, surface diffusion consisting of large numbers of MN atoms moving short distances could expedite dissolution of the LN Hf atoms by decreasing the bond strength of Hf atoms leading to increased dissolution rates in the case of the amorphous solid solution dissolution structure.

An alternative interpretation is that the periodic atomic structure in crystalline alloys is inherently less susceptible to Hf dissolution than the amorphous alloy due to its periodic arrangement of MN atoms that inhibit dissolution. If that were true, the EDS analysis of the dealloyed crystalline alloy would indicate increased Hf (relative to the amorphous dealloyed region.) It is more likely this effect plays a role in the initial

dissolution of the alloy, but surface diffusion of the Cu atoms is the dominant effect at longer times.

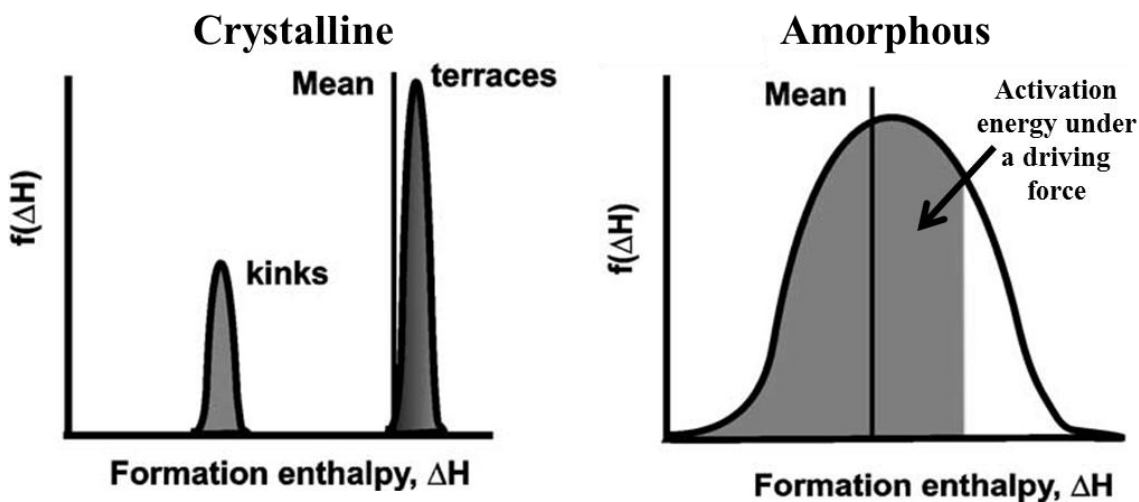


Figure 3.31. Distribution functions for mobile atom formation enthalpies on crystalline and amorphous materials under a given driving force (T , or in this case applied potential). Adapted from [34], with permission from Elsevier BV.

3.6.3 Behavior during Cu and Hf dissolution

Polarizing at potentials above the Cu OCP leads to both Hf and Cu dissolution and interesting comparative behavior in amorphous and crystalline $\text{Cu}_{75}\text{Hf}_{20}\text{Dy}_{05}$. In this potential range both Cu and Hf dissolution is observed, but the Cu dissolution rate is substantially higher than Hf dissolution. Dy over this potential range is a beneficial passivating alloying addition. Both the amorphous and crystalline specimens in the cyclic polarization measurements show an active nose followed by film formation and transient events at higher potentials. The behavior of the amorphous and crystalline specimens was further elucidated using rapid cyclic voltammetry across the Cu dissolution potential. The fast scan rate allows for characterization of the evolution of the surface during the initial stages of Cu dissolution and the overall charge behavior as cycle number increases.

During the first 4 cycles, Figure 3.11, at potentials around 200 mV_{SCE}, the amorphous and crystalline specimens both show an active current nose before the current density decreases to lower, but still active currents. The amorphous specimen has more numerous and larger, in terms of charge, transient current spikes after the current nose than the crystalline alloy. Also, more generally, the current density is higher for the amorphous specimen than the crystalline sample for each comparative cycle. Subsequent cycles lack the current density transients present in the initial cycles, but continue to show key differences between the behavior of the amorphous and crystalline states. The integrated charge per cycle, Figure 3.17, shows the amorphous solid solution alloy continuing to have higher current density per cycle than the crystalline alloy. During the first 10 cycles, dissolution in the amorphous alloy occurs at rates at or above the dissolution current density of high purity Cu. Over the same time frame, dissolution in the crystalline alloy decays to very low current densities. Interestingly, for both amorphous and crystalline alloys the anodic charge decays to values below the Hf dissolution current density.

The current density transients in the amorphous alloy correspond to surface dissolution of about 6-12 monolayers assuming the dissolution were over the entire surface. It is more likely smaller regions experienced a spike in dissolution current density resulting in dissolution locally in excess of the 12 monolayers. As was discussed for the case of the preferential dissolution of Hf atoms from the matrix, dissolution of regions of Cu lacking passivating Dy or Hf atoms which serve as dissolution rate moderators due to its slower dissolution rate would result in spikes of current as these

regions are revealed during dissolution. In the crystalline alloy, the beneficial elements are periodically distributed and the solute lean regions do not exist. The fact that the overall current density was lower for the crystalline structure compared to the amorphous solid solution alloy can be explained by similar arguments.

3.7 Conclusions

For both amorphous and crystalline $\text{Cu}_{75}\text{Hf}_{20}\text{Dy}_{05}$ corroded in HF solution, Hf preferentially dissolves in polarization conditions below the Cu oxidation potential, and the dealloyed region reorganizes to form FCC Cu. This process occurs much more slowly and the pores are less uniform with a smaller diameter in the case of the crystalline structure. The increase in dealloying rate in the amorphous state suggests that dissolution of Hf occurs more easily from the amorphous solid solution alloy. An increase in surface diffusion rate of Cu on the amorphous solid solution alloy is likely due to the lower activation energy barrier for surface diffusion due to the amorphous structure. This results in the increased rate of dissolution by increasing solution penetration via channels and subsequent weakening of the atomic bonding of the Hf atoms at the dissolution front.

At higher potentials, Cu also dissolves from the matrix. In this case, the amorphous alloy sustained higher current density distributions and an increase in current density transients. These results indicate that the crystalline structure slows the dissolution rate of Cu from the matrix. Possible mechanistic causes of this behavior include regular spacing of beneficial solute elements that moderate dissolution, Hf, or are passivating, Dy.

3.8 References

1. Campestrini, P., et al., *Relation between microstructural aspects of AA2024 and its corrosion behaviour investigated using AFM scanning potential technique*. Corrosion Science, 2000. **42**(11): p. 1853-1861.
2. Ilevbare, G.O., et al., *In situ confocal laser scanning microscopy of AA 2024-T3 corrosion metrology - I. Localized corrosion of particles*. Journal of the Electrochemical Society, 2004. **151**(8): p. B453-B464.
3. Williams, D.E., T.F. Mohiuddin, and Y.Y. Zhu, *Elucidation of a trigger mechanism for pitting corrosion of stainless steels using submicron resolution scanning electrochemical and photoelectrochemical microscopy*. Journal of the Electrochemical Society, 1998. **145**(8): p. 2664-2672.
4. Scully, J.R. and A.M. Lucente, *Corrosion of Amorphous Metals*, in *ASM handbook*, C. S.D. and J. Covino, B.S., Editors. 2005, ASM International: Materials Park, OH. p. 476-489.
5. Huang, R., et al., *Localized Corrosion Resistance of Fe-Cr-Mo-W-B-C Bulk Metallic Glasses Containing Mn plus Si or Y in Neutral and Acidified Chloride Solutions*. Corrosion, 2010. **66**(3): p. -.
6. Scully, J.R., A. Gebert, and J.H. Payer, *Corrosion and related mechanical properties of bulk metallic glasses*. Journal of Materials Research, 2007. **22**(2): p. 302-313.
7. Aburada, T., et al., *Effect of Ni as a minority alloying element on the corrosion behavior in Al-Cu-Mg-(Ni) metallic glasses*. Scripta Materialia, 2008. **58**(8): p. 623-626.
8. Hashimoto, K., et al., *Characteristics of passivity of extremely corrosion-resistant amorphous iron alloys*. Corrosion Science, 1976. **16**(2): p. 71-76.
9. Huerta, D. and K.E. Heusler, *Influence of Crystallization of Glassy Co75b25 on Its Dissolution Rates in Acid Sulfate-Solution*. Journal of Non-Crystalline Solids, 1983. **56**(1-3): p. 261-266.
10. Naka, M., K. Hashimoto, and T. Masumoto, *Corrosion Behavior of Amorphous and Crystalline Cu50ti50 and Cu50zr50 Alloys*. Journal of Non-Crystalline Solids, 1978. **30**(1): p. 29-36.
11. Naka, M., K. Hashimoto, and T. Masumoto, *Effect of Heat-Treatment on Corrosion Behavior of Amorphous Fe-Cr-P-C and Fe-Ni-Cr-P-B Alloys in In Hcl*. Corrosion, 1980. **36**(12): p. 679-686.
12. Tong, H.S., *The Corrosion Behavior of a Ni Based Amorphous Alloy - the Effect of Devitrification*. Corrosion, 1985. **41**(1): p. 10-12.
13. Turn, J.C. and R.M. Latanision, *The Influence of Structure on the Corrosion of Glassy Copper-Zirconium Alloys*. Corrosion, 1983. **39**(7): p. 271-279.
14. Wang, Z.M., et al., *Structure inhibited pit initiation in a Ni-Nb metallic glass*. Corrosion Science, 2010. **52**(4): p. 1342-1350.
15. Parks, B.W., J.D. Fritz, and H.W. Pickering, *The Difference in the Electrochemical-Behavior of the Ordered and Disordered Phases of Cu3au*. Scripta Metallurgica, 1989. **23**(6): p. 951-956.

16. Renner, F.U., et al., *In situ x-ray diffraction study of the initial dealloying and passivation of Cu₃Au(111) during anodic dissolution*. Physical Review B, 2008. **77**(23): p. -.
17. Ding, Y., M.W. Chen, and J. Erlebacher, *Metallic mesoporous nanocomposites for electrocatalysis*. Journal of the American Chemical Society, 2004. **126**(22): p. 6876-6877.
18. Koh, S. and P. Strasser, *Electrocatalysis on bimetallic surfaces: Modifying catalytic reactivity for oxygen reduction by voltammetric surface dealloying*. Journal of the American Chemical Society, 2007. **129**(42): p. 12624.
19. Hakamada, M. and M. Mabuchi, *Preparation of nanoporous Ni and Ni-Cu by dealloying of rolled Ni-Mn and Ni-Cu-Mn alloys*. Journal of Alloys and Compounds, 2009. **485**(1-2): p. 583-587.
20. Hayes, J.R., et al., *Monolithic nanoporous copper by dealloying Mn-Cu*. Journal of Materials Research, 2006. **21**(10): p. 2611-2616.
21. Aburada, T., J.M. Fitz-Gerald, and J.R. Scully, *Synthesis of nanoporous copper by dealloying of Al-Cu-Mg amorphous alloys in acidic solution: The effect of nickel*. Corrosion Science, 2011. **53**(5): p. 1627-1632.
22. Abe, H., et al., *Dealloying of Cu-Zr-Ti Bulk Metallic Glass in Hydrofluoric Acid Solution*. Materials Transactions, 2009. **50**(6): p. 1255-1258.
23. James, W.J., J.W. Johnson, and M.E. Straumanis, *The difference effect and anodic behavior of hafnium dissolving in hydrofluoric acid*. Corrosion Science, 1963. **3**(4): p. 273-279.
24. Craig, B.D., *Handbook of corrosion data*. 2nd ed. Materials data series. 1995, Materials Park, OH: ASM International. xi, 998 p.
25. *CRC handbook of chemistry and physics*. 1999, Chapman and Hall/CRCnetBASE: Boca Raton, FL.
26. Puigdomenech, I., *MEDUSA: Make Equilibrium Diagrams Using Sophisticated Algorithms*. 2009: Stockholm, Sweden.
27. James, W.J., W.G. Custead, and M.E. Straumanis, *Dissolution rates, electrochemical and passivation properties of alpha Zr---O solid solutions in HF*. Corrosion Science, 1962. **2**(4): p. 237-254.
28. Rickard, C.E.F. and T.N. Waters, *The hafnium tetrafluoride-water system*. Journal of Inorganic and Nuclear Chemistry, 1964. **26**(6): p. 925-930.
29. Gabathuler, J.P., P. White, and E. Parthe, *Zr₁₄cu₅₁ and Hf₁₄cu₅₁ with Gd_{3.6} Structure Type*. Acta Crystallographica Section B-Structural Science, 1975. **B 31**(Feb15): p. 608-610.
30. Pourbaix, M., *Atlas of electrochemical equilibria in aqueous solutions*. 1974, National Association of Corrosion Engineers: Houston, Tex. p. 183-197, 230-233, 384-392.
31. Erlebacher, J., *An atomistic description of dealloying - Porosity evolution, the critical potential, and rate-limiting behavior*. Journal of the Electrochemical Society, 2004. **151**(10): p. C614-C626.
32. Subramanian, P.R. and D.E. Laughlin, *The Cu-Dy (Copper-Dysprosium) System*. Bulletin of Alloy Phase Diagrams, 1988. **9**(3a): p. 331-408.

33. Dalton, A.S., D. Llera-Hurlburt, and E.G. Seebauer, *Surface diffusion kinetics on amorphous silicon*. Surface Science, 2001. **494**(1): p. L761-L766.
34. Llera-Hurlburt, D., A.S. Dalton, and E.G. Seebauer, *Temperature-dependent surface diffusion parameters on amorphous materials*. Surface Science, 2002. **504**(1-3): p. 244-252.
35. Stoltze, P., *Simulation of Surface-Defects*. Journal of Physics-Condensed Matter, 1994. **6**(45): p. 9495-9517.
36. Avramov, I., *Diffusion on amorphous substrates*. Journal of Physics-Condensed Matter, 1999. **11**(25): p. L267-L272.
37. Dalton, A.S., Y.V. Kondratenko, and E.G. Seebauer, *Diffusion mechanisms on amorphous silicon surfaces*. Chemical Engineering Science, 2010. **65**(6): p. 2172-2176.

4 The Role of Composition and Structure during Dissolution and Passivity/Breakdown in Fe_{1-x}Pd_x alloys

4.1 Abstract

This chapter includes a brief introduction to the Fe-Pd binary alloy system. The basic electrochemical thermodynamics of the Fe-Pd-H₂O system is presented including the effects of H₂O-Cl⁻ environment. In particular, Fe₅₀Pd₅₀ can form ordered and disordered crystalline structures without compositional difference between the phases. The specific metallurgical and electrochemical properties of the Fe-Pd alloy system makes it an ideal model alloy system to study the effect of structure on active corrosion dissolution. This chapter surveys the electrochemical behavior of alloyed Fe and Pd at three different compositions in order to better focus the study of the equiatomic Fe₅₀Pd₅₀ in Chapters 5 and 6.

The effect of Pd alloying is investigated using a series of Fe_{1-x}Pd_x: x=30, 35, and 50 at% alloys. These results will also be discussed in relation to the structural and compositional change in alloys. A survey of electrochemical behavior was conducted in neutral, alkaline and acidic Cl⁻ containing environments. The effect of Pd as a beneficial solute in terms of immunity as well as increased passivity, localized corrosion resistance, and resistance to dealloying will be discussed. A comparison of the breakdown potentials shows no clear correlation to the change in structure. Dealloying Fe₇₀Pd₃₀ occurs in acidic HCl solution, but bulk preferential dissolution of Fe was not observed in either of the higher Pd content alloys. Conditions are identified for the study of Fe₅₀Pd₅₀ in two structural states of the same composition where structure dependent corrosion behavior is observed.

4.2 Introduction

Fe-Pd alloys exhibit fundamentally interesting magnetic behavior. Martensitic twins at low Pd alloying contents are highly dependent on the applied magnetic field leading to controlled shape memory behavior [1]. At higher Pd concentrations, the ferromagnetic $L1_0$ phase has high magnetocrystalline anisotropy [2]. Fe-Pd alloys also show high biocompatibility and low corrosion rates in biological applications. Engineering material applications of these alloys make use of the biocompatibility, corrosion and magnetic properties. A shape memory alloy, $Fe_{70}Pd_{30}$, has been studied for use in dentistry, specifically orthodontic wire where both the shape memory properties and an increase in biocompatibility are sought [3]. Fe-Pd films have been shown to increase the biocompatibility of 316L implants through reduced corrosion and a lack of toxicity [4]. In biological implantations the $Fe_{70}Pd_{30}$ alloy causes less tissue swelling than more typical Ni-Ti shape memory alloys. In contrast, Ni is generally regarded as a toxic biomaterial with harmful systemic effects [5, 6].

The Fe-Pd system provides a model alloy system to study the effect on corrosion properties of

- a) Composition in terms of Pd alloying,
- b) The influence of structure in phases of the same composition where the effect of structure can be isolated from that of composition.

A wide range of compositions can all form a disordered cubic structure γ -phase. The $Fe_{50}Pd_{50}$ composition can form both the disordered cubic structure and an ordered

tetragonal structure at room temperature. At low amounts of Pd alloying bcc, bct and fct martensite can be formed.

In this chapter, the metallurgical and electrochemical properties of the Fe-Pd binary system will be introduced. The effect of Pd alloying, at concentrations of 30, 35 and 50 at% Pd, on electrochemical corrosion properties will be discussed. The concomitant structural change will also be investigated; Fe₇₀Pd₃₀ has a martensitic bct structure, while Fe₆₅Pd₃₅ and Fe₅₀Pd₅₀ both have a disordered fcc structure. The role of structural change without compositional variation between structural states in Fe₅₀Pd₅₀ will be introduced and discussed in detail in Chapters 5 and 6.

4.2.1 Fe_xPd_{1-x} Alloy Production and Synthesis

The Fe-Pd binary phase diagram is shown in Figure 4.1. The high temperature γ -phase is a disordered fcc solid solution. The γ -phase has space group Fm-3m and lattice parameter $a=0.3804$ nm [7]. Each lattice has site occupancy factors (SOF) equivalent to the atomic ratio, 0.5:0.5 for Fe₅₀Pd₅₀ and 0.65:0.35 for Fe₆₅Pd₃₅. The L1₀ phase has an ordered pT structure.

The order-disorder transformation in Fe₅₀Pd₅₀ is a first order transformation that proceeds by a nucleation and growth mechanism [8]. The γ to L1₀ phase transformation involves a lattice expansion in the a and b direction and slight contraction in the c direction as the Pd atoms occupy the $c = \frac{1}{2}$ lattice positions. The L1₀ lattice constants are $a=0.852$ nm and $c=0.3723$ nm. The lattice strain that accompanies this transformation gives rise to a polytwinned microstructure [9]. The two equiatomic phases will be discussed in more detail in Chapter 5. Both phases are readily produced through water

quenching, at the temperatures indicated by the solid circles in Figure 4.1. To achieve an equilibrium disordered γ -phase, $\text{Fe}_{50}\text{Pd}_{50}$ is heat treated above the 2-phase field of γ and L1_0 then water quenched to prevent crystallization to the lower temperature phases, α and L1_0 . Similarly, annealing at the eutectoid temperature in the single phase L1_0 region followed by quenching produces a fully ordered $\text{Fe}_{50}\text{Pd}_{50}$. Quenching $\text{Fe}_{65}\text{Pd}_{35}$ (solid square, Figure 4.1) retains the γ -phase structure, while quenching $\text{Fe}_{70}\text{Pd}_{30}$ (solid square, Figure 4.1) leads to a phase transformation to form a martensitic phase. The structures are summarized in Table 4.1.

The phase transformation of Fe-Pd binary alloys with Pd concentrations between 23 and 33% have been of particular interest due to the martensitic phase formation from the austenitic parent phase [10]. Martensitic phases maintain the composition of the parent phase and for this composition is disordered. The transformation is diffusionless and instead involves cooperative short range atom motion to accommodate an invariant plane strain [11]. Martensitic phases are metastable non-equilibrium phases and have higher energy than the corresponding equilibrium phase. Additionally, twin boundaries are often high strain energy boundaries which lead to preferential etching commonly seen in martensitic alloys.

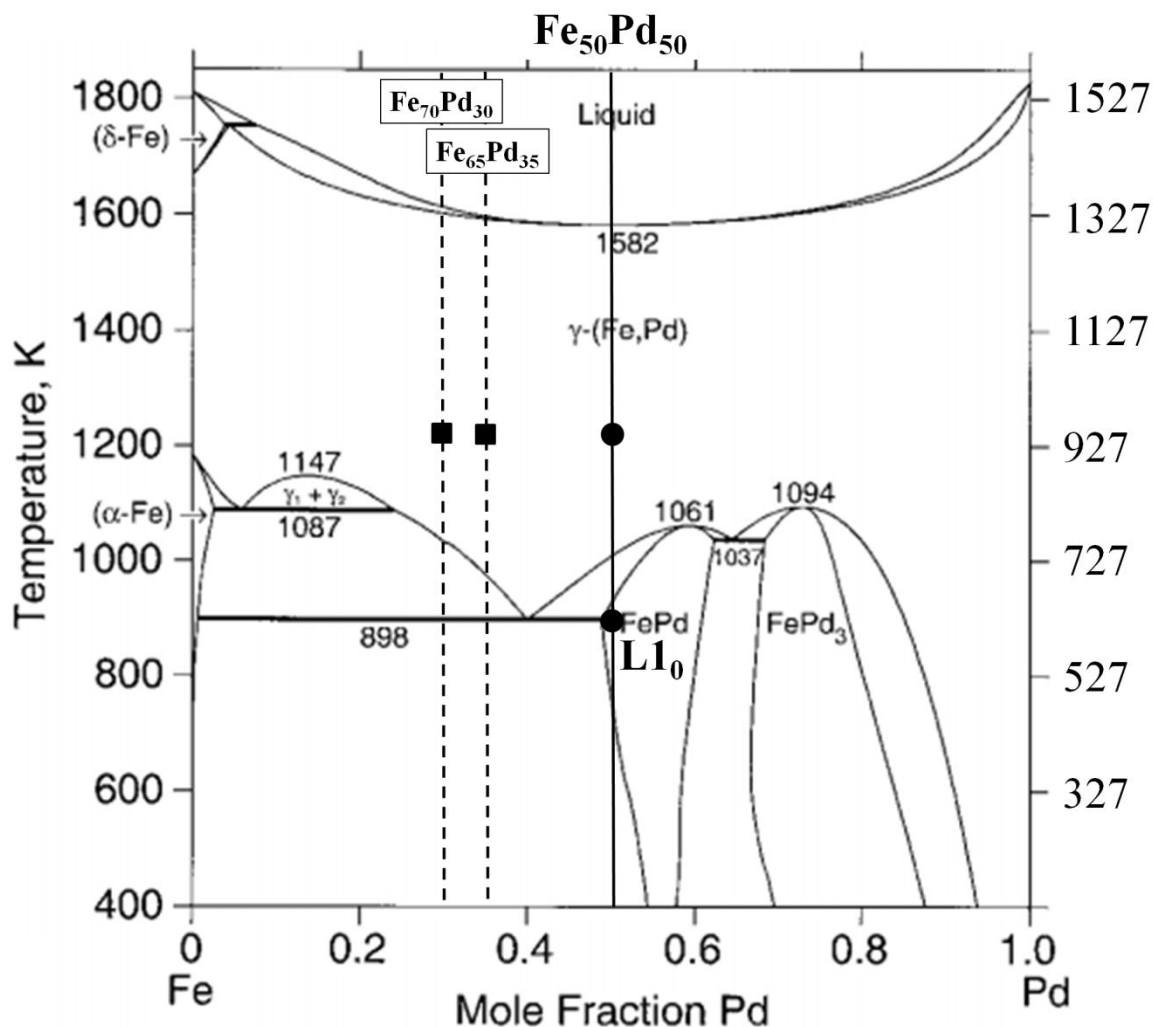


Figure 4.1. Fe-Pd binary phase diagram. The solid line indicates the equiatomic Fe₅₀Pd₅₀ composition and the marked solid circles indicate, at 898 K (625 °C), the ordered L1₀ structure and the high temperature austenite, γ , disordered fcc phase. Earlier versions of the phase diagram show a slight variation in the eutectoid temperature at 878 K (605 °C) [12]. The dashed lines indicate the Fe₇₀Pd₃₀ and Fe₆₅Pd₃₅ compositions. The solid squares indicate the annealing temperature for the disordered fcc phase (Fe₆₅Pd₃₅) and the bct martensite (Fe₇₀Pd₃₀).

Martensitic transformations in this composition range were studied on thin films in a series of work by Oshima et. al. [10, 13-15]. Oshima and coworkers found that at Pd concentrations less than about 32% martensitic transformations take place from the

austenitic γ -phase: At concentrations less than 27%, the γ -phase undergoes a martensitic transformation to bcc martensitic, between 27% and 30% there is a 2 step martensitic transformation first to the fct martensite then the bct martensite, and at concentrations between 30 and 32% the fcc phase transforms to a martensitic fct phase [14]. The lattice parameters for the bct phase were determined to be 0.296 and 0.300 nm for a and c, respectively [14]. The microstructure of the fct phase showed ‘cleanly’ twinned grains while the bct phase showed a mix of the ‘cleanly’ twinned and vertical and horizontal lath regions. The bcc martensite microstructure shows only the latter microstructure. The $\text{Fe}_{70}\text{Pd}_{30}$ (solid square) γ -phase undergoes a martensitic phase transformation to a bct martensite, but there is some ambiguity in what type of martensite is formed.

Table 4.1. Phase, composition and structure for $\text{Fe}_{1-x}\text{Pd}_x$ alloys.

Phase	Composition	Structure	Lattice Parameter (nm)	Density (g/cm^3)
martensite	$\text{Fe}_{70}\text{Pd}_{30}$	bcc	a=0.296, c=0.300	8.912
γ -phase	$\text{Fe}_{65}\text{Pd}_{35}$	fcc	a=0.380	8.874
γ -phase	$\text{Fe}_{50}\text{Pd}_{50}$	fcc	a=0.380	9.790
L1_0	$\text{Fe}_{50}\text{Pd}_{50}$	pT	a=0.852, c=0.372	9.755

4.3 Electrochemical Characteristics of the Fe/Pd - H_2O system and the Effect of Cl^-

A $\text{Fe}_{50}\text{Pd}_{50}$ alloy combines two elements of very different electrochemical nobility Pd has high nobility and shows dissolution only at low pH and high potential. Fe is generally passive in alkaline solutions, while at low pH no passive layer forms to inhibit dissolution [16]. This combination of nobility provides opportunities to study the corrosion behavior in a wide variety of electrochemical situations including situations where both elements are predicted to dissolve or both form passive oxides. Moreover, several intermediate cases may be investigated such as the case where one element is

stable its zero valence state while the other is active, one element is passive and one element is active, etc. A few of these conditions will be described in some detail below in a general Fe/Pd-H₂O case. The role of Cl⁻ in terms of promoting dissolution through complexation and also through absorption will be introduced.

The equilibrium potential-pH diagrams for both Fe and Pd (overlaid) are shown in Figure 4.2. The corresponding oxide stability diagram for Fe is shown in Figure 4.3. For example, at low pH the alloy can be tested in conditions under which Fe is thermodynamically favored to dissolve to Fe²⁺ or Fe³⁺ yet no oxide is formed on Pd. Thus, the structural dependence of Pd atoms to inhibit dissolution of Fe to various oxidation states can be explored on the structure of the alloy (Especially in the case of Fe₅₀Pd₅₀ where there is no composition variation between the disordered fcc and pT structure.) Preferential Fe dissolution is especially possible at pH below 8.

At higher pH, passivity and breakdown can be explored. Fe is most easily forms a passive layer at pH 11 where a minimum concentration of species is required for formation of Fe(OH)₂, see diagram, Figure 4.3. Pd forms an oxide across nearly all pH at elevated potentials. The oxide stability diagram (Figure 4.3) shows that at low pH Fe₂O₃ is the dominant oxide. However, the oxide is stable only at higher potentials and an active-passive transition can be expected for Fe.

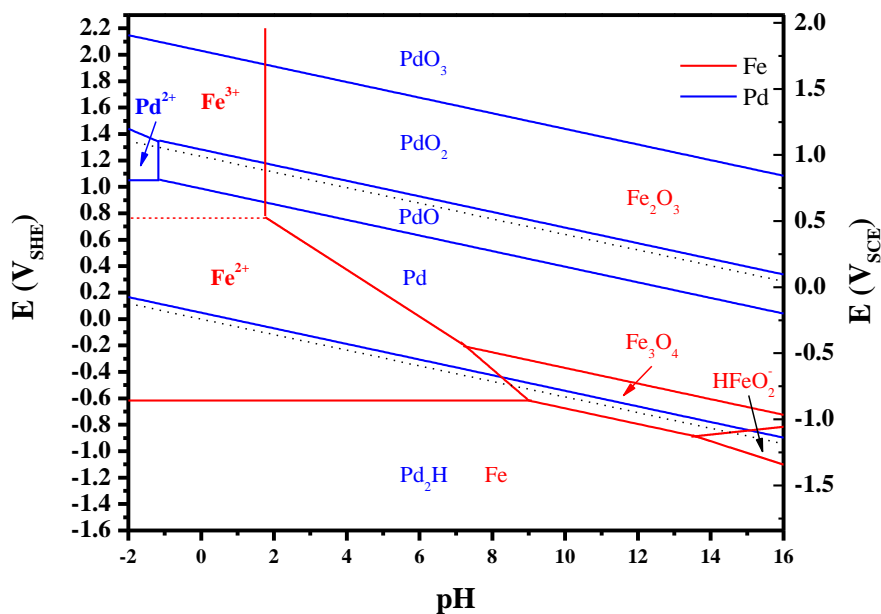


Figure 4.2. Combined Fe-Pd potential-pH equilibrium diagram for Fe/Pd -H₂O system at 25°C and ion concentrations assumed to be 10⁻⁶ [16]. For the Fe and Pd system non-hydroxides are considered. Note the Fe diagram is actually curved at the intersection between the Fe²⁺, Fe³⁺ and Fe₂O₃ species.

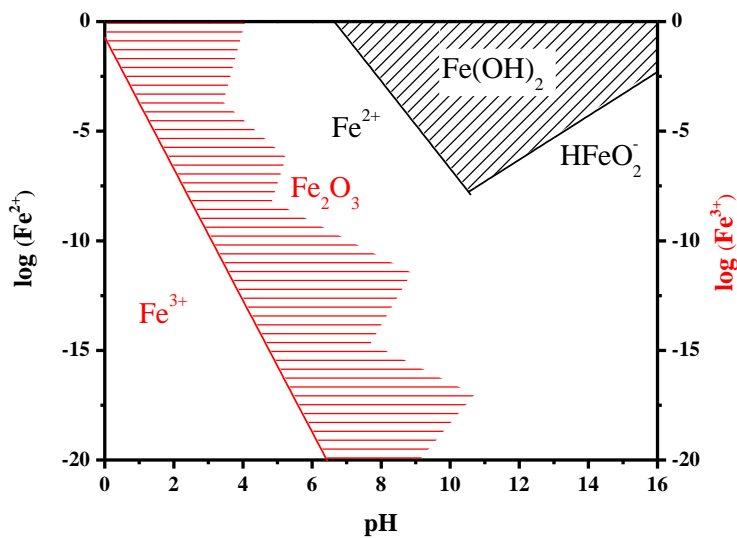


Figure 4.3. Fe Oxide Stability Diagram for Fe₂O₃ (red, right axis) and Fe(OH)₂ (black, left axis) at 25°C and considering only Fe-H₂O system [16]. The oxide stability shows that at low pH Fe₂O₃ is the dominant oxide but only at high potentials where Fe³⁺ is the stable species. At high pH the minimum concentration required for formation of the Fe(OH)₂ is at pH 11.

4.3.1 Chloride Complexation and Absorption

The formation of complex between metal ions and solution species often allows thermodynamically predicted dissolution in conditions (pH, potential) where dissolution is not expected without these considerations.⁹ In Cl^- solutions, Pd forms a complex, PdCl_4^{2-} , at low pH. The formation of the complex decreases the thermodynamically stable PdO region and broadens the Pd^{2+} region of stability as a Cl^- complex, PdCl_4^{2-} . The stable region for PdCl_4^{2-} is shown in Figure 4.2 for 1, 0.1 and 0.01 M $[\text{Cl}^-]$ as indicated by the shaded regions. In 1 M Cl^- , the expected dissolution potential decreases from 0.8 V_{SHE} (in 0 M Cl^- , dissolution to Pd^{2+}) to 0.3 V_{SHE} (0.55 to 0.05 V_{SCE}). Over the same concentrations, the upper pH range prior to the development of passivity increases from 0.9 to 9.2.

Another aspect resulting from the presence of Cl^- is the absorption of Cl^- into the oxide is thermodynamically favored. The primary change in the potential-pH equilibrium diagram (Figure 4.2) is the change in the stable oxide from Fe_2O_3 to $\text{Fe}(\text{OH})_{2.7}\text{Cl}_{0.3}$ from pH 0.9 to pH 11 for 1 M $[\text{Cl}^-]$. A complex of the Fe cations forms in solution (FeCl^+ , FeCl_2^+) but no change in the active region of the diagram is expected.

⁹ One of the best historical examples of dissolution of a noble metal through complexation is the dissolution of gold in cyanide solution.

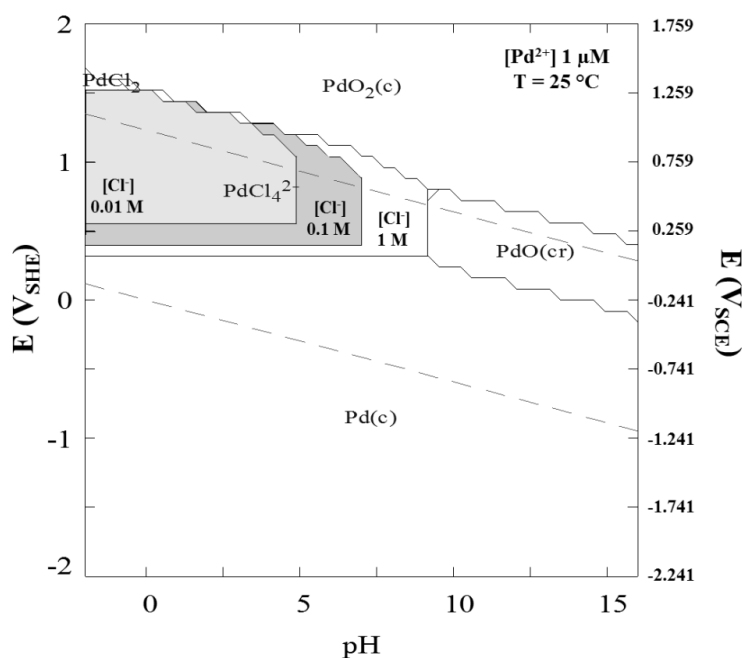


Figure 4.4. Calculated potential-pH equilibrium diagram for the Pd/Cl⁻-H₂O system at 25°C. The series of regions (white, then shaded) indicate the thermodynamically stable region PdCl₄²⁻ at Cl⁻ concentrations of 1 M, 0.1 M and 0.01 M. The Pd²⁺ concentration assumed to be 10⁻⁶ M. Calculated using Medusa [17].

Cl⁻ also undergoes adsorption into bare metal surfaces in addition to oxides and can affect the electrochemical behavior of the system. For Fe, the absorption of Cl⁻ is higher in the passive layer than adsorption on the bare metal (in a base environment of 8.4 borate buffer); both the coverage and absorption concentration vary on applied potential and Cl⁻ concentration [18]. In general, examples of mechanistic interpretations of the effect of Cl⁻ on passivity include Cl⁻ oxide penetration [19, 20] and increasing cation diffusion leading to passive film breakdown [21]. Absorbed Cl⁻ can also affect the kinetics of dissolution reactions. Dissolution of Fe depends on the [Cl⁻] through formation of FeCl_{ads}⁻ which lead to an increase in the dissolution rate [22, 23].

The role of Cl⁻ must be considered when discussing the electrochemical behavior of the Fe-Pd alloys and assumptions of regions of immunity and oxide stability. Cl⁻ is

likely to play a role both in thermodynamics and kinetics of dissolution and passivity of either or both of the elemental species in the alloy.

4.4 Critical Unresolved Issues

The objective of this chapter is to answer two key questions that underlie the behavior of the Fe-Pd system. The first is to gain an understanding of the corrosion and electrochemistry behavior of this binary alloy system as a function of composition by establishing the role of Pd as a beneficial solute element. Selected conditions will probe issues such as noble-active element circumstances. The second is to establish the role of structure at these compositions. A corollary to these objectives is the establishment of the framework of electrochemical behavior to be expanded upon in the detailed study of the Fe₅₀Pd₅₀ γ -phase and L1₀ structural states in the following chapters.

4.5 Experimental

The Fe₅₀Pd₅₀ alloy was produced by the arc-melting technique using high purity 99.99% Fe and 99.999% Pd under an argon atmosphere. Prior to any heat treatments, alloy sections were first encapsulated in quartz tubes under an argon atmosphere. The cast alloy Fe₅₀Pd₅₀ was cold rolled to approximately 0.5 mm. To remove the induced deformation and texture, the alloy was recrystallized at 1100 °C for 24 hours and then water quenched. A final annealing step for each composition was performed followed by water quenching. X-ray diffraction (XRD) characterization was performed using a Scintag XDS-2000 diffractometer with a Cu-K α source ($\lambda = 0.1541$ nm). XRD spectra measurements were conducted in the $\theta/2\theta$ configuration.

Chemical speciation and E-pH species predominance diagrams are created using the Medusa software suite [17]. This freely available suite¹⁰ calculates electrochemical equilibria based on species concentrations. Structural modeling and calculations based on the structure (such as density) were calculated using the Diamond Crystallography Software Suite[24].

Electrochemical measurements were conducted using a traditional 3-electrode setup with an exposed electrically isolated working electrode consisting of polycrystalline Fe₅₀Pd₅₀ sample or Pd and Fe samples. The reference electrode was a saturated calomel type electrode, SCE, and the counter electrode was a platinum mesh. Chemical solutions were produced using reagent grade chemicals and pure water (resistivity 18.2 M Ω /cm) produced by an Academic MilliQ filtration system (MilliPore). Prior to electrochemical experiments the solution was deaerated for at least 2 hours by vigorous sparging of nitrogen through the solution. Polarization experiments were conducted using a Gamry PCI4 potentiostat. High purity element samples of Fe and Pd were used in comparative electrochemistry experiments. Exposed samples had an exposed surface area of approximately 0.005 cm².

JEOL 6700F with an accelerating voltage of 5 keV and a working distance of 5 mm was used to characterize the surface morphology. Composition measurements were made using an attached energy x-ray dispersive spectrometer (EDS). X-ray photoelectron spectroscopy (XPS) composition depth profiling was performed using a PHI Quantera SXM, part of the Institute for Critical Technology and Applied Science at Virginia

¹⁰ Found on the web at <http://www.kemi.kth.se/medusa/>.

Polytechnic Institute. Optical image analysis of pit size and surface coverage was performed using ImageJ image analysis software¹¹.

4.6 Results

4.6.1 Characterization of Fe_{1-x}Pd_x microstructures

To produce the as-quenched γ -phase structure, the samples were annealed at 950 °C and water quenched. To produce the martensitic structure for Fe₇₀Pd₃₀, a higher temperature and longer duration annealing was performed at 1100 °C for 100 hours. The higher temperature was chosen to avoid the two-phase field and along with the longer duration to achieve similar grain size to the γ -phase alloys. The final annealing step and the resultant phase and corresponding grain size is summarized in Table 4.2. The phase identification and corresponding microstructures are presented in more detail in the following sections.

Table 4.2. Fe_{1-x}Pd_x alloy heat treatment table with resulting phase identification. Grain size measurements are based on optical micrographs and electron backscattered diffraction (Fe₅₀Pd₅₀).

Sample	Heat Treatment	Phase	Grain Size (μm)
Fe ₇₀ Pd ₃₀	100 hours at 1100 °C, water quenched	bct (or bcc) martensite	70
Fe ₆₅ Pd ₃₅	10 hours at 950 °C, water quenched	γ (disordered fcc)	21
Fe ₅₀ Pd ₅₀	10 hours at 950 °C, water quenched	γ (disordered fcc)	28

¹¹ Software freely published by the National Institute of Health: <http://rsb.info.nih.gov/ij/>

4.6.1.1 Characterization of the Fe₇₀Pd₃₀ phase

The microstructure of the bulk alloy Fe₇₀Pd₃₀, shown in Figure 4.5, most closely resembles the reported bct martensite microstructure due to its mixture of twin and lath martensitic [10]. To confirm this conclusion, the x-ray diffraction spectrum, Figure 4.6, was analyzed for bct and bcc phases. In a tetragonal structure peak splitting arises due to the loss of symmetrical lattice reflections (e.g., {101} is not symmetric to {110}) but structure. The XRD spectrum does not exhibit tetragonal characteristic peak splitting and shows only the lattice reflections for the bcc structure.

The calculated values for the diffraction peak splitting for the bct structure based on lattice parameters in [14] are tabulated in Table 2.3. However, these differences are likely within the detection limitations of the diffractometer. In this scenario, the peak splitting would instead lead to peak broadening which does seem evident especially at the higher index peaks. The grain size of these samples ranged from 30-120 μm and an average grain size of about 70 μm. Based primarily on the microstructure, characterization of the Fe₇₀Pd₃₀ as-quenched microstructure is bct.

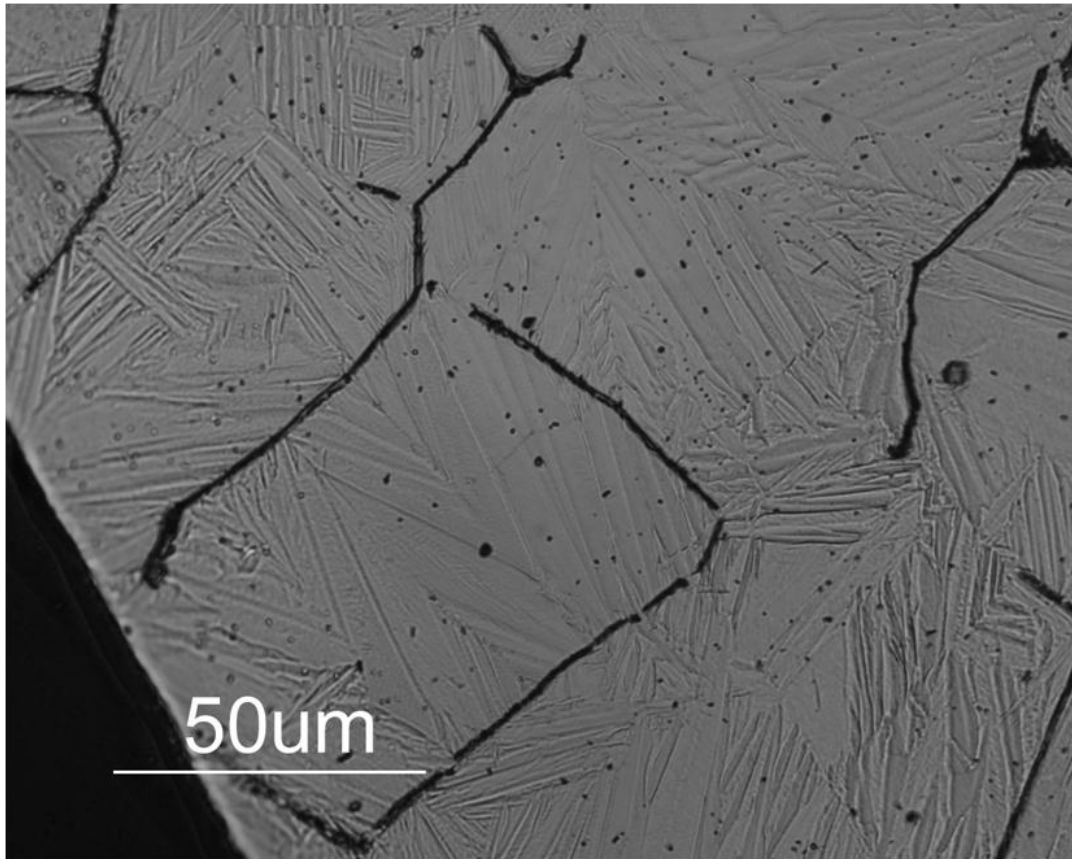


Figure 4.5. Optical micrograph of the Fe₇₀Pd₃₀ microstructure after annealing at annealed at 1100 °C for 100 hours and water quenched. The microstructure was revealed by chemically etching using a mixture of 60 vol% concentrated hydrochloric acid (HCl) and 40% concentrated nitric acid (HNO₃).

Table 4.3. Calculated bcc Fe₇₀Pd₃₀ peak positions assuming lattice parameters a and c are 0.296 and 0.300 nm from [14], respectively.

Allowed Lattice Reflection	Calculated 2 θ Peak Position (°)	Expected peak tetragonal peak splitting (°)
(101)	42.88	0.30
(110)	43.19	
(002)	61.80	0.93
(200)	62.73	
(112)	78.36	0.63
(211)	78.99	
(022)	93.97	0.82
(202)	94.79	

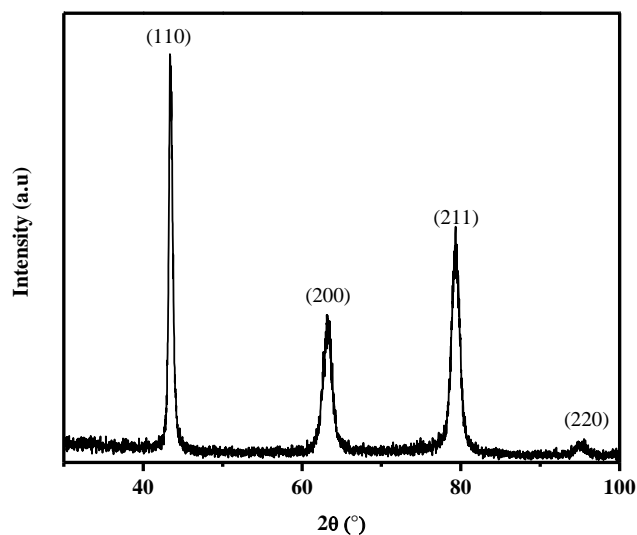


Figure 4.6. X-ray diffraction spectrum of Fe₇₀Pd₃₀ after annealing at 1100 °C for 100 hours and water quenched. Indexed diffraction peaks correspond to a bcc structure with lattice parameter 0.298 nm and site occupancy factors of 0.7 for Fe and 0.3 for Pd. The calculated density based on the crystal structure is 8.912 g/cm³.

4.6.1.2 Characterization of austenitic (γ) Fe₆₅Pd₃₅ and Fe₅₀Pd₅₀

The as-quenched phase of both γ -phase alloys was identified as the disordered fcc phase by XRD. The diffraction patterns are shown in Figure 4.7, with lattice reflections identified as fcc. The average grain size of the Fe₅₀Pd₅₀ alloy was calculated using EBSD

mapping (in Chapter 6) and ranged from 5 to 110 μm with an average grain diameter of 26 μm and a standard deviation of 21 μm (median 19 μm). The $\text{Fe}_{65}\text{Pd}_{35}$ sample had a similar grain size, an example of an etched surface with contrast enhanced to delimit grains is shown in Figure 4.8. The average grain size was measured to be about 28 μm with a large deviation in grain size.

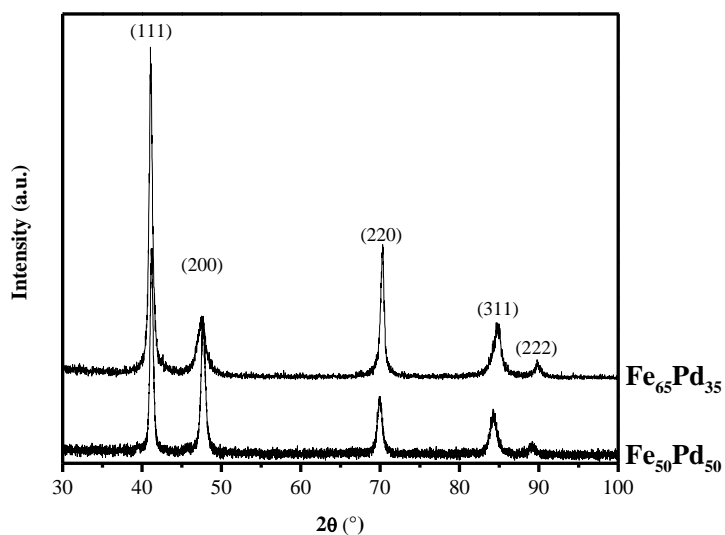


Figure 4.7. X-ray diffraction spectrum for $\text{Fe}_{50}\text{Pd}_{50}$ and $\text{Fe}_{65}\text{Pd}_{35}$ after annealing at 950 $^{\circ}\text{C}$ for 10 hours and water quench. The spectra for both compositions index as the fcc γ structure with allowed lattice reflections marked. The peak intensity of the $\text{Fe}_{50}\text{Pd}_{50}$ sample is the expected trend based for a polycrystalline powder sample. The difference in intensity for the $\text{Fe}_{65}\text{Pd}_{35}$ sample implies a change texture (i.e., change in prevalence of grains and their size which is likely due to the $\text{Fe}_{65}\text{Pd}_{35}$ sample being smaller and having less interaction volume). The calculated density of $\text{Fe}_{65}\text{Pd}_{35}$ is 8.874 g/cm^3 and for $\text{Fe}_{50}\text{Pd}_{50}$ is 9.790 g/cm^3 .

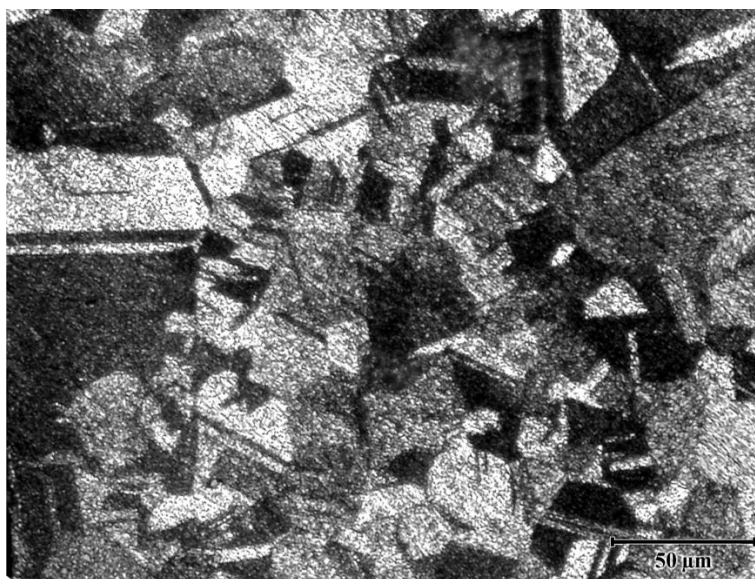


Figure 4.8. Optical micrograph, with increased contrast, of the Fe₆₅Pd₃₅ sample after electrochemical etching by anodic polarization in 0.1 M HCl solution. The grain size ranged from 5 to 100 μm with an average grain size of about 28 μm.

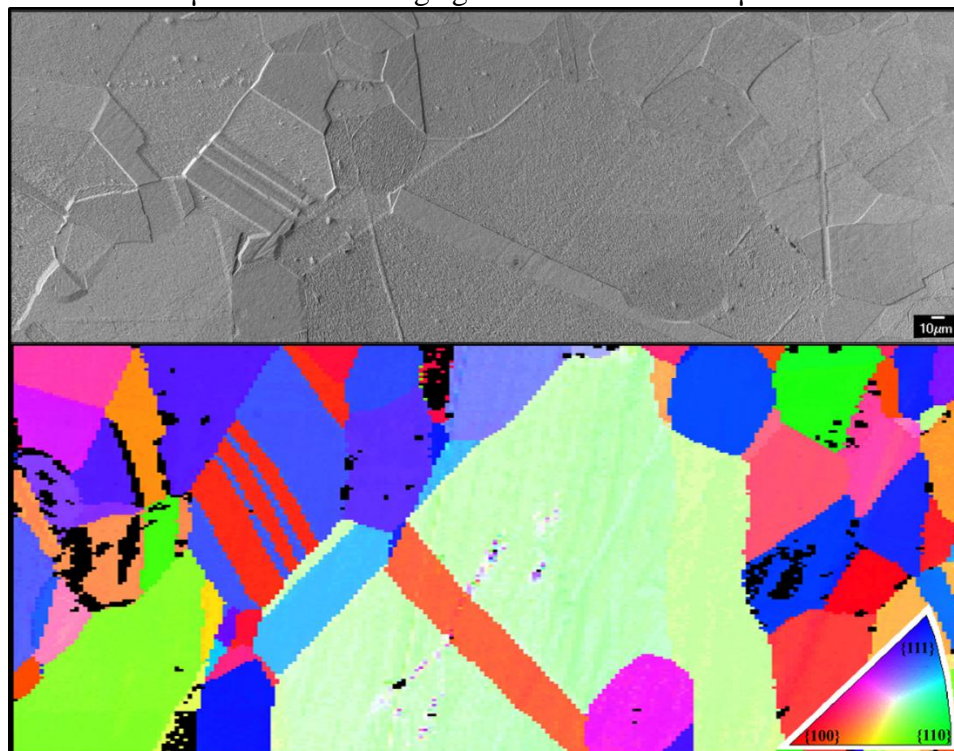


Figure 4.9. SEM micrograph of the Fe₅₀Pd₅₀ sample after electrochemical etching by polarization in 0.1 M HCl solution at 0.45 V_{SCE} for 400 s. An electron backscattered diffraction map (EBSD) of the grain orientations in the sample surface normal direction is also shown to better illuminate grains. The average grain size is 26 μm. A detailed analysis of significance of the orientation on dissolution behavior in HCl solution will be discussed in detail in Chapter 6.

4.6.2 Electrochemical Behavior in Cl⁻ Containing Solutions

The local corrosion behavior was explored over wide range of Cl⁻ concentrations and pH. The objective of this survey of solutions is to establish solution environments and conditions (e.g., polarization potential) where the difference between the compositions of the alloys is significant. Moreover this basic survey will enable a basic understanding of the behavior of this binary alloy in solution. In acidic environments, Cl⁻ promotes dissolution of Pd (Figure 4.4) while in regions of passivity of Fe, Cl⁻ promotes localized breakdown of passive layers.

4.6.2.1 Acidic Environments: Fe active and Pd passive

In HCl solution, Fe is thermodynamically expected to be active while Pd is predominantly immune to corrosion with passive oxide formation at elevated potential. The Cl⁻ anion leads to possible dissolution to form a Cl⁻ complex at higher applied potentials. Cyclic polarization in acidic 0.01, 0.1 and 1 M HCl solution (Figures 4.10, 4.12 and 4.14) indicates Fe dissolution at low over potentials. In contrast, Pd remains at low current densities throughout polarization in 0.01 M HCl solution and is likely immune to corrosion at low applied potential and passive at higher potentials. Similar low current is observed in the more concentrated HCl solutions until 0.6 V_{SCE}. The rise in Pd current density at this potential to 10⁻³ A/cm² and 0.1 A/cm² in 0.1 M and 1 M HCl solution occurs indicates that Cl⁻ complexation has caused dissolution of Pd. Below the critical potential, in all three solutions, the anodic Pd reaction is dominated by the oxidation of absorbed hydrogen to H⁺ (see Chapter 5).

The Fe₇₀Pd₃₀ alloy shows local passivity-breakdown behavior in both 0.01 M (Figure 4.10) and 0.1 M (Figure 4.12) HCl solution concentrations. After polarization in 0.1 M HCl solution, the grain boundaries exhibit preferential etching and pitting events are observed (Figure 4.11). The surface of Fe₇₀Pd₃₀ after exposure in 0.1 M (Figure 4.13) exhibits porous layer cracking indicative of dealloying. After potential reversal (upon reaching an apex current density), the anodic current density remains high until potentials below the open circuit potential. The surface (Figure 4.20) after exposure in 1 M HCl is also indicative of dealloying and is discussed in the next section.

In 0.01 M HCl solution, both Fe₅₀Pd₅₀ and Fe₆₅Pd₃₅ show similar polarization behavior. Both remain at low current densities exhibiting cathodic loops¹² until about 0.4 V_{SCE} where the current increases to 10⁻³ and 10⁻² A/cm², respectively, followed by a decrease in current as the applied potential increases. During the reverse scan (not shown for 0.01 M HCl) the current density remains low. After polarization the surface morphology (Figure 4.11) of the Fe₆₅Pd₃₅ alloy exhibits shows numerous large pitting events. The microstructure of the Fe₅₀Pd₅₀ shows less overall dissolution than the Fe₆₅Pd₃₅ alloy and only small pits or likely pit initiation sites.

The comparison of the E-log*i* behavior (Figure 4.12) of the alloys in 0.1 M HCl solution shows sustained dissolution around 0.4 V_{SCE} in both Fe₆₅Pd₃₅ and Fe₅₀Pd₅₀. Cathodic loops are also observed during the upwards potential scan. During the anodic scan the current density of Fe₆₅Pd₃₅ is higher than Fe₅₀Pd₅₀ indicative of increased

¹² Cathodic loops occur when the cathodic current is > than the anodic (passive or capacitive) current. This behavior in these alloys is likely due to the interplay of Habs oxidation/HER equilibrium reaction (causing the lower potential change from negative to positive current) and the oxidation/reduction reaction of the alloy (which occurs at the a higher potential). Arguments regarding Habs are discussed in Chapter 5.

dissolution. In Figure 4.13, the surface morphology of the Fe₆₀Pd₃₅ alloy indicates a grain etched surface with some grains becoming less reflective due to increased dissolution. This behavior is not seen in Fe₅₀Pd₅₀ except in a few grains; however this is likely due to the difference in total dissolution amounts.

A similar trend in dissolution behavior is observed in 1 M HCl solution (Figure 4.14) but the potentials of sustained dissolution are shifted to lower potentials, about 0.25 V_{SCE}. The E-log*i* behavior is similar for all 3 alloy compositions and all undergo dissolution. As the Pd content increases the dissolution curves are shifted to higher potentials. The surface morphology of this condition will be explored further in the next section.

The current density at a given anodic potential follows the ordinal ranking that Fe₅₀Pd₅₀ < Fe₆₅Pd₃₅ << Fe₇₀Pd₃₀ in all three HCl solution concentrations. The Fe₇₀Pd₃₀ alloy shows a distinctly different surface morphology and uniformly cracked surface indicating substantial preferential dissolution of Fe has occurred. In 0.01 M HCl pitting events are seen for both Fe₆₅Pd₃₅ and Fe₅₀Pd₅₀. Grain dependent dissolution morphology is observed in the more aggressive HCl concentrations. The role of preferential dissolution is presented in the next section.

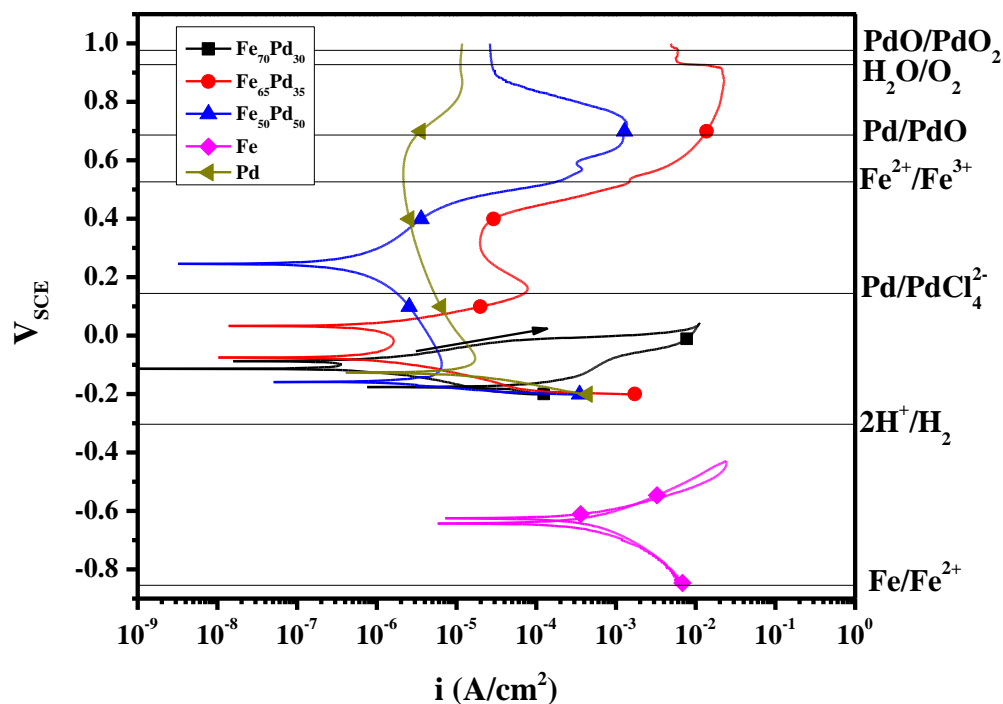


Figure 4.10. E-log*i* behavior in 0.01 M HCl solution at a scan rate of 1 mV/s. For clarity only the anodic portion of the cyclic polarization curve is shown for all alloys except Fe₇₀Pd₃₀. The full scan is shown to show the post activation behavior. For reference, the potentials of various oxidation reactions are shown (solid lines) at pH 2 and species concentrations of 10⁻⁶ M.

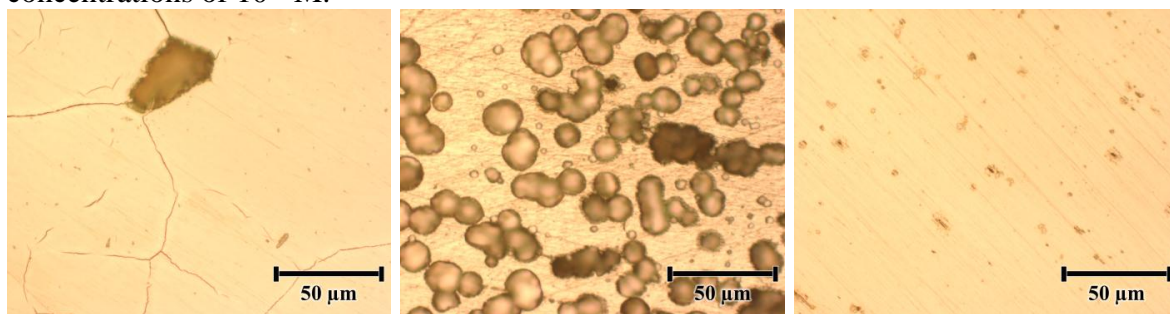


Figure 4.11 Optical micrographs for Fe₇₀Pd₃₀ (left), Fe₆₅Pd₃₅ (center) and Fe₅₀Pd₅₀ (right) after cyclic polarization (Figure 4.10) in deaerated 0.1 M HCl solution showing characteristic surface features. The Fe₇₀Pd₃₀ exhibits grain boundary dissolution and pits initiated along grain boundaries. Fe₆₅Pd₃₅ microstructure exhibits numerous pitting events. The Fe₅₀Pd₅₀ microstructure shows small pitting events. Note that while the Fe₇₀Pd₃₀ sample underwent dissolution at lower applied potentials, the total charge accumulated is less than the case of the Fe₆₅Pd₃₅ resulting in less overall dissolution.

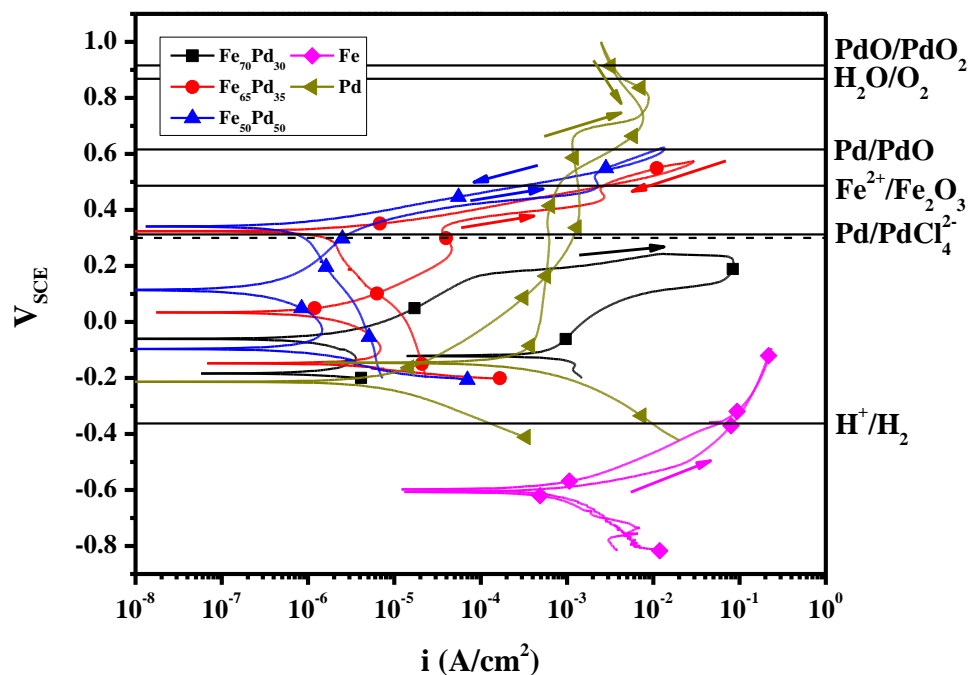


Figure 4.12. Cyclic E-log i behavior in deaerated 0.1 M HCl solution at a scan rate of 1 mV/s (direction indicated by arrows). The current for high purity polycrystalline Fe is above the current cutoff threshold and is represented by a single point. A potentiostatic polarization at 0.3 V_{SCE} , indicated by the dashed line, is shown in Figure 4.15. For reference, the potentials of various oxidation reactions are shown (solid lines) at pH 1 and species concentrations of 10^{-6} M. Oxidation of Fe to aqueous Fe^{2+} cation occurs at -0.86 V_{SCE} .

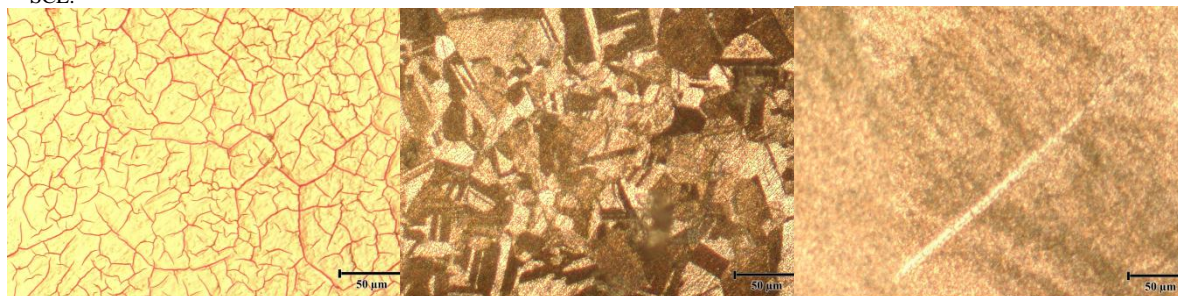


Figure 4.13. Optical micrographs for $Fe_{70}Pd_{30}$ (left), $Fe_{65}Pd_{35}$ (center) and $Fe_{50}Pd_{50}$ (right) after cyclic polarization (Figure 4.12) in deaerated 0.1 M HCl solution showing characteristic surface features. The $Fe_{70}Pd_{30}$ surface shows cracking indicative of reduced volume during preferential dissolution of Fe. $Fe_{65}Pd_{35}$ shows crystallographically dependent dissolution while for the $Fe_{50}Pd_{50}$ alloy the dissolution is predominantly uniform. The dissolution behavior of $Fe_{50}Pd_{50}$ at higher HCl solution concentrations is similar to $Fe_{65}Pd_{35}$ seen here (See the next section, and Chapter 5 and 6).

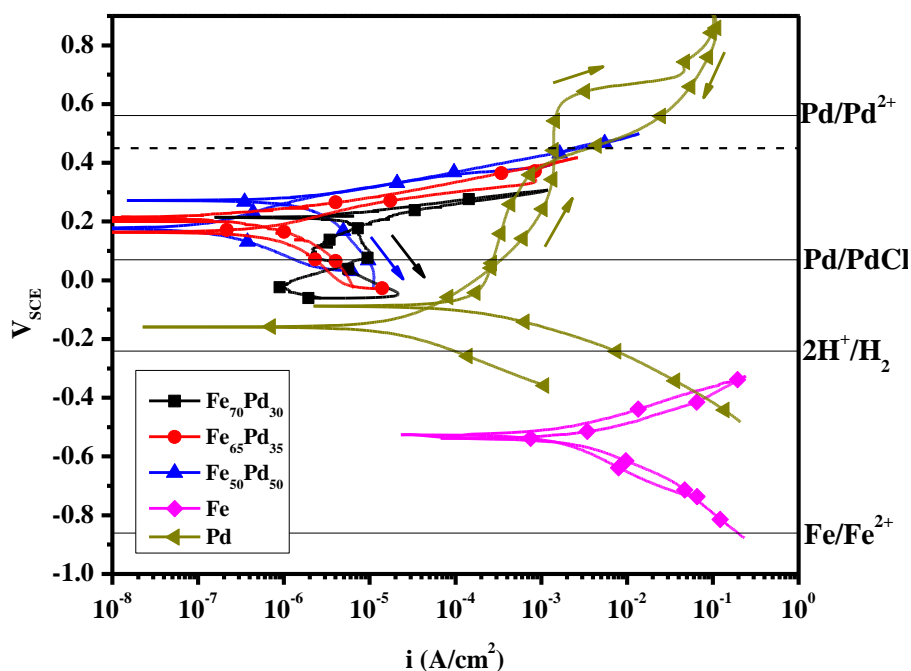


Figure 4.14. Cyclic E-log*i* behavior in deaerated 1 M HCl solution at a scan rate of 1 mV/s. The dashed line on the E-log*i* plot indicates the 0.45 V_{SCE} potential used for the potentiostatic polarization experiments. For reference, the potentials of various oxidation reactions are shown (solid lines) at pH 0 and species concentrations of 10^{-6} M. The corrosion induced surface morphology in 1 M HCl solution is highlighted in the next section.

4.6.2.2 Dealloying behavior in acidic HCl solution

The effect of Pd concentration of Fe-Pd alloys in relation to dealloying was further explored using potentiostatic polarization at 0.3 V_{SCE} in 0.1 M HCl solution, Figure 4.15, followed by composition depth profile measurements. The current density is substantially higher for $Fe_{70}Pd_{30}$ than either $Fe_{65}Pd_{35}$ or $Fe_{50}Pd_{50}$ compositions and the total accumulated anodic charge during exposure was about 26 C/cm^2 . XPS compositional profiles of $Fe_{70}Pd_{30}$, after 1 μm (SiO_2 equivalent) ion milling, show Pd enrichment to 60 at%, twice the bulk composition. The composition depth profiles of $Fe_{50}Pd_{50}$ and $Fe_{65}Pd_{35}$ is shown in Figure 4.16. In both these cases, there was limited

compositional variation measured in the first 20 nm (SiO_2 equivalent). For comparison, Faraday's law was used to calculate the expected dissolution after exposure.

If oxidization of both species to a +2 valence state is assumed, the total accumulated charge of $\text{Fe}_{50}\text{Pd}_{50}$ at 0.3 V_{SCE} over 600 s would amount to total dissolution of 4 nm. If instead only Fe is oxidized forming a 100% Pd dealloyed layer, the dealloyed layer thickness would be about 8 nm. Thus, for the $\text{Fe}_{50}\text{Pd}_{50}$ alloy, the expected dealloyed layer thickness is within the detection limits of depth profile technique. For the $\text{Fe}_{65}\text{Pd}_{35}$ alloy, the expected dealloyed layer thickness would be about 60 nm. Based on the XPS results shown in Figure 4.16, dealloying is limited to the first 20 nm of the surface. These calculations are a lower bound of the dissolution depth. If the dealloyed layer retained some unoxidized Fe atoms, the real dealloyed layer thickness would be significantly larger than the calculated values. At longer exposure times and more total charge, EDS analysis of $\text{Fe}_{50}\text{Pd}_{50}$ does not show any measurable difference between the composition of the exposed and unexposed areas. This indicates that a dealloyed layer does not propagate through the surface layers and is limited to the surface of the $\text{Fe}_{50}\text{Pd}_{50}$ and $\text{Fe}_{65}\text{Pd}_{35}$ compositions.

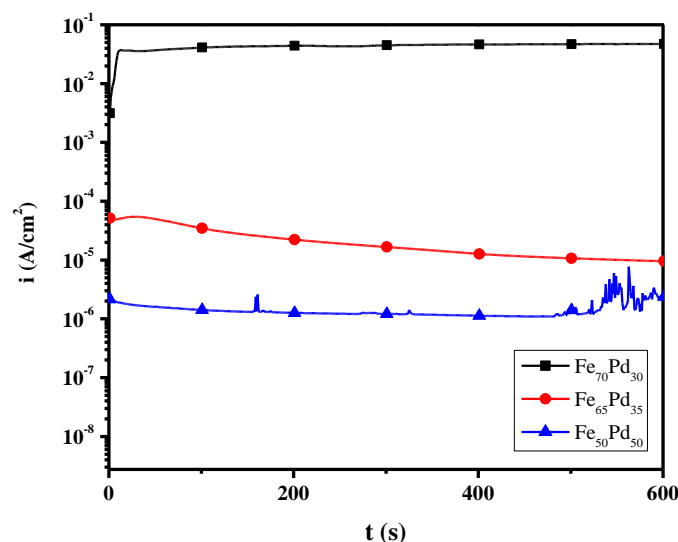


Figure 4.15. Representative potentiostatic polarization behavior in aerated 0.1 M HCl solution at an applied potential of 0.3 V_{SCE} over the initial 600 s of exposure. The total charge for Fe₇₀Pd₃₀ is 26.15 C/cm² (600s exposure). The other two alloys were polarized for 1800s and for Fe₆₅Pd₃₅, the total charge 0.07 C/cm², and for Fe₅₀Pd₅₀ the total charge is 0.01 C/cm².

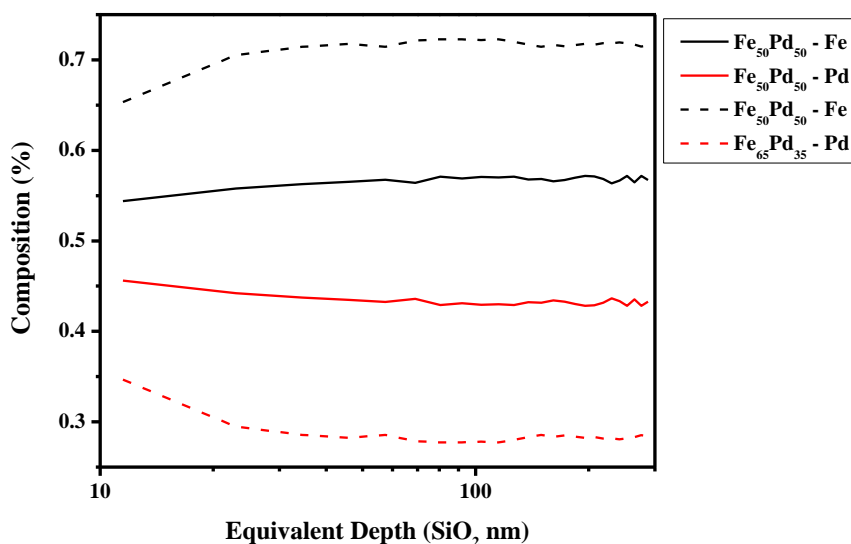


Figure 4.16. XPS depth profiles for Fe₅₀Pd₅₀ and Fe₆₅Pd₃₅. Fe₅₀Pd₅₀ shows little if any Pd enrichment in the first 100 equivalent nm. Fe₆₅Pd₃₅ shows 5% Pd enrichment at the surface layer. There appears to be a shift between the measured concentrations and the bulk concentrations by -5% for Pd and +5% for Fe. For Fe₇₀Pd₃₀, Pd is enriched to a composition of about 60% Pd at an equivalent depths 1000 nm.

In the case of $\text{Fe}_{70}\text{Pd}_{30}$, the calculated dealloyed layer thickness is about 10 μm . The composition after ion milling showed Pd enrichment to 60 at%. This result is corroborated by an EDS line scan analysis in Figure 4.17, which shows the composition from a lacquer protected region (composition $\sim\text{Fe}_{68}\text{Pd}_{32}$, close to the bulk composition) compared to the dealloyed region. The composition of the dealloyed areas was enriched to a Pd concentration of 65-80%. XRD of the surface showed a mixture of $\text{Fe}_{70}\text{Pd}_{30}$ and fcc Pd spectra (Figure 4.18). There is a shift to lower peak positions in the martensitic peaks from the initial spectrum. The shift is expected due to the loss of Pd concentration in the martensite which leads to peaks shifting to higher 2θ as the lattice contracts towards a structure closer to ferritic Fe (see diffraction spectra for $\text{Fe}_{97}\text{Pd}_3$ [25] and Fe [26]). In the dealloyed region substantial cracking occurred likely due to the change in volume as the surface reorganizes to form fcc Pd or due to brittle cracking of the porous structure (e.g., [27]).

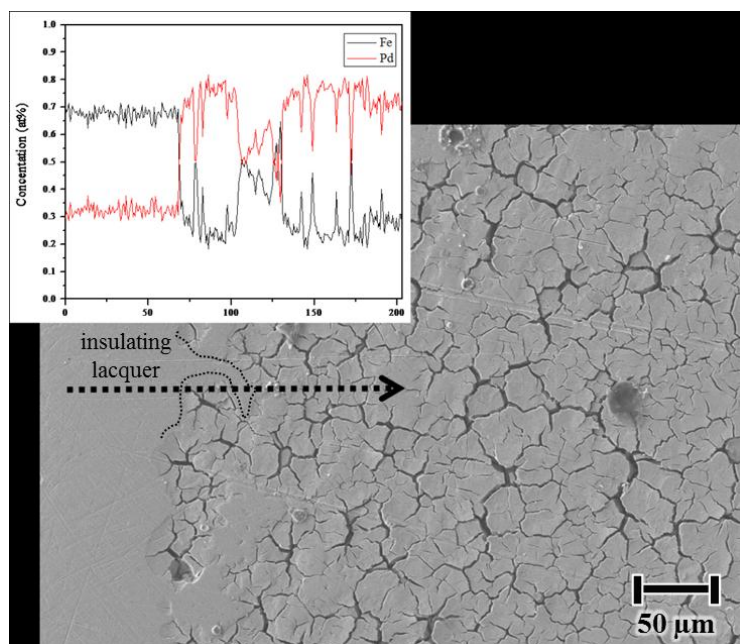


Figure 4.17. SEM micrograph and EDS line (inset) of $\text{Fe}_{70}\text{Pd}_{30}$ scan after potentiostatic polarization in 0.1 M HCl solution at $0.3 V_{\text{SCE}}$. The line scan is across the interface of the lacquered region (dotted line) which is protected from solution to the exposed area. The x-axis of the EDS line scan corresponds with position along the marked line scan indicated by the arrow. In the lacquered region the composition is $\text{Fe}_{68}\text{Pd}_{32}$ approximately the bulk composition. The initial dealloyed region between 50 and 100 μm followed an unexposed region due to coverage of the lacquer. Spikes in the composition values correspond to the cracked areas along the surface. A working distance of 15 mm and 15 kV accelerating voltage was utilized for both the image and EDS analysis.

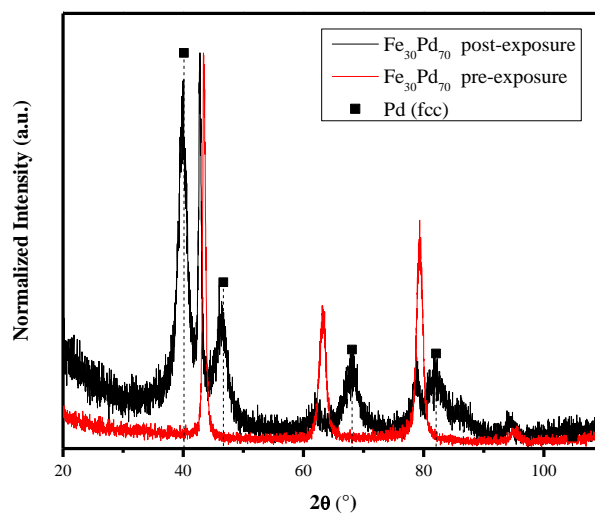


Figure 4.18. XRD of the exposed $\text{Fe}_{70}\text{Pd}_{30}$ shows a mixture of the parent martensitic phase (indicated by the red pre-exposure pattern) and pure Pd (fcc). This spectrum indicates that significant preferential dissolution of iron has occurred and the remaining Pd atoms have reorganized to the form a fcc Pd structure within the first 5 μm of depth. There is a 0.6° phase shift to smaller 2θ after exposure indicating a shift more Pd in the martensitic structure. As the Pd alloying amount in bcc Fe increases from ferrite to $\text{Fe}_{97}\text{Pd}_3$ the bcc peaks shift to lower 2θ .

The presence of dealloying in the higher Pd-content fcc alloys was assessed in more aggressive 1 M HCl solution under an applied potential of 0.45 V_{SCE}.¹³ As the polarization shown in Figure 4.14 indicates, dissolution is expected from all three alloy compositions. The charge density increased as the Pd concentration decreased, see Figure 4.19 and Table 4.4. The dissolution depth calculations based on Faraday's Law predict that for congruent dissolution of the Fe₅₀Pd₅₀ and Fe₆₅Pd₃₅ alloys the alloy surface would have receded 1.74 and 3.24 μm, respectively. If, instead, preferential dissolution were occurring in these alloys, the depth of preferentially dissolved Fe would be approximately twice these depths. The expected depth is within the characteristic X-ray generation depth for Fe-Pd alloys [28]¹⁴. The SEM micrographs and compositional analysis across the interface between the insulated and exposed areas are shown for each alloy in Figures 4.20 (Fe₇₀Pd₃₀), 4.21 (Fe₆₅Pd₃₅), and 4.22 (Fe₅₀Pd₅₀).

Pd surface enrichment is only seen in the case of the Fe₇₀Pd₃₀ microstructure. Congruent dissolution is seen for Fe₆₅Pd₃₅ and Fe₅₀Pd₅₀ and line scans across the protected-exposed interface show no change in composition due to surface dissolution. Dissolution of the Fe₇₀Pd₃₀ alloy results in a microstructure with an appearance resembling fractured islands separated by channels. The islands show 20-30 at% Pd enrichment. The high Fe content regions (however not higher than the starting composition) are measured from within the dissolved region coincident with the channels

¹³ The rationale for this choice was to be in a region of congruent dissolution of both fcc and pT Fe₅₀Pd₅₀ based on results from Chapter 5. This potential was chosen for the orientation dependent studies of the ordered and disordered equiatomic structure in Chapter 6.

¹⁴ For an iron sample, the Monte Carlo simulation under the SEM-EDS detector conditions for the (JEOL 6700F, 15 kV, EDS at 29° from the sample surface) more than 80% of the characteristic x-rays are generated within the first 0.33 μm of the surface. For higher density element, such as Pd, the characteristic x-rays are generated at smaller interaction depths.

between the topographically higher regions. The increased dissolution of the channels has likely revealed alloy matrix that has not undergone preferential dissolution.

SEM micrographs of the post-exposure $\text{Fe}_{65}\text{Pd}_{35}$ and $\text{Fe}_{50}\text{Pd}_{50}$ microstructure are shown in Figure 4.23. The microstructure of these alloys exhibits the grain-distinct dissolution induced faceted morphology hinted at in the optical micrographs after cyclic polarization in 0.1 M HCl solution in Figure 4.13. The $\text{Fe}_{65}\text{Pd}_{35}$ microstructure has a similar grain dependent faceted morphology that the $\text{Fe}_{50}\text{Pd}_{50}$ alloy does, but the differences in grain specific dissolution are less pronounced, i.e. there is less of a difference between the highest and lowest dissolved grains.

Table 4.4. Total charge accumulated during potentiostatic polarization in deaerated 1 M HCl solution at 0.45 V_{SCE} . Faraday's Law was used to calculate the calculated dissolution depth.¹⁵

	Time (s)	Charge (C/cm^2)	Calc. Dissolution Depth (μm)
$\text{Fe}_{70}\text{Pd}_{30}$	200	66.36	26.43
$\text{Fe}_{65}\text{Pd}_{35}$	200	7.51	3.24
$\text{Fe}_{50}\text{Pd}_{50}$	400	3.99	1.73

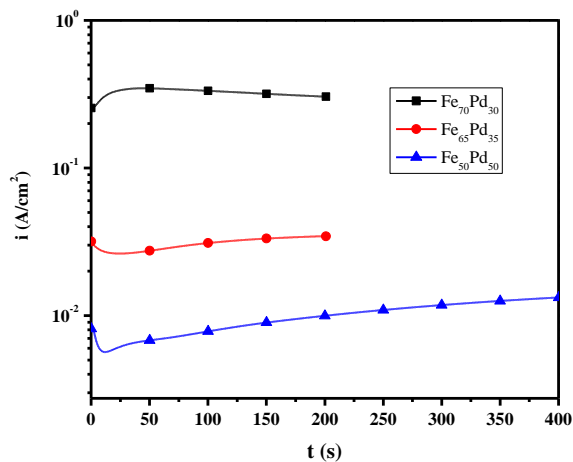


Figure 4.19. Representative potentiostatic polarization behavior in deaerated 1 M HCl solution at an applied potential of 0.45 V_{SCE} for 400 s for $\text{Fe}_{50}\text{Pd}_{50}$ and 200 s for $\text{Fe}_{70}\text{Pd}_{30}$ and $\text{Fe}_{65}\text{Pd}_{35}$. The total accumulated charge density is 66.36, 7.51, and 3.99 C/cm^2 for $\text{Fe}_{70}\text{Pd}_{30}$, $\text{Fe}_{65}\text{Pd}_{35}$, and $\text{Fe}_{50}\text{Pd}_{50}$, respectively.

¹⁵ Oxidation of Fe and Pd to the 2⁺ valence state. Congruent dissolution is assumed for $\text{Fe}_{50}\text{Pd}_{50}$ and $\text{Fe}_{35}\text{Pd}_{65}$ and the density based on the crystal structure. For $\text{Fe}_{70}\text{Pd}_{30}$ total preferential Fe dissolution is assumed.

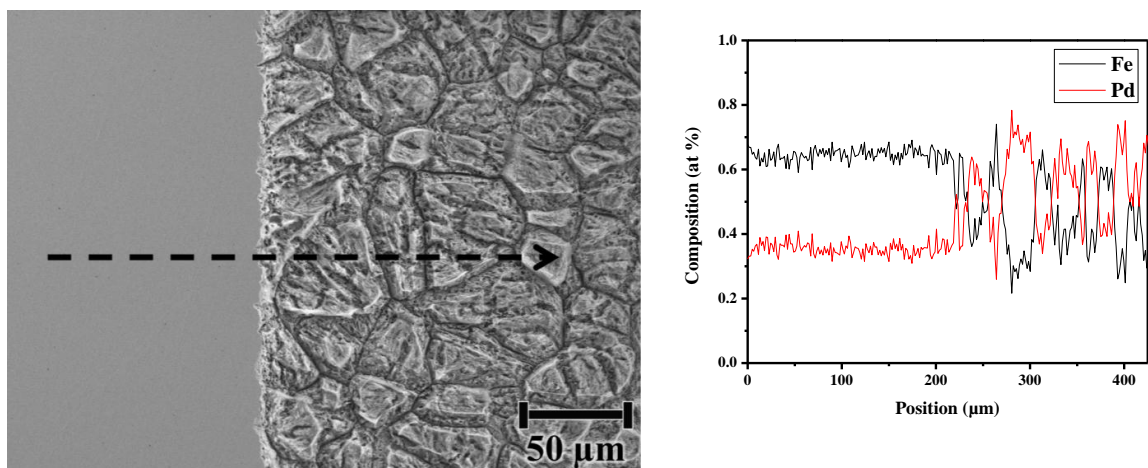


Figure 4.20. SEM micrograph (left) and EDS line (right) scan of $\text{Fe}_{70}\text{Pd}_{30}$ after potentiostatic polarization in 1 M HCl solution at $0.45 \text{ V}_{\text{SCE}}$ for 200 s with total accumulated charge of 66.3 C/cm^2 . The line scan, indicated by the arrow, is across the interface of the lacquered region (on the left) which is protected from solution. The $\text{Fe}_{65}\text{Pd}_{35}$ surface undergoes preferential dissolution of Fe. The accelerating voltage for both the image and EDS analysis is 15 kV and working distance of 15 mm.

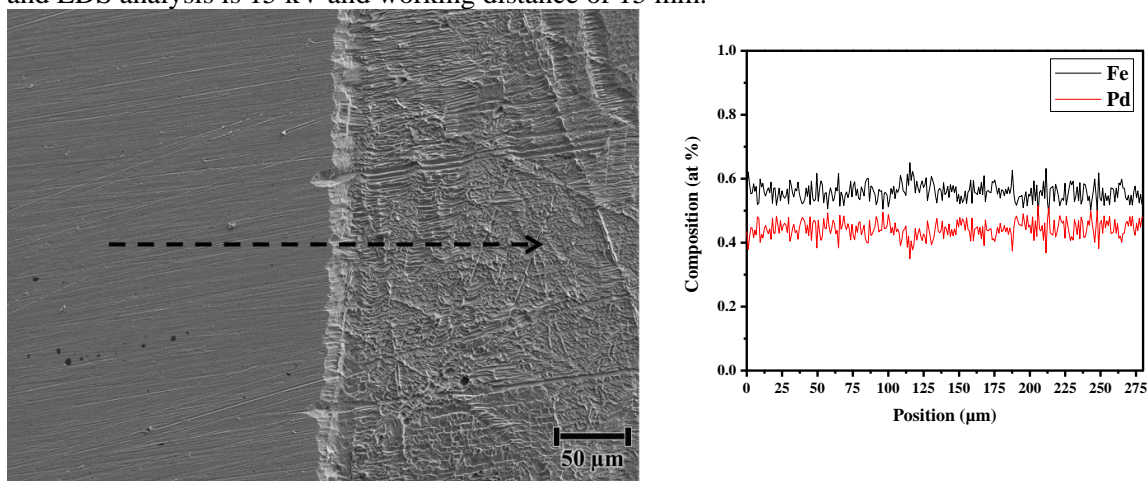


Figure 4.21. SEM micrograph (left) and EDS line (right) scan of $\text{Fe}_{65}\text{Pd}_{35}$ after potentiostatic polarization in 1 M HCl solution at $0.45 \text{ V}_{\text{SCE}}$ for 200 s with total accumulated charge of 7.52 C/cm^2 . The SEM micrograph indicates some grain specific faceted behavior after dissolution. The line scan, indicated by the arrow, is across the interface of the lacquered region (on the left) which is protected from solution. No significant qualitative compositional variations are observed between the protected and dissolved areas. The accelerating voltage for both the image and EDS analysis is 15 kV and working distance of 15 mm.

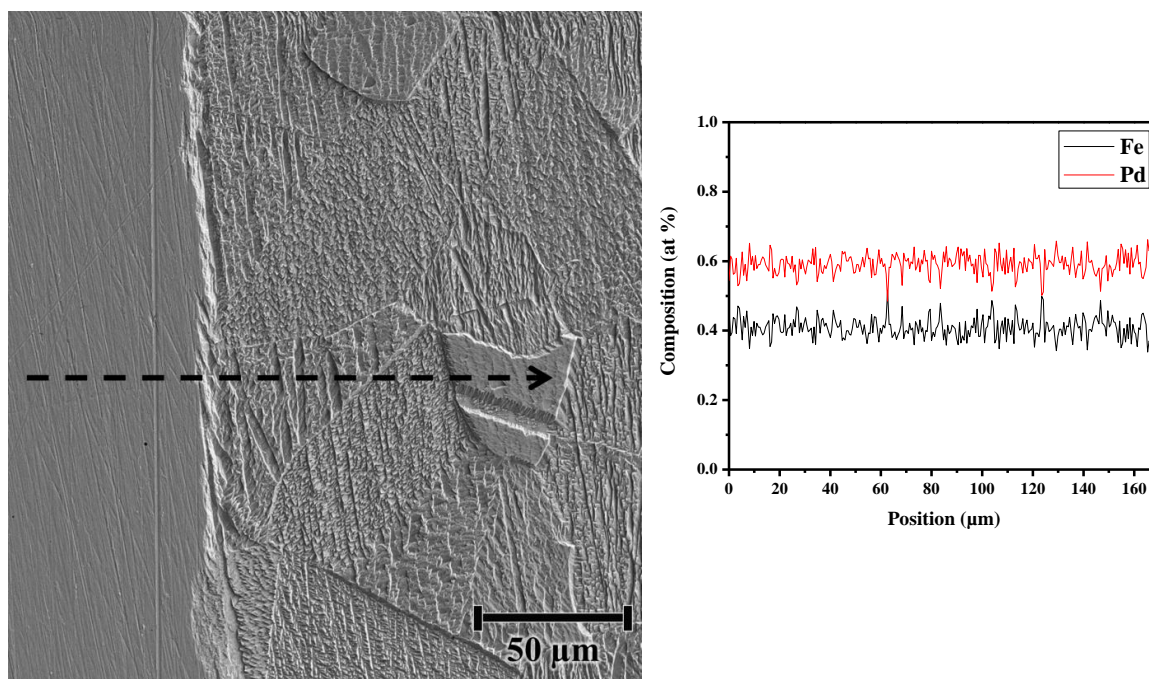


Figure 4.22. SEM micrograph (left) and EDS line (right) scan of $\text{Fe}_{50}\text{Pd}_{50}$ after potentiostatic polarization in 1 M HCl solution at $0.45 \text{ V}_{\text{SCE}}$ for 400 s with total accumulated charge of 3.99 C/cm^2 . The SEM micrograph indicates grain specific faceted behavior after dissolution. The line scan, indicated by the arrow, is across the interface of the lacquered region (on the left) which is protected from solution. No significant qualitative compositional variations are observed between the protected and dissolved areas. The accelerating voltage for both the image and EDS analysis is 15 kV and working distance of 15 mm.¹⁶

¹⁶ The divergence between the EDS measured composition and the nominal composition is due to limiting the beam energy to 15 keV. This energy is only twice the binding energy of Fe ($K_{\alpha} = 6.4$ and $K_{\beta} = 7.1$ keV) resulting in the measured compositions lower in Fe than nominal. This accelerating voltage was used to limit the beam interaction depth to better measure the surface composition.

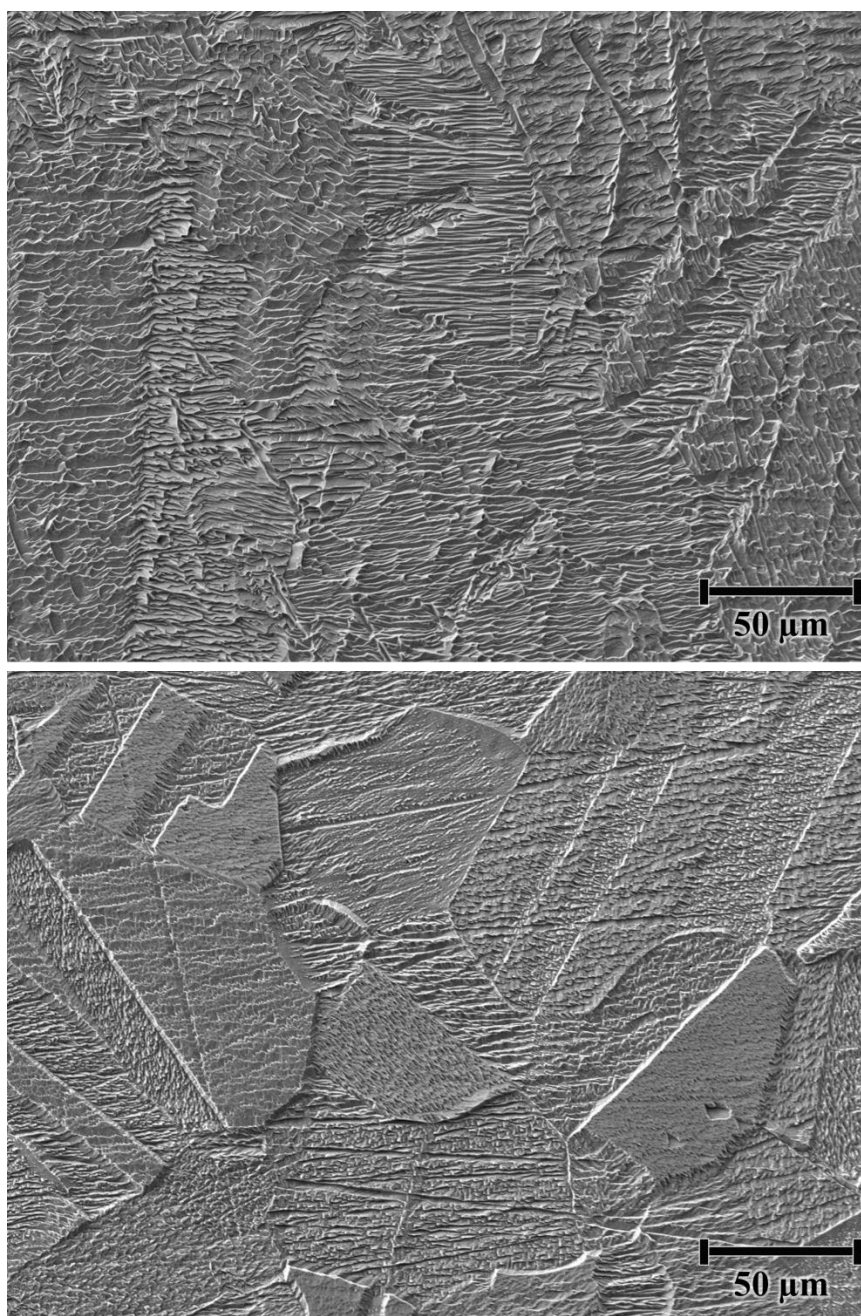


Figure 4.23. SEM micrograph of Fe₆₅Pd₃₅ (top) and Fe₅₀Pd₅₀ (bottom) after potentiostatic polarization in 1 M HCl solution at 0.45 V_{SCE}. Fe₆₅Pd₃₅ was polarized for 200 s with 7.52 C/cm² total accumulated charge and Fe₅₀Pd₅₀ was polarized for 400 s with total accumulated charge of 3.99 C/cm². The Fe₅₀Pd₅₀ microstructure shows distinct dissolution induced grain faceted morphologies and lower dissolution than the Fe₆₅Pd₃₅. The Fe₆₅Pd₃₅ microstructure has similar grain dependent faceted morphology to the Fe₅₀Pd₅₀ but the differences in grain specific dissolution are less pronounced.

4.6.2.3 Electrochemical Corrosion Behavior in Neutral and Basic Environments with Pd and/or Fe in the Passive State

In neutral pH, Pd is passive while Fe is active until around $-0.23 V_{SCE}$ above which a passive film can be formed from dissolved Fe^{2+} cations (Figure 4.2). The cyclic $E\text{-log}i$ behavior of the alloys and polycrystalline Fe and Pd in 0.06 M NaCl solution (pH 6) is shown in Figure 4.24 and 0.6 M NaCl solution (pH 6) in Figure 4.25. Fe exhibits active dissolution in both conditions. Pd is non-Faradaic across this potential range in 0.06 M NaCl solution. A large oxygen evolution peak on Pd is seen above $0.5 V_{SCE}$ in 0.6 M NaCl solution. All three Fe-Pd alloys show the same non-Faradaic behavior as Pd. $Fe_{50}Pd_{50}$ has the highest pitting potential, while the pitting potential is similar for both $Fe_{65}Pd_{35}$ and $Fe_{70}Pd_{30}$. In contrast to both the $Fe_{50}Pd_{50}$ $Fe_{65}Pd_{35}$ phase alloys, the $Fe_{70}Pd_{30}$ alloy does not fully repassivate. The pit size and surface coverage is summarized in Table 4.5 and the pits were between 6-15 μm in diameter for all three alloys. This table is meant to serve as a qualitative indication of the behavior of the three different alloy as both the pit size and coverage are influenced by the apex potential, apex current, and the amount of time spent at higher current densities (resulting in more dissolution). With that caveat, the percent of the surface covered by pits decreases with increasing Pd content. Based on similar pit diameters in all three alloys, it is reasonable to assume that the difference in total charge transferred during the anodic polarization sweep is, in large part, represented by an increase in number of pit initiation sites instead of an increase in pit size.

In 0.6 M NaCl solution at pH 6 a similar trend is seen in cyclic polarization shown in Figure 4.25. The pitting potential of the $Fe_{65}Pd_{35}$ and $Fe_{70}Pd_{30}$ are similar and

lower than the pitting potential of $\text{Fe}_{50}\text{Pd}_{50}$. Again, $\text{Fe}_{70}\text{Pd}_{30}$ does not fully repassivate once pits are formed. The pit diameter, highest for $\text{Fe}_{70}\text{Pd}_{30}$ decreases with increasing Pd content, see optical micrographs in Figure 4.26. The surface coverage of pit sites is similar for $\text{Fe}_{65}\text{Pd}_{35}$ and $\text{Fe}_{70}\text{Pd}_{30}$ and substantially decreased for $\text{Fe}_{50}\text{Pd}_{50}$. These values are shown in Table 4.6.

Table 4.5. Surface area covered by pits after cyclic polarization (Figure 4.24) in 0.06 M NaCl solution. The apex potential was about $0.7 V_{\text{SCE}}$ for all compositions but the sustained current density was higher in the case of $\text{Fe}_{70}\text{Pd}_{30}$. The apex potential for $\text{Fe}_{70}\text{Pd}_{30}$ was $-0.1 V_{\text{SCE}}$. Average pit diameter ranged from 6-15 μm and no significant difference was measured at the different alloy compositions. Pd showed no events, and Fe showed uniform dissolution.

Pit Surface Coverage (%)	
$\text{Fe}_{70}\text{Pd}_{30}$	19
$\text{Fe}_{65}\text{Pd}_{35}$	7
$\text{Fe}_{50}\text{Pd}_{50}$	2

Table 4.6. Pit diameter and pit surface coverage after cyclic polarization (Figure 4.25) in 0.6 M NaCl solution. The apex potential was about 0.6 V_{SCE} for all compositions but the sustained current density was higher in the case of Fe₇₀Pd₃₀. The calculated pit surface area is excluding the area of increased dissolution for Fe₇₀Pd₃₀. The value including this area is shown in parenthesis. Pd showed no events, and Fe showed uniform dissolution.

	Pit Diameter (μm)	Standard Deviation (μm)	Pit Surface coverage (%)
Fe₇₀Pd₃₀	15.93	4.64	8% (19% [†])
Fe₆₅Pd₃₅	12.05	2.65	9%
Fe₅₀Pd₅₀	8.40	2.64	1.5%

[†] including the surface area of increased corrosion damage

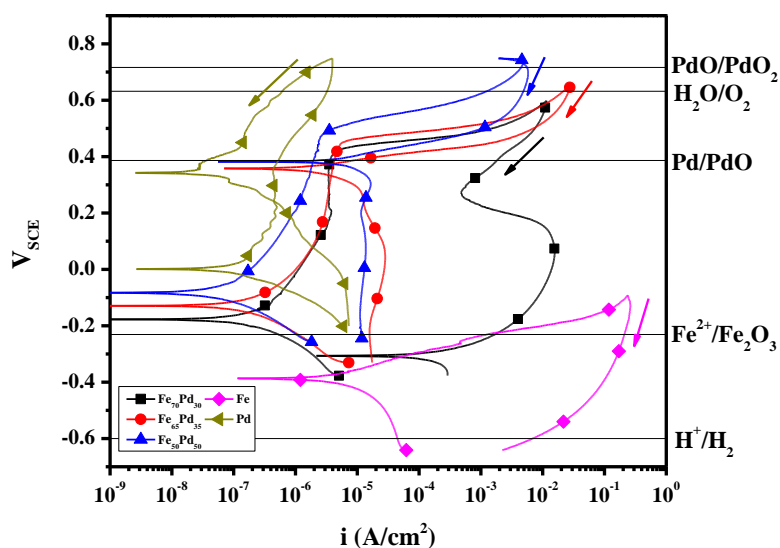


Figure 4.24. Cyclic E-log *i* behavior in 0.06 M NaCl solution at pH 6 at a scan rate of 1 mV/s. For reference, the potentials of various oxidation reactions are shown (solid lines) at pH 6 and species concentrations of 10⁻⁶ M. The Fe oxidation reaction to Fe²⁺ reaction occurs at -0.86 V_{SCE}.

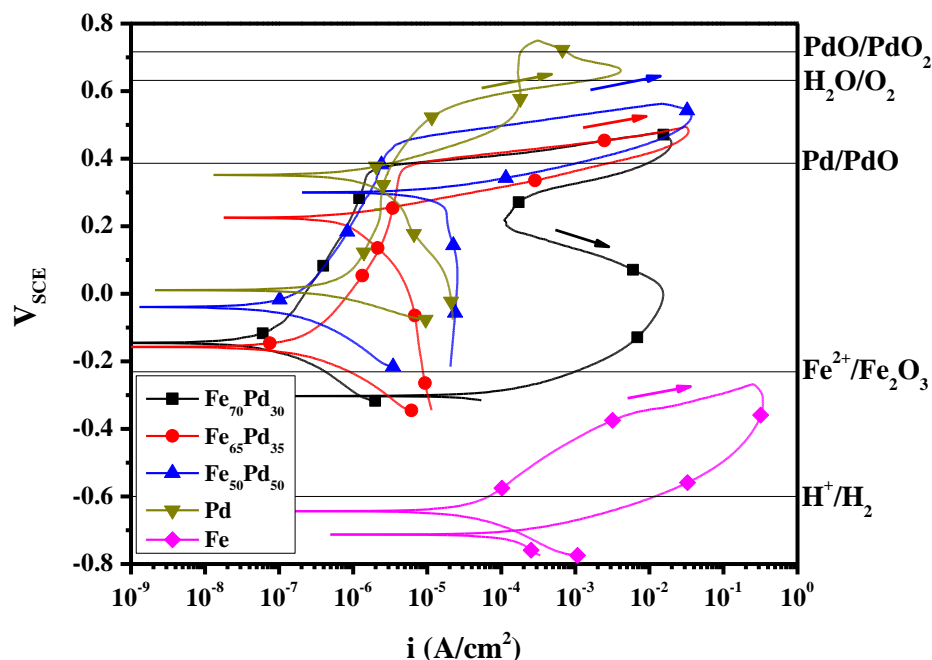


Figure 4.25. Cyclic E-log*i* behavior in 0.6 M NaCl solution at pH 6 at a scan rate of 1 mV/s. For reference, the potentials of various oxidation reactions are shown (solid lines) at pH 6 and species concentrations of 10^{-6} M. Fe oxidation to Fe^{2+} occurs at -0.86 V_{SCE} . No Pd-Cl complex is formed at this pH.

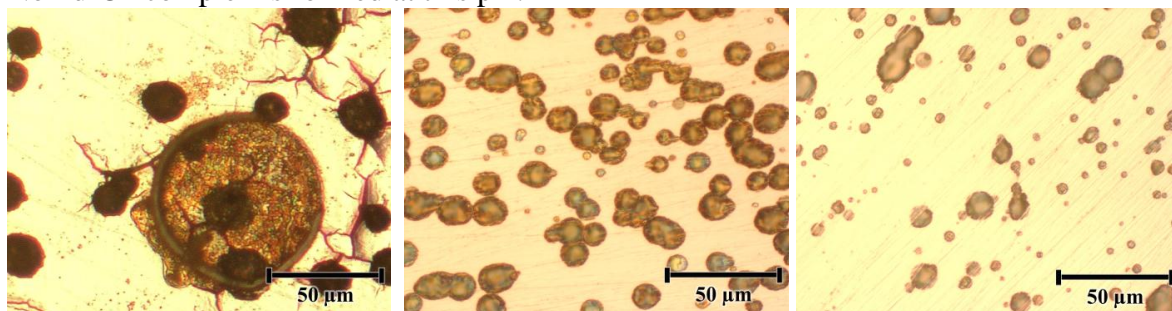


Figure 4.26. Optical micrographs for $\text{Fe}_{70}\text{Pd}_{30}$ (left), $\text{Fe}_{65}\text{Pd}_{35}$ (center) and $\text{Fe}_{50}\text{Pd}_{50}$ (right) after cyclic polarization in deaerated 0.6 M NaCl solution (Figure 4.12) showing characteristic surface features. The apex potentials were between 0.4 and 0.5 V_{SCE} . The $\text{Fe}_{70}\text{Pd}_{30}$ surface shows large pits (due, in part, to the large anodic charge due to lack of repassivation) and regions of increased corrosion damage¹⁷. $\text{Fe}_{65}\text{Pd}_{35}$ and $\text{Fe}_{50}\text{Pd}_{50}$ show pitting corrosion but generally pitting events on $\text{Fe}_{50}\text{Pd}_{50}$ are smaller and have a lower density than $\text{Fe}_{50}\text{Pd}_{35}$.

¹⁷ Acid spillover (due to acidification within pit due to cation hydrolysis) is likely inducing dealloying resulting in the cracks. As in the acidic HCl solution studies, similar behavior is not seen in $\text{Fe}_{65}\text{Pd}_{35}$.

The oxide stability diagram (Figure 4.3) indicates that Fe(OH) oxide is most readily formed at pH 11. At this pH, Fe is passive while Pd is immune at low potentials and forms a passive film above $0.1 V_{SCE}$. Cyclic E-log*i* behavior in 2M NaCl at pH 11 is shown in Figure 4.27. Fe now exhibits passive behavior then pits at $-0.26 V_{SCE}$. Pd shows non-Faradaic behavior until PdO is formed and then at higher potentials OER occurs. During the reverse scan on Pd the ORR occurs at $0.4 V_{SCE}$. Then, as the scan sweeps to lower potentials, the anodic current density decreases around $0 V_{SCE}$ indicative of the reduction of the PdO film (which produces a negative current offsetting the non-Faradaic current).

The pitting potential increases as the Pd alloying concentration increases for the Fe-Pd alloys. Fe₇₀Pd₃₀ alloy shows similar repassivation behavior to Fe₅₀Pd₅₀ and Fe₆₅Pd₃₅ alloys, but never fully repassivates. This behavior is similar to the behavior of Fe₇₀Pd₃₀ in HCl solution. The open circuit potential preceding polarization (Figure 4.28) shows an increase in open circuit potential as the Pd alloying concentration increases. After the polarization, the Fe₇₀Pd₃₀ shows similar open circuit behavior to Fe. Fe₆₅Pd₃₅ and Fe₅₀Pd₅₀ alloys show behavior similar to Pd and over the initial 400 seconds the potential rapidly rises to about $0 V_{SCE}$. The rise is fastest for Pd, second fastest for Fe₅₀Pd₅₀ and slowest for Fe₆₅Pd₃₅.¹⁸

The post corrosion morphology is shown in a series of micrographs in Figure 4.29. Fe₅₀Pd₅₀ shows orientation dependent dissolution with some pitting events. The

¹⁸ Similar behavior is also seen, though not shown here in the HCl solutions; the open circuit potential of the γ phase alloy increases to higher potentials and the Fe₇₀Pd₃₀ alloy has a potential similar to Fe. The mechanistic interpretation of this behavior will be discussed in detail in Chapter 5.

SEM micrograph shows dissolution revealed steps that seem to have some grain dependence. In contrast, the surface morphology of $\text{Fe}_{65}\text{Pd}_{35}$ shows only pitting events and revealed no grains specific dissolution. Larger pits and an increase in the amount of corrosion product were observed the case of $\text{Fe}_{70}\text{Pd}_{30}$.

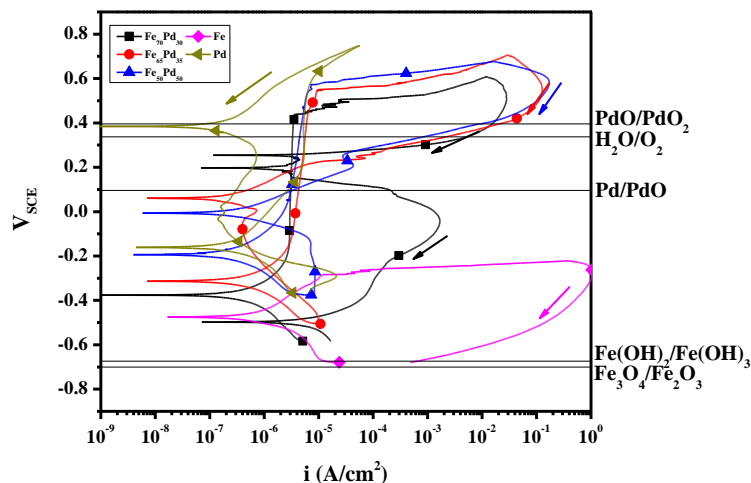


Figure 4.27. Cyclic E-log i behavior in 2 M NaCl at pH 11.0 with a scan rate of 1 mV/s. For reference, the potentials of various oxidation reactions are shown (solid lines) at pH 11 and species concentrations of 10^{-6} M. The $\text{Fe}/\text{Fe}(\text{OH})_2$ reaction occurs at $-0.94 V_{\text{SCE}}$, $\text{Fe}/\text{Fe}_3\text{O}_4$ occurs at $-0.98 V_{\text{SCE}}$, and hydrogen evolution (H^+/H_2) occurs at $-0.90 V_{\text{SCE}}$.

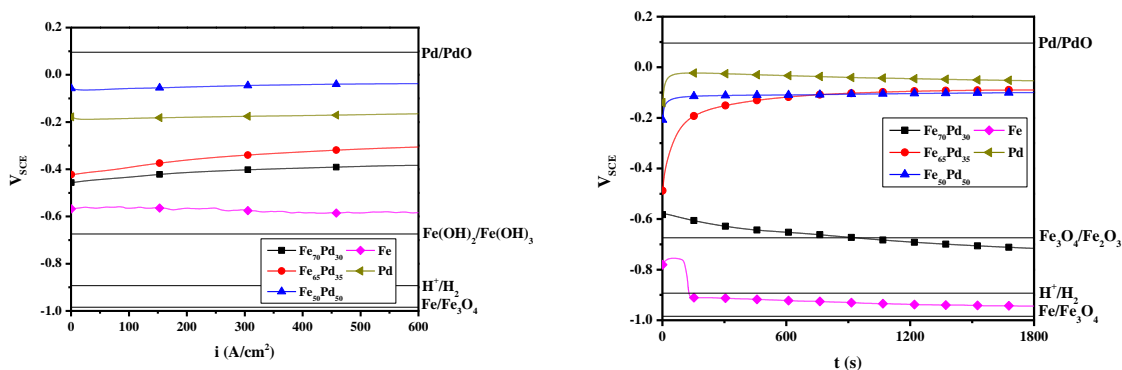


Figure 4.28. Open circuit before and after cyclic before (left) and after (right) cyclic polarization 2 M NaCl pH 11.0. For reference, the potentials of various oxidation reactions are shown (solid lines) at pH 6 and species concentrations of 10^{-6} M. Prior to polarization the open circuit of the alloys increase with increasing Pd concentration. After the experiment, the open circuit potential of Pd, $\text{Fe}_{50}\text{Pd}_{50}$ and $\text{Fe}_{65}\text{Pd}_{35}$ follow a similar trend, while Fe and $\text{Fe}_{70}\text{Pd}_{30}$ exhibit similar behavior.

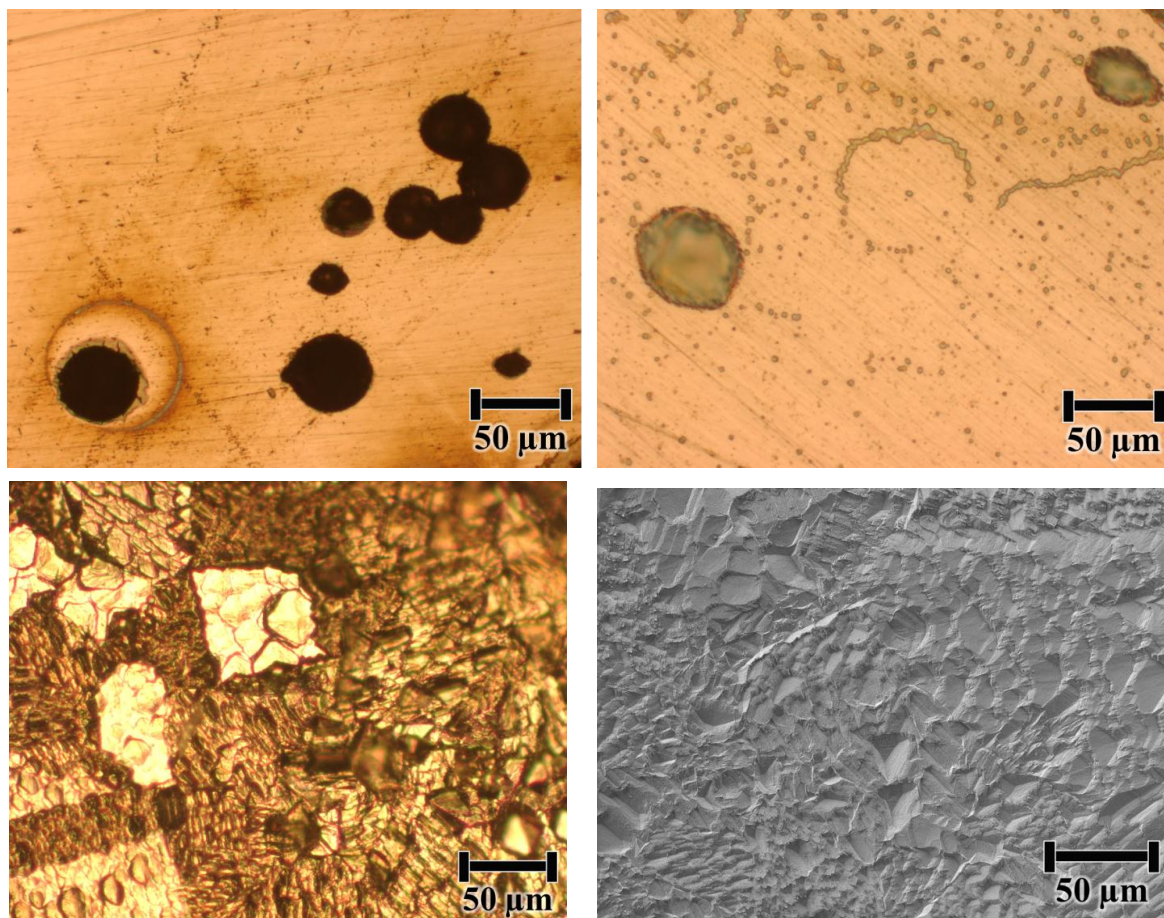


Figure 4.29. Optical micrographs of $\text{Fe}_{70}\text{Pd}_{30}$ (top left), $\text{Fe}_{65}\text{Pd}_{35}$ (top right), $\text{Fe}_{50}\text{Pd}_{50}$ (bottom left and SEM, bottom right) surface after cyclic polarization in 2 M NaCl solution at pH 11. The $\text{Fe}_{65}\text{Pd}_{35}$ and $\text{Fe}_{70}\text{Pd}_{30}$ alloys show behavior dominated by pitting events. In the $\text{Fe}_{50}\text{Pd}_{50}$ alloy (SEM image, bottom right) the surface shows uniform dissolution type behavior with some grain dependent morphological features. Some pit-like regions of increased dissolution relative to the neighboring region (sub grain sized) is also present. The surface of the $\text{Fe}_{50}\text{Pd}_{50}$ alloy shows grain dependent dissolution characteristics typical of both $\text{Fe}_{65}\text{Pd}_{35}$ and $\text{Fe}_{50}\text{Pd}_{50}$ alloys in acidic Cl^- solutions.

4.7 Discussion

For this binary alloy system at these concentrations, there are two parallel mechanisms: The effect of alloying concentration and the role of structural change from the disordered, fcc state in $\text{Fe}_{50}\text{Pd}_{50}$ and $\text{Fe}_{65}\text{Pd}_{35}$ to the martensitic state in $\text{Fe}_{70}\text{Pd}_{30}$. Separation of variable issues makes definitive interpretations of these results difficult. The primary objective here is to establish a set of environmental conditions and corrosion regimes to further explore the role of structure when it can be analyzed independently from composition in the fcc and pT $\text{Fe}_{50}\text{Pd}_{50}$.

4.7.1 Interpretation of the Critical Potential and the Effect of Pd content

Across the Cl^- concentrations and pH studied, the behavior of the martensitic $\text{Fe}_{70}\text{Pd}_{30}$ phase is markedly different than the two disordered, fcc alloys. In 0.1 M and 1 M HCl solution it was shown that the $\text{Fe}_{70}\text{Pd}_{30}$ undergoes preferential Fe dissolution while both disordered, fcc alloys exhibit congruent dissolution (Figures 4.16 and 4.20-4.22). A systematic lack of repassivation is shown after pitting in acidic, neutral and basic environments the case of the $\text{Fe}_{70}\text{Pd}_{30}$ alloy, in marked contrast to both $\text{Fe}_{35}\text{Pd}_{65}$ and $\text{Fe}_{50}\text{Pd}_{50}$ which show typical repassivation behavior (Figures 4.24, 4.25 and 4.27). The lack of repassivation is driven by the acidification of the pit due to hydrolysis. The change in repassivation behavior and dissolution rate indicates some underlying role of the change in structure from the disordered, fcc structure to the martensitic structure. Alternatively, a large effect of composition could be dominating any structural effect.

The pitting potentials are lowest for $\text{Fe}_{70}\text{Pd}_{30}$ in all cases except at pH 6 where they are similar to $\text{Fe}_{65}\text{Pd}_{35}$. The critical potentials are summarized in Table 4.7 and color

coded by type. Both pitting potential dependency and the repassivation effect is likely compositionally dependent [29, 30]. Other alloy systems, such as stainless steel, rely on elements (Cr and Mo) in solid solution to increase passive layer formation [30]. The solid solution effect in these alloys seems to dominate the structure effect and similar passivating composition thresholds are seen for bcc, fcc and martensitic stainless steels [29].

Table 4.7. Table of critical potentials (V_{SCE}). Colored shading is indicates the operating corrosion mechanism. Blue shaded boxes are indicative of dealloying, Red indicates pitting, and Green indicates uniform-type dissolution showing grain specific morphological faceting. To convey the potential dependence of dissolution, the critical potential for the Fe-Pd alloys during active dissolution (e.g., see Figure 4.14) is defined as the potential at a current of 10^{-4} A/cm².

Solution	1 M HCl	0.1 M HCl	0.01 M HCl	0.06 M NaCl	0.6 M NaCl	2 M NaCl
pH	0	1	2	6	6	11
Fe ₇₀ Pd ₃₀	0.27	0.16	-0.01*	0.42	0.38	0.44
Fe ₆₅ Pd ₃₅	0.3	0.37	0.45†	0.44	0.38	0.55
Fe ₅₀ Pd ₅₀	0.37	0.42	0.51†	0.49	0.46	0.58
Fe	active	active	active	active	active	-0.26
Pd	0.63‡	0.68‡	immune	immune	immune	immune

* intergranular corrosion is seen, † does not fully activate, ‡ increase in current density from capacitive (non-Faradaic current) due to Cl⁻ complexation

To discuss the Fe-Pd system the effect of composition and effect of structure must be separated. The possibility of a critical alloying concentration to induce passivity or drastically diminish dissolution rate must be discussed. This argument is similar to 12 at% Cr required for passivity in steel [31-33]. At the critical concentration of the oxide forming solute a geometric based argument that a specific concentration is required to form an oxide.

A similar argument can be made about a non-dissolving species (Pd) impeding dissolution of a species favorable to dissolution (Fe) by forming more dissolution

resistant Fe-Pd bonds. Higher alloying concentrations of Pd would lead to each Fe atom having a higher nearest neighbor concentration. In the case of a disordered structure, the compositionally random arrangement could further improve dissolution resistance. The disordered surface can form a surface with Fe atoms bonded to an above average number of Pd atoms compared to a periodic crystalline structure. A periodic structure is constrained to certain nearest neighbor (NN), 2nd NN concentration, etc. If, say, a hypothetical threshold concentration were required to forestall dissolution and the periodic structure is slightly below this concentration threshold. The random fluctuations in NN concentration in the disordered state leads to a continuum of states of binding energy and therefore susceptibility to dissolution. The most susceptibly bound Fe atoms would dissolve and an overall surface richer in beneficial states than the periodic nature would be the effective surface. Thus, the effective concentration of beneficial solutes is higher in a disordered case. The compositionally disordered effect is explored in Chapter 5 and 6. In this chapter, the role of composition would likely dominate the disordered effect.

Both arguments apply to the passive case where Fe forms an oxide and Pd is either immune to dissolution or also forms an oxide. If the critical concentration required to form a protective layer of noble atoms or passive film is between 30 and 35 at% Pd, then below this concentration there would be a drastic increase in susceptibility to corrosion.

Indeed, this seems true in the 0.1 M and 1 M HCl solution where the dissolution leads to the formation of a Pd enriched region of the surface (Figure 4.17, Figure 4.20) in

the case of the $\text{Fe}_{70}\text{Pd}_{30}$ alloy and no significant preferential dissolution occurs in the higher Pd content alloys. It is important to consider the parting limit of the alloy. The parting limit is defined as “minimum concentration of the more noble component of an alloy above which dealloying does not occur” [34]. Cu-Pd in SO_4^{2-} solution has a parting limit between 20 and 30 at% Pd [35]. In 12 M LiCl solution the parting limit of AgPd, CuPd and NiPd is less than 20 at% Pd [36]. It is possible that the parting limit of Fe-Pd alloys in HCl solution could be between 30 and 35 at% and above this limit there is not enough Fe to enable bulk dealloying by preferential dissolution.

Both $\text{Fe}_{65}\text{Pd}_{35}$ and $\text{Fe}_{50}\text{Pd}_{50}$ exhibit congruent dissolution instead of dealloying. Both also exhibit significant dissolution compared to the high purity Pd case (Figure 4.14). This suggests a mechanistic change from preferential dissolution to more uniform dissolution of the surface in acidic HCl environments. In addition to the composition effect, the change to a martensitic structure is likely also playing a role in this behavior.

In the passive environments, there is no indication of drastic changes in the critical potential for pitting due to the martensitic structure in $\text{Fe}_{70}\text{Pd}_{30}$. There is a fairly linear relationship between pitting potential and alloying content in the environments studied. That is, there are no huge gaps between measured pitting potentials and also the pit morphologies are similar. Thus, it is unlikely that a critical alloying concentration of Pd for loss of passivity in these environments has been met.

4.7.2 Effect of Structure and Orientation: Dissolution Revealed Microstructure

After dissolution of the disordered fcc structure a grain dependent morphology is revealed. Some grains appear ‘shiny’ and have dissolved less than other neighboring

grains. The cases where this is true are: Fe₅₀Pd₅₀ 2M NaCl pH 11 solution (Figure 4.29), Fe₆₅Pd₃₅ 0.1 M HCl solution (Figure 4.13) and both Fe₆₅Pd₃₅ and Fe₅₀Pd₅₀ 1 M HCl solution (Figure 4.23). There appears to be a composition and ‘corrosion severity’ dependence.

In the case of 2 M NaCl solution at pH 11 (Figure 4.29), the surface of the Fe₅₀Pd₅₀ composition shows this behavior. Yet, in the case of the lower Pd concentration in Fe₆₅Pd₃₅ typical pitting behavior is seen. The Pd concentration is likely not high enough in Fe₆₅Pd₃₅ to impede dissolution to the point of revealing the grain dependent behavior. Another interpretation is that there is an underlying change in the ability to form an Fe-based oxide in the Fe₅₀Pd₅₀ compared to the higher Fe content alloys.

In the case of the Fe₆₅Pd₃₅ in 0.1 M HCl solution, the grain surface features do not appear in the Fe₅₀Pd₅₀ state due to the solution severity/conditions not causing significant dissolution (Figure 4.13). There is some indication of this behavior on a few grains, but overall the corrosion appears uniform across the polycrystalline surface. In more severe 1 M HCl solution exposures, grain dependent dissolution is also seen for Fe₅₀Pd₅₀. In Figure 4.23, each grain for Fe₅₀Pd₅₀ exhibits characteristic structural faceting and an apparent characteristic dissolution depth. The exploration of this behavior for disordered (introduced here) and ordered Fe₅₀Pd₅₀ is studied at length in Chapter 5 and 6.¹⁹

4.8 Conclusion

The high dissolution susceptibility of Fe₇₀Pd₃₀ in acidic environments is attributed to the role of the alloying concentration which enables preferential dissolution of Fe and

¹⁹ The role of structure is studying by comparing the fcc to the pT structural state at the same composition (thereby removing the role of the Pd alloying effect)

subsequent reorganization of a Pd rich layer. Congruent dissolution is observed for Fe₆₅Pd₃₅ and Fe₅₀Pd₅₀ in acidic HCl environments. In pitting environments, an increase in Pd alloying concentration increases the critical pitting potential. Fe₆₅Pd₃₅ and Fe₅₀Pd₅₀ shows dissolution induced grain specific structural facets after dissolution in HCl environments. Similar behavior is seen in Fe₅₀Pd₅₀ basic environments after passive layer breakdown likely due to acidification of the solution.

These experiments revealed an ideal set of conditions to study the role of structure with no composition variation in the disordered (fcc) and ordered (pT) states of Fe₅₀Pd₅₀. In particular, the grain specific faceted structure suggests that the atomic arrangement is important. This work importantly established that no bulk preferential dissolution of Fe₅₀Pd₅₀ occurs during dissolution. These experiments provide a framework for the study of the role of structure on corrosion properties which are presented in Chapter 5 and 6.

4.9 References

1. Furuya, Y., N.W. Hagood, P. Kimura, and T. Watanabe, *Shape memory effect and magnetostriction in rapidly solidified Fe-29.6 at %Pd alloy*. Materials Transactions Jim, 1998. **39**(12): p. 1248-1254.
2. Klemmer, T., D. Hoydick, H. Okumura, B. Zhang, and W.A. Soffa, *Magnetic Hardening and Coercivity Mechanisms in L1(0) Ordered FePd Ferromagnets*. Scripta Metallurgica Et Materialia, 1995. **33**(10-11): p. 1793-1805.
3. Miyazaki, S., K. Otsuka, and C. Wayman, *Medical and dental applications of shape memory alloys*. 1998: Cambridge University Press.
4. Cheng, H.X., H.C. Wang, J. Zhang, R.Q. Zhang, Z.T. Yu, J.L. Niu, Z.X. Li, and L. Zhou, *Effects of Surface Palladium/Ferrum Film on the Biocompatibility of 316L Stainless Steel*. Rare Metal Materials and Engineering, 2008. **37**(11): p. 2037-2040.
5. Kimura, H. and T. Sohmura, *Application of Fe-Pd System Shape Memory Alloys to Dentistry(Part 2) : On the Anodic Polarization Behavior and Biological Reaction*. Journal of the Japanese Society for Dental Materials and Devices, 1984. **3**(6): p. 821-825 %U <http://ci.nii.ac.jp/naid/110002990253/en/>.

6. Kimura, H. and T. Sohmura, *Application of Fe-Pd System Shape Memory Alloys to Dentistry : Part 1 On the Shape Memory Effect, Corrosion Resistance and Mechanical Properties*. Journal of the Japanese Society for Dental Materials and Devices, 1984. **3**(4): p. 500-507 %U <http://ci.nii.ac.jp/naid/110002988680/en/>.
7. Yiping, L., G.C. Hadjipanayis, C.M. Sorensen, and K.J. Klabunde, *Structural and Magnetic-Properties of Ultrafine Fe-Pd Particles*. Journal of Applied Physics, 1994. **75**(10): p. 5885-5887.
8. Soffa, W.A. and D.E. Laughlin, *Decomposition and Ordering Processes Involving Thermodynamically 1st-Order Order-]Disorder Transformations*. Acta Metallurgica, 1989. **37**(11): p. 3019-3028.
9. Zhang, B. and W.A. Soffa, *Magnetic Domains and Coercivity in Polytwinned Ferromagnets*. Physica Status Solidi a-Applied Research, 1992. **131**(2): p. 707-725.
10. Oshima, R., *Successive Martensitic Transformations in Fe-Pd Alloys*. Scripta Metallurgica, 1981. **15**(8): p. 829-833.
11. Reed-Hill, R.E. and R. Abbaschian, *Physical metallurgy principles*. 3rd ed. The PWS-Kent series in engineering. 1992, Boston: PWS-Kent Pub. xv, 926 p.
12. Burton, B.P., *Fe-Pd (Iron-Palladium)*, in *Binary alloy phase diagrams*, T.B. Massalski, Editor. 1990, ASM International: Materials Park, Ohio. p. p 1749-1751.
13. Oshima, R., K. Kosuga, M. Sugiyama, and F.E. Fujita, *Phase-Transition in Fe-Pd Alloys*. Science Reports of the Research Institutes Tohoku University Series a-Physics Chemistry and Metallurgy, 1981. **29**: p. 67-72.
14. Oshima, R. and M. Sugiyama, *Martensite Transformations in Fe-Pd Alloys*. Journal De Physique, 1982. **43**(Nc-4): p. 383-388.
15. Sohmura, T., R. Oshima, and F.E. Fujita, *Thermoelastic Fcc-Fct Martensitic-Transformation in Fe-Pd Alloy*. Scripta Metallurgica, 1980. **14**(8): p. 855-856.
16. Pourbaix, M., *Atlas of electrochemical equilibria in aqueous solutions*. 1974, National Association of Corrosion Engineers: Houston, Tex. p. 307-321, 358-363.
17. Puigdomenech, I., *MEDUSA: Make Equilibrium Diagrams Using Sophisticated Algorithms*. 2009: Stockholm, Sweden.
18. Jovancicevic, V., J.O. Bockris, J.L. Carbajal, P. Zelenay, and T. Mizuno, *Adsorption and Absorption of Chloride-Ions on Passive Iron Systems*. Journal of the Electrochemical Society, 1986. **133**(11): p. 2219-2226.
19. Bohni, H. and H.H. Uhlig, *Environmental Factors Affecting the Critical Pitting Potential of Aluminum*. Journal of the Electrochemical Society, 1969. **116**(7): p. 906-910.
20. Pou, T.E., O.J. Murphy, V. Young, J.O.M. Bockris, and L.L. Tongson, *Passive films on iron: the mechanism of breakdown in chloride containing solutions*. Journal of the Electrochemical Society, 1984. **131**: p. 1243.
21. Lin, L.F., C.Y. Chao, and D.D. Macdonald, *A Point-Defect Model for Anodic Passive Films .2. Chemical Breakdown and Pit Initiation*. Journal of the Electrochemical Society, 1981. **128**(6): p. 1194-1198.

22. Chin, R.J. and K. Nobe, *Electrodissolution Kinetics of Iron in Chloride Solutions*. Journal of the Electrochemical Society, 1972. **119**(11): p. 1457-1461.
23. McCafferty, E. and N. Hackerman, *Kinetics of Iron Corrosion in Concentrated Acidic Chloride Solutions*. Journal of the Electrochemical Society, 1972. **119**(8): p. 999-1009.
24. Brandenburg, K., *Modelling performed using Diamond Crystallography Software* (<http://www.crystalimpact.com/>).
25. Abrahamson, E.P. and S.L. Lopata, *The Lattice Parameters and Solubility Limits of Alpha Iron as Affected by Some Binary Transition-Element Additions*. S. L. Trans. Met. Soc AIME 236, 1966. **76**.
26. Swanson, H.E., R.K. Fuyat, and G.M. Ugrinic, Natl. Bur. Stand. (U.S.) Circ. 539, 1955. **3**: p. 75.
27. Aburada, T., J.M. Fitz-Gerald, and J.R. Scully, *Pitting and Dealloying of Solute-Rich Al-Cu-Mg-based Amorphous Alloys: Effect of Alloying with Minor Concentrations of Nickel*. Journal of the Electrochemical Society, 2011. **158**(9): p. C253-C265.
28. Joy, D.C., *Monte Carlo modeling for electron microscopy and microanalysis*. Oxford series in optical and imaging sciences 9. 1995, New York: Oxford University Press. viii, 216 p.
29. Sedriks, A.J. and Electrochemical Society., *Corrosion of stainless steels*. 2nd ed. Corrosion monograph series. 1996, New York: Wiley. xviii, 437 p.
30. Szklarska-Smialowska, Z., *Pitting and crevice corrosion*. 2005, Houston, Tex.: NACE International : Corrosion Society. xiii, 590 p.
31. McCafferty, E., *Relationship between graph theory and percolation approaches in the passivity of Fe-Cr binary alloys*. Journal of the Electrochemical Society, 2008. **155**(10): p. C501-C505.
32. Sieradzki, K. and R.C. Newman, *A Percolation Model for Passivation in Stainless-Steels*. Journal of the Electrochemical Society, 1986. **133**(9): p. 1979-1980.
33. Fujimoto, S., R.C. Newman, G.S. Smith, S.P. Kaye, H. Kheyrandish, and J.S. Colligon, *Passivation thresholds in iron-chromium alloys prepared by ion-beam sputtering*. Corrosion Science, 1993. **35**(1-4): p. 51-55.
34. Baboian, R., *Corrosion tests and standards : application and interpretation*. 2nd ed. ASTM manual series. 2005, West Conshohocken, PA: ASTM International. xii, 882 p.
35. Pickering, H.W., *Characteristic features of alloy polarization curves*. Corrosion Science, 1983. **23**(10): p. 1107-1120.
36. Landolt, D., *Contributions of surface analysis to corrosion science: Selective dissolution and oxidation phenomena in alloy corrosion*. Surface and Interface Analysis, 1990. **15**(7): p. 395-404.

5 Electrochemical Behavior of pT and fcc Fe₅₀Pd₅₀ during Active, Passive and Localized Corrosion

5.1 Abstract

The effects of the differences in structure between disordered fcc and ordered pT Fe₅₀Pd₅₀ on electrochemical corrosion behavior are discussed. These two structural states were studied in the passive, active, and passive-localized corrosion breakdown conditions through studies encompassing a wide range of pH and solution environments, including those with and without Cl⁻.

Significant differences in the behavior of fcc and pT Fe₅₀Pd₅₀ in the active state in acidic Cl⁻ environments were observed. Dissolution features of the fcc Fe₅₀Pd₅₀ structure exhibit grain dependent characteristic 3-fold and 4-fold features during initial stages of dissolution in Cl⁻. Increased dissolution leads to specific grain specific morphological faceting. In the pT structure, initial dissolution highlights show a microstructural dependence, but increased dissolution produced behavior where there was no grain dependence. Similar behavior was observed in passive and passive-localized breakdown conditions for fcc and pT Fe₅₀Pd₅₀. Conditions were identified where congruent dissolution of a binary Fe₅₀Pd₅₀ alloy could be studied in the active state and as a function of crystal facet orientation.

As a supplement to these studies, the role of Pd as a hydrogen electrode was evaluated. Rapid hydrogen evolution reaction depended on structure under open circuit potentials. This behavior was correlated to the role of H absorption in the two different structures of the Fe₅₀Pd₅₀ alloy.

5.2 Introduction

This chapter focuses on the corrosion behavior of the equiatomic composition, Fe₅₀Pd₅₀ alloys. At this composition both a disordered fcc phase and an ordered pT structure can be formed. By forming Fe₅₀Pd₅₀ alloys of these two structures with similar grain sizes, the role of structure on corrosion can be studied in the absence of compositional differences between the two structural states.

5.2.1 Fe₅₀Pd₅₀ Alloy Synthesis and Phase Transformation Characteristics

The high temperature austenitic γ -phase is a disordered fcc solid solution. Upon cooling, Fe₅₀Pd₅₀ transforms by a nucleation and growth mechanism to an ordered primitive tetragonal phase, L1₀. The L1₀ phase is the single phase field at 50-60 at% Pd. The phase diagram and relevant phases are described in the introduction to the Fe-Pd alloy system in Chapter 4.

The disordered fcc and L1₀ unit cells are shown in Figure 5.1 and Figure 5.2, respectively. The ordered primitive tetragonal phase, L1₀, has symmetry P4/mmm with lattice constants $a=0.3852$ nm and $c=0.3723$ nm. [1]. The L1₀ structure has Pd atoms at the $c=1/2$ face positions and Fe atoms at the vertices. The disordered γ fcc phase has site occupancy factors (S.O.F.) of 0.5 for Fe and Pd at the lattice sites. The fcc phase has symmetry Fm-3m and lattice parameter $a=0.3804$ nm [2]. The radial distribution of atoms from a given atom is shown for the fcc and L1₀ structures in Figure 5.3 and Figure 5.4, respectively. These plots show the expected radial distance from an atom to its neighboring atoms. In the case of the disordered fcc structure, within 0.30 nm of a given atom there are 12 atoms each with equal probability to be either Fe or Pd. An additional 6

atoms lie between 0.30 and 0.40 nm. For the pT structure, the structure is expanded and there are fewer atoms within this range: there are 4 Pd and 4 Fe atoms within 0.30 nm of a given Pd atom and 10 total Pd atoms with 0.40 nm.

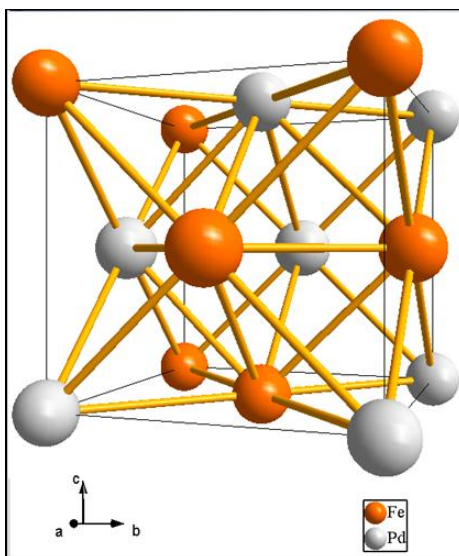


Figure 5.1. Schematic model $\text{Fe}_{50}\text{Pd}_{50}$ fcc disordered γ phase with representative random site occupancy shown. The fcc phase (Fm-3m) has lattice constant $a=0.3804$ nm and a site occupancy factor of 0.5, the atomic ratio. The density is 9.790 g/cm³. Model created using Diamond Crystallography Software [3].

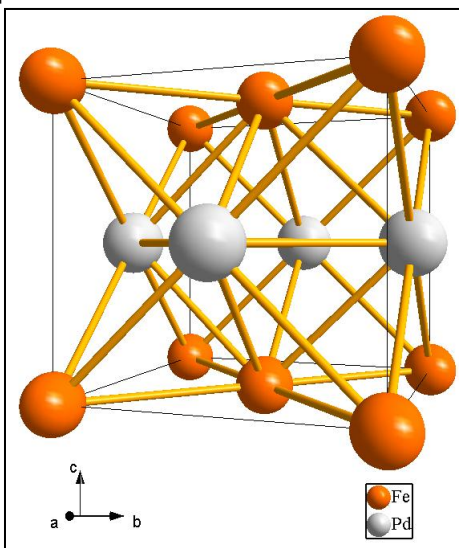


Figure 5.2. Schematic model of $\text{Fe}_{50}\text{Pd}_{50}$ $L1_0$ structure. The $L1_0$ phase has symmetry P4/mmm with lattice constants $a=0.3852$ nm and $c=0.3723$ nm and a density of 9.755 g/cm³. Pd atoms lie at the $c=1/2$ lattice sites while Fe atoms occupy the vertices. Model created using Diamond Crystallography Software [3].

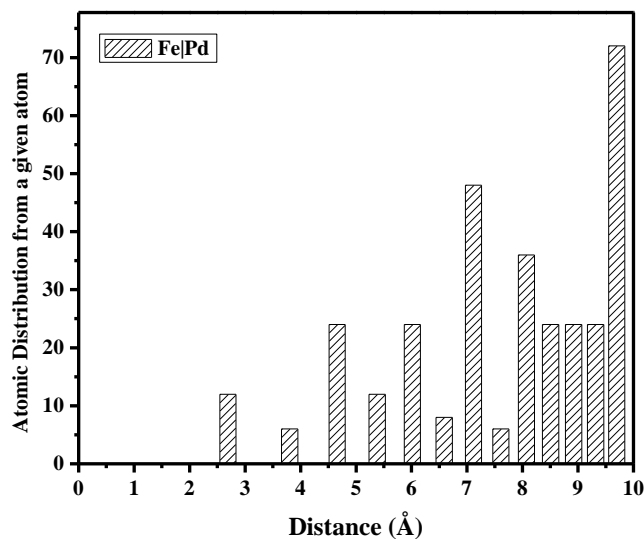


Figure 5.3. The number of atoms at a given distance from a given atom in the disordered fcc structure. Each atom site has an occupancy of 0.5 for Fe and Pd. Interatomic distances determined using Diamond Crystallography Software [3].

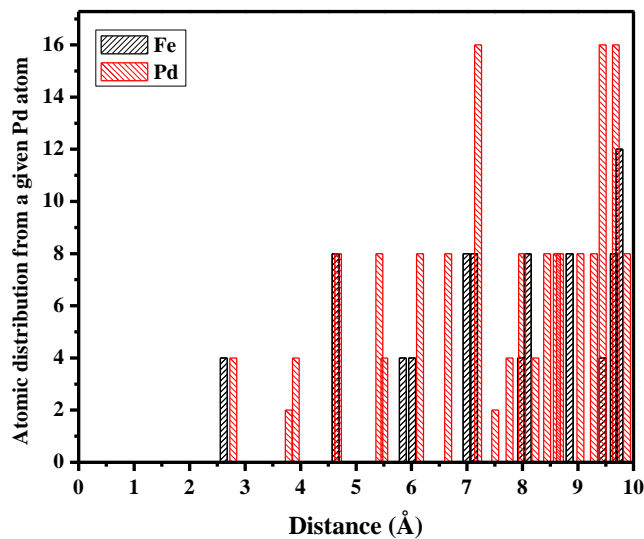


Figure 5.4. The number of Fe and Pd atoms from a given atom in the ordered pT structure. Interatomic distances determined using Diamond Crystallography Software [3].

5.3 Critical Unresolved Issues

The objective of this chapter is to determine the role of structure on active, passive and localized corrosion behavior of fcc and pT Fe₅₀Pd₅₀. This comprehensive set of studies will elucidate under what corrosion regimes structure plays a definitive role on the corrosion behavior of the two structural states of Fe₅₀Pd₅₀.

5.4 Experimental

The Fe₅₀Pd₅₀ alloy was produced by the arc-melting technique using high purity 99.99% Fe and 99.999% Pd under an argon atmosphere. Prior to any heat treatments, alloy sections were first encapsulated in quartz tubes under an argon atmosphere. The cast alloy Fe₅₀Pd₅₀ was cold rolled to approximately 0.5 mm. To remove the induced deformation and texture, the alloy was recrystallized at 1100 °C for 24 hours and then water quenched. A final annealing step for each composition was performed followed by water quenching. X-ray diffraction (XRD) characterization was performed using a Scintag XDS-2000 diffractometer with a Cu-K α source ($\lambda = 0.1541$ nm). XRD spectra measurements were conducted in the $\theta/2\theta$ configuration. The surface morphology was characterized by optical microscopy and SEM using a JEOL 6700F with an accelerating voltage of 5 keV and a working distance of 15 mm. EDS analysis was conducted at 15 kV and a working distance of 15 mm. At this accelerating voltage the depth of interaction is roughly 0.33 μm .

Electrochemical measurements were conducted using a traditional 3-electrode setup with an exposed electrically isolated working electrode consisting of polycrystalline Fe₅₀Pd₅₀ sample or Pd and Fe samples. The reference electrode was a saturated calomel

type electrode, SCE, or in Cl^- free environments was a saturated $\text{Hg}/\text{Hg}_2\text{SO}_4$, MSE. The counter electrode was a platinum mesh. Chemical solutions were produced using reagent grade chemicals and pure water (resistivity $18.2 \text{ M } \Omega / \text{cm}$) produced by an Academic MilliQ filtration system (MilliPore). Prior to electrochemical experiments the solution was deaerated for at least 2 hours by vigorous sparging of nitrogen through the solution. Polarization experiments were conducted using a Gamry PCI4 potentiostat and a Biologic SP-150 potentiostat. The scan rate was typically 1 mV/s and during cyclic scans the current reverse threshold was typically 0.1 mA (around 0.01 A/cm^2). High purity polycrystalline samples of Fe and Pd were used in comparative electrochemistry experiments. Exposed samples had an exposed surface area of approximately 0.005 cm^2 .

5.5 Results

5.5.1 Characterization of $\text{Fe}_{50}\text{Pd}_{50}$ Microstructures

Annealing in the disordered region at $950 \text{ }^\circ\text{C}$ for 10 hours and water quenching produced a single phase alloy with disordered fcc structure. Annealing at $605 \text{ }^\circ\text{C}$ produced a single phase alloy with ordered pT structure. The phase identification of the different heat treatments of the $\text{Fe}_{50}\text{Pd}_{50}$ alloy is shown in Figure 5.10 for the disordered fcc phase and Figure 5.11 for the pT phase. The grain size was measured as a function of heat treatment duration, summarized in Table 2.3. After annealing for 4 weeks, the grains size ranged from 15 to $250 \text{ } \mu\text{m}$ with an average grain size of $39 \text{ } \mu\text{m}$, which is comparable

to the fcc grain size²⁰. Samples from this heat treatment were used in the electrochemical testing. A typical polytwinned surface of the Fe₅₀Pd₅₀ pT sample is shown in the SEM micrographs in Figure 5.7.

Table 5.1. Annealing temperature, resulting phase and grain size of Fe₅₀Pd₅₀ alloy.

Sample	Heat Treatment	Phase	Average Grain Size (μm)
Fe ₅₀ Pd ₅₀	10 hours at 950 °C, water quenched	γ (fcc)	28 [†]
Fe ₅₀ Pd ₅₀	100 hours at 605 °C, water quenched	L1 ₀	~5*
Fe ₅₀ Pd ₅₀	2 Weeks (330 hours) at 605 °C, water quenched	L1 ₀	~10*
Fe ₅₀ Pd ₅₀	4 Weeks (670 hours) at 605 °C, water quenched	L1 ₀	39 [‡]

[†]Determined by EBSD mapping of grain orientations. *Measured by ion etching, approximate.

[‡]Measured using an etched surface. Etching performed by short duration exposure in 1 M HCl solution at an applied potential of 0.45 V_{SCE}.

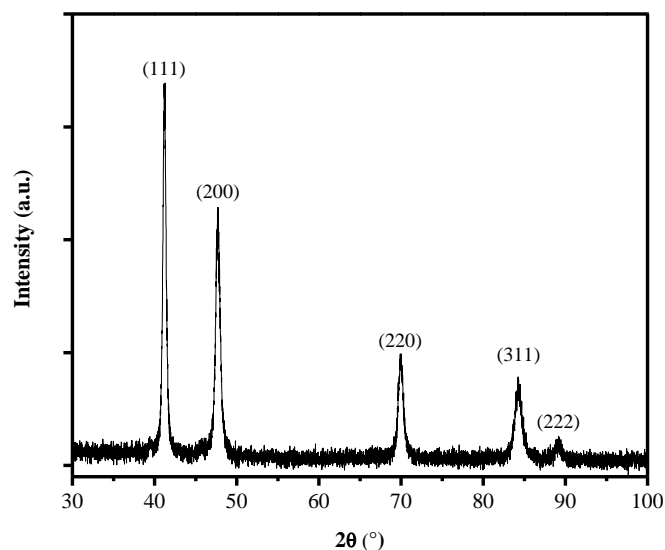


Figure 5.5. X-ray diffraction spectrum of the disordered fcc Fe₅₀Pd₅₀ sample after annealing at 950 °C for 10 hours and water quenched. The 5 indexed peaks all corresponded to the fcc γ-phase structure with lattice parameter $a = .3804$ nm and site occupancy coefficient of 0.5 for both Fe and Pd.

²⁰ The Fe₅₀Pd₅₀ pT grain growth was fit using $d \propto k \cdot t^{1/2}$ where d is the average grain size and k is an Arrhenius type constant. The constant term from the grain growth fit is $2.93 \cdot 10^{-5}$ μm/s^{1/2} with a root mean square error of 4.77.

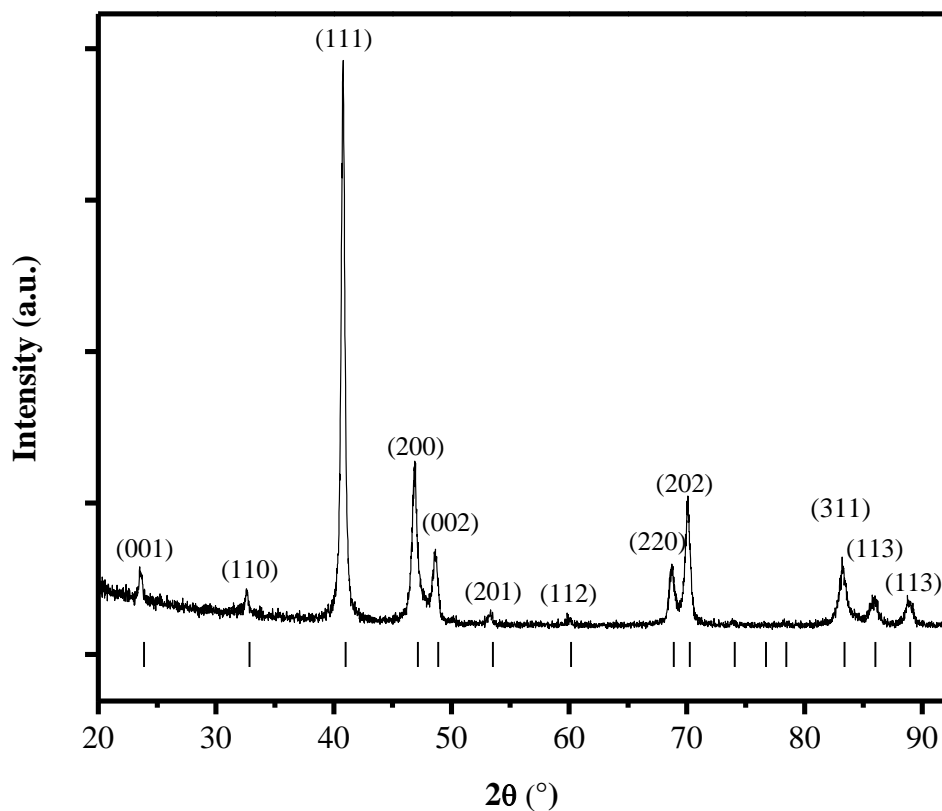


Figure 5.6. X-ray diffraction spectrum of the ordered pT $\text{Fe}_{50}\text{Pd}_{50}$ sample after annealing at 605 °C for 30 days and water quenched. The indexed peaks, indicated by vertical dashes and labeled, corresponded to the pT L1_0 phase which has space group $P4/mmm$ with lattice constants $a=3.852\text{Å}$ and $c=3.723\text{Å}$. [1]. In the L1_0 structure, Pd atoms occupy the $c=1/2$ lattice positions and Fe atoms at the unit cell corners.

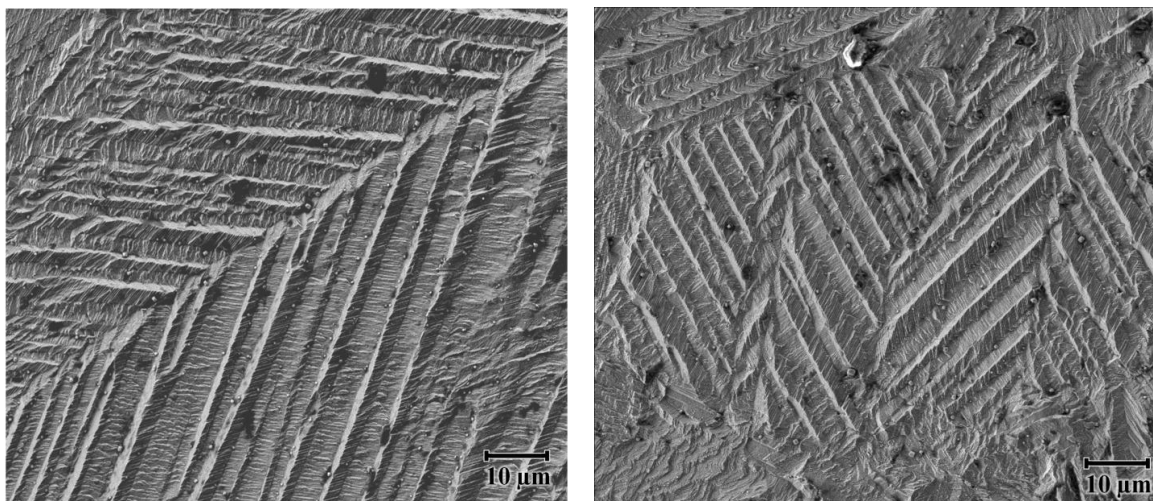


Figure 5.7. SEM micrographs of the polytwinned structure in pT $\text{Fe}_{50}\text{Pd}_{50}$ after potentiostatic polarization at 0.45 V_{SCE} for 400 s and a total accumulated charge density of 10.5 C/cm^2 .

5.5.2 Electrochemical Behavior in the Active State

5.5.2.1 Electrochemical Behavior in Active non-Cl⁻ Containing Solutions

The open circuit and E-log*i* behavior 0.5 M H₂SO₄ solution are shown in Figure 5.8. During the open circuit period, the potentials of both structural states of Fe₅₀Pd₅₀ rise toward the more noble Pd open circuit potential. During the E-log*i* scan, Fe undergoes active dissolution. Pd shows non-Faradaic current density-potential dependence until an increase at a potential near the Pd/PdO half-cell potential indicative of oxide formation. The low current density during the reverse scan, after reaching the apex potential, is due to the offsetting (negative) PdO reduction reaction which occurs below the Pd/PdO half-cell potential. Both structural states of the Fe₅₀Pd₅₀ alloys show similar current density-potential behavior similar to Pd. The current of the Fe₅₀Pd₅₀ alloys increases at the Pd/PdO potential, indicating formation of a protective oxide, but as the potential decreases from the apex current density it is slightly increased. This behavior is typical of dissolution reactions.

Cyclic scans at a scan rate of 20 mV/s were run from -0.6 to 0.3 V_{SCE}, as indicated by the arrows between the dashed lines in Figure 5.8, are shown in Figure 5.9. This potential range allows investigation of incipient Fe dissolution during the first cycles by measuring any current associated with Fe dissolution. However, this current will be hard to separate from any absorbed H oxidation. Measurements were made in 0.1 M, 0.5 M and 1 M H₂SO₄. The open circuit potential increases with time for both structural states in all three solution concentrations. The total anodic charge of both structural states followed similar trends, and both were lower than Pd. Potentiostatic polarization at the

apex potential, $0.3 \text{ V}_{\text{SCE}}$, of these scans, Figure 5.10, shows Pd having a higher sustained oxidation current density than either structural state of $\text{Fe}_{50}\text{Pd}_{50}$ after 300 s. The Pd open circuit potential is controlled by the HER and absorbed H oxidation reactions instead of a Pd oxidation reaction. No mass loss (surface damage) is seen for Pd at applied potentials below Cl^- dissolution. This effect is likely due to Pd acting as a hydrogen electrode (see the Appendix, Section 5.8). During the first 300 s, the increased current density for both states is higher than the Pd current density. This current likely corresponds to Fe dissolution from the $\text{Fe}_{50}\text{Pd}_{50}$ alloys and is higher in the case of the disordered fcc structural state.

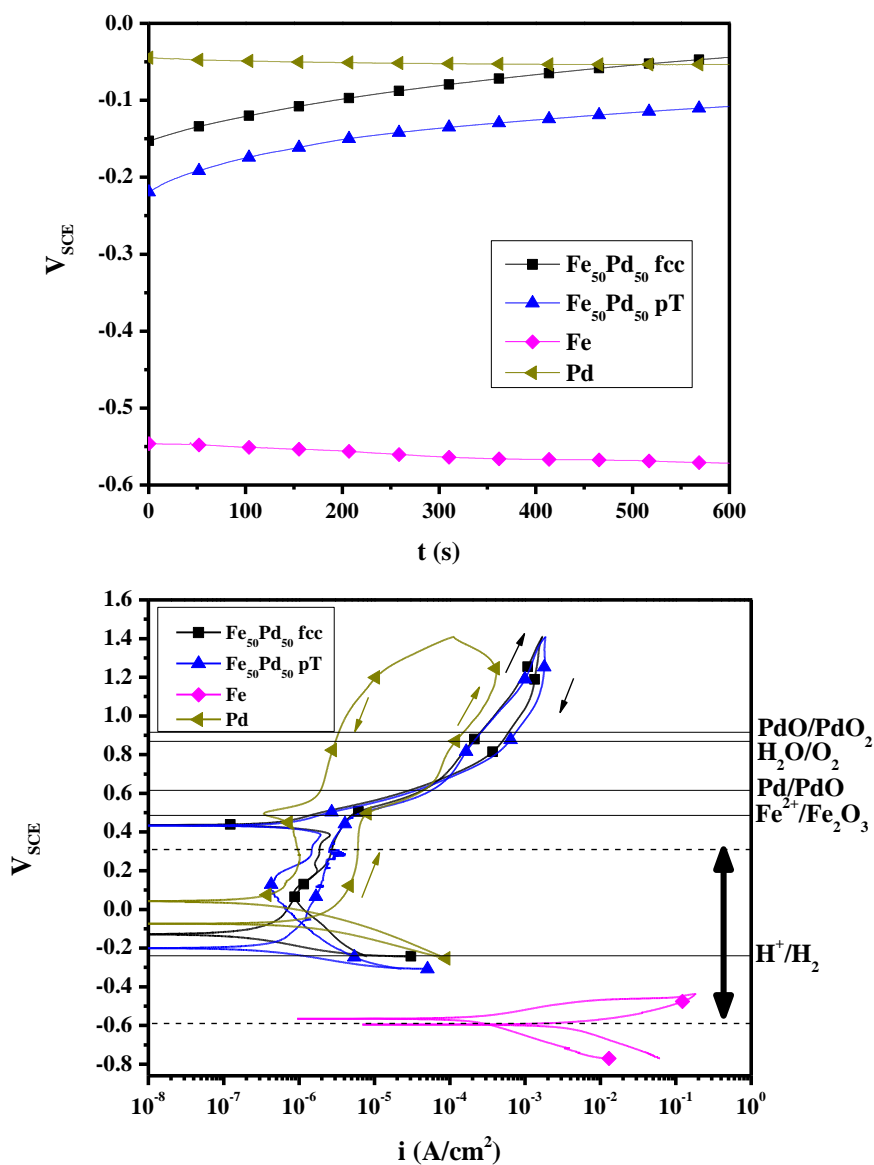


Figure 5.8. Open circuit potential (top) and E-log i behavior (bottom) in deaerated 0.5 M H_2SO_4 solution at a scan rate of 1 mV/s. Dashed lines indicate the potential range for cyclic voltammetry potential sweep. For reference, the potentials of various oxidation reactions are shown (solid lines) at pH 1 and species concentrations of 10^{-6} M. Oxidation of Fe to aqueous Fe^{2+} cation occurs at -0.86 V_{SCE}.

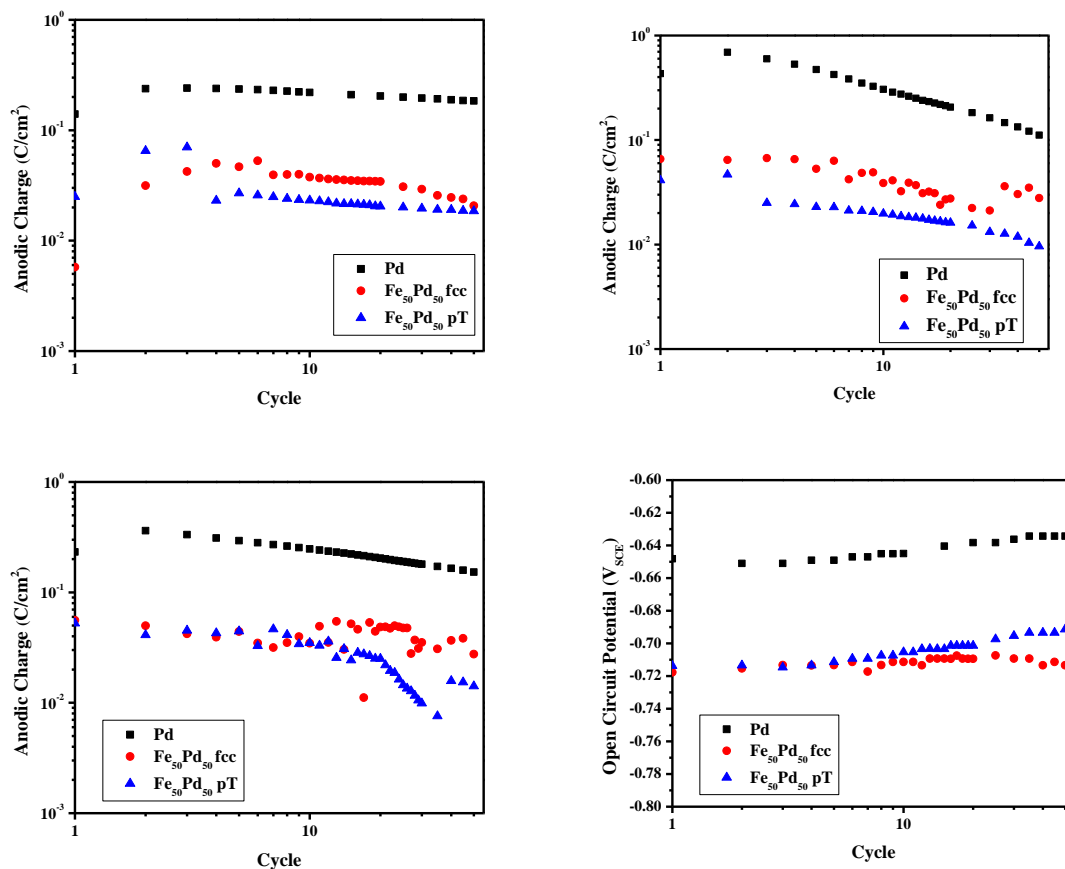


Figure 5.9. Total anodic charge during potential cycles from -0.59 to 0.31 V_{SCE} at a scan rate of 20 mV/s in deaerated 0.1 M (top-left), 0.5 M (top-right), 1 M (bottom-left) H₂SO₄ solution. The total anodic charge is similar for both structural states in all three solution concentration. A representative plot of the open circuit behavior in 0.5 M H₂SO₄ solution is shown (bottom-right). The OCP for both fcc and pT structural states increases in all concentrations.

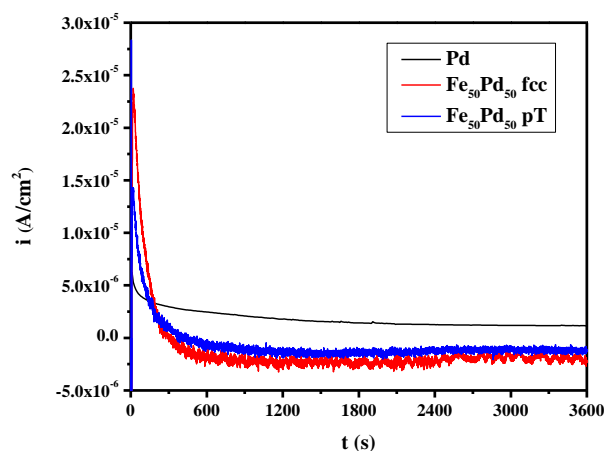


Figure 5.10. Potentiostatic polarization in deaerated 1 M H₂SO₄ at 0.31 V_{SCE}. Both structural states show initial current decay to very small current densities and slightly higher overall current in fcc Fe₅₀Pd₅₀. The high current density on Pd is likely due to an H oxidation current density. No surface damage was observed (see appendix).

5.5.2.2 Electrochemical Behavior in Active Cl⁻ Containing Solutions

The polarization behavior in 0.1 M and 1 M HCl solution are shown in Figure 4.12 and Figure 5.12, respectively. The structural states of the Fe₅₀Pd₅₀ alloys are compared to high purity polycrystalline Fe and Pd. During the open circuit measurement, Fe has a negative open circuit potential while Pd has an intermediate value 0.55 V higher. As was introduced in the preceding section, Pd acts as a hydrogen electrode (see appendix, Section 5.8). The fcc and pT Fe₅₀Pd₅₀ alloys have the highest open circuit potential in both solution concentrations and over the first 200 s the potential increases and stabilizes at 0.2 V_{SCE}. This increase is likely due to the interplay between the fast kinetics of the hydrogen evolution reaction on the Pd containing Fe₅₀Pd₅₀ alloy and the restricted oxidation reactions, and not due to ennoblement of the surface layers by Fe dissolution²¹. The open circuit rise and analysis in the case of acidic Cl⁻ containing solutions is presented in Section 5.8.3.

The cyclic polarization behavior, Figure 4.12 and Figure 5.12, shows that high purity Fe dissolves at high current densities at very low over-potentials. Pd remains uncorroded until the critical potential at 0.6 V_{SCE} in both concentrations where dissolution occurs. In 0.1 M HCl solution (Figure 4.12), the polarization of the Fe₅₀Pd₅₀ in the two structural states is similar, but the current density for the pT structural state is higher at potentials above 0.5 V_{SCE}. The fcc structure shows a characteristic peak (the current is briefly independent of potential from 0.5 to 0.55 V_{SCE}, Figure 4.12, near the

²¹ Depth profile XPS results, Ch. 4, indicate only 10 nm (SiO₂ equivalent) of preferential dissolution on the order of a few at % after potentiostatic polarization in 0.1 M HCl solution after a total charge of 0.1 C/cm². Congruent dissolution is seen after polarization at high applied potential in 1 M HCl solution, see Figure 4.22 and Figure 5.21.

apex potential) that is not seen in the pT structure. This behavior is very similar to the behavior of high purity Pd. Potentiostatic polarization, Figure 5.13, in 0.1 M HCl solution at a series of potentials shows good agreement with the current density magnitude at those potentials in the cyclic polarization scan. At most potentials, the total charge is higher in the case of the pT structure.

The surface morphology in Figure 5.14 indicates general dissolution of the Pd surface after polarization to high potentials in 1 M solution. In acidic Cl^- environments, Pd is expected to dissolve and form a PdCl_4^{2-} complex at $0.7 \text{ V}_{\text{SCE}}$ based on thermodynamic principles [4] (see Chapter 4). However, potentiostatic polarization of Pd at $0.45 \text{ V}_{\text{SCE}}$, below the critical dissolution potential from the polarization scans shows no apparent dissolution, see Figure 5.15. The increase in the current density seen at $0.65 \text{ V}_{\text{SCE}}$ likely corresponds to the switch from current primarily due to H oxidation to a dissolution type reaction.

Optical images, Figure 5.16, after the cyclic polarization experiments in 1M HCl indicate that grain anisotropy in terms of the dissolution behavior exists in the case of the fcc structure, but not in the pT structural state. SEM microscopy and potentiostatic polarization were used to further elucidate this behavior. SEM micrographs after the cyclic polarization scan are shown in Figure 5.17. It is apparent that the dissolution is proceeding crystallographically; each grain exhibits characteristic dissolution morphology and structural features are aligned along specific directions. Moreover, incipient dissolution has 3 or 4-fold symmetry depending the grain. This behavior is often

seen in etched surfaces where different crystallographic orientations and dislocations show characteristic etch pit symmetry [5].

Potentiostatic polarization at $0.45 V_{SCE}$ in deaerated 1 M HCl solution was used to compare the behavior of the fcc and pT $Fe_{50}Pd_{50}$ structural states under conditions of congruent dissolution. In the case of the pT structure, Figure 5.18, the current density is higher than in the case of the fcc structure, Figure 5.19. The total charge density (per time) in the pT case is an order of magnitude higher than the fcc structure. The surface morphology of fcc $Fe_{50}Pd_{50}$ shows dissolution that depends specifically on grains. In contrast, while dissolution of the pT surface is not perfectly uniform it does not correlate to each grain. The faceted features are less distinct than the grain size of the pT $Fe_{50}Pd_{50}$ sample. In contrast, the grains in the fcc $Fe_{50}Pd_{50}$ sample have corroded to distinctly different depths. The grain orientation-dissolution depth relationship is presented in Chapter 6.

SEM/EDS analysis was used to show that Fe and Pd are dissolving from both structural states congruently during polarization of the $Fe_{50}Pd_{50}$ alloys at $0.45 V_{SCE}$.²² This analysis was presented in Chapter 4 for the Fe-Pd alloys, including fcc $Fe_{50}Pd_{50}$. The SEM micrographs and compositional analysis across the interface between the insulated and exposed areas are shown for here for the fcc (Figure 4.22) and pT (Figure 5.21) structural states of $Fe_{50}Pd_{50}$. The total charge density on the exposed region of the fcc structure is $3.99 C/cm^2$ and the pT structure is $6.5 C/cm^2$. The fcc structure shows the expected grain dependent morphology. The pT structure shows some grain dependent

²² More than 80% of the characteristic x-rays are generated within the first $0.33 \mu m$ of the surface at an accelerating voltage of 15 kV (See Chapter 4).

morphology that is not seen after increased dissolution (compare Figure 5.21 to Figure 5.18, the latter case total charge density of 11.1 C/cm^2 , nearly 2 times higher than Figure 5.21). The early stage dissolution growth of pT $\text{Fe}_{50}\text{Pd}_{50}$ is also discussed in Chapter 6.

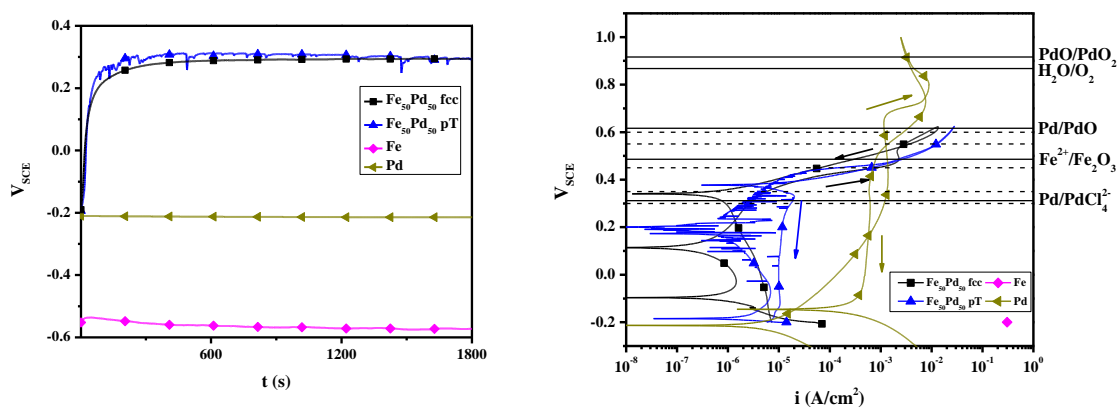


Figure 5.11. Open circuit (left) and Cyclic E-log i (right) behavior in deaerated 0.1 M HCl solution at a scan rate of 1 mV/s (direction E indicated by arrows). Dashed lines indicate potentiostatic polarization potentials. The current for high purity polycrystalline Fe is above the current cutoff threshold and is represented by a single point. For reference, the potentials of various oxidation reactions are shown (solid lines) at pH 1 and species concentrations of 10^{-6} M. Oxidation of Fe to aqueous Fe^{2+} is at $-0.86 V_{\text{SCE}}$ and HER is at $-0.3 V_{\text{SCE}}$.

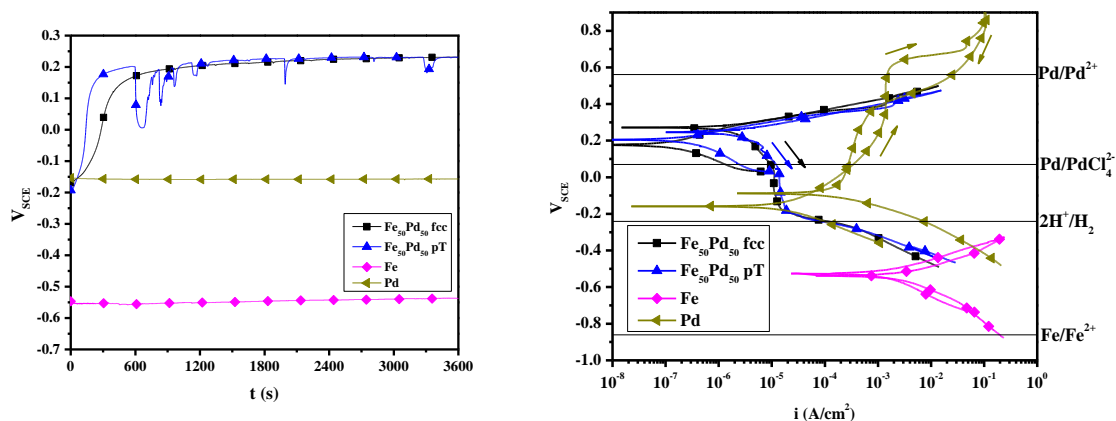


Figure 5.12. Open circuit (left) and Cyclic E-log i (right) behavior in deaerated 1 M HCl solution at a scan rate of 1 mV/s. The dashed line on the E-log i plot indicates the $0.45 V_{\text{SCE}}$ potential used for the potentiostatic polarization experiments. For reference, the potentials of various oxidation reactions are shown (solid lines) at pH 0 and species concentrations of 10^{-6} M.

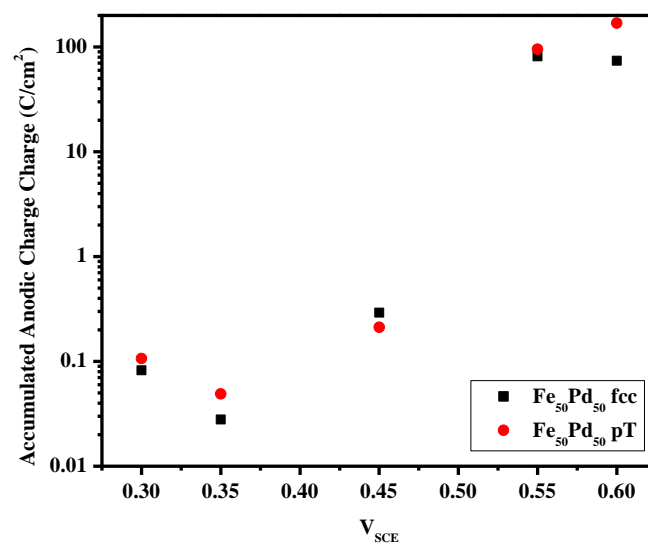


Figure 5.13. Total accumulated anodic charge for Fe₅₀Pd₅₀ fcc and pT during a 2 hour potentiostatic polarization in 0.1 M HCl solution. The structural state with the higher charge at each potential corresponds to the state with higher current density at that potential during cyclic polarization in Figure 4.12.

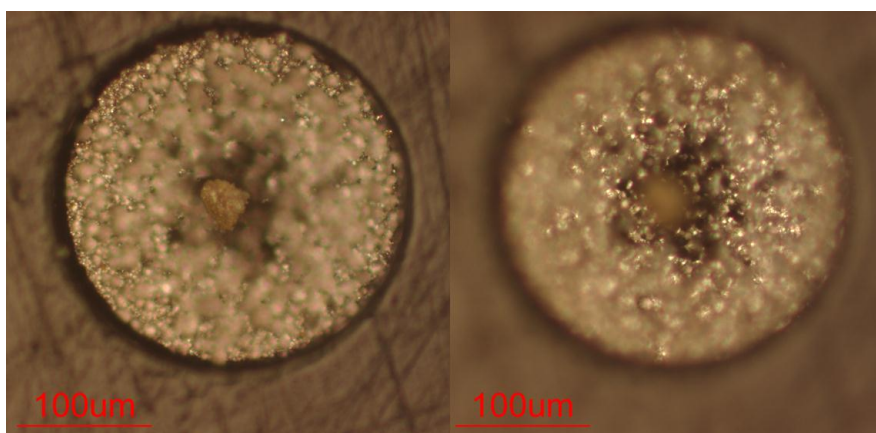


Figure 5.14. Through focus optical micrographs of the Pd surface after polarization to $0.9 V_{SCE}$ in deaerated 1 M HCl solution (Figure 5.12) showing significant Pd dissolution.

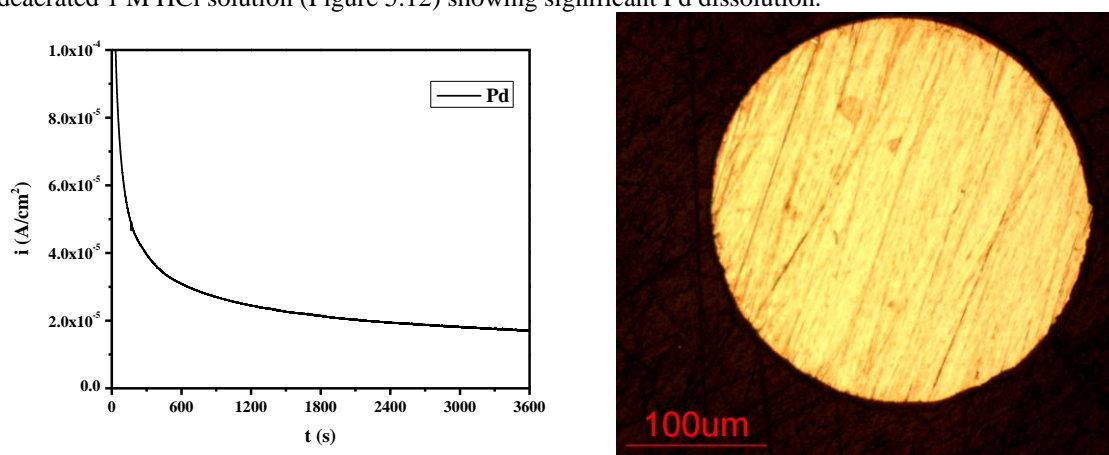


Figure 5.15. Potentiostatic polarization of Pd (left) in deaerated 1 M HCl solution at $0.45 V_{SCE}$ for 3600 s. The optical micrograph shows little corrosion of the surface. It is worth noting that the potential was applied immediately after contact with the solution (no OCP hold) and therefore limited H charging of the Pd, see Section 5.8.

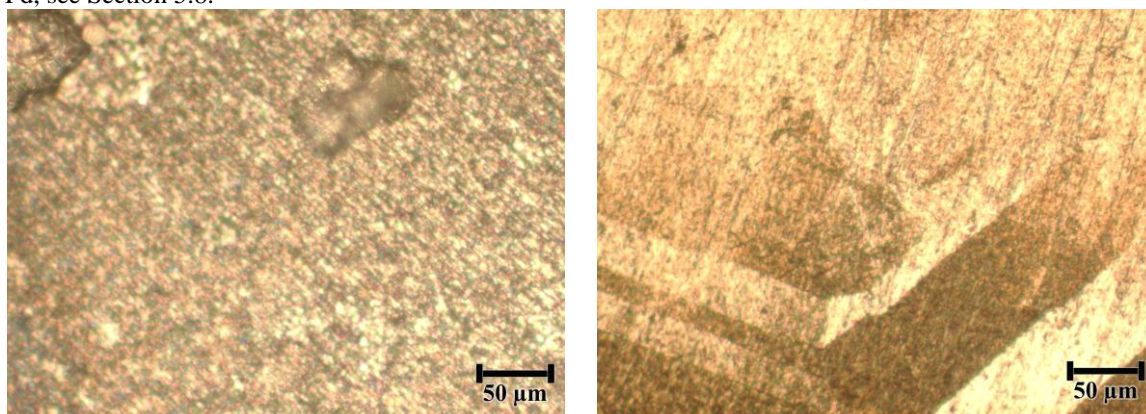


Figure 5.16. Optical micrographs of the surface of pT (left) and fcc (right) $Fe_{50}Pd_{50}$ after polarization in deaerated 1 M HCl solution to $0.6 V_{SCE}$ (Figure 5.12). The pT structural state generally uniform surface morphology with region of increased morphology. The fcc structure shows grain dependent etched-like morphology.

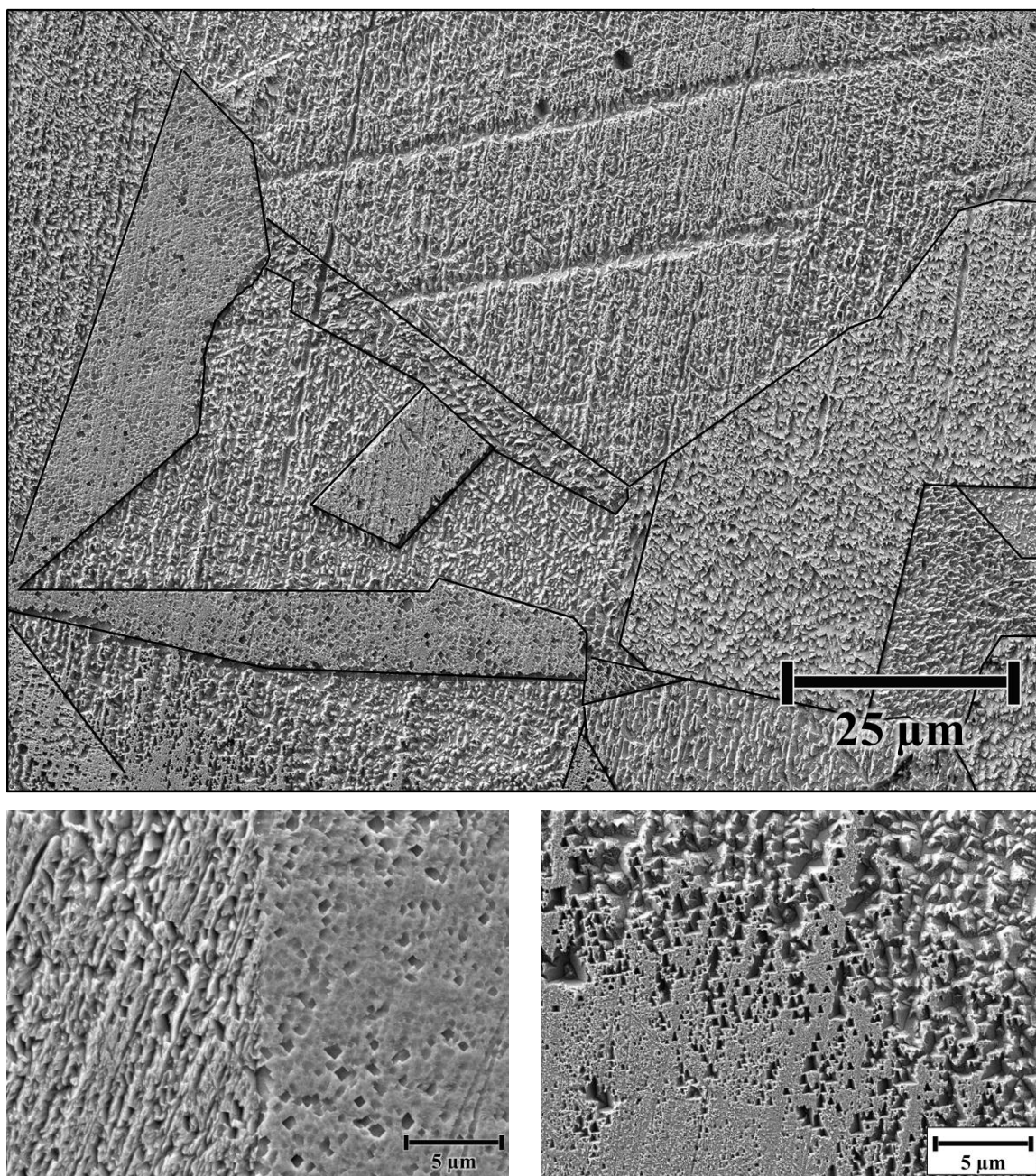


Figure 5.17. SEM micrographs of the surface morphology of fcc $\text{Fe}_{50}\text{Pd}_{50}$ after a 1 hour open after open circuit potential and cyclic polarization in 1 M HCl solution. Grains (top, outlines added for illustration) show crystallographic dependent dissolution characteristics. The higher magnification micrographs show 'etch-pit' dissolution with four-fold symmetry (lower left, right grain) and three fold symmetry (lower right) in a different grain.

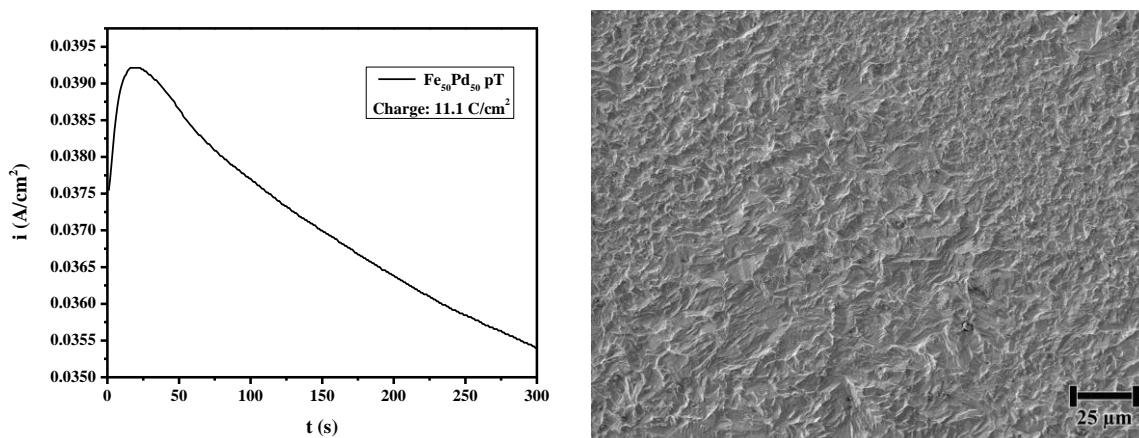


Figure 5.18. Potentiostatic polarization of pT Fe₅₀Pd₅₀ at 0.45 V_{SCE} in deaerated 1 M HCl solution (left). The total charge during polarization is 11.1 C/cm². The SEM micrograph (right) shows the post corrosion surface morphology. Some faceting is seen, but at length scales smaller than the grain size.

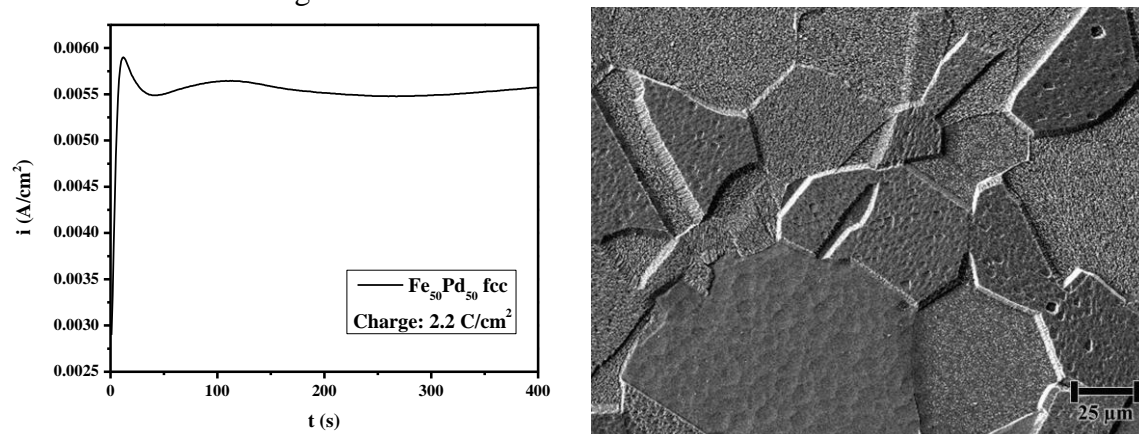


Figure 5.19. Potentiostatic polarization of fcc Fe₅₀Pd₅₀ at 0.45 V_{SCE} in deaerated 1 M HCl solution (left). The total charge during polarization is 2.2 C/cm². The SEM micrograph (right) shows the post corrosion surface morphology which indicates a strong grain dependence.

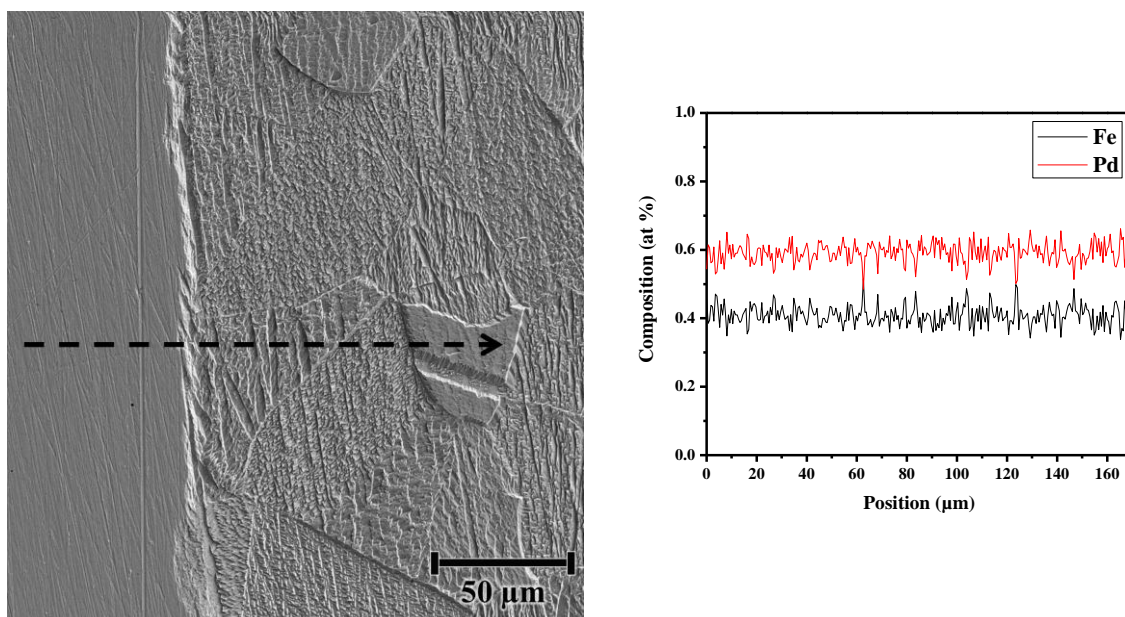


Figure 5.20. SEM micrograph (left) and EDS line (right) scan of fcc $\text{Fe}_{50}\text{Pd}_{50}$ after potentiostatic polarization in 1 M HCl solution at $0.45 \text{ V}_{\text{SCE}}$ for 400 s with total accumulated charge of 3.99 C/cm^2 . The SEM micrograph indicates grain specific faceted behavior after dissolution. The line scan, indicated by the arrow, is across the interface of the lacquered region (on the left) which is protected from solution. No significant qualitative compositional variations are observed between the protected and dissolved areas.²³

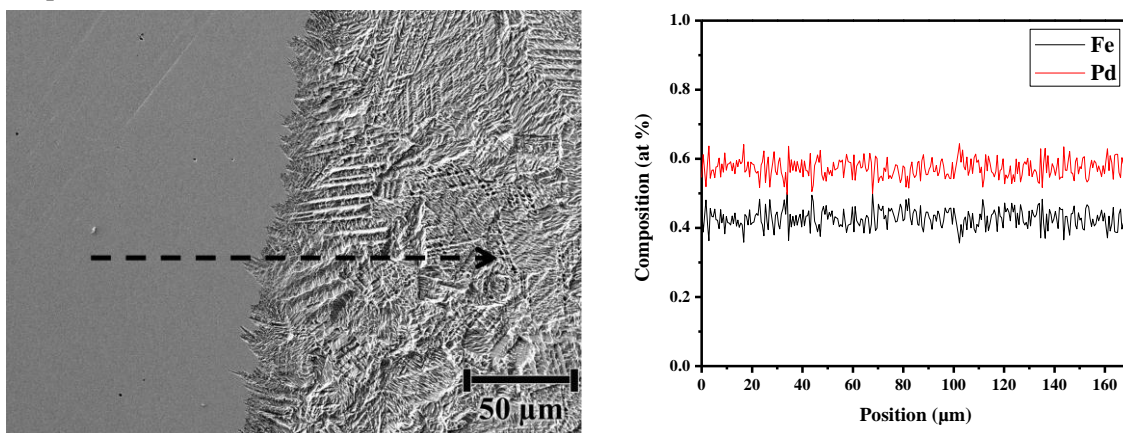


Figure 5.21. SEM micrograph (left) and EDS line (right) scan of pT $\text{Fe}_{50}\text{Pd}_{50}$ after potentiostatic polarization in 1 M HCl solution at $0.45 \text{ V}_{\text{SCE}}$ for 400 s with total accumulated charge of 6.50 C/cm^2 . The line scan, indicated by the arrow, is across the interface of the lacquered region (on the left) which is protected from solution. No significant qualitative compositional variations are observed between the protected and dissolved areas.

²³ The divergence between the EDS measured composition and the nominal composition is due to limiting the beam energy to 15 keV. This energy is only twice the binding energy of Fe ($K_{\alpha} = 6.4$ and $K_{\beta} = 7.1$ keV) resulting in the measured compositions lower in Fe than nominal. This accelerating voltage was used to limit the beam interaction depth to $0.33 \mu\text{m}$ to better measure the surface composition.

5.5.3 Electrochemical Behavior in Passive Environments and Localized Breakdown

Passive behavior is expected for both Fe and Pd at high pH except that the Pd/PdO reaction requires quite oxidizing potentials [6]. Polarization at pH 11 in NaOH, shown in Figure 5.22, shows passive behavior for Fe and both states of Fe₅₀Pd₅₀ all with passive (and/or non-Faradaic) current densities less than 10⁻⁵ A/cm². The current increase around 0.75 V_{SCE} is likely due to oxygen evolution (no dissolution is apparent in optical micrographs, not shown here). The anodic peak on Pd around 0.3 V_{SCE} is likely due to formation of the PdO or PdO₂ oxides. The half-cell potential for Pd oxide formation (PdO) is 0.1 V_{SCE}. The downward scan on Pd produces higher open circuit potentials which suggest reduction of produced O₂ (ORR) and reduction of the oxide. The passive current density of the fcc Fe₅₀Pd₅₀ is similar to Fe and is larger than that for the pT structure (Figure 5.22, left). The ORR influenced open circuit potential on the downward scan is the same on both alloys but the current density remains slightly higher in the fcc structure.

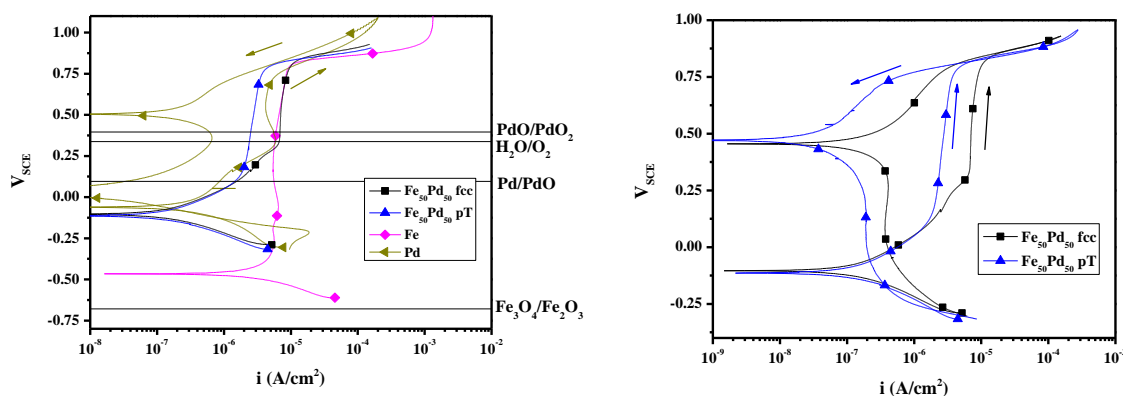


Figure 5.22. E-log *i* behavior in deaerated 1 mM NaOH (pH 11) at scan rate of 1 mV/s. The full scan for fcc and pT Fe₅₀Pd₅₀ is expanded on the right. For reference, the potentials of various oxidation reactions are shown (solid lines) at pH 11 and species concentrations of 10⁻⁶ M. At this pH, Fe oxidation Fe/Fe₃O₄ is at -0.98 V_{SCE} and HER is at -0.89 V_{SCE}.

The dependence of passive film breakdown on the fcc and pT Fe₅₀Pd₅₀ structure was studied in basic Cl⁻ environments. The E-log*i* behavior in 2 M Cl⁻ at pH 11 is shown in Figure 5.23. In this alkaline environment Fe undergoes passive film breakdown at -0.3 V_{SCE}. Pd remains non-faradaic and then passive over this potential range. At the highest potentials, Pd exhibits OER. Behavior is similar to the pH 11 solution without chloride. In the reverse scan, fast ORR produces high open circuit potentials. The fcc and pT Fe₅₀Pd₅₀ samples show similar breakdown potentials at about 0.6 V_{SCE}. Little discernible difference in E-log*i* behavior exists between the two structural conditions (Figure 5.23). However, the surface morphology is different. The morphology of the fcc structure shows some grain dependent dissolution similar to behavior observed in HCl environments. The pT structure shows a more uniform type of dissolution morphology.

Polarization behavior in 0.06 M NaCl (pH 6) and 0.6 M NaCl (pH 6) solution is shown in Figure 4.24 and Figure 4.25, respectively. In these environments, Fe is fully active and does not exhibit any passivity. Pd shows non-Faradaic/passive behavior with current density less than 10⁻⁶ M/cm². A slight current increase is observed at potentials where formation of PdO would be expected. The two structural forms of Fe₅₀Pd₅₀ both exhibit pitting behavior. Micrographs of the surface morphology are shown in Figure 5.26 (0.06 M NaCl) and Figure 4.26 (0.6M NaCl). Both alloys exhibit slightly more rapid repassivation during downward scans in contrast to the higher pH and Cl⁻ environment where dissolution was sustained. The breakdown potentials are summarized in Table 4.7. The critical potentials appear systematically lower in the case of the fcc structure suggesting some underlying structure dependent passivity. Similar behavior was observed

through three experiment repetitions in each condition, but sufficient experimental repetitions to satisfy statistical analysis of such similar potentials were not undertaken.

Table 5.2. Table of critical potentials (V_{SCE}) in neutral and basic NaCl environments. In neutral environments both structural states of $Fe_{50}Pd_{50}$ undergo pitting type breakdown of the passive film. In 2 M NaCl+NaOH solution a more uniform type of dissolution is observed.

Solution	0.06 M NaCl	0.6 M NaCl	2 M NaCl
pH	6	6	11
$Fe_{50}Pd_{50}$ fcc	0.50	0.46	0.58
$Fe_{50}Pd_{50}$ pT	0.49	0.41	0.55
Fe	active	active	-0.26
Pd	immune	immune	immune

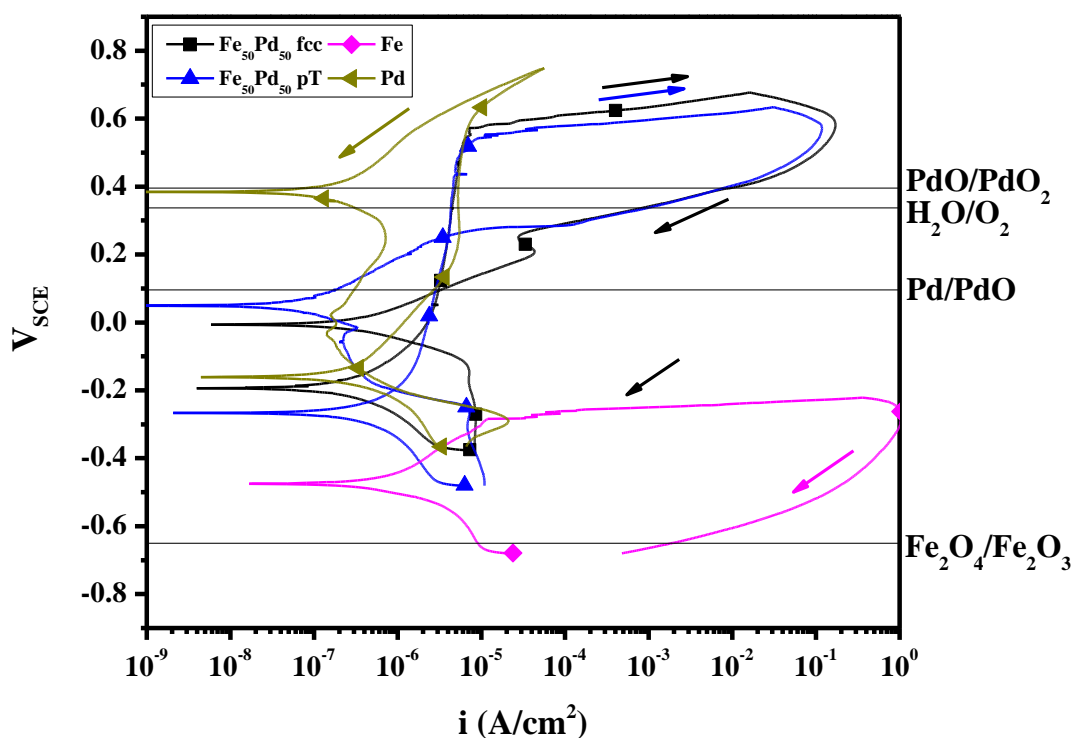


Figure 5.23. $Fe_{50}Pd_{50}$ E-log*i* behavior in deaerated 2 M NaCl + 1 mM NaOH solution (pH 11) at 1 mV/s. For reference, the potentials of various oxidation reactions are shown (solid lines) at pH 11 and species concentrations of 10^{-6} M. At this pH, Fe oxidation Fe/Fe_3O_4 occurs at $-0.98 V_{SCE}$ and the reversible potential for HER occurs at $-0.89 V_{SCE}$.

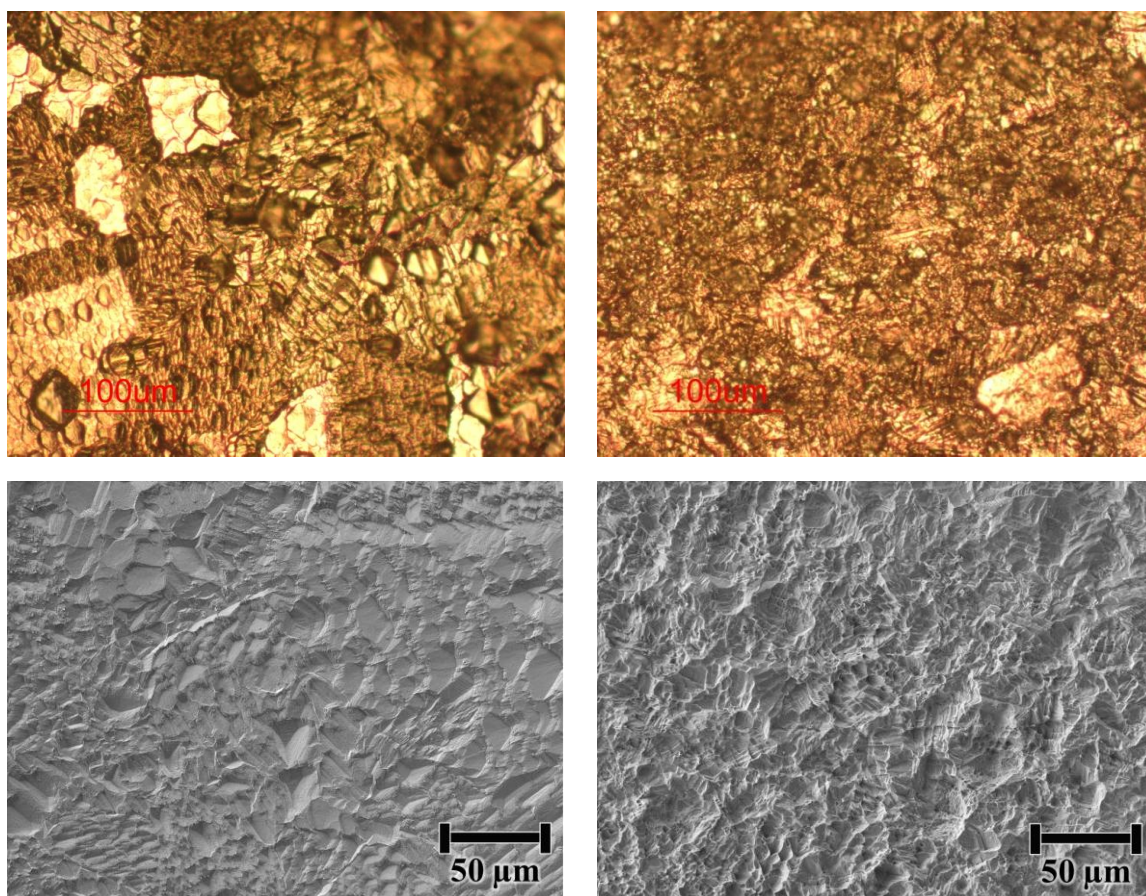


Figure 5.24. Optical micrographs (top) and SEM micrographs (bottom) of Fe₅₀Pd₅₀ fcc (left) and pT (right) surface after cyclic polarization in 2 M NaCl solution at pH 11 to a peak potential of about 0.65 V_{SCE} (Figure 5.23). In the fcc structure areas showing pit-like features, but is dominated by grain dependent dissolution characteristics typical of the fcc structure Cl⁻ solutions. The pT shows some grain dependence in its dissolution behavior but the morphology is predominantly more uniform type corrosion.

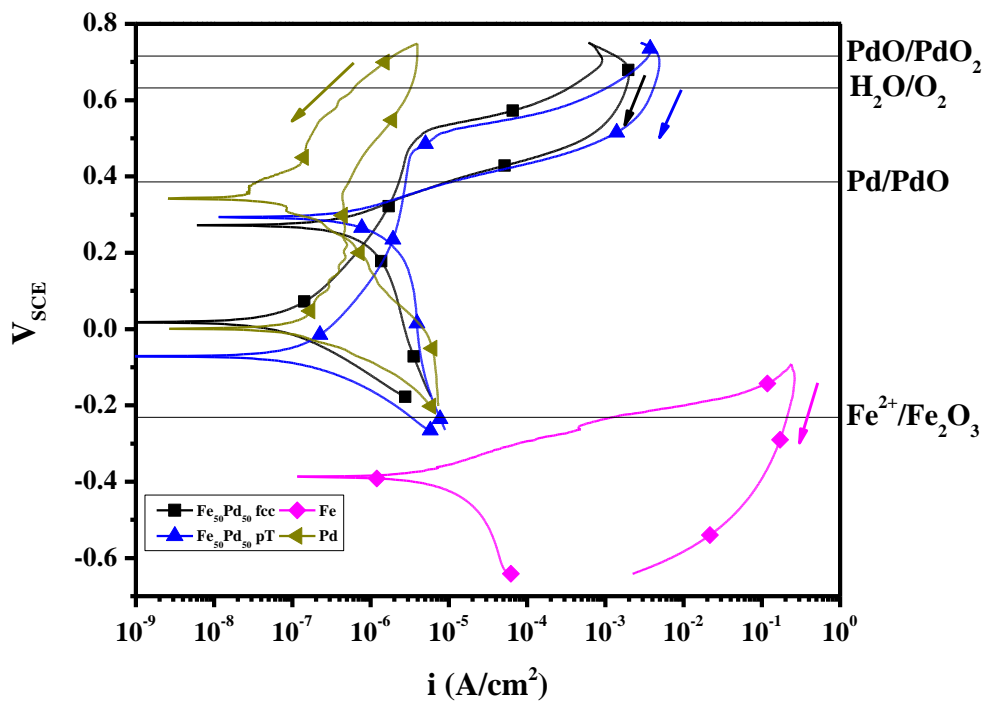


Figure 5.25. Cyclic E-log *i* behavior in 0.06 M NaCl solution at pH 6 at a scan rate of 1 mV/s. For reference, the potentials of various oxidation reactions are shown (solid lines) at pH 6 and species concentrations of 10^{-6} M. The Fe/Fe²⁺ (aq) reaction is at -0.86 V_{SCE} and hydrogen evolution (H⁺/H₂) reaction is at -0.60 V_{SCE}. No Pd-Cl⁻ complex is formed at this pH.

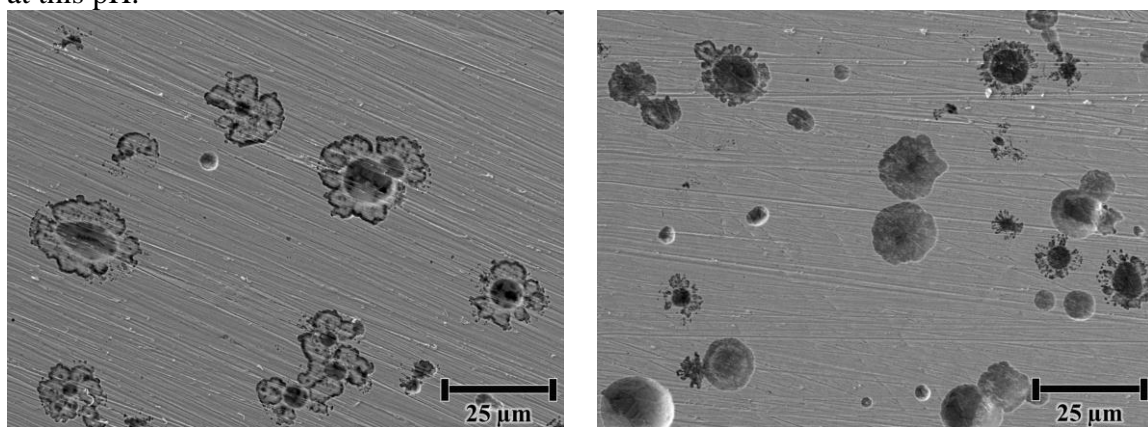


Figure 5.26. SEM micrographs for fcc Fe₅₀Pd₅₀ (left) and pT Fe₅₀Pd₅₀ (right) after cyclic polarization in deaerated 0.6 M NaCl solution (Figure 4.24) showing characteristic surface features. The accelerating voltage is 15 kV and working distance is 15 mm.

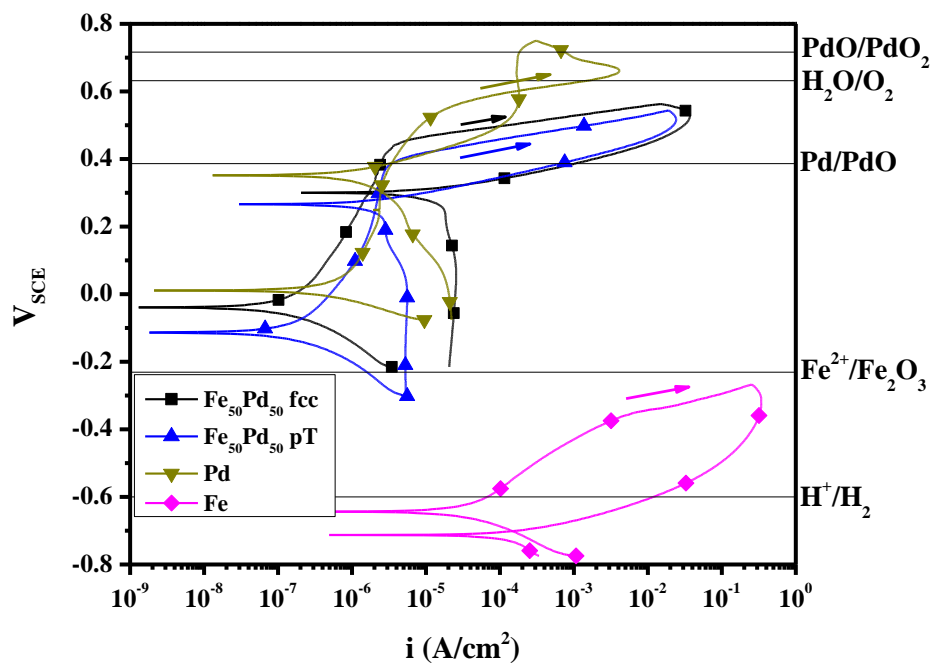


Figure 5.27. Cyclic E-log*i* behavior in 0.6 M NaCl solution at pH 6 at a scan rate of 1 mV/s. For reference, the potentials of various oxidation reactions are shown (solid lines) at pH 6 and species concentrations of 10^{-6} M. Fe oxidation to Fe^{2+} occurs at -0.86 V_{SCE} . No Pd-Cl complex is formed at this pH.

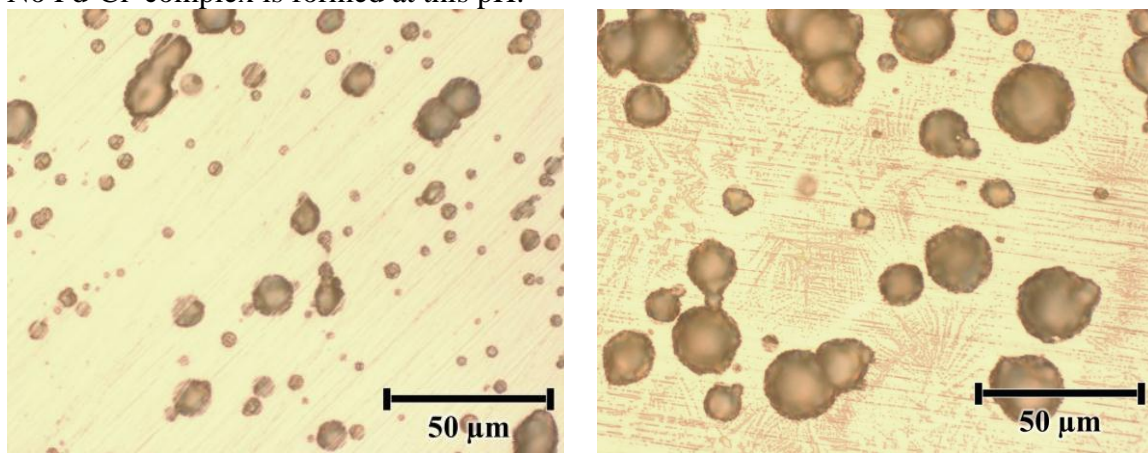


Figure 5.28. Optical micrographs for fcc $\text{Fe}_{50}\text{Pd}_{50}$ (left) and pT $\text{Fe}_{50}\text{Pd}_{50}$ (right) after cyclic polarization in deaerated 0.6 M NaCl solution (Figure 4.25) showing characteristic surface features. The apex potentials were between 0.4 and 0.5 V_{SCE} . Both structural states exhibit pitting behavior.

5.6 Discussion

5.6.1 Benefit of Pd

High purity, polycrystalline Pd has a high anodic current density despite the fact that immune behavior is expected thermodynamically [6]. In the results section and the appendix to this chapter (Section 5.8) it was shown that dissolution does not occur at these potentials. Instead Pd is acting as a hydrogen electrode due to absorption and subsequent oxidation of H.

In acidic chloride environments, Pd exhibits dissolution at elevated potentials (Figure 5.12) due to Cl⁻ complexation to PdCl₄²⁻. While in non-Cl⁻ acidic environments formation of a passive film on Pd is seen at 0.6 V_{SCE} in 1M H₂SO₄ solution (Figure 5.8). In this environment, Pd serves as a beneficial solute by suppressing dissolution of both structural states of Fe₅₀Pd₅₀ in H₂SO₄. The effect of the change between fcc and pT Fe₅₀Pd₅₀ in structure is minimal. At 50 at% Pd, the Pd is likely higher than the parting limit (see discussion of Chapter 4) preventing preferential Fe dissolution from penetrating the alloy. In the potential range lower than Pd oxidation, Fe dissolution is prevented due to dissolution moderating effect of Pd alloying. In the disordered structure where fluctuations in structure are higher than in a compositionally periodic structure, the concentration of Pd remains high enough around each Fe atom to inhibit dissolution (Figure 5.3-5.4). It is likely that the concentration of Pd is reasoned to remain high enough that any effect due to disordered structure is minimal.

In the passive (No Cl⁻) case where both Fe and Pd are passive, Pd alloying appears to lower the passive current density for ordered pT Fe₅₀Pd₅₀, see Figure 5.22,

compared to the fcc case. Dissolution in acidic environments and localized breakdown of the passive films (Table 4.7) both occur at elevated potentials compared to Fe, likely due to the effect of Pd alloying. There seems to be a systematic dependence on structure and pitting potential, but the potentials are within a 5 mV and any difference has a minimal effect. This behavior is also seen in the basic-pitting environment (Figure 5.23), but the more profound structure dependence is observed in the surface morphology (Figure 4.29). The fcc surface is similar to that observed in acidic conditions in that grains show grain specific features.

5.6.2 Morphological Difference Due to Structure

The alloy structure has a pronounced effect on the morphology after corrosion. This effect is one of the areas where the role of structure is extremely apparent. This behavior was observed under passive-localized breakdown conditions and also in acidic chloride environments. Acidic chloride environments share some similarities to the basic-pitting case as during localized pitting events hydrolysis of the cation ($\text{Fe}/\text{Fe}^{2+}/\text{Fe}^{3+}$) acidifies the solution which could in turn create situations where complexation of Pd is likely. In acidic environments this behavior is much more easily controlled using simple electrochemical techniques.

Potential controlled dissolution and subsequent surface morphology of pT (Figure 5.18) and fcc (Figure 5.19) $\text{Fe}_{50}\text{Pd}_{50}$ highlights this effect. Polarization to an anodic potential of 0.45 V_{SCE} is above the oxidation potential of both Fe/Fe^{2+} and $\text{Pd}/\text{PdCl}_4^{2-}$. Moreover, the alloy does not exhibit any through-thickness preferential dissolution of Fe in either structural state of $\text{Fe}_{50}\text{Pd}_{50}$ (Figure 4.22 and Figure 5.21). These conditions (1 M

HCl solution and an applied potential of $0.45 V_{SCE}$) are ideal for studying the underlying structure dependence of the dissolution induced surface morphology.

The fcc structure showed crystallographic dependent dissolution. Incipient dissolution pits on the surface show three-fold and four-fold symmetry (Figure 5.17) which is often indicative of the underlying grain orientation. For example, pits of a CdTe cubic structure has been shown to exhibit two-fold symmetry in $\{110\}$ orientated grains, three-fold in $\{111\}$ oriented grains and four-fold symmetry in $\{100\}$ oriented grains [7]. Different grains within the fcc $Fe_{50}Pd_{50}$ surface exhibit different amounts of dissolution (Figure 5.19-4.22). This suggests that the amount of dissolution has an underlying dependence on the grain orientation. Chapter 6 presents a detailed study correlating the dissolution rate to the grain orientation in fcc $Fe_{50}Pd_{50}$.

At early stages of the dissolution (also at $0.45 V_{SCE}$ in 1 M HCl solution: Figure 5.7 and 5.21), the poly-twinned surface structural features are easily identifiable. After increased dissolution, any grain dependence appears to be lost (Figure 5.18). Moreover, during polarization the pT structure had a significantly higher total anodic charge indicative of an increase in dissolution compared to the fcc structure.

In Chapter 6, the crystallographic dependence on dissolution in fcc $Fe_{50}Pd_{50}$ will be correlated with the initial grain orientation. This behavior will be compared and contrasted at different amounts of total dissolution to the behavior of the pT structure.

5.7 Conclusion

Pd bestows immunity from corrosion in the $Fe_{50}Pd_{50}$ alloys in H_2SO_4 solution up to $0.6 V_{SCE}$. No significant difference between fcc and pT $Fe_{50}Pd_{50}$ was observed. In

environments that enable passivity, the structural effect is also not very pronounced. In neutral environments, both structural states undergo localized breakdown of the passive film at similar potentials. In basic environments similar breakdown potentials are observed for both crystalline states, but distinctly different surface morphologies are apparent.

The effect of structural change from the disordered fcc and ordered pT $\text{Fe}_{50}\text{Pd}_{50}$ is most readily apparent in the dissolution rate and corrosion induced morphology in acidic Cl^- environments. The disordered fcc structure undergoes less dissolution than the pT structure and it displays grain characteristic morphology. This grain dependent morphology can be investigated in HCl solution under conditions of congruent dissolution of both Fe and Pd from both crystalline states of $\text{Fe}_{50}\text{Pd}_{50}$.

5.8 Appendix 1. H Absorption on Pd and Fe₅₀Pd₅₀

5.8.1 Pd as a Hydrogen Electrode

In this section it will be shown that Pd is acting as a hydrogen electrode and that H oxidation dominates the E-log*i* behavior of Pd. This behavior is suggested due to the sustained high current densities during polarization in acidic environments (e.g., see Figure 5.12) and no corresponding dissolution of the surface. The first step of the hydrogen evolution reaction (HER) is the deposition of H from solution H⁺ solution to form H_{abs}:

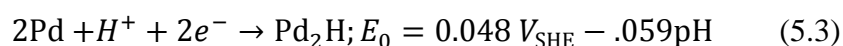
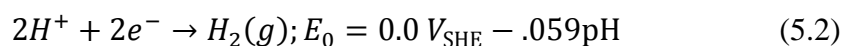


where M is a metal. To form H₂ some an additional mechanism must also occur. Two examples are recombination (with another H_{abs}) or a reaction with another H⁺ cation in solution. In the case of Pd, HER has an extremely high exchange current density (*j*_o), >10⁻⁴ A/cm², which is higher than all other pure metals except Pt [8]. Moreover, Pd acts as oxygen electrode as is apparent by cathodic current corresponding to the oxygen reduction reaction (ORR) potential during the reverse scan following anodic oxygen evolution (see Ch. 4 and around 0.5 V_{SCE} in Figure 5.22). The high rate of these reactions underlies the use of Pd as a catalyst in fuel cells and other applications (e.g., HER [9] and ORR [10]).

The solubility limit of H in Pd is about 0.69 M H_{abs} per M of Pd [11, 12]. H absorbs into interstitial octahedral sites in the Pd fcc lattice resulting in a lattice expansion. At H concentrations up to 1.5%, the lattice expands from 0.3889 nm to 0.3894 nm, and H is absorbed into the α-phase; above this concentration, the hydride β-phase,

PdH_2 , is formed which entails a further expansion of the lattice parameter to 0.404 nm [13]. The H diffusivity of α -phase Pd at room temperature determined by electrochemical permeation studies is on the order of $10^{-7} \text{ cm}^2/\text{s}$: $3.3 \cdot 10^{-7} \text{ cm}^2/\text{s}$ [14] and $1.25 \cdot 10^{-7} \text{ cm}^2/\text{s}$ [15] and $6.3 \cdot 10^{-7} \text{ cm}^2/\text{s}$ [16]. For comparison, H_{diff} for metals with high H_{diff} , in cm^2/s : Ti (10^{-7}); V (10^{-5}), Nb (10^{-6}), Ta (10^{-6}) [16], Fe (10^{-5}) [17]. The mechanism of H diffusion involves jumps between adjacent octahedral sites in both the α and β -phase [18, 19]. High H_{diff} and large H solubility are why Pd and alloys involving Pd are often considered for H storage and membranes [20], and underlie the high exchange current densities for both HER and ORR.

At open circuit, there are two cathodic reactions and one anodic reaction. The cathodic reactions and their corresponding Nernst potentials, E_0 , are HER, Eq. 5.2, and formation of the Pd hydride, Eq. 5.3.



The anodic reaction is the oxidation of the intermediary H_{abs} , reverse of Eq. 5.2, and the Pd_2H , reverse of Eq. 5.3. On Pd, the equilibrium between these anodic and the cathodic reactions defines the open circuit, which operates as a hydrogen electrode. At pH 0, as in 1 M HCl solution, the Nernst potentials of HER are $-0.241 V_{\text{SCE}}$ and the Pd hydride formation potential is $-0.193 V_{\text{SCE}}$. The experimental open circuit potential dependence on $[\text{H}^+]$ for three concentrations of HCl is in Table 5.3. The open circuit potential in 1 M HCl solution corresponds to an equilibrium potential determined by the Pd_2H oxidation. However, the difference between these values is 0.03 V. Based on the pH dependence in

Eq. 5.2 and 5.3, the expected difference is 0.059 V. The difference is likely due to kinetic considerations.

Table 5.3. Pd experimental open circuit potential in HCl solution at three concentrations. The open circuit potentials are constant with respect to time and they increase by 0.30 V per order of magnitude increase $[H^+]$ The open circuit potentials are reproduced here from Figure 5.33.

HCl solution concentration	Exp. Open Circuit Potential (V_{SCE})	Nernst Potential (V_{SCE}) (PdH₂ oxidation)
0.01 M	-0.24	-0.311
0.1 M	-0.21	-0.252
1.0 M	-0.18	-0.193

At potentials higher than HER, H absorption can still occur despite that that H oxidation is the thermodynamically favored reaction. This process is well known on Pd electrodes and other noble metals, and is called under potential adsorption because on a negative scale potential it is lower than the HER potential [21]. Under potential absorption gives rise to additional absorption that is not expected from considering just the Nernst potentials.

The effect of absorbed H on the E-log*i* behavior of a Pd electrode is demonstrated in cyclic voltammetry (CV) experiments in 1 M HCl, shown in Figure 5.29. To oxidize any absorbed H, the Pd electrode was held at 0.3 V_{SCE} , an over-potential of 0.4 V with respect to the open circuit potential, for 10 hours. During the H oxidation conditioning stage, the current decayed to a steady state of $1.3 \cdot 10^{-5}$ A/cm². The initial cycle of the CV began at 0.1 V_{SCE} to avoid any H charging effect. The upwards scan showed non-faradaic behavior and the current depends only on the capacitive current ($I = C \cdot dV/dt$). The minimum potential of the downward sweep of the CV was -0.5 V_{SCE} . This portion of the CV charged the Pd electrode with H. During the second upward scan the current

increases by two orders of magnitude due to oxidation of the H_{abs} . Thus, H_{abs} is oxidized and dominates the E-log*i* behavior and Pd oxidation (Pd/Pd^{2+}) is not operative until the Pd^{2+} chloride complex, PdCl_4^{2-} , is formed.

A series of charging and discharging potentiostatic polarizations corroborates this behavior. The charging cycles were at a potential of $-0.35 V_{\text{SCE}}$ (under-potential of 0.25 V with respect to open circuit) and discharge cycles were at $0.35 V_{\text{SCE}}$ (over-potential of 0.45 w.r.t. open circuit). Again, these potentials were chosen because they are well below and well above the Nernst potential for the $H_{\text{abs}}/H_{\text{abs}}$ oxidation reactions, $E_0 = -0.193 V_{\text{SCE}}$. The current profiles during these steps are shown in Figure 5.30. The cathodic charging steps (of 1 hour, cycle 1, and about 2 hours, cycle 2) showed the same trend in current time behavior. The discharge cycles shows an increase in overall anodic current density from the open circuit discharge cycle (no under-potential charging stage) to the cycles with charging stages. The anodic current increases with charging duration. These results are summarized in Table 5.4.

Table 5.4. Pd charge density during H charging and discharging stages in deaerated 1 M HCl solution. Charging was performed using potentiostatic polarization at $-0.35 V_{\text{SCE}}$ (under-potential of 0.15 V w.r.t. E_0) and discharge cycles at $0.35 V_{\text{SCE}}$ (over-potential 0.55 V w.r.t. E_0).

Stage	Potential (V_{SCE})	Time (s)	Charge (C/cm^2)
Discharge After OCP	0.20	3600	0.372
Charge 1	-0.35	3600	-0.710
Discharge 1	0.20	3600	0.555
Charge 2	-0.35	6200	-1.178
Discharge 2	0.20	3600	1.114 [†]

[†] An extrapolation of the discharge cycle to the background value was used because the sample was not fully discharged after 3600 s.

The current density of the hydrogen discharge depends on the diffusivity, D_H , the diffusible hydrogen concentration $C_{H,diff}$ and the time as shown in Eq. 4,

$$C_{H,diff} = \frac{i}{nF} \left(\frac{D_H}{\pi t} \right)^{-1/2} \quad (4)$$

where n is the oxidation number of H [22]. Thus, the current due to H diffusing out of metal is proportional to $t^{-1/2}$. The discharge cycles are plotted as a function of the square root of time in Figure 5.31. The slope of both discharging cycles is about $1 \cdot 10^{-5} \text{ A} \cdot \text{cm}^2/\text{s}^{1/2}$. After 900 s ($30 \sqrt{\text{s}}$) the discharge curve for cycle one deviates from linearity and asymptotically approaches the background. Similarly, for cycle two this deviation occurs at about at 1200 s ($35 \sqrt{\text{s}}$). The behavior during the OCP-discharge cycle shows similar characteristics to the charge-discharge curve. The initial behavior is similar and there is a linear region, albeit a different slope, and a similar asymptotic tail, but the curve is dominated by the underlying background behavior. It is likely that some hydrogen absorption occurred during the OCP hold and some occurs during the discharge cycle due to under-potential absorption. The increase in maximum current density after increased charging duration suggests that the overall solubility limit of H_{abs} in Pd has not been reached.

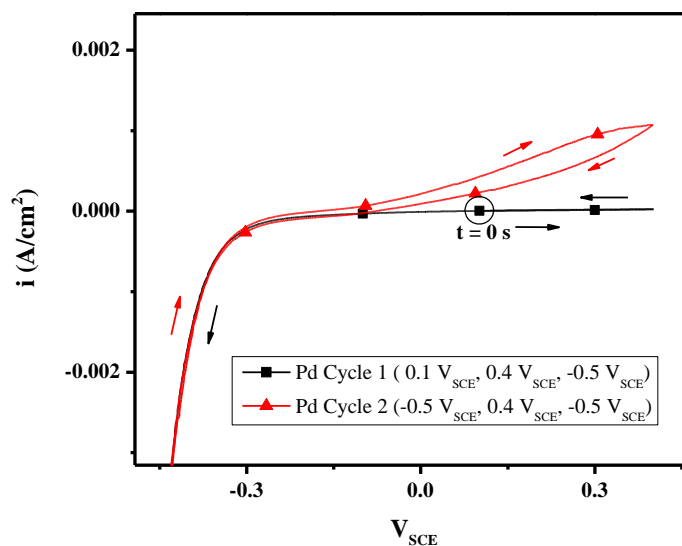


Figure 5.29. Cyclic E-logi behavior in deaerated 1 M HCl solution at 1 mV/s. The sample was initially conditioned by charging at 0.2 V_{SCE} for 8 hours to remove any absorbed H. The initial cycle began at 0.1 V_{SCE} , an over-potential to the H_{abs} reaction, and cycled to 0.4 V_{SCE} . The polarization behavior is non-Faradaic and is the capacitive current ($i = C \cdot dV/dt$) on Pd. The downward scan to -0.5 V_{SCE} induces H absorption ($H^+ + e^- \rightarrow H_{abs}$) and the subsequent cycle shows an increase in the current density due to the H_{abs} oxidation to H^+ oxidation reaction.

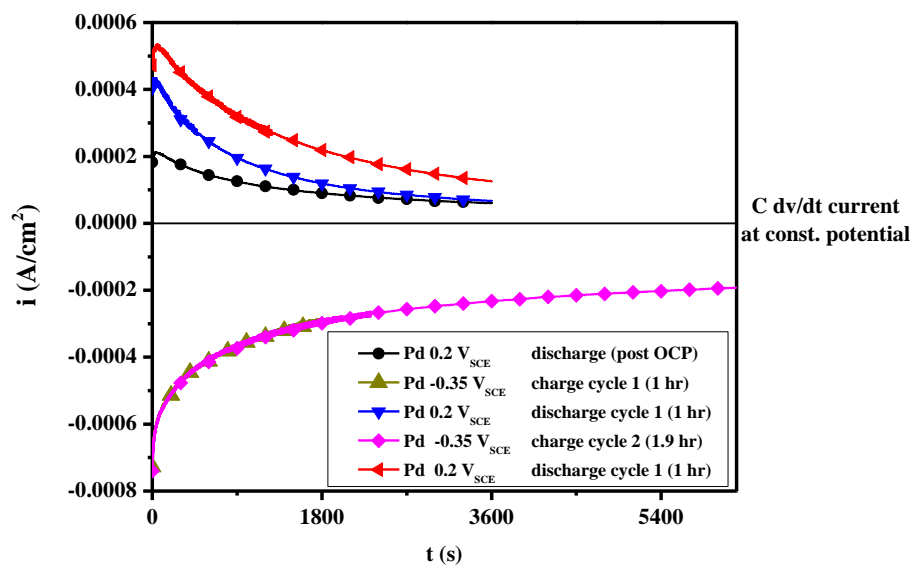


Figure 5.30. Pd current vs. time behavior during alternating H charging and discharging cycles as a function of charging duration. H charging was performed using potentiostatic polarization at -0.35 V_{SCE} (under potential -0.15 V) and H discharge cycles at 0.2 V_{SCE} (over potential 0.2 V_{SCE}). At 3600 s, the current during discharge decays to $6 \cdot 10^{-5}$, and at 18 ks (not shown) the current decays to steady state at $2.4 \cdot 10^{-5}$ A/cm². At 36 ks, the current showed limited decay to $1.28 \cdot 10^{-5}$ A/cm².

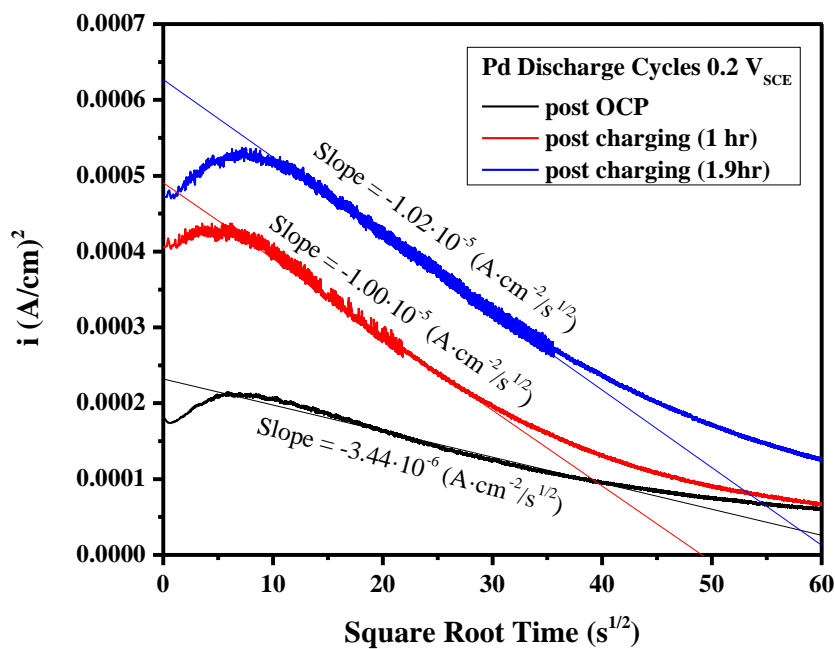


Figure 5.31. Pd current- \sqrt{t} dependence during the discharge cycles at 0.2 V_{SCE} in deaerated 1 M HCl solution. The current increases with respect to charging time. The slope of the discharging current is linear (with respect to \sqrt{t}) from 10 to 30 \sqrt{s} . The slopes of after both charging cycles is about $1 \cdot 10^{-5} A \cdot cm^2 / s^{1/2}$.

5.8.2 The Role of H absorption on Pd

In acidic Cl⁻, the behavior of Pd and the Fe₅₀Pd₅₀ alloys merit careful analysis. The polarization curve in the 1 M HCl condition is reproduced in Figure 5.32, with likely underlying reactions shown schematically for illustration purposes. At elevated potentials, the PdCl₄²⁻ complex is responsible for the increase in current as was described in Figure 5.15. The current density is independent of potential indicating a diffusion limited current density, i_{lim} , of $1.4 \cdot 10^{-3}$ A/cm². The anodic limiting current for the H⁺→H+e⁻ or PdH→H⁺+Pd+e⁻ reaction is:

$$i_{lim} = \frac{nFD_H C_H}{\delta}, \quad (5)$$

where δ is the diffusion layer thickness, D_H is the diffusivity of H in Pd, n is the number of electrons (1) per H and C_H is the absorbed H concentration. If δ is assumed to be 10 μ m, and the D_H is $3.3 \cdot 10^{-7}$ cm²/s, the limiting current density can be used to calculate the concentration of H in Pd. Under these assumptions and with $i_{lim} = 1.4 \cdot 10^{-5}$, the concentration of H in Pd is $4.4 \cdot 10^{-5}$ mol/cm³. The volume of 1 mol of Pd is 8.851 cm³/mol. The molar ratio of absorbed hydrogen to result in this limiting current density is $3.89 \cdot 10^{-4}$ [H]/[Pd]. This concentration is well within the solubility limit of Pd (0.69) and also the α -phase Pd solubility limit of 0.015.

The total charge during the scan above the open circuit potential and below the critical potential is approximately 1.1 C/cm² assuming no contribution of the underlying Pd dissolution reaction to the critical potential. The total charge during the charging portion of the cycle below open circuit is 0.1 C/cm² during the charging portion of the

cycle. This suggests substantial H absorption during the open circuit (1 hr, proceeding E-*logi* scan) and also under potential H absorption above the open circuit potential.

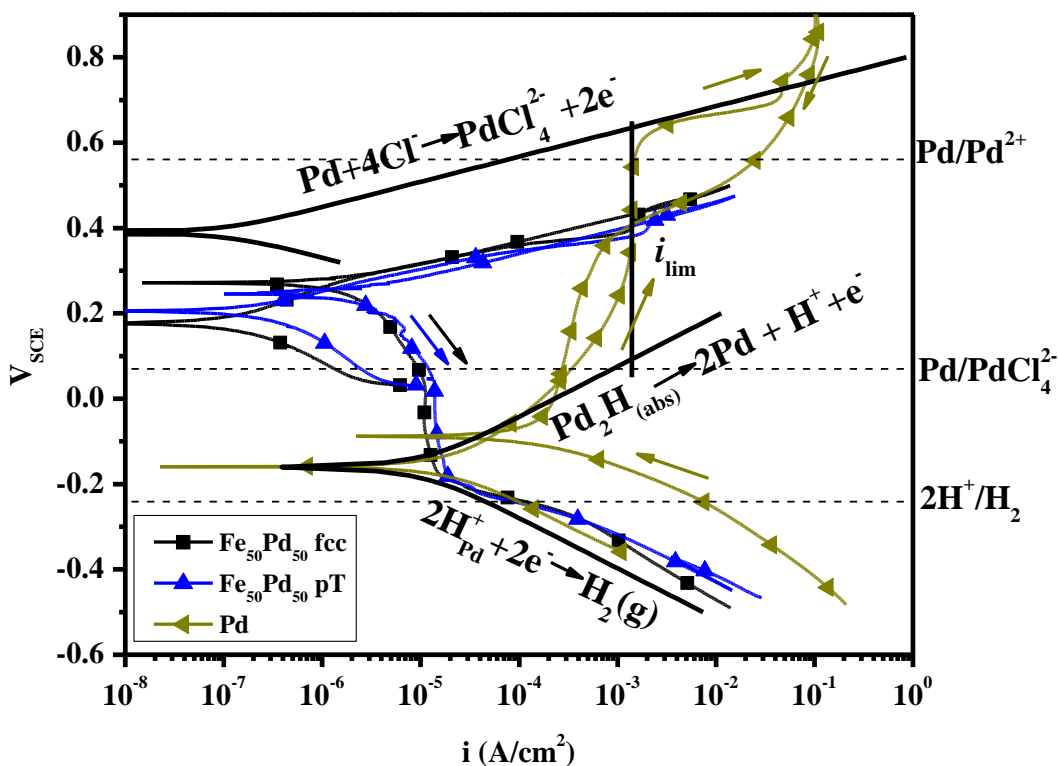


Figure 5.32. E-*logi* behavior in deaerated 1 M HCl solution with likely operating reactions illustrated. The Tafel slope of the HER assumed to be 118 mV/decade and corrosion current density is 10^{-5} A/cm². The hypothetical Pd oxidation reaction (Pd/PdCl₄²⁻) has a 59mV/decade Tafel slope and exchange current density of 10^{-7} A/cm². The limiting current density, i_{lim} , is about $1 \cdot 10^{-3}$ A/cm². Based on the observed behavior, it is likely that the HER reaction has a very high exchange current density (10^{-4} A/cm² [8]) while the Pd oxidation reaction has a much lower exchange current density.

The open circuit corrosion rate and subsequent anodic current density including the limiting current density is drastically lower in the 0.5 M H₂SO₄ solution which has the same concentration of [H⁺]. At similar overpotential to the open circuit the current density is three orders of magnitude higher with 1 M Cl⁻ in solution. The reason for the behavior is unclear. Cl⁻ could be acting to accelerate the H absorption and the HER

reaction. There could be electrostatic attraction between surface Cl^- and H^+ cations. Bare metal absorption on Fe is about 10^{-9} mol/cm² in 10^{-3} Cl^- concentration [23]. Cl^- adsorption on the surface could also facilitate the H_{abs} reactions thereby increasing HER. Alternatively, SO_4^{2-} could be inhibiting the HER reaction.

5.8.3 Effect of Hydrogen during Open Circuit Behavior: Structure Dependence

In a wide variety of solution environments the open circuit increases from an initial potential roughly equivalent to the expected HER potential to one at least 300 mV higher. This potential rise occurs over the first few hundred seconds of the open circuit measurement. In Chapter 4, this behavior was seen for both fcc compositions in acidic HCl solution and neutral and basic NaCl solution. In this chapter, similar behavior was seen for both fcc and pT Fe₅₀Pd₅₀ in acidic HCl solutions, without Cl^- anions in acidic H₂SO₄ solution, and in basic NaCl solution. The rise in potential is seen in open circuit potentials after a cyclic scan to potentials below HER, but is not seen after a potentiostatic polarization at anodic potentials. This suggests that the underlying behavior is determined by hydrogen. This behavior is not a function of Cl^- and also is most likely not due to any dealloying effects. Dismissing dealloying effects is supported by similar behavior observed in pH 11 NaCl solution where Fe is passive and not expected to dissolve. Additionally, this behavior occurs within the first few hundred seconds of the open circuit. Even at high open circuit corrosion current densities, the dissolution rate is too low for any significant dealloying effect.²⁴

²⁴ Let's assume the corrosion current density is 10^{-6} A/cm², as in the 1 M HCl solution experiments. If the duration of the dealloying behavior is 600 s, then a total charge on the samples is 0.6 mC/cm². This charge

The focus of this section is to analyze the potential rise using a series of long duration open circuit potentials with minimized time between solution contact with the working electrode before the start of data acquisition. Using these experiments the structural dependence of HER and H_{abs} can be explored for both $\text{Fe}_{50}\text{Pd}_{50}$ structures.

The series of open circuit measurements in deaerated 0.01 M, 0.1 M and 1 M HCl solution for each structural state and Pd are shown in Figure 5.33. In all three concentrations, the open circuit potential of Pd, as a hydrogen electrode, does not vary significantly. Both pT and fcc $\text{Fe}_{50}\text{Pd}_{50}$ structural states show the characteristic increase during the initial few hundred seconds in all conditions except pT in 0.01 M. the time until a change in convexity, τ , during the rise in the open circuit potential was determined for each solution concentration is plotted in Figure 5.33. The pT condition shows smaller τ values in all the conditions.

amounts to the dissolution of $1.2 \cdot 10^{-10}$ m based on Faraday's law. With a lattice parameter of 0.38 nm, about 0.5 monolayer of Fe dissolution would have occurred. In the less caustic environments the corrosion current density is lower, and any dissolution would be correspondingly lower.

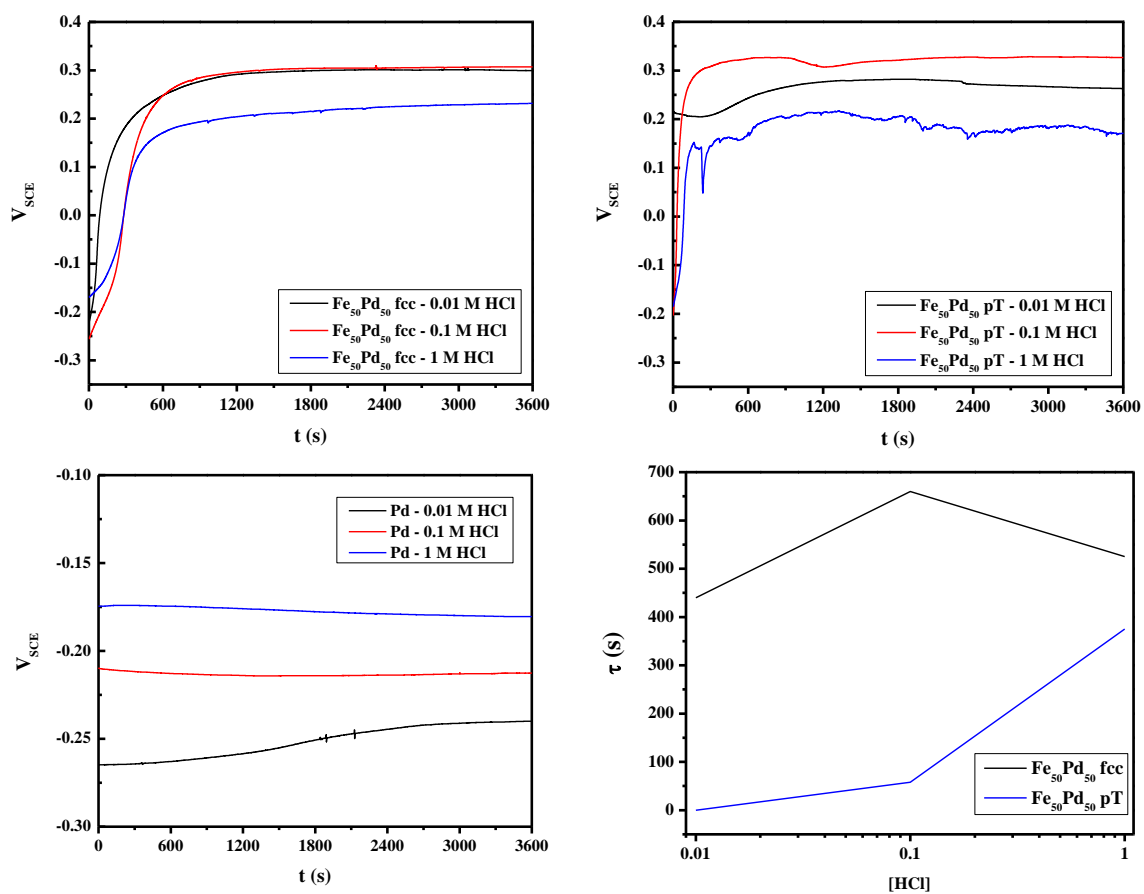


Figure 5.33. Open circuit behavior in 0.01, 0.1 and 1 M HCl solution for $Fe_{50}Pd_{50}$ fcc (upper left), $Fe_{50}Pd_{50}$ pT (upper right), and Pd (lower left). The τ -concentration plot (lower right) shows the time until a change in convexity of the potential rise during the open circuit exposures as a function of HCl solution concentration. The open circuit potential of the $Fe_{50}Pd_{50}$ pT structure rises more rapidly than the fcc structure.

5.8.4 Effect of Structural Change on the HER reaction

The rise in open circuit potential is faster for ordered pT Fe₅₀Pd₅₀ than the disordered fcc Fe₅₀Pd₅₀ (Figure 5.33). The structural dependence is likely due to the effect of the different structural states on the kinetics of the HER reaction. Possible factors contributing to this behavior are discussed.

Alloying of Pd with transition metals generally reduces the exchange current density, i_o , of HER [8] compared to pure Pd. In bimetallic systems it has been shown that Pd over-layers on different metal substrates effects the surface reaction rate on Pd and the free energy of H_{abs} resulting in large changes to the surface coverage and decreasing i_o by two orders of magnitude [24, 25].

Alloying Pd would also reduce the solubility of H into the alloy matrix compared, but the total dissolved hydrogen is likely below this limit. The diffusivity typically decreases due to alloying. In Pd-Ag alloys, such a trend is seen [26]. H diffusion also occurs by interstitial motion [27], and in pure bcc Fe H_{diff} is about 10⁻⁵ cm²/s [17], which is faster than H_{diff} for fcc Pd. While these are not directly applicable to the Fe₅₀Pd₅₀ system, the key observation is that the structural state of the alloy can also affect both the solubility and the diffusivity. Diffusion in a disordered structure involves atomic motion that is not as bound by the constraints due the ordered crystalline structure. In amorphous alloys, which are neither ordered nor crystalline, the atomic diffusion rate is thought to be higher, although that is not universally true [28]. H_{diff} can change based on an amorphous, crystalline and deformed crystalline structure; for the amorphous structure H_{diff} increase by several orders of magnitude at low [H_{abs}] likely due to density of favorable sites for

hydrogen diffusion [29, 30]. The number of dislocations in a metal can also be detrimental to the diffusivity. In cold worked Pd, the diffusivity of H was greatly reduced compared to annealed Pd at concentrations below 10^{-3} [H]/[Pd] [29].

5.9 References

1. Hultgren, R. and C.A. Zappfe, *The Crystal Structures of the Iron-Palladium Superlattices*. Kristallchem, 1938. **99**(509).
2. Yiping, L., G.C. Hadjipanayis, C.M. Sorensen, and K.J. Klabunde, *Structural and Magnetic-Properties of Ultrafine Fe-Pd Particles*. Journal of Applied Physics, 1994. **75**(10): p. 5885-5887.
3. Brandenburg, K., *Modelling performed using Diamond Crystallography Software* (<http://www.crystalimpact.com/>).
4. Puigdomenech, I., *MEDUSA: Make Equilibrium Diagrams Using Sophisticated Algorithms*. 2009: Stockholm, Sweden.
5. Ives, M.B., *Localized corrosion*, in *International corrosion conference series*, U.R. Evans, et al., Editors. 1974, National Association of Corrosion Engineers: Houston, Tex. p. 78-103.
6. Pourbaix, M., *Atlas of electrochemical equilibria in aqueous solutions*. 1974, National Association of Corrosion Engineers: Houston, Tex. p. 307-321, 358-363.
7. Inoue, M., Teramoto, I., Takayanagi, S., *Etch pits and polarity in CdTe crystals*. Journal of Applied Physics, 1962. **33**(8): p. 2578-2582.
8. Conway, B. and J.O.M. Bockris, *Electrolytic hydrogen evolution kinetics and its relation to the electronic and adsorptive properties of the metal*. The Journal of Chemical Physics, 1957. **26**: p. 532.
9. Ha, S., R. Larsen, and R. Masel, *Performance characterization of Pd/C nanocatalyst for direct formic acid fuel cells*. Journal of Power Sources, 2005. **144**(1): p. 28-34.
10. Nørskov, J.K., J. Rossmeisl, A. Logadottir, L. Lindqvist, J. Kitchin, T. Bligaard, and H. Jonsson, *Origin of the overpotential for oxygen reduction at a fuel-cell cathode*. The Journal of Physical Chemistry B, 2004. **108**(46): p. 17886-17892.
11. Flanagan, T.B. and F. Lewis, *Hydrogen absorption by palladium in aqueous solution*. Trans. Faraday Soc., 1959. **55**: p. 1400-1408.
12. Züttel, A., C. Nützenadel, G. Schmid, C. Emmenegger, P. Sudan, and L. Schlapbach, *Thermodynamic aspects of the interaction of hydrogen with Pd clusters*. Applied Surface Science, 2000. **162-163**(0): p. 571-575.
13. Jamieson, H., G. Weatherly, and F. Manchester, *The [beta]-->[alpha] phase transformation in palladium-hydrogen alloys*. Journal of the Less Common Metals, 1976. **50**(1): p. 85-102.
14. Kirchheim, R. and R.B. McLellan, *Electrochemical methods for measuring diffusivities of hydrogen in palladium and palladium alloys*. Journal of the Electrochemical Society, 1980. **127**: p. 2419.
15. Devanathan, M.A.V. and Z. Stachurski, *The Adsorption and Diffusion of Electrolytic Hydrogen in Palladium*. Proceedings of the Royal Society of London. Series A. Mathematical and Physical Sciences, 1962. **270**(1340): p. 90-102.
16. Boes, N. and H. Züchner, *Electrochemical methods for studying diffusion, permeation and solubility of hydrogen in metals*. Journal of the Less Common Metals, 1976. **49**: p. 223-240.

17. Oriani, R., *Hydrogen embrittlement of steels*. Annual Review of Materials Science, 1978. **8**(1): p. 327-357.
18. Nelin, G. and K. Sköld, *Diffusion of hydrogen in the β -phase of Pd-H studied by small energy transfer neutron scattering*. Journal of Physics and Chemistry of Solids, 1975. **36**(11): p. 1175-1182.
19. Sköld, K. and G. Nelin, *Diffusion of hydrogen in the α -phase of Pd-H studied by small energy transfer neutron scattering*. Journal of Physics and Chemistry of Solids, 1967. **28**(12): p. 2369-2380.
20. Knapton, A., *Palladium alloys for hydrogen diffusion membranes*. Platinum Metals Review, 1977. **21**(2): p. 44-50.
21. Jerkiewicz, G., *Hydrogen sorption at/in electrodes*. Progress in Surface Science, 1998. **57**(2): p. 137-186.
22. Deluccia, J.J. and D.A. Berman, *An Electrochemical Technique to Measure Diffusible Hydrogen in Metals (Barnacle Electrode) in Electrochemical Corrosion Testing, ASTM STP 727*, F. Mansfield and U. Bertocci, Editors. 1981, American Society for Testing and Materials: Philadelphia, PA. p. 256-273.
23. Jovancicevic, V., J.O. Bockris, J.L. Carbajal, P. Zelenay, and T. Mizuno, *Adsorption and Absorption of Chloride-Ions on Passive Iron Systems*. Journal of the Electrochemical Society, 1986. **133**(11): p. 2219-2226.
24. Greeley, J., T.F. Jaramillo, J. Bonde, I. Chorkendorff, and J. Norskov, *Computational high-throughput screening of electrocatalytic materials for hydrogen evolution*. Nature Materials, 2006. **5**(11): p. 909-913.
25. Greeley, J., J.K. Nørskov, L.A. Kibler, A.M. El Aziz, and D.M. Kolb, *Hydrogen evolution over bimetallic systems: Understanding the trends*. ChemPhysChem, 2006. **7**(5): p. 1032-1035.
26. Holleck, G.L., *Diffusion and Solubility of Hydrogen in Palladium and Palladium-Silver Alloys*. Journal of Physical Chemistry, 1970. **74**(3): p. 503-&.
27. Jiang, D.E. and E.A. Carter, *Diffusion of interstitial hydrogen into and through bcc Fe from first principles*. Physical Review B, 2004. **70**(6): p. 064102.
28. Zhu, A., G.J. Shiflet, and S.J. Poon, *Diffusion in metallic glasses: Analysis from the atomic bond defect perspective*. Acta Materialia, 2008. **56**(14): p. 3550-3557.
29. Kirchheim, R., *Solubility, diffusivity and trapping of hydrogen in dilute alloys. Deformed and amorphous metals—II*. Acta Metallurgica, 1982. **30**(6): p. 1069-1078.
30. Kirchheim, R., *Hydrogen solubility and diffusivity in defective and amorphous metals*. Prog. Mater. Sci., 1988. **32**(4): p. 262-325.

6 Dissolution Anisotropy in Fe₅₀Pd₅₀

6.1 Abstract

Dissolution of disordered fcc equiatomic FePd in 1 M HCl solution was strongly related to crystallographic orientation. The susceptibility to dissolution in this acidic environment was characterized over a wide variety of grain surface plane orientations forming a representative picture the crystallographic nature of dissolution and surface roughness as a function of grain orientation. The near {100} oriented grains had low surface roughness and showed the highest resistance to dissolution. Grains with orientation within 2° the {111} plane normal were also morphologically smooth after a period of dissolution and were nearly as dissolution resistant as the {100} grains. Post corrosion surface roughness and dissolution were substantially increased for grain orientations near {110}. The orientations with the highest surface roughness and most dissolution represented by a dense set of terraces and ledges had orientations between 10 and 20° from the {111} plane normal. Overall dissolution depth was found to linearly depend on angle from the {100} plane normal up to 40°. A linear dependence on angle was also seen up to 10° from the {111} plane normal; however, the rate of increase in dissolution (per °) was higher than that measured from the {100} plane normal. In contrast, no linear dependence was observed for orientations near the {110}. During dissolution the grains form a series of characteristic surface facets consisting of low dissolution rate terraces and faster dissolving ledges. The overall corrosion rate of an irrational given orientation is determined by how readily the surface can form low index facets.

Similar dissolution behavior was not observed for equiatomic ordered pT. Some grain based corrosion morphology is observed after low amounts of total dissolution, but this is predominantly obscured after increased dissolution. As the amount of dissolution increases the surface structure shows an increasing number of sub-grain sized pits 5-10 μm in diameter. Dissolution occurs more quickly from the ordered pT structure than from the disordered fcc structure. This behavior is likely due to inherent differences in the bond strength between each state.

6.2 Introduction

Many forms of corrosion exhibit a rate dependence that depends on crystallographic orientation, but the governing structural factors are not well understood. An early and prevalent example of corrosion anisotropy is etch pitting [1] which often results in a characteristic pit formation shape depending on the orientation of the grain, e.g., two-fold symmetry in $\{110\}$ orientated grains, three-fold in $\{111\}$ oriented grains and four-fold symmetry in $\{100\}$ oriented grains [2]. The difference in corrosion behavior dependent on crystallographic orientations allows for fundamental explorations of the role of atomistic bonding, surface energy, surface relaxation and reconstruction and other structural factors on electrochemically controlled dissolution [3-7] and the metal-oxide-solution interface during passivation and pitting corrosion [8-12].

There are typically two ways to investigate the influence of orientation on corrosion properties. The first is to utilize single crystals with surfaces of a specific orientation [6, 8, 11, 12], but these studies are often logistically limited to a few different orientations. Studies of polycrystalline samples [3, 5, 9, 10, 13, 14] enable the systematic analysis of many orientations, but there can be difficulty in achieving any specific orientation of interest or slight variation between orientations due to inherent crystallographic texture (e.g. developed during mechanical processing) which prevents access to certain orientations. Therefore, there are huge gaps in experimental findings regarding the crystallographic dependence of dissolution. The advent of somewhat automated electron backscattered diffraction (EBSD) coupled with confocal laser scanning microscopy (CLSM) or other surface topography measurement methods for

measuring dissolution depths and surface roughness now enables the detailed analysis of a sufficient number of contiguous grains to achieve true understanding of dissolution in polycrystalline systems as a function of crystal orientation. These results can be compared to materials factors such as surface energy and electron density.

Dissolution of single crystal Al [5] in alkaline NaOH solution environments showed increased dissolution on {111} oriented grains. When Al was alloyed with minor additions of Zn, Mg, Si in solid solution [4, 13], an increase in dissolution was seen as the grain surface orientation approached {111}. In the case of Holme [4], a wide range of orientations (approximately 90) of Al-Mg-Si-Zn (precipitate hardened and not a complete solid solution) was studied and a linear dependence of dissolution depth on orientation was observed for Zn alloying concentrations above 0.2%. However, the orientation dependence of Al dissolution is clouded by the role of crystallographic orientation dependent Zn enrichment. Results of microcapillary experiments on specific orientations of bcc Fe in H₂SO₄ solution show that corrosion activity for the low index orientations decreases from highest activity to lowest from {001} > {111} > {101} based on the corrosion potential and Tafel slopes [3]. Detailed simulations of dissolution of hcp Mg, which considered the effect of surface relaxation, showed that the required dissolution potential is lower for atoms on (0001) plane compared to the (10-10) plane. This corresponded to a chemical potential difference of 50 meV with lower potential for the (10-10) plane [6]. There exist significant discrepancies regarding which orientations result in the least corrosion resistant, to dissolution or pitting, orientation. To date, no complete experimental dissolution study of a wide range and high number of fcc

orientations including orientations near the three low index orientations in the absence of enrichment and redeposition has been presented. Most studies neglect solid solution alloys and none have compared the effect of ordered vs. disordered states on this process.

The aim of this work is to analyze the orientation dependence of dissolution on a model fcc Fe₅₀Pd₅₀ disordered solid solution alloy over a wide range of orientations including many small variations in orientation. Studying a model binary solid solution in HCL solution system benefits from a lack of precipitates and secondary phases found in many engineering alloys and allows for a fundamental investigation into the role of the surface structural orientation as it pertains to active electrochemical dissolution resistance.

Results are presented on recrystallized polycrystalline disordered fcc Fe₅₀Pd₅₀, with no rolling or processing texture, after potential controlled dissolution in HCl under strongly oxidizing conditions above the dissolution potential Pd/Pd²⁺ (to PdCl₄²⁻) reaction where no significant redeposition or enrichment of Pd occurred. An analysis of 300 individual grains was performed. The orientation was determined for 7 regions each containing 30-50 grains. Subsequently, the depth of dissolution and resulting surface roughness were determined. Results are then correlated to surface orientation and comments are made regarding governing nanostructural features.

6.2.1 Electron Backscatter Diffraction

EBSD characterization is based on electron diffraction being used to form a characteristic pattern can be used to identify and the orientation of the grain and also its phase. When incident electrons interact with crystal planes, an incoherent scattering event

followed by Bragg scattering gives rise to intensity variations in the emitted electron intensity. The electron intensity variations form crystal plane dependent lines called Kikuchi lines. Each diffracting plane within a crystal orientation forms a Kikuchi band, or the 2 Kikuchi lines attributed to each plane. The superposition of these bands, from all the diffracting planes, forms a Kikuchi map and the location of the Kikuchi band intersection is defined by the orientation of a crystal. The Kikuchi map can be compared to all possible calculated Kikuchi maps based on the crystal structure and orientation of the unit cell. Thus, EBSD can be used to determine the orientation of a grain. Conventionally, electron diffraction is achieved in an SEM by tilting the sample to high tilt angles, see schematic in Figure 6.1. The raster of the electron beam across the surface allows for the accumulation of EBSD patterns. The patterns can be indexed across the surface of the specimen and provide the orientation of all the grains within the raster region. For a more complete summary of this technique and its use for texture determination see Dingley or Randle [15, 16].

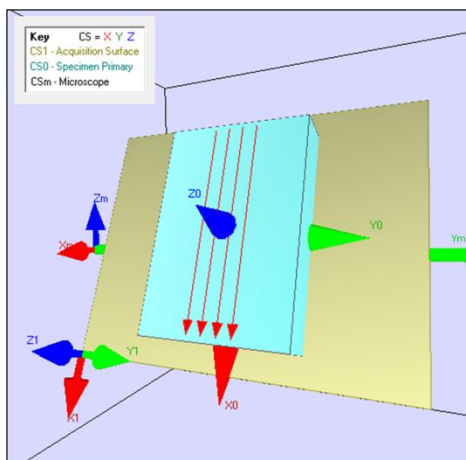


Figure 6.1. The virtual sample chamber shows the specimen - microscope orientation configuration for EBSD characterization. The three coordinate systems are identified by their subscripts: m indicates the microscope orientation, 0 is the specimen primary orientation, and 1 is the orientation of EBSD acquisition. During EBSD acquisition, the specimen rotated about the y_m and y_0 axis to a tilt of 70° .

Orientation relations are typically described using Euler angles which describe the orientation as an ordered series of rotations to reorient the reference frame. The Bunge convention defines the Euler angles as ϕ_1 , Φ , and ϕ_2 , shown in Figure 6.2 [17]. Euler angles can be used to calculate the orientation, $\{hkl\}$, along different directions in different reference frames, e.g. normal direction and the two perpendicular directions: loading and transverse direction. To fully define the orientation of a grain, the orientation must be determined in 2 of the 3 orthogonal directions. $\{hkl\}$ mapping, in one direction, is colored using the inverse pole figure method (IPF) shown in Figure 6.3. The low index plane orientations are colored as follows: $\{001\}$ are red, $\{111\}$ are blue, and $\{101\}$ are green. Also labeled are the higher index planes: $\{112\}$, $\{122\}$, $\{012\}$ and $\{123\}$.

To describe the index of each plane, $\{hkl\}$, several variables are defined in Figure 6.4, which depicts a given $\{hkl\}$ on an inverse pole figure (IPF). The $\{hkl\}$ is defined in terms of β_i , the angle measured from a primary low index cubic plane normal to the $\{hkl\}$

of interest and α_i the angle between β_i and either the line from $\{100\}$ to $\{110\}$ or from $\{100\}$ and $\{111\}$. The Euler angle Φ from the Bunge convention is synonymous with $\beta_{\{100\}}$ used here [17].

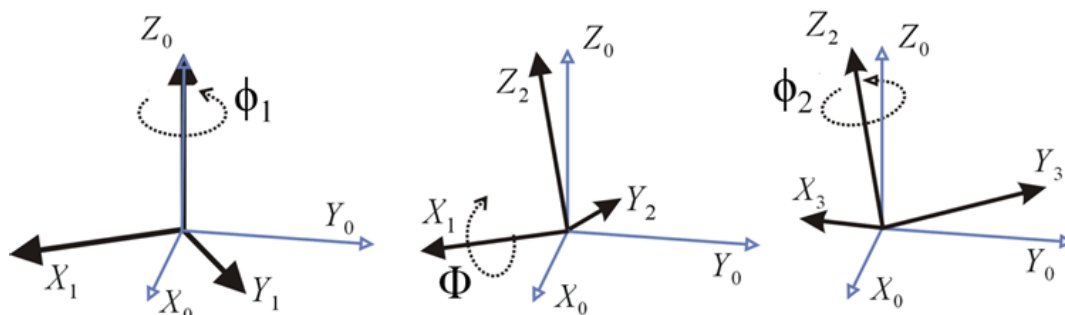


Figure 6.2. The Bunge Euler angle convention is depicted by the coincident axes (X_0 , Y_0 , Z_0) and the three rotations: ϕ_1 , Φ , ϕ_2 . The angle between the surface normal direction (for Cubic crystals $\langle hkl \rangle$) and the $\{100\}$ plane normal is defined by Φ . Figure adapted from [18].

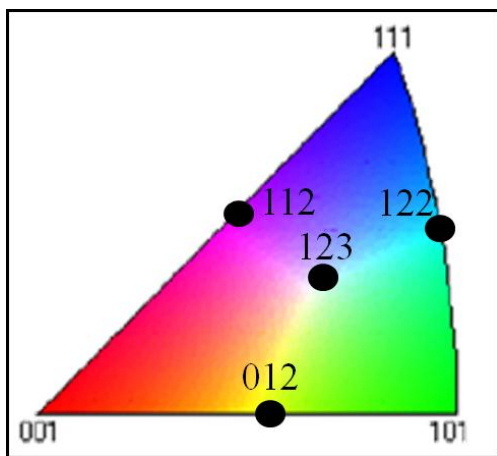


Figure 6.3. Inverse pole figure (IPF) coloring scheme to represent crystal orientations.

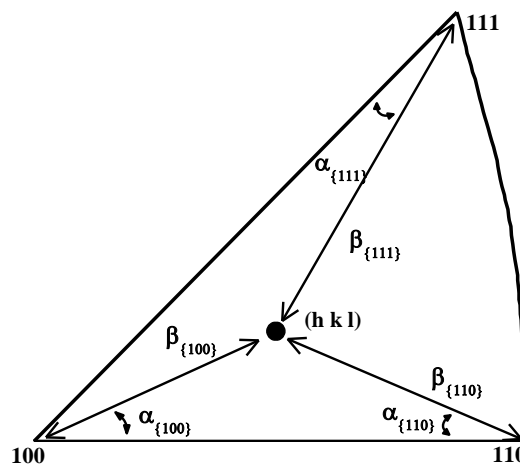


Figure 6.4. Schematic representation of $\{hkl\}$ positions defined by the angular distance, β_i , from the 3 low index cubic planes: $\{100\}$, $\{110\}$ and $\{111\}$. α_i represents the angle between β_i and the linear lines between the $\{100\}$ and $\{110\}$ poles for $\alpha_{\{100\}}$ and $\alpha_{\{110\}}$ and between the $\{100\}$ and $\{111\}$ poles for $\alpha_{\{111\}}$. As in *Nicolas* [19].

6.2.2 Critical Unresolved Issues

There are two key issues brought up by the results in this chapter. The first relates to the general dissolution behavior of the solid solution binary alloys. What are the underlying structural phenomena resulting in the increase in dissolution rate for the pT structure compared to the fcc structure? The second focuses on the orientation dependent dissolution apparent in the fcc structure? What causes the grain orientations to have such an orientation dependent dissolution? Lastly, why does the pT structure not exhibit such orientation dependent behavior?

6.3 Experimental

The fcc and pT Fe₅₀Pd₅₀ alloys were produced by the arc-melting technique using high purity 99.99% Fe and 99.999% Pd under an argon atmosphere. Prior to any heat treatments, the alloy sections were first encapsulated in quartz tubes under an argon atmosphere. The cast alloy Fe₅₀Pd₅₀ was cold rolled to approximately 0.5 mm. To remove the induced deformation and texture, the alloy was recrystallized at 1100 °C for 24 hours and then water quenched. The final heat treatment to produce the fcc structure was at 950 °C for 10 hours followed by water quenching. To produce pT Fe₅₀Pd₅₀ of a similar grain size to the fcc structure (average 30 μm), the sample was annealed 605 °C for 670 hours.²⁵

X-ray diffraction (XRD) characterization was performed using a Scintag XDS-2000 diffractometer with a Cu-K α source ($\lambda = 0.1541$ nm). XRD spectra measurements were conducted in the $\theta/2\theta$ configuration. The surface morphology was characterized by

²⁵ See Chapter 5.

optical microscopy and SEM using a JEOL 6700F with an accelerating voltage of 5 keV and a working distance of 15 mm. EDS analysis was conducted at 15 kV and a working distance of 15 mm. At this accelerating voltage the depth of interaction is roughly 0.33 μm .

Grain orientations of the polished surface were determined prior to electrochemical investigations using a scanning electron microscope, JEOL 840a SEM with LAB₆ filament, equipped with an electron backscatter detector (EBSD). EBSD mapping was performed at a magnification of 500 x and a working distance of 20 mm with a 20 kV accelerating voltage. The EBSD data acquisition and analysis was performed using the HKL Technology™ EBSD software suite. Indexing the EBSD images required 6 Kikuchi bands to match a specific calculated orientation. EBSD maps were made using a step size of 1 or 1.25 μm . The volume of interaction is roughly 50 nm deep. The step size was sufficient to determine the orientations of the smallest grains. Grain orientation maps, by grain HKLs, and the associated reduced inverse pole figures, IPFs, were made in the three sample orientations: Z (surface normal orientation), X and Y. The average orientation for each grain was used to determine the miller indices, {hkl}, of the surface plane. Texture determinations were based on the EBSD orientation maps.

To determine the relative amounts of dissolution of different grain orientations a confocal scanning laser microscope (CLSM) was used to create a topographical map of the polycrystalline surfaces. The CLSM, model Zeiss LSM 510, utilized a 543 nm wavelength HeNe laser with a pinhole size of 0.30 Airy units. A CLSM image is composed of a series of images of z direction slices (perpendicular to the sample surface).

The series of images can then be combined to resolve topographical information. For the following images the step size between vertical slices is 0.1 μm . Lateral resolution of this technique is about 0.3 μm (compared to a minimum grain size of 5 μm and average grain size of 30 μm). The 3D topographical maps typically shown have been processed with a 3x3 Gauss averaging. Using this data, the relative Z-depth of grains in any characterized region can be quantitatively calculated. It will prove convenient, discussed later, to use a relative metric for each region. Thus, the relative dissolution depth is determined relative to the highest, least susceptible to corrosion grains. The total amount of dissolution from the sample surface was determined using topographical maps including the epoxy mount which is flush with the pre-dissolution bare metal surface. This serves as the reference point of zero dissolution. For the series of increased dissolution measurements (where individual orientations were not determined), an area average of the dissolved sample surface (not normalized to each grain) was used to determine the average depth of dissolution.

Topographical information, with no statistical processing, was also used to calculate the microscopic surface roughness. The arithmetic mean deviation surface roughness, S_a , defined in Equation 6.1, was used to calculate the surface roughness. The surface roughness is the summation over all points, N , in an area of the absolute value difference between the height, z , of all points, (x_i, y_j) , in an area and the mean height over that area, S_c .

$$S_a = \frac{1}{N_x N_y} \sum_{i=1}^{N_x} \sum_{j=1}^{N_y} |z(x_i, y_j) - S_c| \quad 6.1$$

The surface topography of different grains were made using a field emission gun SEM, JEOL 6700F with an accelerating voltage of 5 keV and a working distance of 15 mm. Composition measurements were made using an attached energy x-ray dispersive spectrometer (EDS).

The samples were mounted in insulating epoxy, EPO-Thin, with an exposed surface area of approximately 0.5 cm^2 . To mitigate charging effects during SEM characterization, the epoxy was coated with carbon paint. The fcc $\text{Fe}_{50}\text{Pd}_{50}$ sample surface was polished using successively finer Si-carbide, 400-600-800-1200 grit, grinding paper followed by polishing using $1 \mu\text{m}$ alumina. Prior to EBSD characterization a final polishing step using $0.05 \mu\text{m}$ diamond slurry was performed. The sample surface was lightly Ar ion etched using a Gatan precision etching and coating system at 5 keV and $250 \mu\text{A}$ for 10 minutes to further reduce deformation induced by mechanical polishing to improve the diffraction pattern quality. After EBSD characterization but prior to electrochemical exposure, the sample was minimally re-polished using $1 \mu\text{m}$ alumina to remove carbon buildup²⁶.

Electrochemical measurements were conducted using a traditional 3-electrode setup with an exposed electrically isolated working electrode consisting of the fcc and pT polycrystalline $\text{Fe}_{50}\text{Pd}_{50}$ samples. The reference electrode was a saturated calomel type electrode, SCE, and the counter electrode was a platinum mesh. Chemical solutions were produced using reagent grade chemicals and pure water (resistivity $18.2 \text{ M } \Omega / \text{cm}$)

²⁶ The carbon buildup during EBSD mapping was found to inhibit dissolution of the EBSD characterized region during exposure in 1 M HCl solution. To remove carbon, the sample was polished for ~10 seconds using $1 \mu\text{m}$ alumina.

produced by an Academic MilliQ filtration system (MilliPore). Prior to electrochemical experiments the solution was deaerated for at least 2 hours by vigorous sparging of nitrogen through the solution. Polarization experiments were conducted using a Gamry PCI4 potentiostat. Potential controlled dissolution experiments were performed at 0.45 V_{SCE} for 400 – 2500 s. High purity element samples of Fe and Pd were used in comparative electrochemistry experiments. Exposed samples had surface area of approximately 0.3 cm^2 . Characterized regions, typically between 20 and 40 grains, were well away from any epoxy-sample interface to avoid any associated edge effects. Potentiostatic polarization experiments were performed on each of 3 sets of EBSD characterized regions²⁷. The measured charge during each exposure was within about 10% of the average value from all EBSD characterized regions to ensure similar dissolution amounts. For the calculations involving Faraday's Law, oxidation to Fe^{2+} and Pd^{2+} ($Pd_2Cl_4^{2-}$) and congruent dissolution was assumed. The applied potential (0.45 V_{SCE}) is well above the reversible potential for the dissolution reaction for both species. The

²⁷ Each EBSD characterized region contained between 20 and 40 different grains. However, not all orientations in terms of least and most susceptible to dissolution are represented in all regions. To account for regions that lack grains with dissolution rates on either end of the spectrum, the following data processing steps were used. Within each EBSD characterized region, Region 1 and 2 are two such characterized regions, the dissolution depth was measured relative to the grain with the least dissolution in that region. The depth of dissolution was found to linearly depend on $\beta_{\{100\}}$ up to 40°. For each region, the dissolution depth with respect to $\beta_{\{100\}}$ was fit by a linear least squares fitting with a freely varying intercept. The slope and intercept of the fit was calculated. The slopes of the fitted lines were found to be within 5% of the same value for all of characterized regions containing more than 20 grains of orientation $\beta_{\{100\}} < 40^\circ$. The average of these slopes was then used to fit all of the EBSD regions including regions not meeting this criterion. A total of about 60 grains (of the 300 total grains) are within these regions. The slopes of the linear fit for these regions vary by about 20% from the average slope used. The total shift in intercepts is about 0.3 μm , therefore introduced error from the data processing is not significant compared to the observed trends. The intercept of these fitted lines was set to the same value, 0, for each data set by means of adding or subtracting a correction factor to the intercept of all data sets.

density, calculated from the crystal structure, is 9.789 g/cm^3 for the fcc structure and 9.760 g/cm^3 for the pT structure.

6.4 Results

6.4.1 Materials Characterization

The XRD spectrum for fcc $\text{Fe}_{50}\text{Pd}_{50}$ after recrystallization is shown in Figure 6.5. The phase is identified as the disordered γ -phase which is the fcc equilibrium phase with lattice site occupancy factors (S.O.F.) of 0.5 for Fe and Pd. The γ -phase has symmetry Fm-3m and lattice parameter $a=3.804 \text{ \AA}$ [20]. The grain size, determined from the EBSD grain maps, ranged from 5 to 110 μm with an average grain diameter of 26 μm and a standard deviation of 21 μm (median 19 μm).

Heat treatment of the $\text{Fe}_{50}\text{Pd}_{50}$ at the eutectoid temperature, 605 $^{\circ}\text{C}$, is within the single L1_0 -phase field at the $\text{Fe}_{50}\text{Pd}_{50}$ composition [21]. The XRD spectrum is shown in Figure 6.6 and was identified as the ordered L1_0 phase. After a 670 hour annealing at 605 $^{\circ}\text{C}$, the average grain size was about 39 μm grain diameter ranging from about 15 to 250 μm . Prior to electrochemical experiments, the as-polished surface roughness was 0.030 μm .

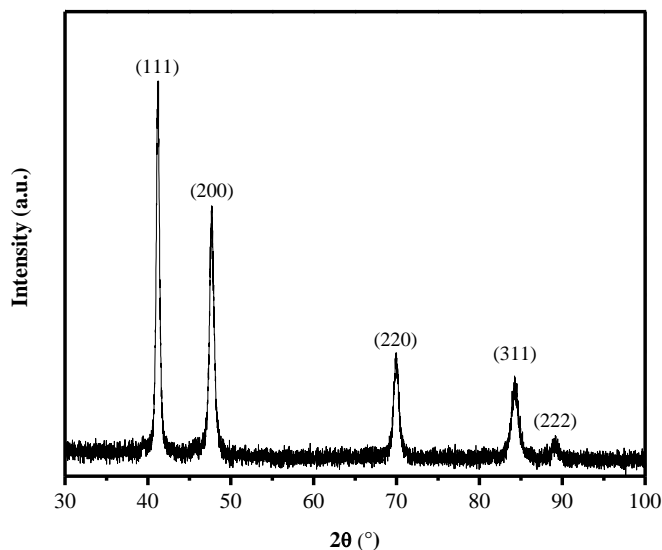


Figure 6.5. X-ray diffraction spectrum of the disordered fcc $\text{Fe}_{50}\text{Pd}_{50}$ sample after annealing at 950 °C for 10 hours and water quenched. The 5 indexed peaks all corresponded to the fcc γ -phase structure with lattice parameter $a = .3804$ nm and site occupancy coefficient of 0.5 for both Fe and Pd.

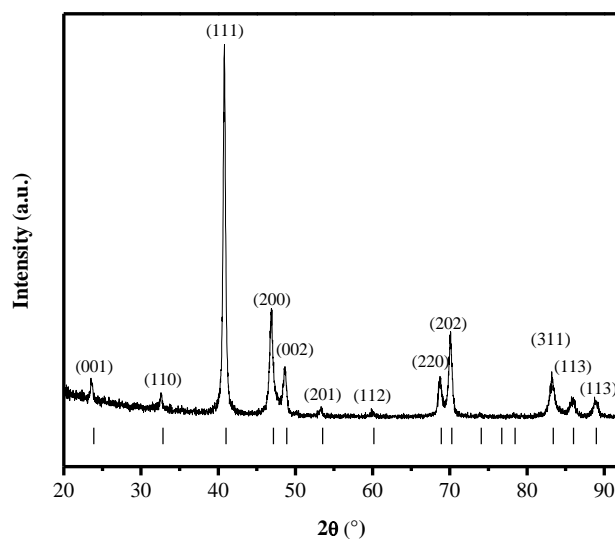


Figure 6.6. X-ray diffraction spectrum of the ordered pT $\text{Fe}_{50}\text{Pd}_{50}$ sample after annealing at 605 °C for 30 days and water quenched. The indexed peaks, indicated by vertical dashes and labeled, corresponded to the pT $L1_0$ phase which has space group $P4/mmm$ with lattice constants $a=3.852\text{\AA}$ and $c=3.723\text{\AA}$. [22]. The transformation from fcc γ -phase to $L1_0$ involves Pd atoms occupying the $c=1/2$ lattice positions and Fe atoms at the vertices.

6.4.2 Electrochemical Behavior in HCl Solution

The corrosion behavior was explored in deaerated 1 M HCl using a 1 hour open circuit measurement followed by cyclic polarization shown in Figure 6.7. The fcc and pT $\text{Fe}_{50}\text{Pd}_{50}$ structural states are compared to pure polycrystalline Fe and Pd. During the open circuit measurement, Fe has a very low open circuit potential while Pd has an intermediate value, $-0.15 \text{ V}_{\text{SCE}}$. The Pd open circuit potential is controlled by the redox potential associated with the reversible hydrogen electrode reaction instead of Pd/PdO or Pd/PdCl₄²⁻ oxidation half-cell reaction coupled with some cathodic reaction associated with the oxidizing power of the solution. The pT and fcc structural states of $\text{Fe}_{50}\text{Pd}_{50}$ have the highest open circuit potential which increases over the first 200 s then stabilizes at $0.2 \text{ V}_{\text{SCE}}$. The ordered pT structural state has an unstable open circuit potential. The high OCP of both states of the $\text{Fe}_{50}\text{Pd}_{50}$ alloy likely indicates the benefit of the transition metal noble metal mixture lowering the exchange current of hydrogen oxidation or enhancing HER.

The cyclic polarization behavior shows that pure Fe dissolves at high current densities at very low over-potentials. The Pd/Pd²⁺ dissolution pathway is enabled at the critical potential at $0.6 \text{ V}_{\text{SCE}}$ where the dissolution reaction dominates the underlying H oxidation reaction. In this solution, Pd is expected to dissolve and form a PdCl₄²⁻ complex at $0.07 \text{ V}_{\text{SCE}}$ based on thermodynamic principles [23]. The two $\text{Fe}_{50}\text{Pd}_{50}$ states show similar behavior and have an elevated open circuit potential due to beneficial Pd alloying. The surface morphology of the fcc $\text{Fe}_{50}\text{Pd}_{50}$ sample (Chapter 5) after the cyclic polarization experiments indicate that grain anisotropy in terms of the dissolution

behavior exists. Further elucidating this behavior exhibited by fcc Fe₅₀Pd₅₀ is the primary focus of this chapter. The EBSD characterized regions of fcc Fe₅₀Pd₅₀ were dissolved under potential controlled conditions at 0.45 V_{SCE}, indicated by the dashed line in Figure 6.7. This potential is above the reversible potential for both dissolution reactions and the global corrosion behavior is active dissolution with current densities of approximately 5 mA/cm².

At this potential, Fe and Pd undergo congruent dissolution. SEM-EDS analysis of the surface²⁸ shows no chemical composition difference between grains of limited and increased dissolution indicating no significant role of Pd enrichment. At the operating accelerating voltage, the majority of the characteristic x-rays for EDS analysis are generated within 0.33 μm of the surface [24]²⁹. After longer exposure times, grains can still be indexed by EBSD. Electron diffraction occurs from a limited interaction volume within about 50 nm, about 200 atomic layers, of the surface [25]. Surface reorganization and the resulting change in the crystal structure of the surface would alter the Fe₅₀Pd₅₀ backscattered diffraction pattern and is not observed.

The clear grain dependent structure induced by dissolution is not observed pT structured Fe₅₀Pd₅₀. Some grain dependent dissolution behavior is observed but only after the early stages of dissolution of the pT Fe₅₀Pd₅₀ alloy (Chapter 5). This contrast in

²⁸ SEM-EDS line profiles (Ch. 5) show no change in composition from an insulated alloy surface to a region exposed at 0.45 V_{SCE} for 400 s in both fcc and pT Fe₅₀Pd₅₀. Additionally, depth profile XPS results indicate only 10 nm (SiO₂ equivalent) of preferential dissolution on the order of a few at % after potentiostatic polarization in 0.1 M HCl solution.

²⁹ Monte Carlo simulations performed for pure Fe. Pd, a higher Z element, would have a smaller interaction volume. Thus, 0.33 μm is an upper bound.

behavior, indicative of the effect of the underlying change in structure will also be explored under similar conditions to the Fe₅₀Pd₅₀ fcc grain orientation study.

Both states of Fe₅₀Pd₅₀ were potentiostatically polarized at 0.45 mV_{SCE}, indicated by the dashed line in Figure 6.7. At this potential, the fcc Fe₅₀Pd₅₀ global corrosion behavior is active dissolution with current densities of approximately 5 mA/cm². The duration of the potentiostatic polarization in deaerated 1 M HCl solution was 400 s, 1500 s and 2500 s. A representative potentiostatic polarization curve is shown in Figure 6.8. A comparison of the total accumulated charge is tabulated in Table 6.2. The predicted depth of dissolution based on Faraday's for each experiment is calculated and a comparison to the experimental depth of dissolution of each structure state will be discussed in the sections to follow.

For the detailed analysis of the grain dependent dissolution of the disordered fcc Fe₅₀Pd₅₀, the 400 s exposure was repeated for each set of EBSD characterized regions. For each polarization the current after the initial 100 s was fairly uniform for each experiment with values between 6 and 9 mA/cm². The total charge during the 3 potentiostatic polarization experiments is shown in Table 6.2. A new exposure was required for each set of EBSD characterized regions.

It is worth noting that after longer exposure times, grains can still be indexed by EBSD. Electron diffraction occurs from a limited interaction volume within about 50 nm, about 200 atomic layers, of the surface [25]. Surface reorganization and the resulting change in the crystal structure of the surface would alter the backscattered diffraction pattern.

Table 6.1. Total accumulated charge density during potentiostatic polarization at 0.45 V_{SCE} in deaerated 1 M HCl solution. At each measured interval, the total charge during polarization is significantly higher for the ordered pT structural state than the disordered fcc state.

Polarization Duration (s)	Disordered fcc Charge Density (C/cm²)	Ordered pT Charge Density (C/cm²)
400	3.58	10.48
1500	24.21	54.37
2500	48.87	94.56

Table 6.2. Total accumulated charge during potentiostatic polarization of fcc Fe₅₀Pd₅₀ at 0.45 V_{SCE} for 400 s in deaerated 1 M HCl solution. The total charge is used to calculate the average expected depth of dissolution using Faraday's Law. Each experiment had similar charge accumulation and correspondingly similar expected depth of dissolution.

	Accumulated Charge (C/cm²)	Charge Deviation from Avg.	Calculated Avg. Depth of Dissolution (μm)
Exposure 1	3.46	-3.4%	1.20
Exposure 2	3.29	-8.2%	1.14
Exposure 3	4.00	11.6%	1.38

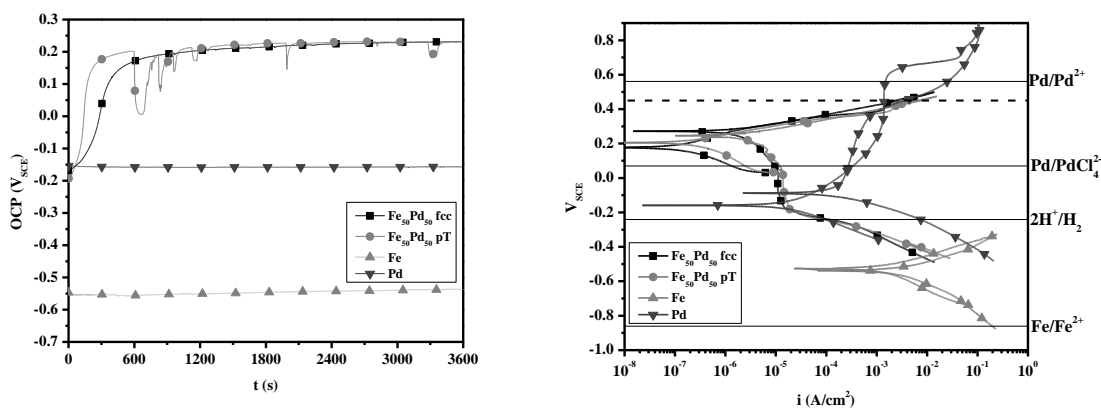


Figure 6.7. Open circuit (left) and E-log i (right) behavior in deaerated 1 M HCl solution at a scan rate of 1 mV/s. The dashed line on the E-log i plot indicates the 0.45 V_{SCE} potential used for the potentiostatic polarization experiments.

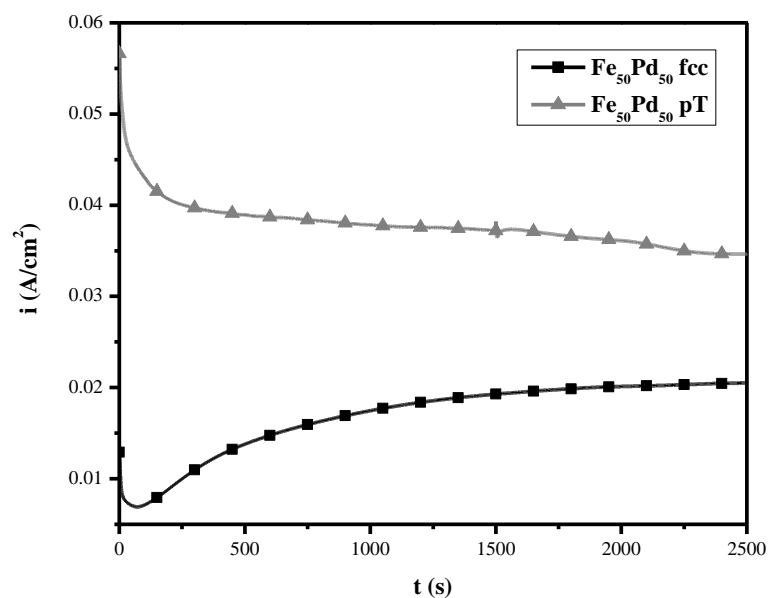


Figure 6.8. Representative i - time behavior of ordered-fcc and disordered-pT during potentiostatic polarization at 0.45 V_{SCE} in deaerated 1 M HCl solution.

6.4.3 Relationship between Dissolution Behavior and Crystallographic Orientation in Disordered fcc Fe₅₀Pd₅₀

The orientation of each grain with in the sample coordinate system was determined by EBSD. To describe the index of each plane, {hkl}, several variables are defined in Figure 6.4, which depicts a given {hkl} on an inverse pole figure (IPF). The dissolution behavior of the grains was found to correlate to the orientation in the surface normal direction, i.e. the orientation of the plane of the interface between the solution and the sample. Table 6.3 lists grain information from selected SEM images, CLSM images, orientation maps and surface morphology. These results are followed by the orientation vs. dissolution depth and surface roughness plots for all grains analyzed.

The CLSM topographical map of Region 1, with a total accumulated anodic charge of 3.29 C/cm², is shown in Figure 6.9 and the corresponding grain orientations are shown in Figure 6.10, both as an EBSD map and the grain orientations depicted on the IPF. The total measured charge during exposure in 1 M HCl solution was 3.29 C/cm² (Table 6.2). In the CLSM topographical map, the red regions correspond to the highest, or least corroded, grains; whereas the blue-purple colored grains indicate those that experienced the greatest depth of dissolution. It is obvious from these plots that there is significant crystallographic dependence of dissolution. At first glance, the near {100} planes, red on the EBSD map and near the {100} pole on the associated IPF, show the lowest qualitative depth of dissolution. The high index planes between 10 and 20° of the {111} pole, purple-blue on the EBSD map, show the highest corrosion susceptibility. SEM micrographs of this region are shown in Figure 6.11.

Region 2 has some grains with orientation very near, $\beta_i < 1^\circ$, both the $\{100\}$ and $\{111\}$ axes. The topographical map of Region 2, total accumulated charge 3.46 C/cm^2 , is shown in Figure 6.12 and the orientation map and corresponding IPF are shown in Figure 6.13. Grains 11 and 12 respectively in Figure 6.14, show that the near $\{100\}$ grain has undergone less dissolution than the $\{111\}$. In the case of this $\{111\}$ grain, the dissolution depth is lower than many of the grains which are still quite close to the $\{100\}$ orientation, for example the adjacent grains (pink colored in the EBSD map). At higher divergence from the $\{111\}$, grain 15, the dissolution rate is significantly higher. Table 6.3 summarizes the surface roughness, relative height and orientation for each grain. The dissolution depth for grains within Region 1 and 2 is plot as a function of β_i in Figures 6.16 and 6.17. For each grain all 3 β_i are shown and these plots indicate that the dissolution depth has a linear relationship to $\beta_{\{100\}}$ over a very wide range of angles. Grains with orientation near $\{110\}$ do not show the decrease in corrosion susceptibility that accompanies grains with orientations near the $\{100\}$ or $\{111\}$.

Beta Dependence on Dissolution Depth in Disordered fcc Fe₅₀Pd₅₀

The dissolution depth as function of orientation was combined for all regions³⁰. Figure 6.18 shows the dissolution depth as a function of $\beta_{\{100\}}$. The dissolution depth increases as a linear function of angle, slope $-0.71 \mu\text{m}/^\circ$. The most susceptible region is between 35 and 45° from the $\{100\}$. The corrosion depth near the $\{111\}$ plane is significantly lower. When $\beta_{\{111\}}$ is less than 10° , indicated by the triangles, the depth of dissolution decreases rapidly as the orientation becomes closer to $\{111\}$. For orientations

³⁰ The intercept for each $\beta_{\{100\}}$ plot corresponding to each region, e.g. for Region 1-2 in Figure 6.16-6.17, was set to 0. See Experimental section for details.

near the $\{110\}$, indicated by the circles, the corrosion depth remains high. Figure 6.19 shows the dependence of the corrosion rate on direction, $\alpha_{\{100\}}$, from the $\{100\}$ plane normal. The corrosion depth towards the $\{110\}$, α_{100} between 0 and 10° , is compared to towards the $\{111\}$, α_{100} between 35 and 45° . No significant deviation is observed between the two directions. Similar plots have been made for both $\beta_{\{111\}}$, Figure 6.20, and $\beta_{\{110\}}$, Figure 6.21. For $\beta_{\{111\}} < 10^\circ$ from the $\{111\}$, the depth of dissolution increases linearly with a slope of $-0.24 \mu\text{m}/^\circ$ divergence, which is 4 times higher than the similar plot for $\beta_{\{100\}}$. Between 10 and 20° , the dissolution depth is at a maximum. The corrosion rate at $\beta_{\{110\}} < 20^\circ$, shown in Figure 6.21, shows no statistically significant trend. The corrosion depth as a function of grain orientation is plotted on an IPF in Figure 6.22.

6.4.4 Surface Roughness: Faceted Grain Morphology and Correlation to Dissolution in Disordered fcc Fe₅₀Pd₅₀

The differences in the microscopic surface roughness of different grains are apparent in the SEM micrographs. The morphological distinction among grains is shown in the SEM micrographs in Figures 6.11, 6.14 and 6.15, which indicate the surface roughness features associated with each grain orientation. The morphologically smooth grains, 1 and 7, correspond to regions near $\{100\}$ which have undergone limited dissolution. Grain 6, $\beta_{\{111\}} = 7^\circ$, has undergone significantly more dissolution than grains near the $\{100\}$. In contrast, Grain 2 with an orientation of $\{533\}$ and $\beta_{\{111\}} = 13^\circ$ has undergone significantly increased dissolution and has a higher surface roughness. Grains with orientations near $\{110\}$ are shown in Figure 6.15. The surface roughness remains high even for Grain 24 which has an orientation within 2° of the $\{110\}$ plane normal. To

quantify the roughness of a surface, Eq. 1 is used to calculate the deviation of the peaks and valleys from the average value. Grain 24 has a surface roughness of $0.18\ \mu\text{m}$, twice as rough as smooth grains. Grains 1, 3 and 6 are near either the $\{100\}$ or $\{111\}$ and have a surface that appears smooth and have a corresponding surface roughness of less than $0.09\ \mu\text{m}$. The most dissolved grains, such as Grain 2 and 8, also have the highest surface roughness, $0.25\ \mu\text{m}$.

The surface roughness of a representative subset of grains is plotted on an IPF in Figure 6.23. As the SEM micrographs and the CLSM topography indicate, the grains with the highest roughness correlate to the grains of highest dissolution. This can be seen by comparison of the inverse pole figures in Figure 6.22 and Figure 6.23. There are exceptions to this rule; Orientations along the great circle between $\{110\}$ and $\{111\}$ orientations show similar increased dissolution (Figure 6.23 e.g., Grain 15 in Figure 6.14), but comparatively decreased microscopic surface roughness compared to other orientations at similar dissolution depths ($\beta_{\{111\}}$ between 10 and 20°).

6.4.5 Morphological Evolution after Increased Dissolution in Disordered fcc $\text{Fe}_{50}\text{Pd}_{50}$

After longer polarization times and increased dissolution, the surface morphology retains the crystallographic faceted structure characteristic of each grain. Three grains, Figure 6.28, show the surface morphology of $\{100\}$ and $\{111\}$ oriented grains. These grains show characteristic scalloped morphology with no apparent crystallographic dependence. Also shown is a grain with a $\{533\}$ orientation. This orientation, with $\beta_{\{111\}} = 16^\circ$, is one of the most highly dissolving orientations and shows a dissolution revealed

surface morphology consisting of a series of terraces and steps. The steps also show microscopic features along the steps indicating that dissolution is occurring. These features are more apparent after increased dissolution.

Figure 6.25 shows the CLSM topography of a region of the surface after polarization for 2500 s and a total accumulated charge of 48.87 C/cm^2 . The difference between the highest and lowest grains is $25 \text{ }\mu\text{m}$. Even at the significantly increased dissolution, compared to 400 s exposure, the grains remain distinct entities and are still highly faceted. The surface morphology is shown in Figure 6.26, and the faceted nature of distinct grains is clearly shown. The higher magnification of the highest grain (least dissolution) in the CLSM region shows a surface dominated by terraces with a scalloped nature punctuated by rectangular dissolution areas. These rectangular areas are observed on $\{100\}$ orientations (Grain 11, Figure 6.14).

Two additional grains, shown in Figure 6.27 and 6.28, have electrochemically dissolved into a series of terraces and steps. A grain likely with near $\{100\}$ orientation is shown in Figure 6.27 after significantly increased dissolution. The steps show clear microscopic kink features indicating that dissolution is proceeding along the kinks on steps more quickly than dissolving the terraces. The terraces of the grain shown in Figure 6.28 have the characteristic rectangular feature seen on $\{100\}$ orientations. The orientation of the faceted structure is very crystallographic in nature, i.e. features within a grain are aligned along specific directions.

Table 6.3. Tabulated roughness, S_a , and relative dissolution depths for selected grains shown in Figures 6.11, 6.14, and 6.15, delimited by thick lines. All 3 β_i values are listed for each grain. The grey shaded β_i regions indicate orientations within 10° of a primary cube plane normal. Grains with the roughest surface and highest amount of dissolution have $\beta_{\{111\}}$ between 10 and 20° (red shaded).

Grain	{hkl}	$\beta_{\{100\}}$ (°)	$\beta_{\{110\}}$ (°)	$\beta_{\{111\}}$ (°)	$\alpha_{\{100\}}$ (°)	$\alpha_{\{110\}}$ (°)	$\alpha_{\{111\}}$ (°)	S_a (μm)	Rel. depth of diss. (μm)
1	{610}	9.1	36.3	47.0	15.9	3.9	5.4	0.055	-0.42
2	{533}	41.2	28.1	13.9	40.9	62.9	12.3	0.231	-2.82
3	{310}	17.1	28.3	42.5	7.7	4.6	14.1	0.064	-0.63
4	{430}	36.3	8.7	34.7	3.6	14.1	40.8	0.14	-1.91
5	{621}	21.1	25.2	36.6	20.5	16.3	13.8	0.118	-1.07
6	{665}	51.2	31.8	4.3	42.4	78.3	33.1	0.088	-1.88
7	{611}	10.0	37.1	44.7	33.7	8.6	2.5	0.099	-0.67
8	{533}	39.1	28.7	15.7	43.9	58.2	2.7	0.276	-3.53
9	{520}	21.7	23.4	40.7	4.6	4.3	20.2	0.111	-1.47
10	{530}	31.1	14.7	34.3	5.7	12.0	32.3	0.155	-2.00
11	{100}	1.6	43.6	53.6	28.5	1.0	0.5	0.052	-0.37
12	{111}	54.3	34.2	1.0	45.0	79.2	1.7	0.051	-0.62
13	{554}	50.9	29.2	6.2	39.7	79.8	49.1	0.050	-1.16
14	{421}	31.4	19.9	27.3	22.3	36.7	25.1	0.140	-2.39
15	{221}	47.5	20.7	14.2	31.2	79.8	52.6	0.093	-2.77
16	{641}	36.5	9.9	31.1	9.3	32.1	39.7	0.193	-2.26
17	{641}	36.2	10.7	31.1	12.4	38.8	38.8	0.182	-2.03
18	{531}	30.1	17.7	30.4	19.8	31.4	25.0	0.176	-1.73
19	{641}	35.3	11.9	29.9	15.0	39.9	36.1	0.235	-2.03
20	{540}	39.2	6.5	32.1	9.7	46.1	44.9	0.170	-2.08
21	{530}	30.7	14.4	36.6	5.7	12.0	32.1	0.113	-1.72
22	{542}	41.2	18.6	18.7	29.4	65.7	36.3	0.228	-2.37
23	{651}	41.2	6.6	30.1	8.3	51.2	47.8	0.174	-1.99
24	{110}	43.1	1.9	34.5	6.0	64.3	51.9	0.182	-2.09

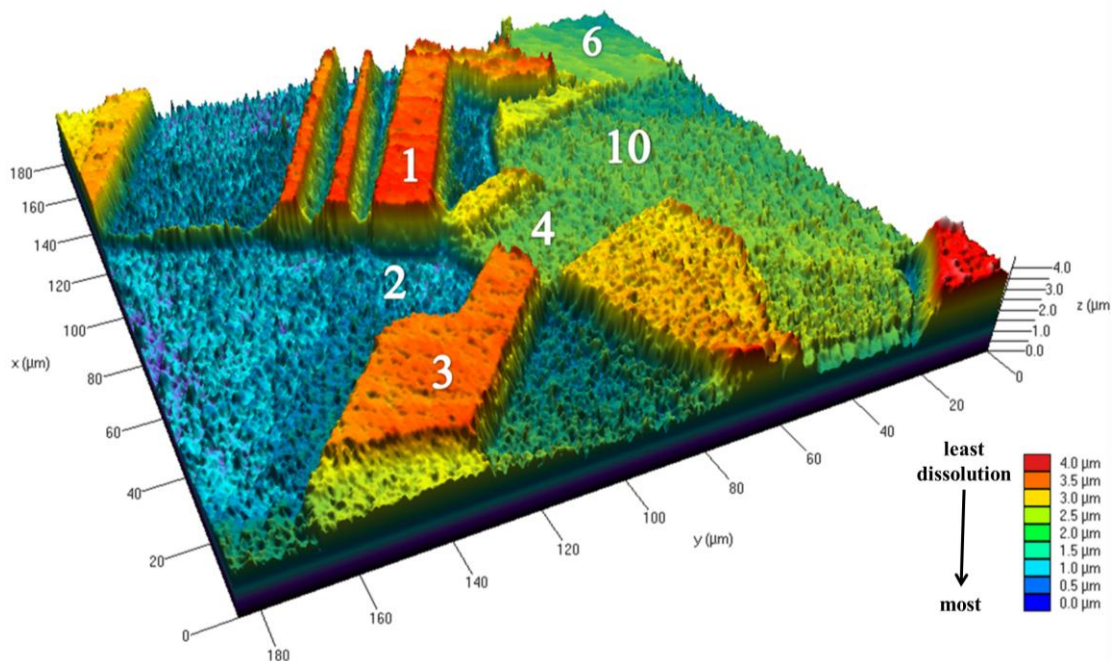


Figure 6.9. CLSM topographical plot of disordered fcc $\text{Fe}_{50}\text{Pd}_{50}$, Region 1 after potentiostatic polarization at $0.45 V_{\text{SCE}}$ in deaerated 1 M HCl solution with total accumulated charge 3.29 C/cm^2 (Exposure 2, Table 6.2). Numbers indicate specific grains used to identify regions in micrographs, with properties listed in Table 6.3.

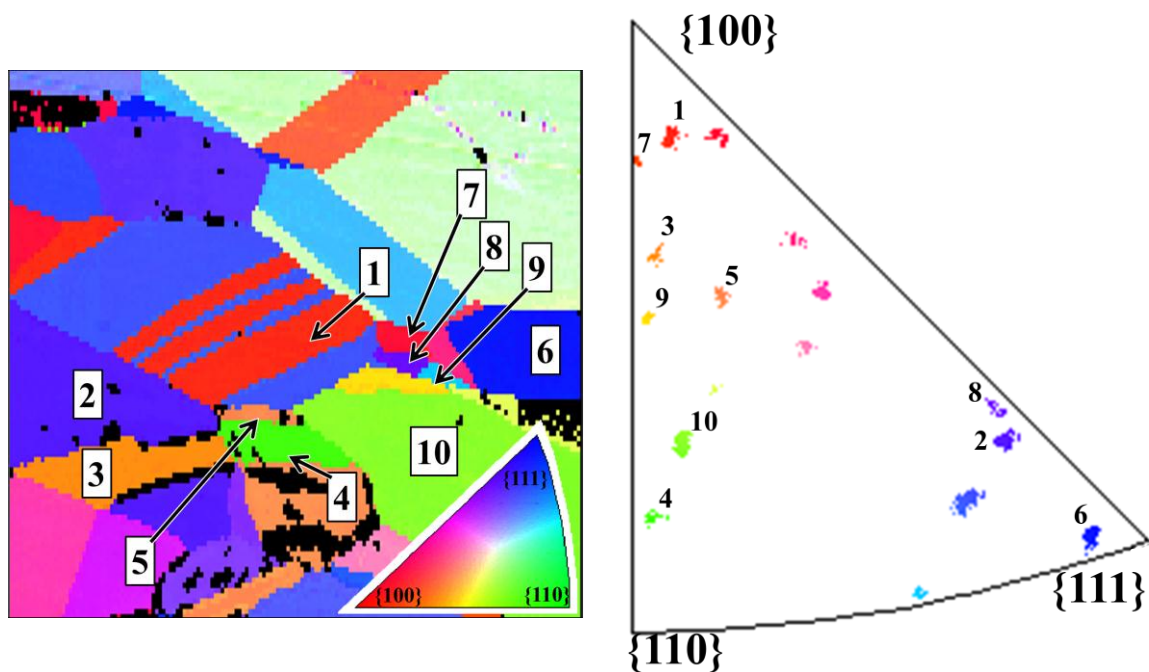


Figure 6.10. EBSD mapping (left) and corresponding reduced IPF (right) of Region 1 in the sample normal direction with an EBSD step size of $1 \mu\text{m}$. Black points on the EBSD map indicate areas that failed to index to a grain orientation.

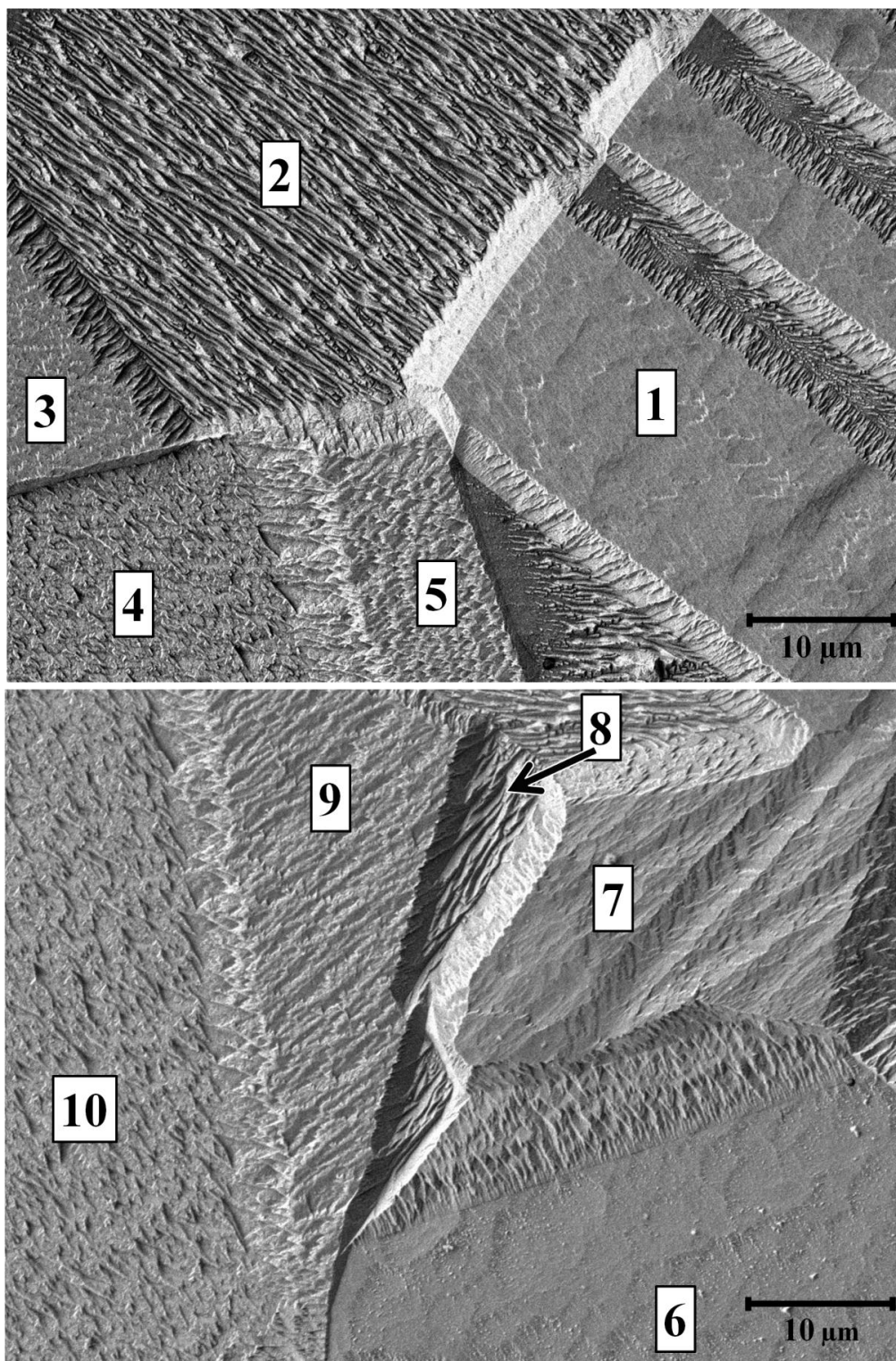


Figure 6.11. SEM micrographs from Region 1 of disordered fcc $\text{Fe}_{50}\text{Pd}_{50}$, with 3.29 C/cm^2 of total anodic charge and select grains identified. Grains 1 and 7 are within 10° of the $\{100\}$ plane normal. Grain 6 is within 5° of the $\{111\}$, while Grains 2 and 8 are about 15° from the $\{111\}$. Grains 4 and 10 are within 15° of the $\{110\}$ plane normal. Grain orientation approximate $\{hkl\}$: Grain 1 $\{610\}$, Grain 2 $\{533\}$, Grain 3 $\{310\}$, Grain 4 $\{430\}$, Grain 5 $\{621\}$, Grain 6 $\{665\}$, Grain 7 $\{611\}$, Grain 8 $\{533\}$, Grain 9 $\{520\}$, and Grain 10 $\{530\}$.

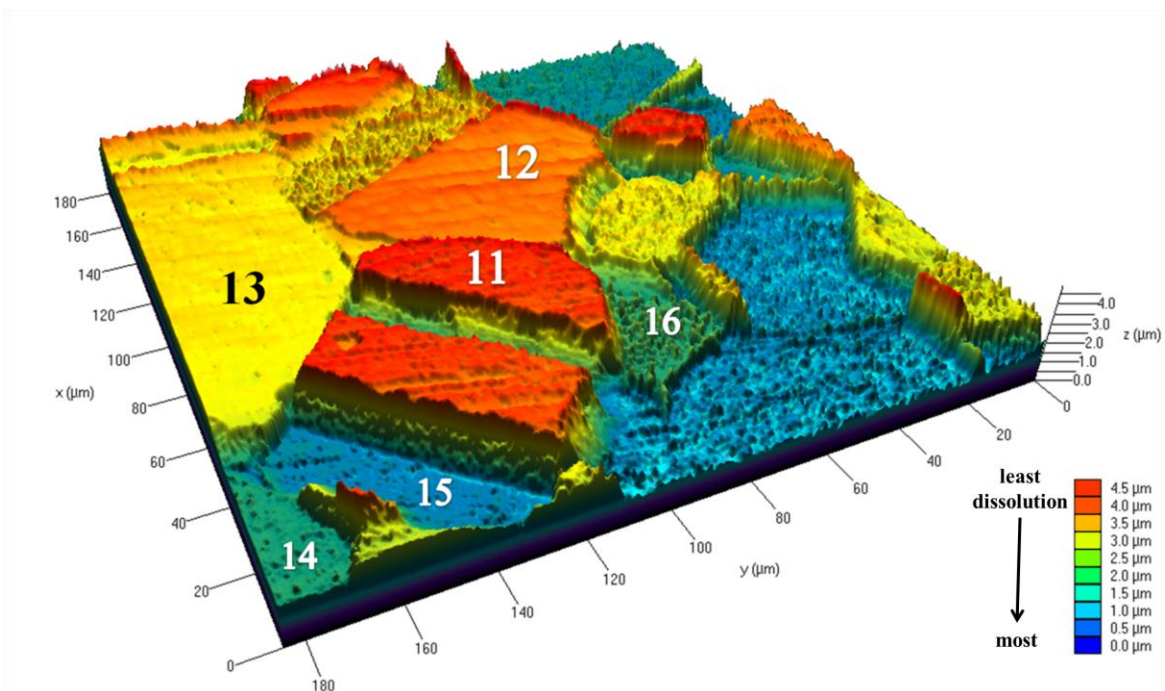


Figure 6.12. CLSM topographical plot of Region 2 of disordered fcc $\text{Fe}_{50}\text{Pd}_{50}$ after potentiostatic polarization at $0.45 V_{\text{SCE}}$ in deaerated 1 M HCl solution with total accumulated charge of 3.46 C/cm^2 (Exposure 1, Table 6.2). Numbers indicate specific grains used to identify regions in micrographs, with properties listed in Table 6.3.

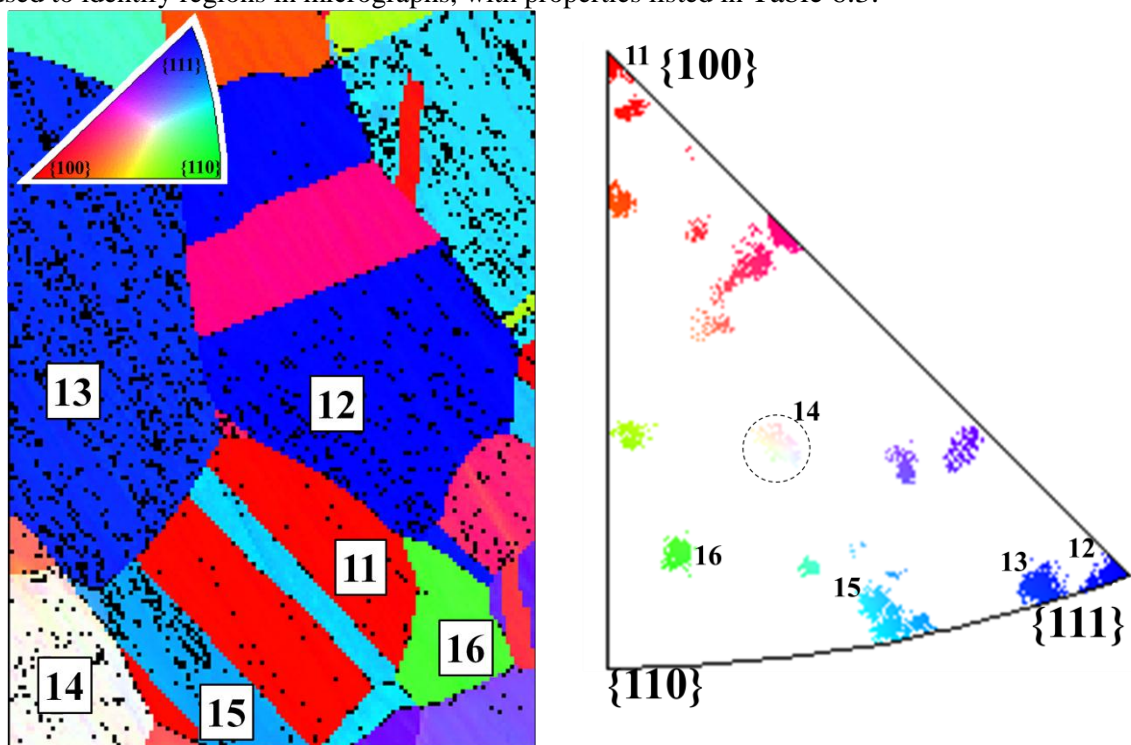


Figure 6.13. EBSD mapping (left) and corresponding reduced IPF (right) of Region 2 in the sample normal direction. EBSD step size $1 \mu\text{m}$. Black points on the EBSD map indicate steps that failed to index. Grain 14, indicated by the dashed circle in the IPF, has orientation near $\{123\}$ and is white on the IPF.

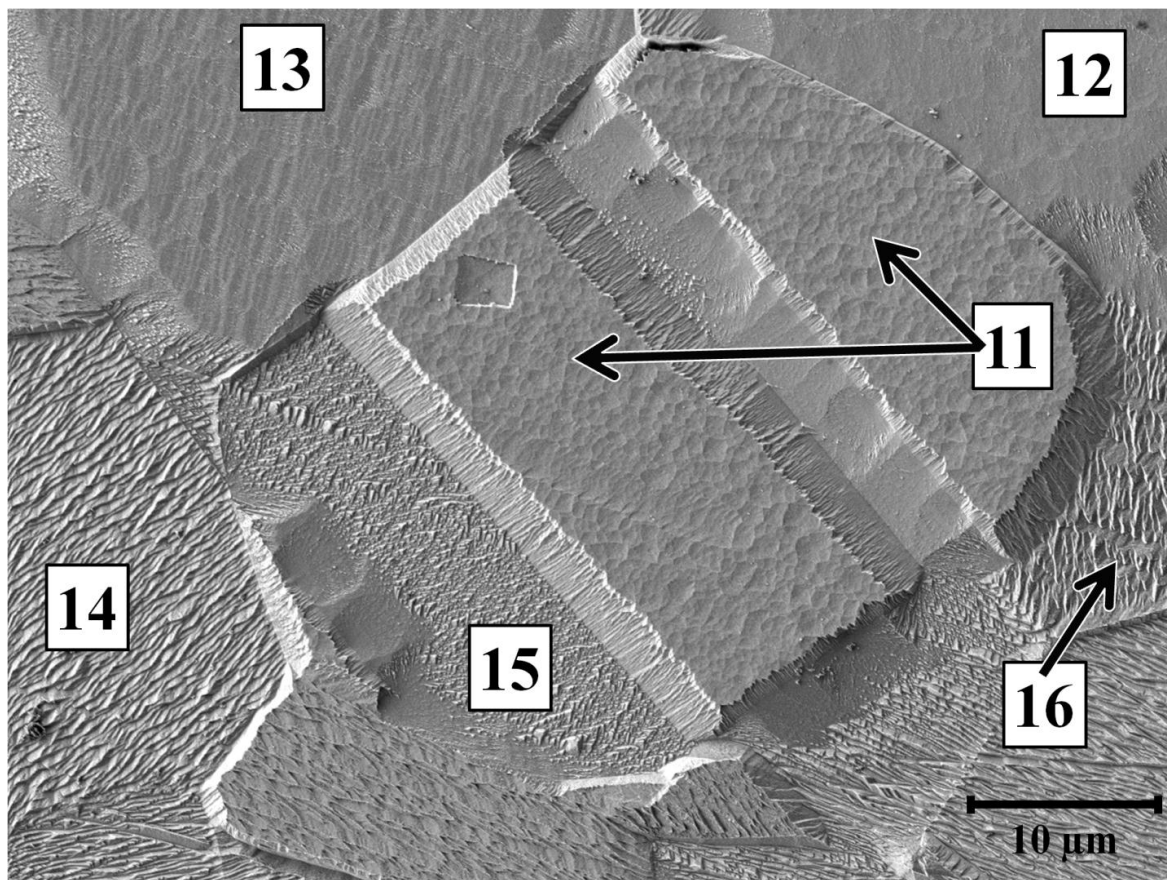


Figure 6.14. SEM micrograph of Region 2 of disordered fcc $\text{Fe}_{50}\text{Pd}_{50}$ with 3.46 C/cm^2 of total anodic charge and grains 11-16 identified. Grain 11 is within 2° of the $\{100\}$ plane normal. Grain 12, 13, and 15 are 1° and 6° and 14° from the $\{111\}$ plane normal, respectively. Grain 14 and 16 are 20° and 10° from the $\{110\}$ plane normal, respectively. Grain orientation approximate $\{hkl\}$: Grain 11 $\{100\}$, Grain 12 $\{111\}$, Grain 13 $\{554\}$, Grain 14 $\{421\}$, Grain 15 $\{221\}$, Grain 16 $\{641\}$, Grain 7 $\{611\}$, Grain 8 $\{533\}$, Grain 9 $\{520\}$, and Grain 10 $\{530\}$.

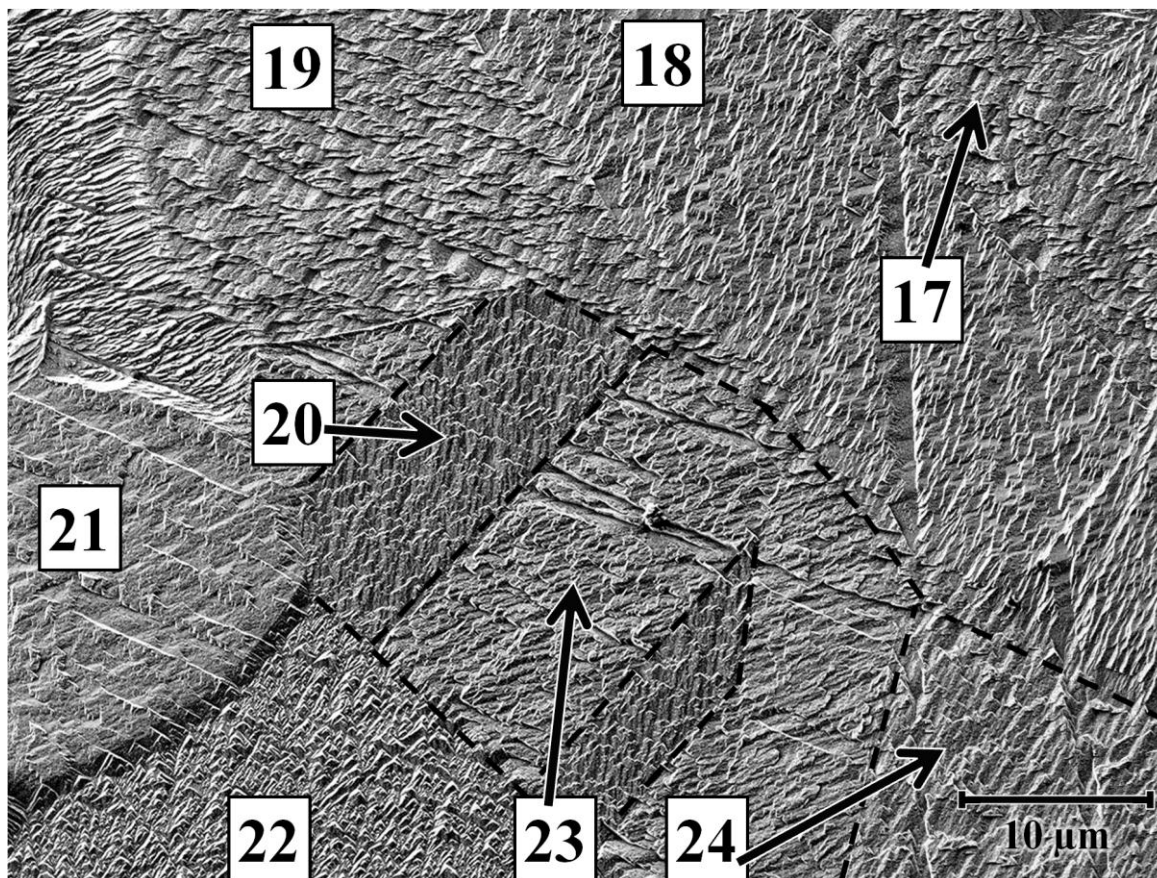


Figure 6.15. SEM micrograph of disordered fcc Fe₅₀Pd₅₀ grains with orientations near {110}. Grains 20, 23 and 24 have orientations within 7° of the {110} plane normal, while 17, 19 and 21 are within 15°. These grains are a subset of Region 3 which had a total charge during potentiostatic polarization of 4.00 C/cm² (Exposure 3, Table 6.2). Dashed lines indicate grain boundaries of limited contrast. CLSM topographical map and EBSD maps are not shown for this region. Grain orientation approximate {hkl}: Grain 17 {641}, Grain 18 {531}, Grain 19 {641}, Grain 20 {540}, Grain 21 {530}, Grain 22 {542}, Grain 23 {651}, and Grain 24 {110}.

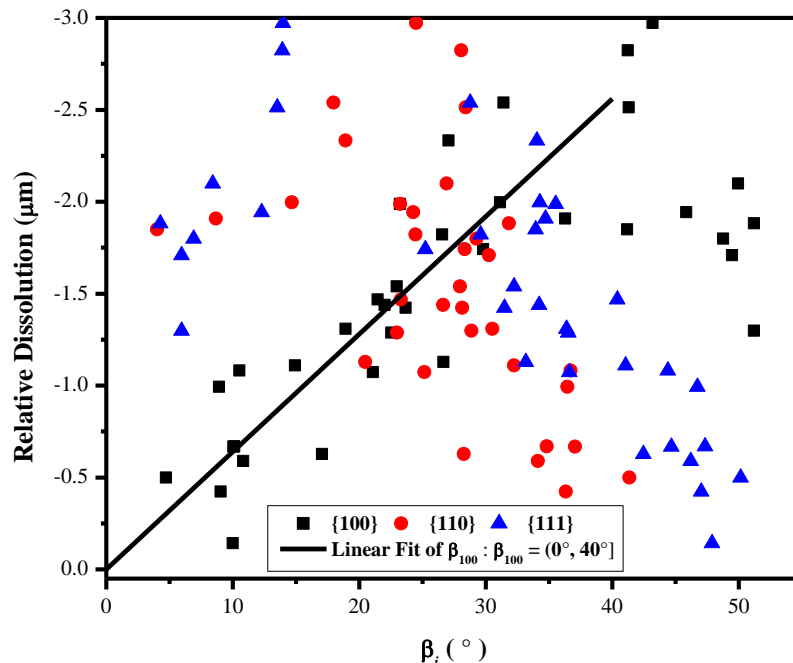


Figure 6.16. Relative dissolution depth of disordered fcc $\text{Fe}_{50}\text{Pd}_{50}$ as a function of β_i for each grain in Region 1. Each grain has the three β_i associated with the primary cube zone axis. A linear fit of $\beta_{\{100\}}$ up to 40° has a slope of $-0.064 \mu\text{m} / ^\circ$ angular deviation from $\{100\}$ excluding $\beta_{\{111\}} < 10^\circ$. The root mean square error of this fit is 0.852. This plot includes grains adjacent to Region 1 which are not shown in the plots in Figure 6.9-6.11.

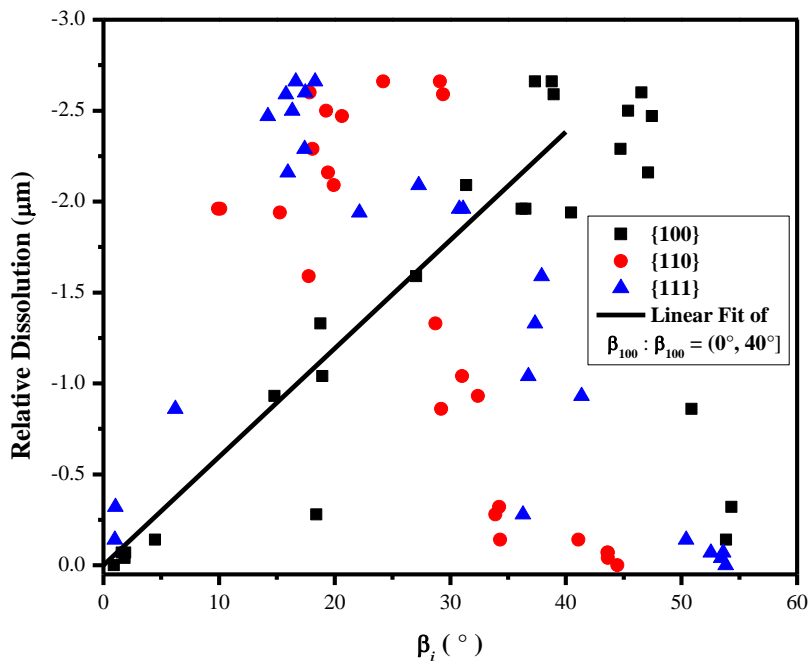


Figure 6.17. Relative dissolution depth is plotted as a function of β_i for each grain in Region 2 (Figure 6.12-6.14). Each grain has the three β_i associated with the primary cube zone axis. A linear fit of β_{100} up to 40° has a slope of $-0.060 \mu\text{m} / ^\circ$ angular deviation from $\{100\}$, excluding $\beta_{\{111\}} < 10^\circ$. The RMS error of the linear fit is 0.955

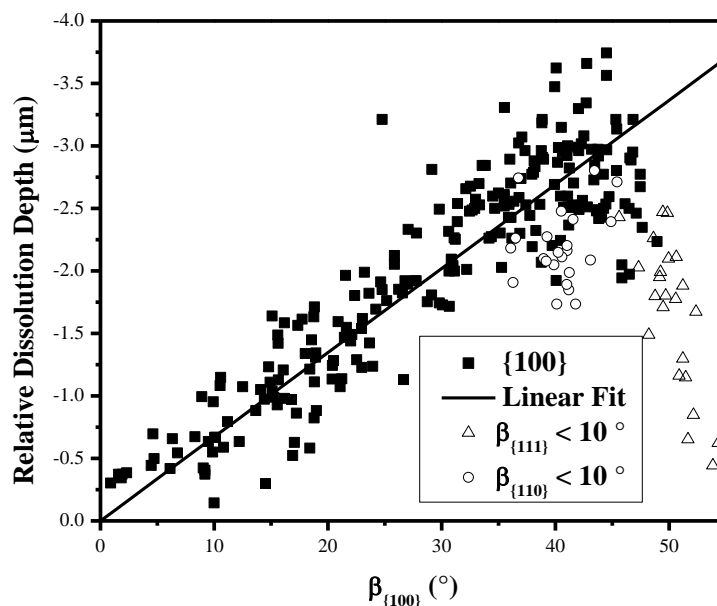


Figure 6.18. Relative dissolution depth of disordered fcc $\text{Fe}_{50}\text{Pd}_{50}$ as a function $\beta_{\{100\}}$. Regions within 10° of the $\{111\}$ and $\{110\}$ plane normals are indicated by open triangle and open circle symbols, respectively. A linear fit of the data over the first 40° , excluding data within 10° either $\{100\}$ and $\{110\}$ plane normal, has a slope of $-0.071 \mu\text{m}/^\circ$ and a RMS error of 0.33.

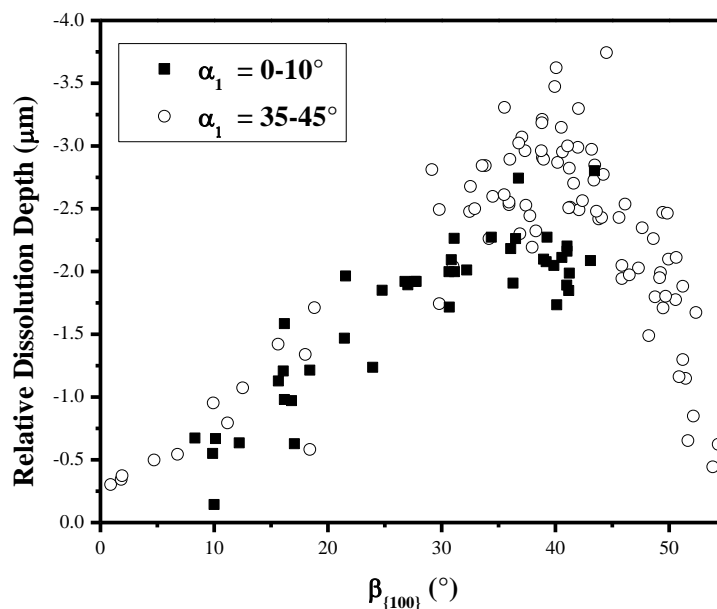


Figure 6.19. Relative dissolution depth disordered fcc $\text{Fe}_{50}\text{Pd}_{50}$ as a function $\beta_{\{100\}}$ of plotted for $\alpha_{\{100\}} = 0 - 10^\circ$ (in the direction of the $\{110\}$ plane normal) and $35 - 45^\circ$ (in the direction of the $\{111\}$ plane normal). The decrease at high $\beta_{\{100\}}$ for large $\alpha_{\{100\}}$ is due to proximity to the $\{111\}$ orientation.

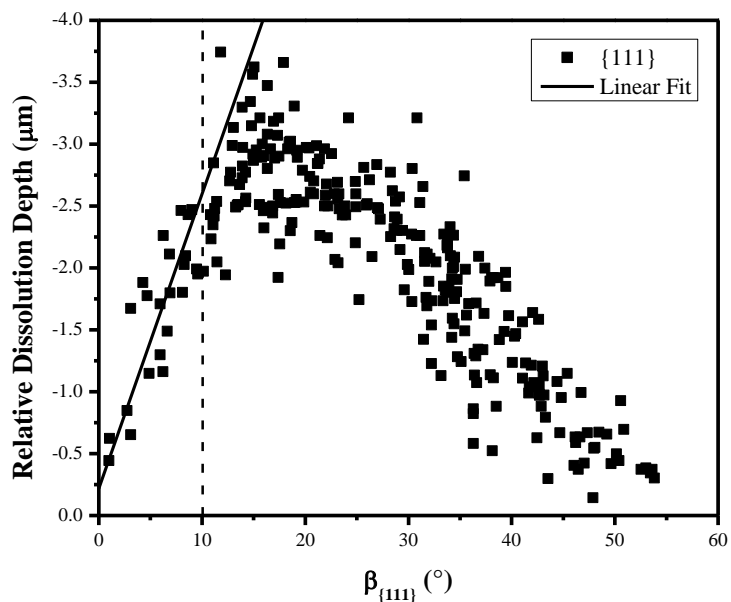


Figure 6.20. Relative dissolution depth of disordered fcc $\text{Fe}_{50}\text{Pd}_{50}$ as a function $\beta_{\{111\}}$. A linear fit, solid line, of the first 10° (delimited by the dashed line) has a slope of $-0.24 \mu\text{m}/^\circ$ and an intercept $-0.22 \mu\text{m}$ and RMS error of 1.56.

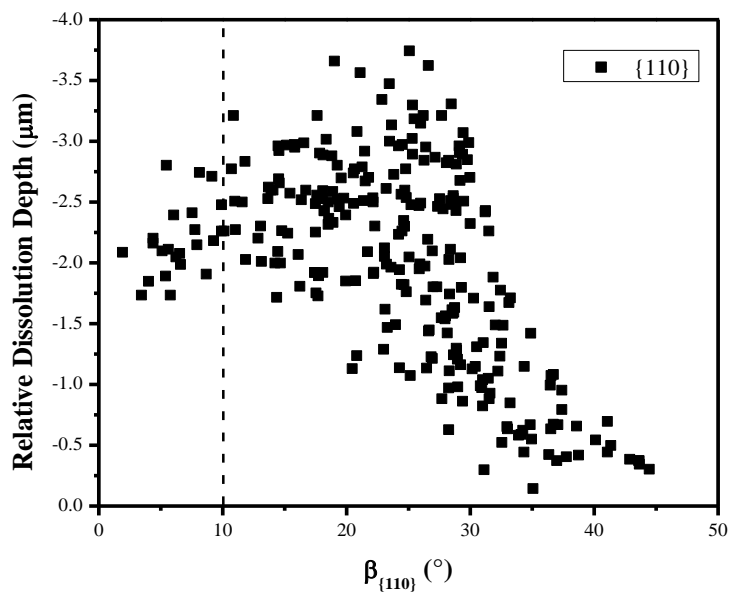


Figure 6.21. Relative dissolution depth of disordered fcc $\text{Fe}_{50}\text{Pd}_{50}$ as a function $\beta_{\{110\}}$. No statistically significant trend at $\beta_{\{110\}} < 20^\circ$ is observed.

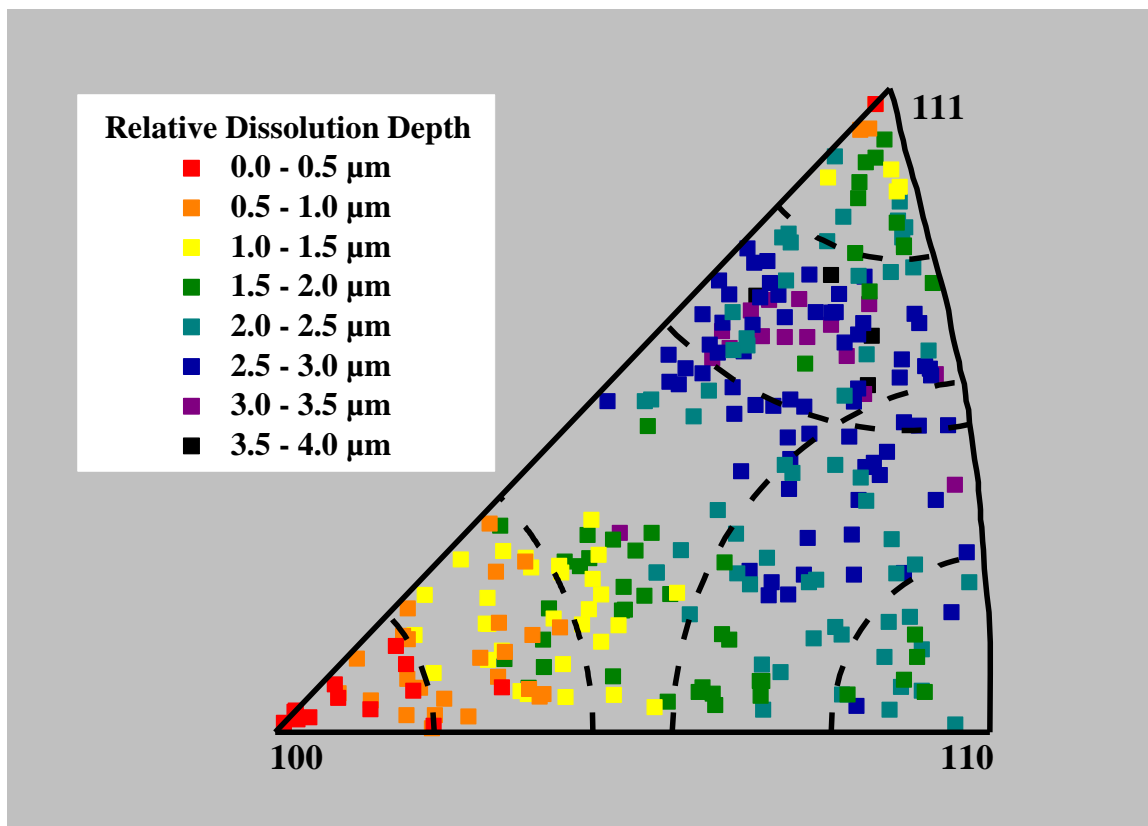


Figure 6.22. Relative depth of dissolution of individual disordered fcc $\text{Fe}_{50}\text{Pd}_{50}$ grains as a function of crystallographic orientation plotted on an equal area inverse pole figure in the sample normal (z) direction. The region with highest dissolution is between 10 and 20° from the $\{111\}$ plane normal. Dashed lines indicate 10° degree increments from the three low index cube plane normals: $\{100\}$, $\{110\}$ and $\{111\}$.

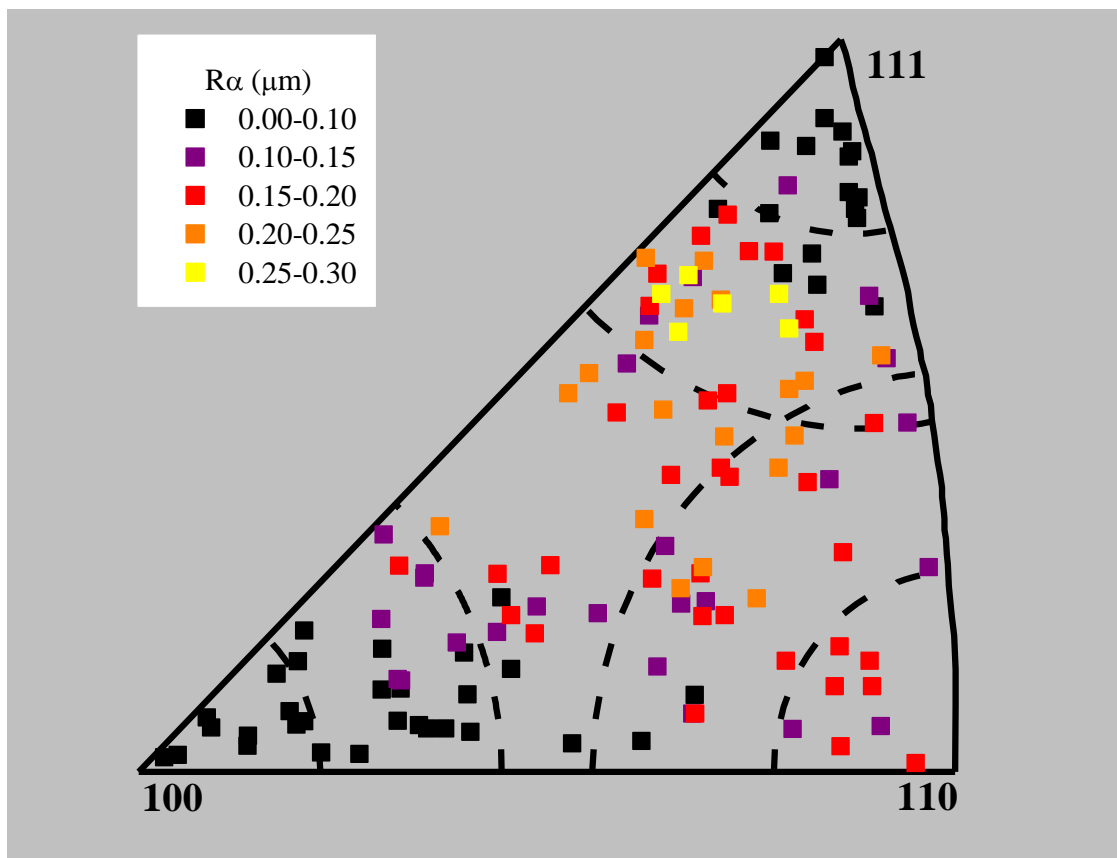


Figure 6.23. Calculated arithmetic mean deviation surface roughness, S_a , of disordered fcc Fe₅₀Pd₅₀ plotted on an equal area inverse pole figure. The smoothest grains are less than 20° from the {100} and 10° from the {111} plane normals. The roughest region is between 10 and 20° from the {111} plane normal which corresponds to the region of most dissolution (Figure 6.22).

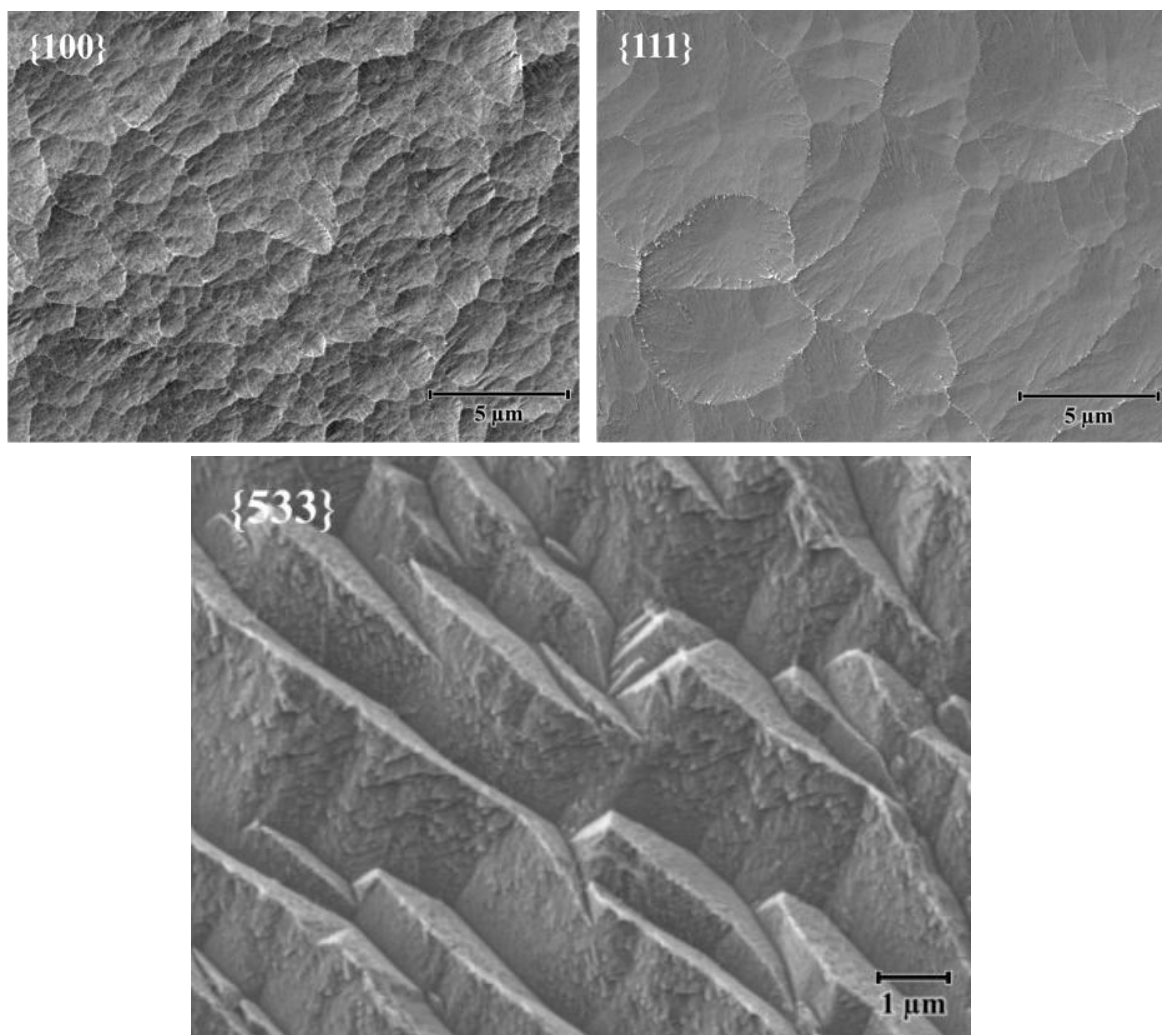


Figure 6.24. Surface morphology of three disordered fcc Fe₅₀Pd₅₀ grains after potentiostatic polarization in deaerated 1 M HCl solution for 1000 s. During polarization the total accumulated charge was 10.8 C/cm² equivalent to a calculated average depth of dissolution of 3.75 μm. Both the {100} and {111} oriented grains, Grain 12 from Figure 6.14, show characteristic scalloped morphology. The {533} oriented grain has a $\beta_{\{111\}}$ of 16 °, which is one of the highest dissolution susceptible orientations. The morphologically smooth, low corroding regions cover a small fraction of the exposed surface. The larger areas have significant morphological features indicative of dissolution.

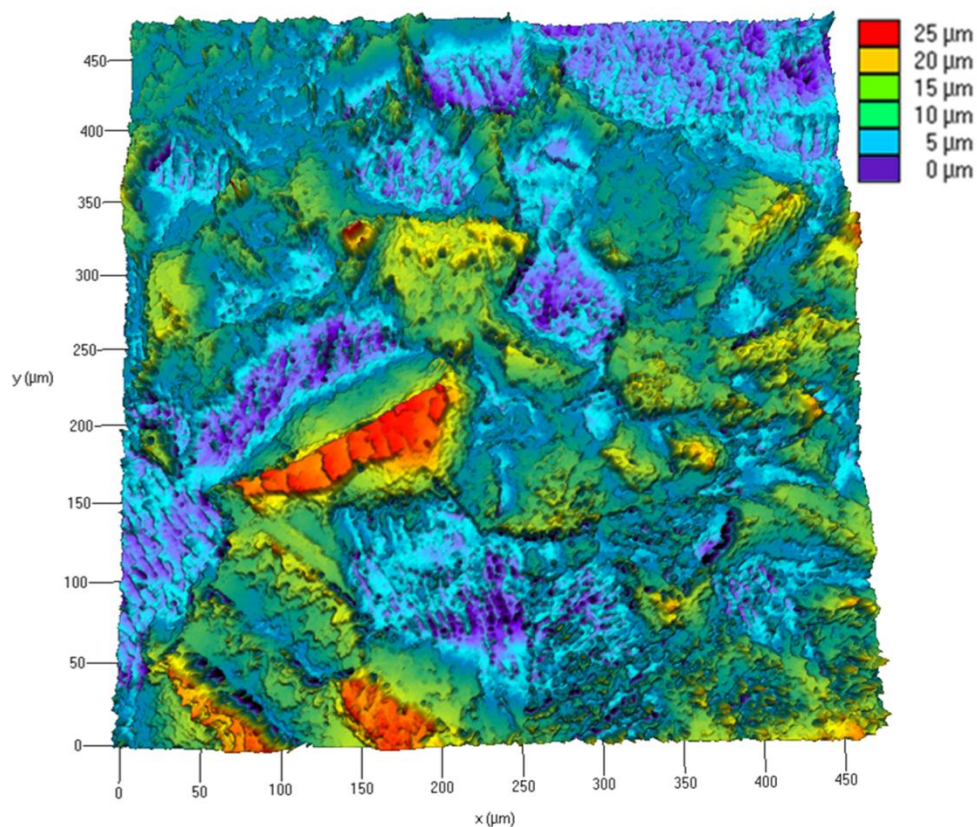


Figure 6.25. CLSM topographical image of a selected region of disordered fcc $\text{Fe}_{50}\text{Pd}_{50}$ after potentiostatic polarization at $0.45 \text{ V}_{\text{SCE}}$ for 2500 s and a total accumulated charge density of 48.87 C/cm^2 .

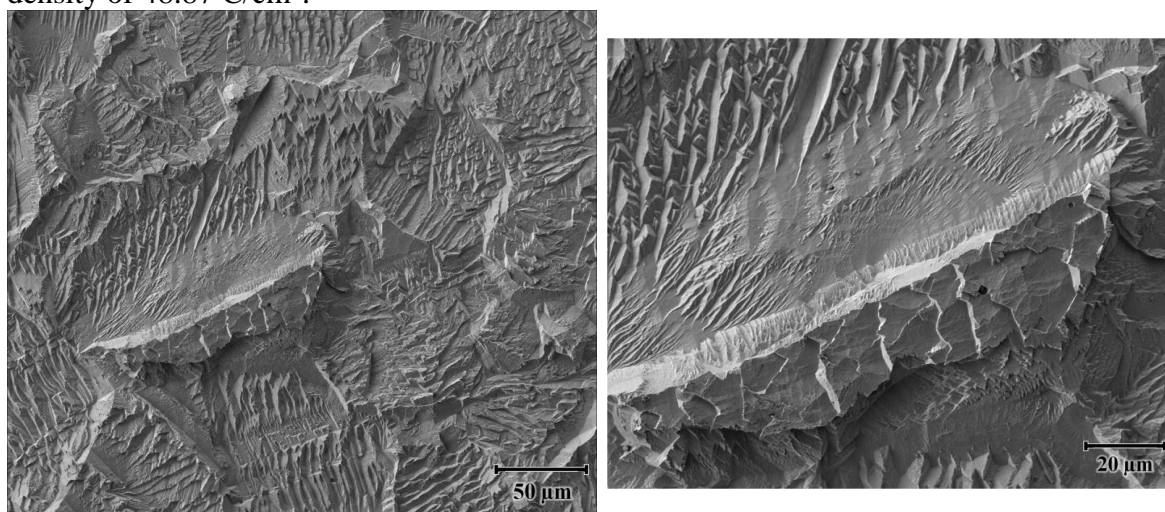


Figure 6.26. SEM micrographs of the surface morphology of disordered fcc $\text{Fe}_{50}\text{Pd}_{50}$ after potentiostatic polarization at $0.45 \text{ V}_{\text{SCE}}$ for 2500 s and a total accumulated charge density of 48.87 C/cm^2 , shown in Figure 6.25.

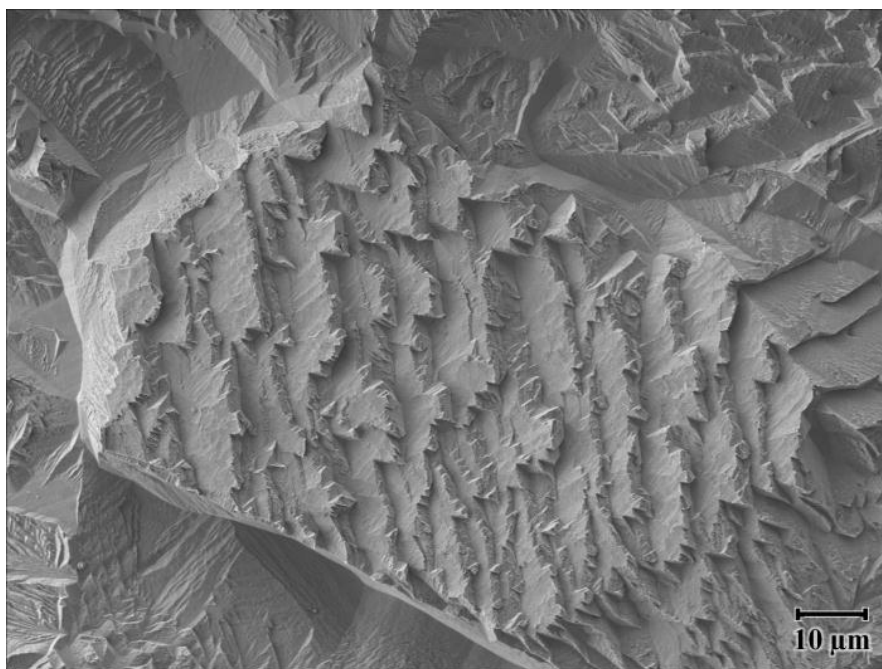


Figure 6.27. Surface morphology of a grain disordered fcc Fe₅₀Pd₅₀ after potentiostatic polarization in deaerated 1 M HCl solution for 2500 s and a total accumulated charge density of 48.87 C/cm². After increased dissolution grains remain distinct and show a terrace-ledge type structure with additional microscopic kinks on the ledges.

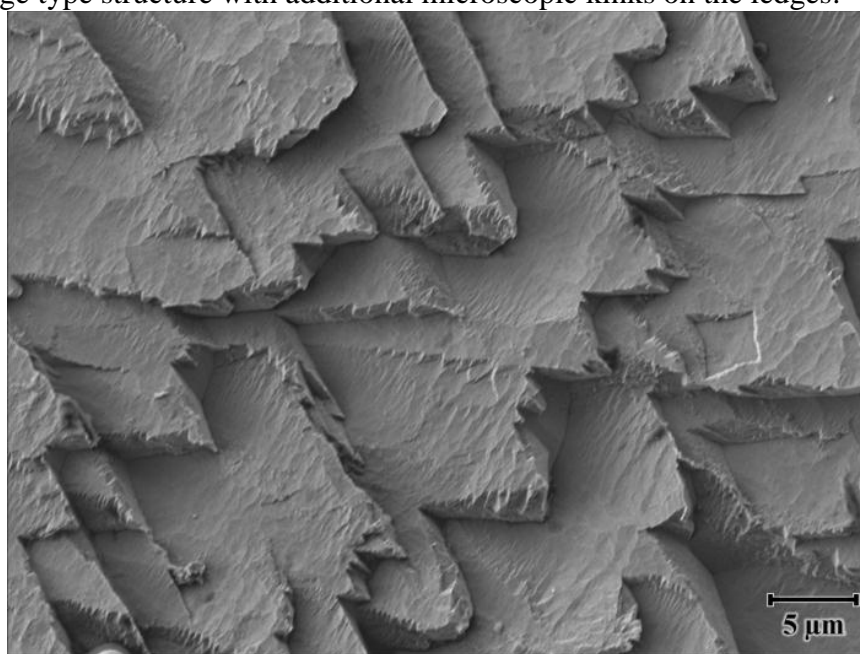


Figure 6.28. Surface morphology of two grains after potentiostatic polarization in deaerated 1 M HCl solution for 2500 s and a total accumulated charge density of 48.87 C/cm². The terrace shows the rectangular characteristic feature seen during dissolution of {100} orientations.

6.4.6 Dissolution Behavior of Ordered pT Fe₅₀Pd₅₀

After polarization in HCl solution for 400 s the Fe₅₀Pd₅₀ pT structure has four times more total accumulated charge compared to the structurally disordered fcc state. At this exposure time, there is some orientation dependence on the dissolution behavior as indicated by the CLSM topography in Figure 6.29 and the corresponding optical micrographs in Figure 6.30. The height difference between the highest and lowest regions is 7 μm, and seemingly most of the grains show similar dissolution behavior. The poly twin boundaries, Figure 6.31-6.32, show increased dissolution. Sub-grain sized regions show pit like events of increased dissolution. Three such pits are shown in the optical micrograph in Figure 6.33. As the surface dissolves, these pitting events become more prevalent and grain specific dissolution behavior, is lost. After polarization for 1500 s the total accumulated charge has increased to 54.4 C/cm². The CLSM images, shown in Figure 6.34-6.35, show that the surface morphology has numerous 5-10 μm pits with depths greater than 10 μm relative to the adjacent surfaces. A few grains exhibit uniform dissolution behavior even at this amount of dissolution.

After polarization for 2500 s, the total charge increased to 94.6 C/cm² and the maximum difference in dissolution depth is about 25 μm. The CLSM image in Figure 6.36 shows pits, with slightly increased diameter, 25 μm lower than adjacent regions. The post dissolution surface morphology is shown in Figure 6.37. Some sub grain sized regions show faceted dissolution, but the overall dissolution appearance is much more uniform in terms of systematic grain dissolution.

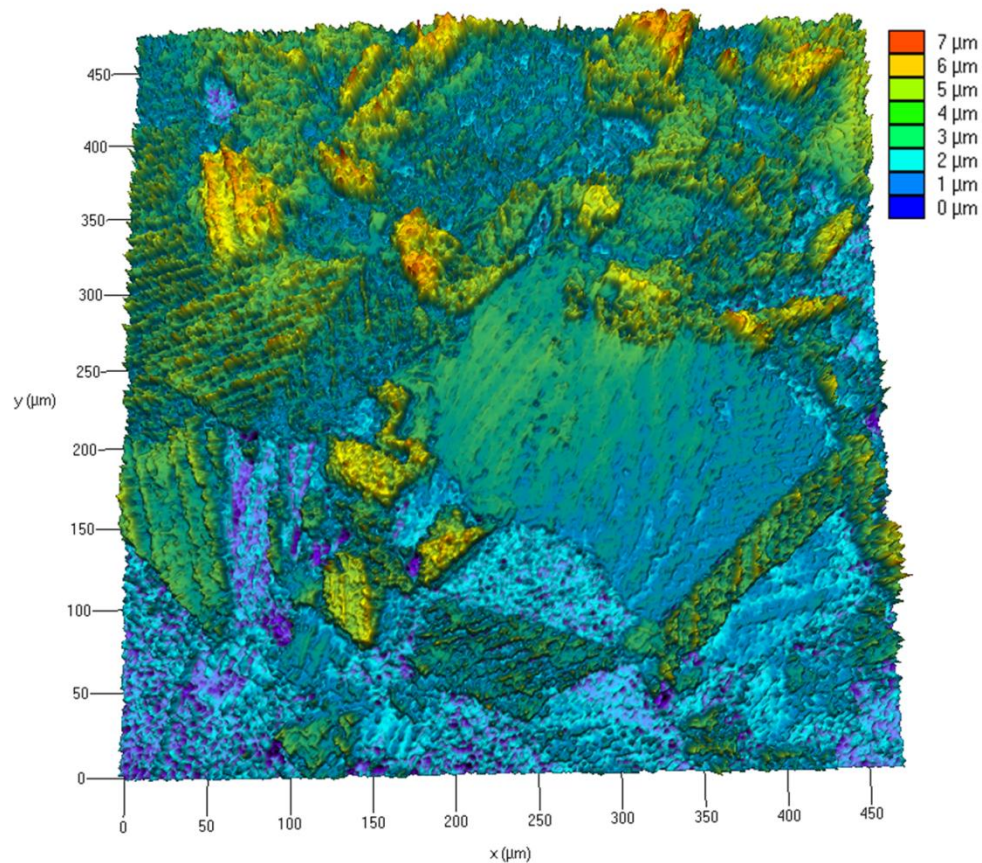


Figure 6.29. CLSM topographical image of the optical region shown in Figure 6.30 of disordered fcc $\text{Fe}_{50}\text{Pd}_{50}$ after potentiostatic polarization at $0.45 \text{ V}_{\text{SCE}}$ for 400 s and a total accumulated charge density of 10.5 C/cm^2 . Grains exhibit anisotropic total depth of dissolution during the initial stages of dissolution.

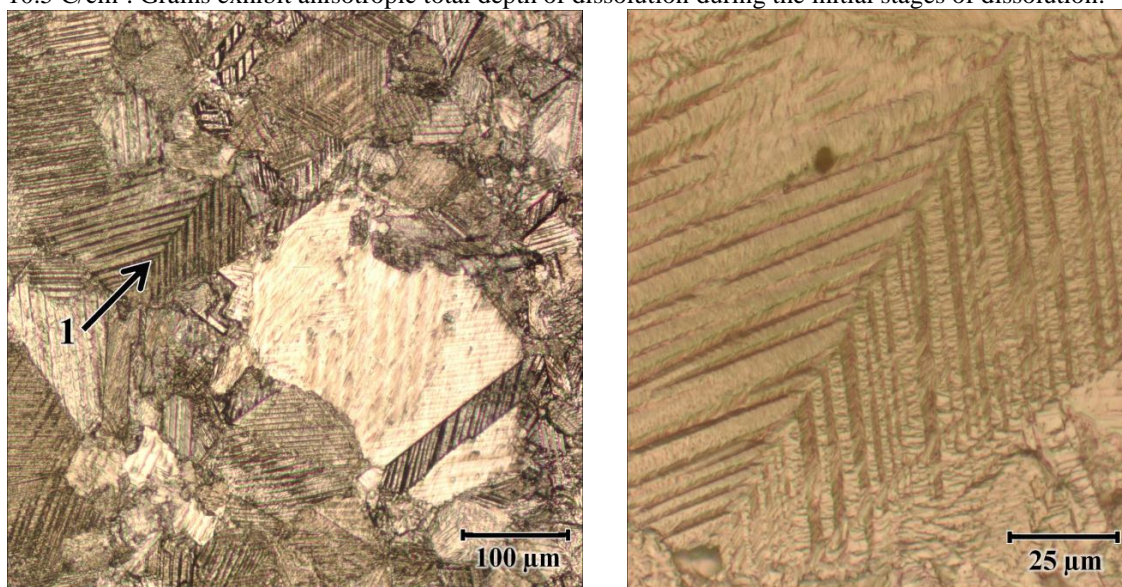


Figure 6.30. Optical micrographs reveal the polytwinned structure of ordered pT $\text{Fe}_{50}\text{Pd}_{50}$ after potentiostatic polarization at $0.45 \text{ V}_{\text{SCE}}$ for 400 s and a total accumulated charge density of 10.5 C/cm^2 . The expanded image, right, of area 1 shows that the twin boundaries are preferentially dissolving.

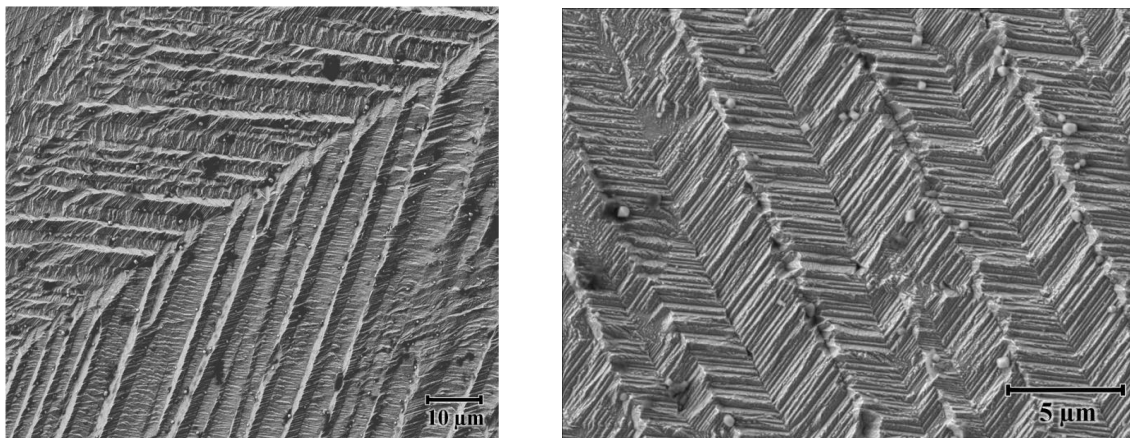


Figure 6.31. SEM micrograph of the polytwinned structure in pT Fe₅₀Pd₅₀ shown in Area 1 of Figure 6.30 after potentiostatic polarization at 0.45 V_{SCE} for 400 s and a total accumulated charge density of 10.5 C/cm².

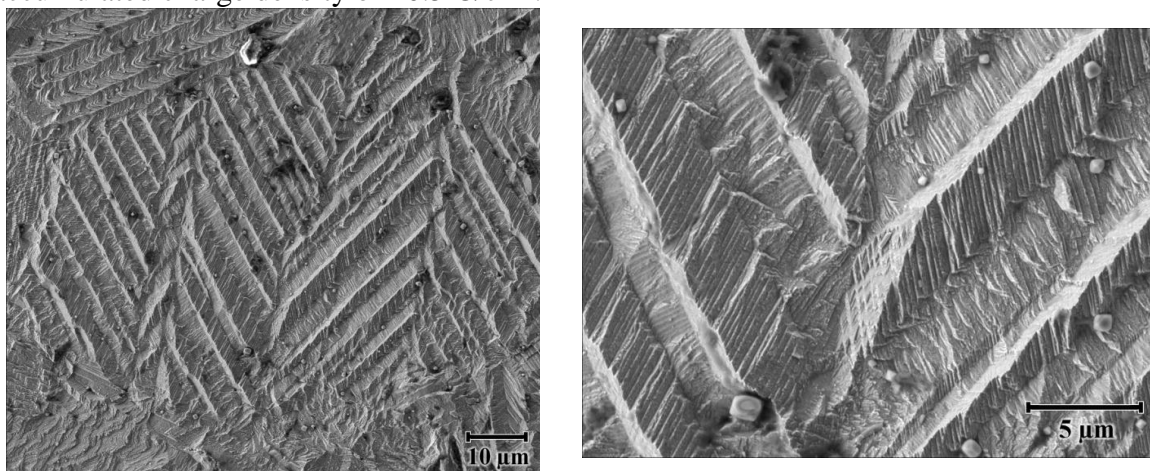


Figure 6.32. SEM micrograph of an additional polytwinned grain in pT Fe₅₀Pd₅₀. after potentiostatic polarization at 0.45 V_{SCE} for 400 s and a total accumulated charge density of 10.5 C/cm².

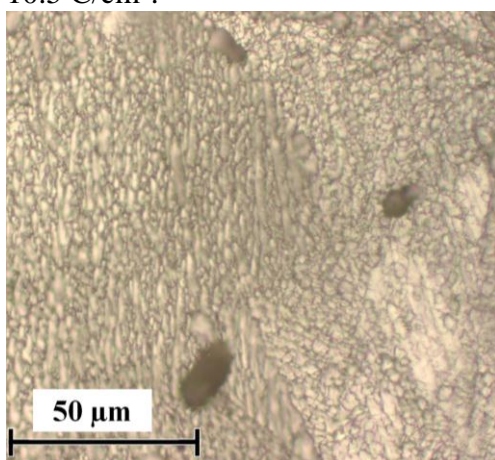


Figure 6.33. Optical micrograph of pits in ordered pT Fe₅₀Pd₅₀ after potentiostatic polarization at 0.45 V_{SCE} for a total accumulated charge density of 7.1 C/cm².

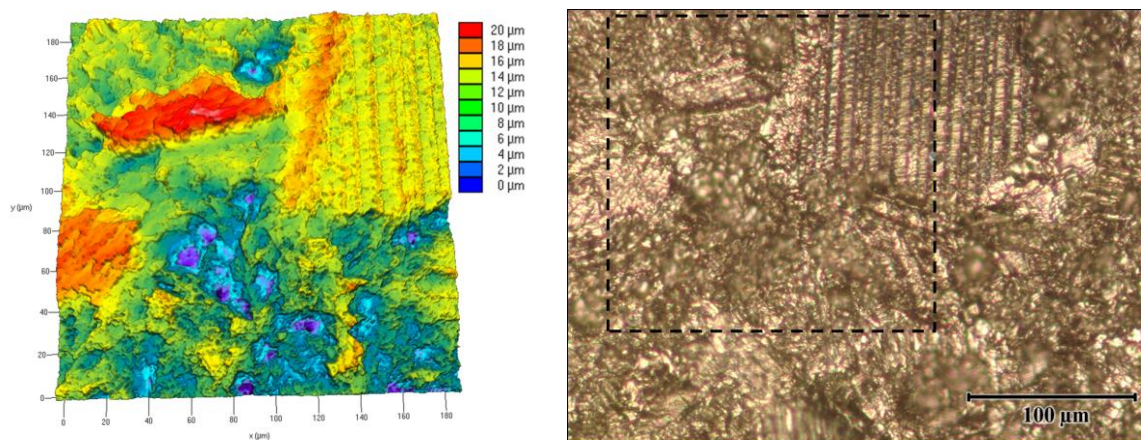


Figure 6.34. CLSM topographical map (left) and Optical micrograph of ordered pT $\text{Fe}_{50}\text{Pd}_{50}$ after potentiostatic polarization at $0.45 \text{ V}_{\text{SCE}}$ for 1500 s and a total accumulated charge density of 54.5 C/cm^2 . The region indicated by the dashed box on the optical micrograph corresponds to the CLSM image.

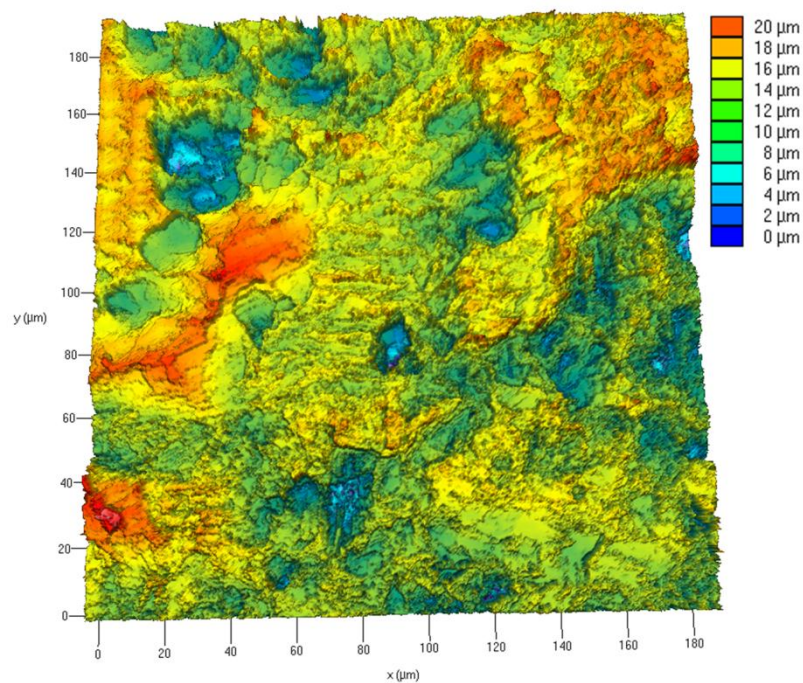


Figure 6.35. CLSM topographical map of an additional region of ordered pT $\text{Fe}_{50}\text{Pd}_{50}$ after potentiostatic polarization at $0.45 \text{ V}_{\text{SCE}}$ for 1500 s and a total accumulated charge density of 54.4 C/cm^2 . Some grains show anisotropic dissolution but the surface also has 5-10 μm pits.

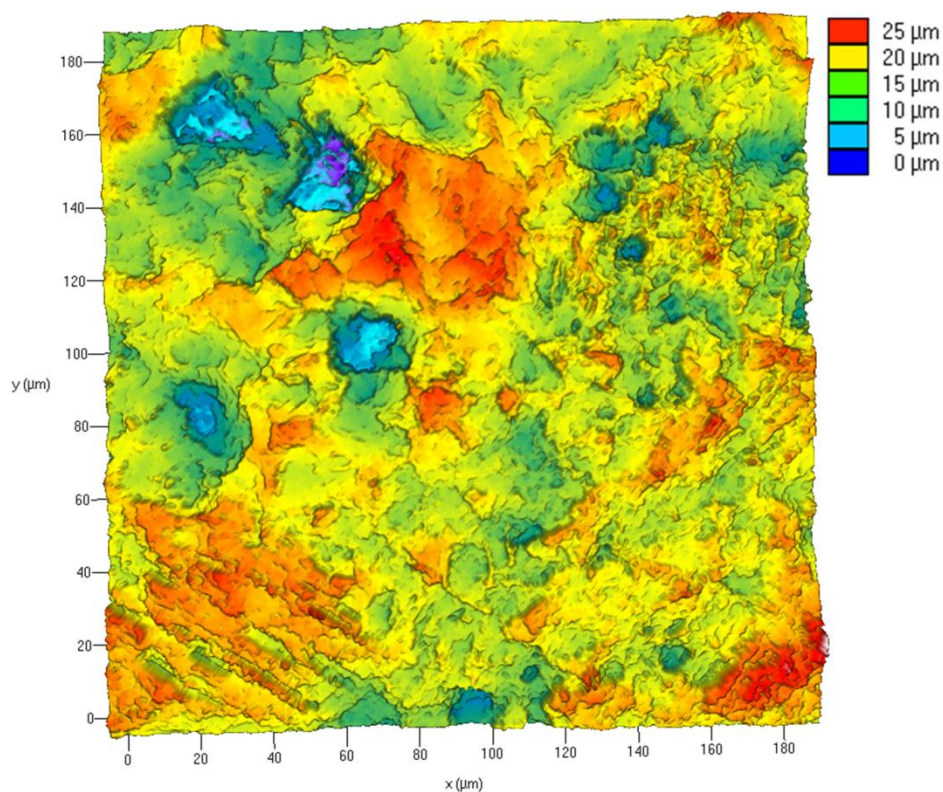


Figure 6.36. CLSM topographical image of a selected region of ordered pT Fe₅₀Pd₅₀ after potentiostatic polarization at 0.45 V_{SCE} for 2500 s and a total accumulated charge density of 94.6 C/cm². Pits have increased in diameter to about 20 μm.

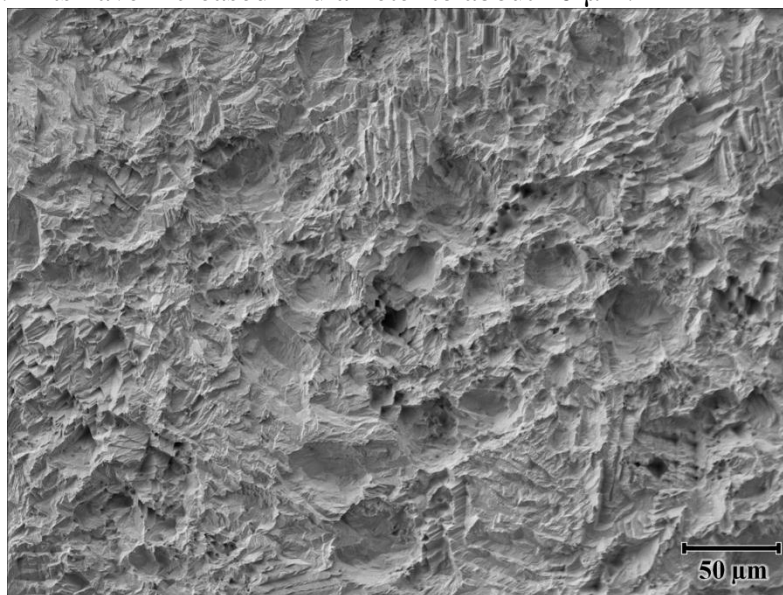


Figure 6.37. SEM micrograph of the surface morphology of ordered pT Fe₅₀Pd₅₀ after potentiostatic polarization at 0.45 V_{SCE} for 2500 s and a total accumulated charge density of 94.6 C/cm².

6.4.7 Comparison between Dissolution Behavior of fcc and pT Fe₅₀Pd₅₀

The total depth of dissolution was measured after each of the three polarization durations for both structural states. The measured depth measured is an area average of the surface; i.e., there is no normalization for grain size. To account for large grains skewing the results several regions were tabulated. These results as a function of exposure duration are summarized using a statistical box plot in Figure 6.38. The average dissolution depth (indicated by the open squares) increased more quickly for the ordered pT structure than the disordered fcc structure. The contrast between the 99th and the 95th percentiles and minimum and maximum dissolution depth reinforces and quantifies the observations from the previous sections.

For the fcc structure, the maximum depth of dissolution is close to both the 99th and 95th percentile of the dissolution depth indicating small variation in the overall depth of dissolution. In contrast, the difference between the maximum and 95th percentile values is sizable for the pT structure: 6 μm at 400 s and 12 μm at 1500 s. The pits that exist on the surface of the ordered pT surface have very high dissolution depths and small surface area leading to the large difference in these values. The decrease in the difference (about 8 μm) at 2500 s is a result of the area fraction of pits increasing as the pits enlarge which shifts the distribution. The minimum dissolution for the disordered fcc structure remains with ~ 2 μm of the surface even at the 2500 s exposure while the minimum dissolution surface for pT structure increases much more rapidly.

The minimum, maximum and average dissolution are normalized to the total accumulated charge in Figure 6.39. Linear fits (dissolution per charge density) for each structure type are shown in Table 6.4. The slope of the average dissolution depth curve

for both fcc and pT is about $0.355 \mu\text{m}/\text{cm}^2$. This value is in good agreement with the calculated slope $0.433 \mu\text{m}/\text{cm}^2$ using Faraday's law assuming both species are dissolving to the +2 valence state and congruent dissolution of both species³¹. The density used for these calculations is based on the crystal structure. The slope of the minimum dissolution depth for the fcc structure is three times smaller than the corresponding slope for the pT structure. A similar trend, fcc structure having a smaller slope, is seen for the maximum dissolution depth, but these linear fits have high errors.

Table 6.4. Slope and root-mean-square (RMS) error of linear fits of the charge vs. minimum, maximum and average depth of dissolution for disordered fcc and ordered pT $\text{Fe}_{50}\text{Pd}_{50}$.

Dissolution Depth	Disordered fcc $\text{Fe}_{50}\text{Pd}_{50}$		Ordered pT $\text{Fe}_{50}\text{Pd}_{50}$	
	Slope ($\mu\text{m}/\text{C}\cdot\text{cm}^{-2}$)	Error (RMS error)	Slope ($\mu\text{m}/\text{C}\cdot\text{cm}^{-2}$)	Error (RMS error)
Minimum	0.036	0.345	0.110	1.701
Maximum	0.507	3.979	0.530	7.330
Average	0.360	2.422	0.351	0.784

³¹ Interestingly, if a +3 valence state is assumed for Fe, the predicted slope is $0.347 \mu\text{m}/\text{cm}^2$, which is remarkably close to the measured values. The driven potential, $0.45 \text{ V}_{\text{SCE}}$, is lower than the Fe 2+/3+ equilibrium potential at $0.527 \text{ V}_{\text{SCE}}$.

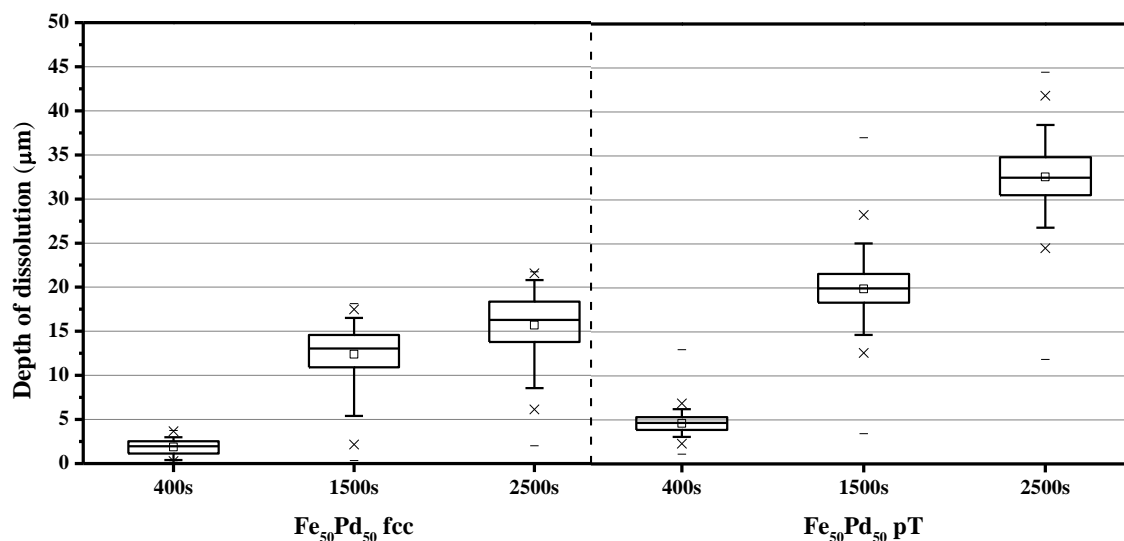


Figure 6.38. Box plots showing the depth of dissolution during potentiostatic polarization at $0.45 V_{SCE}$ in 1 M HCl solution for disordered-fcc (left) and ordered-pT (right) $Fe_{50}Pd_{50}$. The solid lines in the box indicate the 25th, 50th and 75th percentiles. The extended whisker shows the 5th and 95th percentile, and the crosses (x) indicate the 1st and 99th percentile. The open square is the set average and the horizontal dashes (—) are the set minimum and maximum. The data represents the depth of dissolution as an area average of the sample surface in all cases except the fcc 400 second condition which is normalized to each grain.

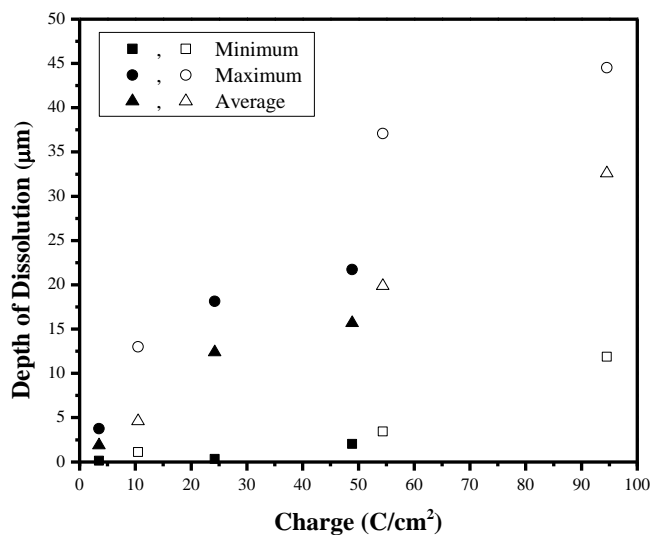


Figure 6.39. Plot of the minimum, maximum and average depth of dissolution for disordered fcc (solid symbols) and ordered pT (open symbols) $Fe_{50}Pd_{50}$ as function of total accumulated charge density during potentiostatic polarization at $0.45 V_{SCE}$ in 1 M HCl solution.

6.5 Discussion

6.5.1 Orientation Dependent Dissolution in Disordered fcc Fe₅₀Pd₅₀

Dissolution depth during potentiostatic polarization of fcc Fe₅₀Pd₅₀ in HCl solutions was found to depend strongly on grain orientation. The orientation dependency was also apparent in corrosion induced surface roughening and facet development. The {100} orientation is the most dissolution resistant orientation, and the {111} shows only slightly decreased dissolution resistance compared to the {100} orientation (Figure 6.22). Grains with these orientations showed the lowest surface roughness (Figure 6.23). In contrast, the {110} orientation is significantly more susceptible to dissolution than the other two low index orientations and shows no similar decrease in surface roughness at near {110} orientations. The most corrosion susceptible region, which also has the highest surface roughness after exposure, is orientations between 10 and 20° from the {111} (Figure 6.20). Of the low index planes the least close packed orientation, {110}, showed the most dissolution. Atomic packing density does not necessarily govern dissolution behavior, however, since the {111} orientation, the most densely packed plane, dissolves more easily than the less dense {100} orientation.³² However, both are more dissolution resistant and more dense than the {110} orientation.

In dissolution studies on polycrystalline fcc Al and Al alloys³³, the {111} plane typically showed the most dissolution in NaOH solution [4, 5, 13], but Zn enrichment on the least dissolved {100} orientations was significant [4, 13]. As the dissolution of the near {111} orientations revealed {111} terraces [5, 13], it seems likely that the {111} orientation would show a decreased dissolution rate. This is because fast {111}

³² For the fcc Fe₅₀Pd₅₀ crystal structure the low index plane densities are: {111} = 15.96 atoms/nm³, {100} = 13.82 atoms/nm³, and {110} 9.77 atoms/nm³.

³³ Not completely solid solution alloys.

dissolution would reveal other slower dissolving orientations and these orientations would then form the terrace-ledge structure. However, Holme studied a wide range of grain orientations, including several orientations near the $\{111\}$, and found no decrease in dissolution rate near that orientation [4].

In bcc Fe, the $\{100\}$ orientation is the least densely packed and shows the highest dissolution rate [3, 26]. Fushimi reported [3] that the most dissolution susceptible orientation is the $\{100\}$ orientation. Similarly behavior was seen in NO_3^- solution [26]. A peak in the dissolution at intermediate orientations has not yet been reported. However in pitting behavior on bcc stainless steel, a peak number of pitting events was observed around $\beta_{\{100\}}$ of 25° [10].

As mentioned in the results section, a linear dependence of dissolution depth on $\beta_{\{100\}}$ (Figure 6.18) and $\beta_{\{111\}}$ (Figure 6.19) was observed. A linear dependence of corrosion on crystal orientation has been reported previously in several alloys, solution environments and corrosion regimes. König [14] studied oxidation of Ti of about 20 different grain orientations by measuring the oxide interference patterns. A linear dependence on β was observed. Grains near the (0001) basal plane had a thinner oxide and higher oxygen evolution current density. At higher β , the oxide was thicker and oxygen evolution current density was lower. Schreiber [9] measured the current of the first oxidation peak on iron for 11 orientations and found a linearly increasing current with respect to β from the $\{100\}$ to the $\{111\}$ plane normal. No dependence on α , defined in Figure 6.4, was observed. Holme [4] measured Zn induced alkaline etching dissolution depth in a predominantly Al alloy. The $\{111\}$ orientation showed the most dissolution;

dissolution depth decreased linearly with $\beta_{\{111\}}$. The underlying mechanisms responsible for these observations are still unclear. Several possibilities will be considered.

6.5.1.1 Surface Energy Considerations

It is reasonable to expect that dissolution occurs more readily from grains with higher surface energy where the activation energy to dissolution is likely at a minimum. Correspondingly, the dissolution rate would be least in grains with the lowest surface energy. The change in Gibb's free energy, ΔG , can be written as the sum of the chemical potential, μ , of the species in the reaction (bulk term) and to accommodate the change in surface energy between the oxidized and reduced states, γ (surface term):

$$\Delta G(\gamma) = G_{oxidized} - G_{reduced} = \sum v\mu_{oxid} - \sum v\mu_{red} + \sum vk\gamma_{red-oxid} \quad (6.2)$$

where v is the stoichiometric coefficient and k is a correction factor. This equation can be used to calculate the electrochemical half-cell potential, E^0 , as a function of surface energy of a specific $\{hkl\}$ as follows:

$$\Delta G(\gamma) = -nFE^0 \quad (6.3)$$

$$E^0 = \frac{\sum v\mu_{oxid} - \sum v\mu_{red} + \sum vk(\gamma_{\{hkl\}} - \gamma_{oxid})}{nF} \quad (6.4)$$

The number electrons transferred, n , and F is Faraday's constant. The E^0 value for a specific $\{hkl\}$ determines η , the overpotential, and thereby the dissolution of the reaction at an applied potential of $0.45 V_{SCE}$.

$$E_{app}(0.45 V_{SCE}) - E_{\{hkl\}}^0 = \Delta\eta_{\{hkl\}} \quad (6.5)$$

A grain orientation with high surface energy compared to a low surface energy would lead to a lower Nernst potential and at the $0.45 V_{SCE}$ applied potential (E_{app}) a faster dissolution rate. The difference in surface energy between different orientations is needed to approximate the difference in the Nernst potential.

Calculations of the surface energy by Nicolas [27, 28] were made by taking into account the number of broken bonds of each atom on an ideal fcc crystal surface assuming no surface relaxation (see selected crystallographic models for select orientations in Appendix 1). Thus, orientations with a high number of broken bonds per unit area would have the highest surface energy. Refinements to these calculations accounted for broken bonds up to many next-nearest neighbor interactions. Recently, modeling techniques have been applied to calculate the surface energy of fcc materials. Zhang [29] calculated the surface energy of a series of fcc surfaces for 15 metals using a modified embedded atom approach, MEAM. For all the metals modeled including Pd, the densely packed {111} plane had the minimum surface energy. On average the {110} orientation was 22% higher and the {100} orientation was 20% higher compared to the minimum surface energy of the {111} plane. The difference in surface energy calculations of the minimum and maximum {hkl} ranged from 0.1-0.6 J/m².

Using this range in surface energy calculations, the difference in E^0 between different orientations can be approximated using Equation 6.4. If the largest difference (0.6 J/m²) is assumed, then the difference in E^0 is 0.135 V.³⁴ Thus, for the higher surface energy orientations, the effective overpotential (η) is 0.135 V higher increasing the current density (Equation 6.6) 14-fold for those high energy orientations relative to lower energy orientations assuming β , the charge transfer coefficient, is 0.5 and 2 electrons (n) are transferred during the reaction.

$$i = i_0 e^{\frac{\beta n F \eta}{RT}} \quad (6.6)$$

³⁴ The surface energy change (between the extreme values) was used to calculate the energy per mol of atoms (2615 J/mol) assuming $1.4 \cdot 10^{15}$ atoms/cm².

R is the universal gas constant. The exchange current density, i_0 , also likely changes based on the surface energy ($i_0 \propto \exp(-\Delta G/RT)$) and other electrode characteristics (for example the adsorption of Cl⁻ is a likely reaction step and may show an orientation dependence).

The trends in the surface energy do not exactly correspond to the surface energy. Zhang's calculations show that the maximum calculated surface energy was typically at $\alpha = 0$ i.e., orientations between the {100} and {110} plane normals e.g., {210}, {310} and {520}. Grochola [30] calculated the surface energy of the three low index planes of fcc iron at equilibrium temperatures and also at 0 K. For equilibrium temperatures between 1200 and 1600 K, the surface energy of the orientations ordered from lowest to highest is {111} \ll {100} < {110} while at 0 K {111} < {110} < {100}. The ordinal ranking of the low index orientations and the orientations of maximum surface energy are consistent in both the broken bond model and the MEAM simulations. Measurements of the surface energy are generally consistent with these calculations [31].

The surface energy calculations for pure Pd and Fe are shown Figure 6.40 and in the case of Pd the α -dependency is also shown. The dissolution susceptibility (Figure 6.19) does not directly correspond to the surface energy calculations for pure elements. In Fe₅₀Pd₅₀, the {111} orientation is more susceptible to dissolution than the likely higher surface energy {100} orientation. Figure 6.12 and Figure 6.13 show a direct comparison between a {100} orientation, grain 11 ($\beta_{\{100\}}$ of 1.6°), and a {111} orientation, grain 12 ($\beta_{\{111\}}$ of 1.0°) with the later showing an increased dissolution rate. The measured regions of maximum dissolution are between 10 and 20° from the {111} plane normal (Figure 6.22), which does not coincide with the maximum surface energy. In fact, the calculated

surface energy for these orientations is comparatively low (Figure 6.40). The calculation of the expected change in the Nernst potential of the dissolution reaction due to the difference between $\{hkl\}$ surface energy suggests the root cause of dissolution differences with orientation is not based on thermodynamic considerations and instead may be based on kinetics.

6.5.1.2 Experimental Determinations of Surface Energy

It is clear that the surface energy changes as a function of orientation. At equilibrium, high surface energy orientations can achieve a lower energy by faceting to a series of low energy planes (e.g., $\{110\}$ plane faceting to a $\{100\}$ and $\{111\}$, see Wulff construction, γ , and γ^{-1} plots, [32]). Experimental determinations of the equilibrium surface energy based on the equilibrium crystal shape better represent the actual behavior of real crystals because relaxation and surface reconstruction phenomena are present. Heyraud and Metois [33] measured the equilibrium shape of fcc Pb at a series of temperatures and found that the $\{111\}$ orientation had the lowest surface energy while the $\{100\}$ and $\{110\}$ orientations were approximately 2% and 5% higher, respectively. Another interesting feature of these plots is that the slope of increase in surface energy as a function of angle from the $\{100\}$ orientation is much lower than that of the $\{111\}$ orientation, while there is little to no decrease near the $\{110\}$ orientation. These features are even more pronounced in similar measurements of the surface energy of Cu by McLean [34]. The surface energy increases very gradually up to 40° from the $\{100\}$ orientation then decreases sharply to the minima at $\{111\}$. Similarly, no decrease is measured in proximity to the $\{110\}$ zone, see Figure 6.41. Additionally, the maximum surface energy is within 20° of the $\{111\}$ axis. The slopes of these lines are somewhat

similar to those observed in Figure 6.18; however; the minimum surface energy is still the close packed {111} plane. These plots vary for different temperatures and the correlation of the dependence of surface energy on orientation to the dependence of dissolution with orientation is unclear.

6.5.1.3 Effect of Surface Relaxation

It is unlikely that surface reconstruction is playing a dominant role after the initial dissolution behavior. Surface relaxation is typically the first few layers of atoms. For Pd, it is typically limited to the first 3 monolayers [35]. The fcc structure dissolves 18 monolayers per second based on the average dissolution rate ($0.0063 \mu\text{m/s}$) and the pT structure dissolves faster. Surface diffusion in solution coefficients are on the order of $10^{-11} \text{ cm}^2/\text{s}$ [36]. It is likely that the surface is dissolving more quickly than surface reconstruction based on surface diffusion could occur. The dissolution rate is most likely determined by the properties that govern which irrational planes are revealed during dissolution and what their dissolution rate is.

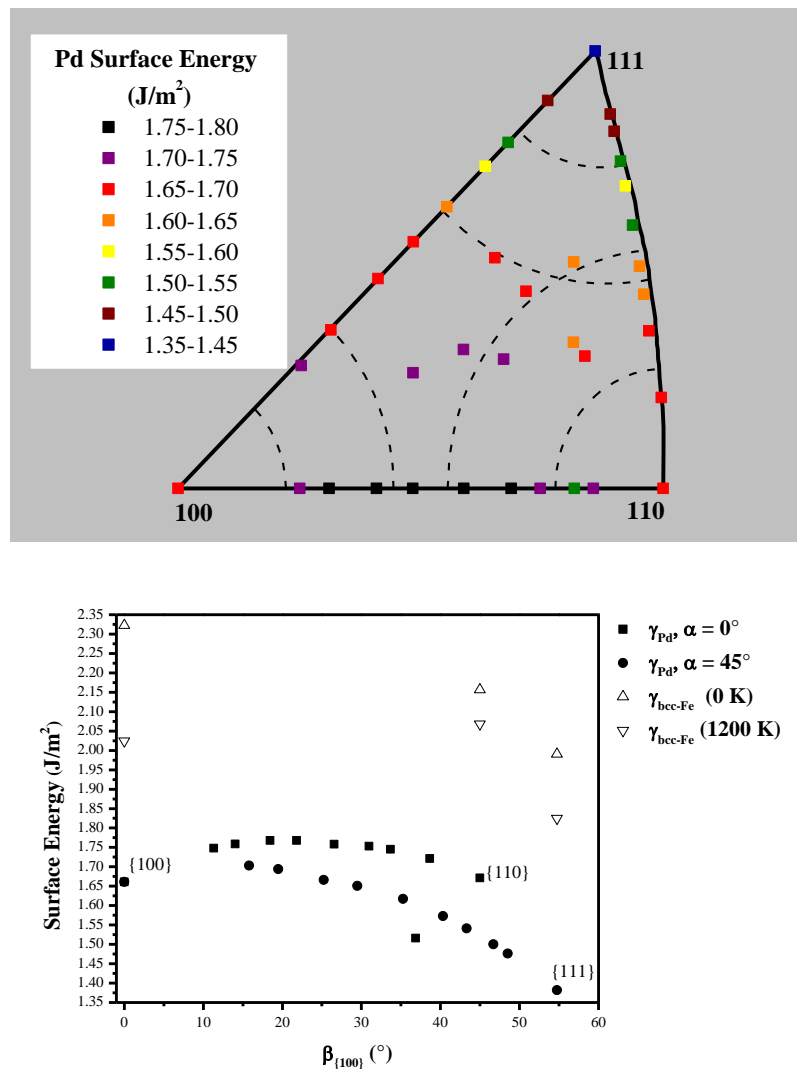


Figure 6.40. Calculated surface energy, γ , of Pd on the IPF (top) and as a function of $\beta_{\{100\}}$ (bottom) at $\alpha = 0$ and 45° . There is a pronounced dependence of the surface energy on α . The highest surface energy occurs at orientations around $\beta_{\{100\}}$ $20 - 30^\circ$ and $\alpha = 0^\circ$ for Pd. The fcc orientation energy based on MEAM calculations from Zhang [29], the calculated surface energies for bcc Fe at 0 K and 1200 K (equilibrium) based on calculations from Grochola [30] (also by the MEAM method).

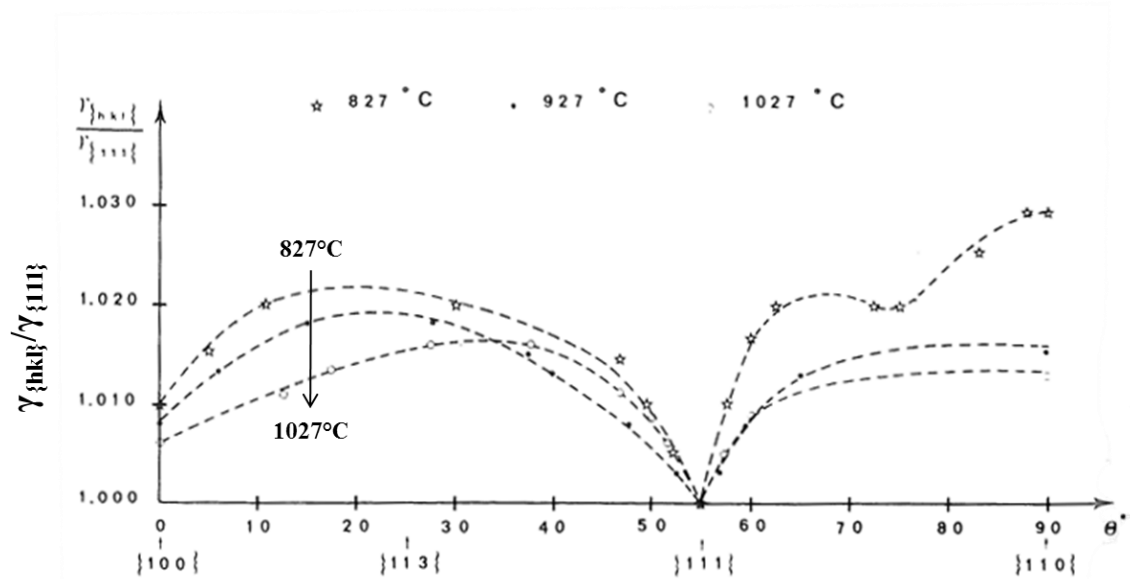


Figure 6.41. Surface energy anisotropy for Cu at three different annealing temperatures, adapted from [34]. Reprinted from [33] with permission from Elsevier BV.

6.5.1.4 Terrace and Ledge Structure

The morphology of post exposure grains is dominated by relatively flat but microscopic terraces and ledges. Grains with orientations near $\{100\}$ and $\{111\}$ have scalloped like structure with no apparent terraces or ledges, are shown in Figure 6.14 and Figure 6.28 after various levels of dissolution. These grains exhibit the lowest surface roughness. Grains at higher $\beta_{\{100\}}$ (and $\beta_{\{111\}}$ greater than 10°) have micrometer scale structural features dominated by terraces and ledges. For instance, Grains 2 and 8 (Figure 6.11) are good examples of highly dissolved, high surface roughness grains which develop a corrosion induced characteristic faceted structure. After increased dissolution the micrometer scale faceted structure becomes more pronounced (Figure 6.28-6.27). These results are consistent with published results for fcc Al where high index orientations dissolve to form $\{111\}$ and $\{100\}$ terraces and the $\{111\}$ terraces dissolve in a $\langle 110 \rangle$ direction [5].

Grains with the highest surface roughness show similar characteristic crystallographic features. These grains also have the highest dissolution rate. Interestingly, some highly dissolving grains very near the great circle between $\{110\}$ and $\{111\}$ do not show significant crystallographic facets or roughness suggesting some underpinning structural mechanism in terms of a α dependence, but this effect is only applicable to a few grains and is not a dominant feature.

As the fcc $\text{Fe}_{50}\text{Pd}_{50}$ grain orientation diverges from the $\{100\}$ orientation, micrometer scale ledges become increasing prevalent. Comparisons of Grain 1, 3 and 5 which have increasing $\beta_{\{100\}}$ from 9.1 to 17.1 to 21.1°, respectively, reveal this feature. After increased dissolution, the structural features become even more apparent, Figure 6.28. This correlation supports the idea that the dissolution rate of a given grain orientation is predominantly determined by the dissolution rate of the slowly dissolving low index terraces and the lateral³⁵ dissolution of the likely higher index ledges. Another example supports the idea that dissolution is likely dissolution is dominated by ledge dissolution, which has a specific orientation and corresponding susceptibility to dissolution. In the $\{533\}$ grain in Figure 6.27, consists of a mixture of two facet types smooth and rough. The facet making up the larger surface area is morphologically rough, indicative of increased dissolution whereas the other facet type is comparatively smooth. This surface falls within orientation range of highest dissolution. Thus the large surface area of highly dissolving facets leads to the overall high dissolution susceptibility.

After increased dissolution (Figure 6.28), the terraces exhibit micrometer scale kinks which can further enhance dissolution by providing an irrational surface even more favorable to dissolution. This grain behavior is consistent with the mechanistic

³⁵ Lateral with respect to the terrace, often not the original orientation surface orientation.

interpretation of these results; the overall dissolution rate is determined by type and fraction of surface coverage of steps and terraces.

6.5.2 The Role of Crystal Structure during Dissolution of fcc and pT Fe₅₀Pd₅₀

One clear conclusion drawn from these results is that the pT structure dissolves more quickly than the fcc structure. To compare the surface morphologies it is best the surfaces after similar total accumulated charge density, and thus, similar amounts of overall dissolution. At 1500s the pT structure has undergone a similar amount of dissolution as the fcc state after the 2500 s polarization. Comparison of the surface morphology between ordered pT (Figure 6.34) and disordered fcc (Figure 6.25-6.28) show that the disordered fcc state surface maintains grain integrity with grain-characteristic faceting; dissolution of the pT structure results in pit formation and only limited grain specific dissolution morphology. The fact that the grain structure is maintained and pits do not form during all stages of the fcc structure dissolution is a key difference in behavior resulting from the change in structure in Fe₅₀Pd₅₀.

The change from fcc to pT structure involves a slight lattice expansion along the c-direction to accommodate the Pd atoms occupying the $c = 1/2$ lattice sites. Thus, the Fe and Pd atoms alternate layers within the crystal. The lattice expansion results in an accompanying decrease in density from 9.789 g/cm³ for the fcc structure to 9.755 g/cm³ for the pT structure. The formation of polytwins can amount to additional pseudo-grain boundaries (if incoherent) and during the initial dissolution these boundaries preferentially dissolve (Figure 6.32). The chemical organization of atoms to specific atomic positions, lattice expansion, and increase and polytwinned structure each likely

contribute to the increase in dissolution in the ordered state compared to the disordered state.

Effect on bond strength due to chemical ordering

The bond strength of an atom can be influenced by up to the third nearest neighbor [37]. In its simplest interpretation, the act of dissolution involves the separating an atom from the underlying atoms that remain bound to the metal. In the disordered alloy each atom is surrounded by neighboring atoms each with a 50% chance to be a Pd atom. Thus, significant differences in the bond strength between Fe-Fe and Pd-Pd vs Fe-Pd result in a distribution of atoms being more strongly bound than others. Based on the polarization scans, Figure 6.7, high purity Pd dissolving to the equilibrium PdCl_4^{2-} complex is dominated by the HER likely due to kinetic limitations. At higher applied potentials, dissolution behavior dominates. At the applied potential of the dissolution experiments ($0.45 \text{ V}_{\text{SCE}}$) the dissolution rate of Pd is orders of magnitude lower than the Fe dissolution rate. While alloying Pd into Fe does not result in passivity, it is likely some dissolution moderating effect is played by Pd atoms. As dissolution occurs, the more strongly bound atoms resist dissolution while the more weakly bound atoms dissolve more easily, similar to how adatoms dissolve before kink sites, etc. If there is a significant enough delay between the dissolution of the two types (a continuum of binding strengths would exist in reality) then the comparative ease of dissolution of weakly bound atoms will result in a shift of the surface towards a larger density of harder to dissolve, more tightly bound atoms. The periodic nature of the ordered pT structure is constrained by the compositional ordering in the alloy. The binding strength of these atoms would be a series of discrete states unlike the continuum in the disordered

structure. As atoms dissolve, the revealed layer will follow the same periodic set of atoms. This feature speculatively decreases the dissolution resistance and clearly outweighs any beneficial contribution by the ability of the pT structure to form uniform sheets of Pd atoms (e.g. (100) orientations that would reveal uniform sheets of Pd atoms, and be more dissolution resistant).

6.6 Conclusion

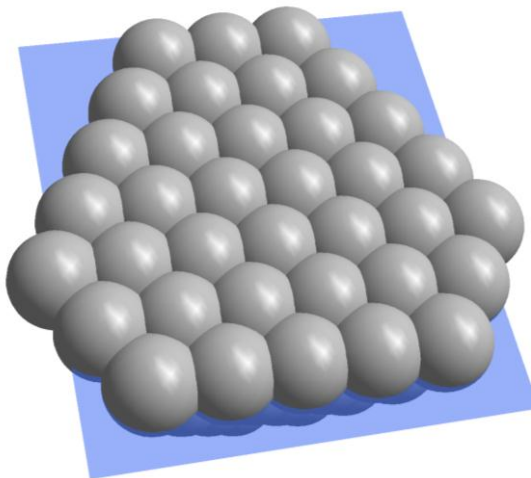
Disordered fcc Fe₅₀Pd₅₀ undergoes crystallographic dependent dissolution during polarization well above reversible electrode potentials for both elements in HCl solution. The dissolution depth after a given time was found to depend on the grain normal direction or the plane of the polished surface. Of the 300 orientations measured, the {100} and {111} orientations were found to be the most dissolution resistant. The {100} orientation is slightly more resistant than the {111} orientation. The most corrosion susceptible region was between 10 and 20° from the {111} plane normal. Dissolution increased linearly as a function of the angle between the plane normal and the pole normal up to 40° from the {100} plane normal and up to 10° from the {111} plane normal. The increase in dissolution with crystallographic angle from the {100} orientation was substantially lower than from the {111} orientation. No such dependence was observed for orientations near the {110} plane normal.

The corrosion-induced micrometer scale surface roughness and faceted structure was found to correlate with {hkl} dissolution depth. The surface faceting and roughness was highest in regions of highest dissolution; while orientations near the {100} and {111} orientations were the relatively smooth. Dissolution resulted in well-defined crystallographic terrace and ledge features. The terrace-ledge structure was maintained in

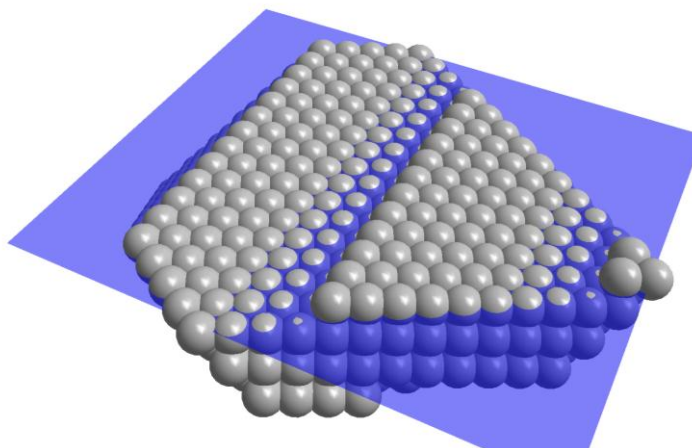
individual grains after increased dissolution. These observations are consistent with dissolution eventually revealing low index terraces and steps, and further dissolution proceeding most rapidly laterally on the ledge and kink facets. A comparison to surface energy revealed similar trends, but an exact correlation was not confirmed.

6.7 Appendix 1. Crystallographic Models of Selected Orientations

{111}



{544}



{432}

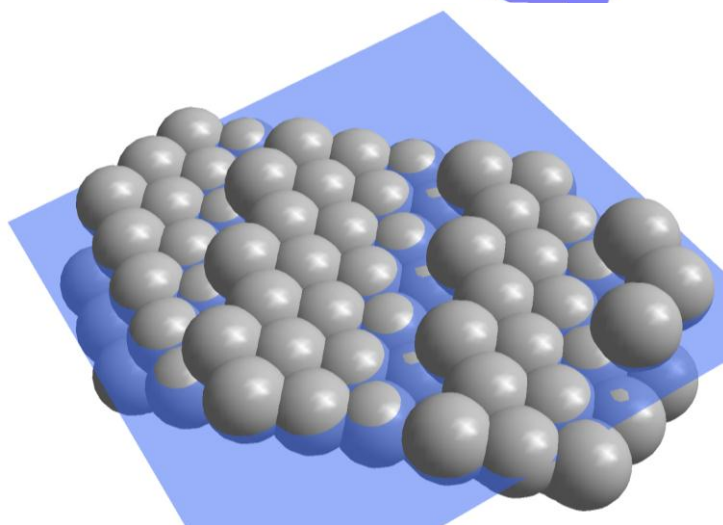


Figure 6.42. Crystallographic models of the orientations near the {111} plane normal. {544} is 6° from the {111} plane normal ($\beta_{\{111\}} = 6.2^\circ$). {432} is 15° from the {111} plane normal and lies in the region of orientations with the highest susceptibility to dissolution. Models created using Diamond Crystallography Software (<http://www.crystalimpact.com/>).

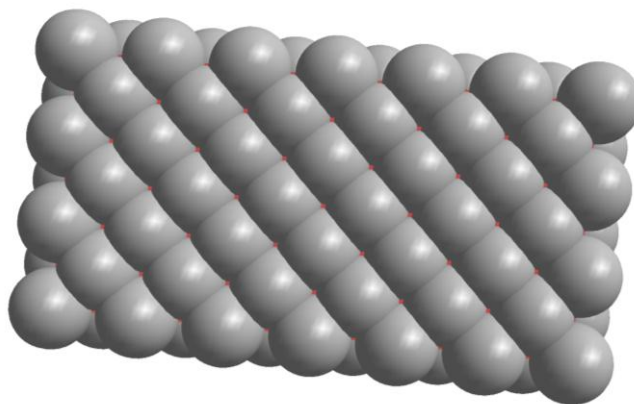
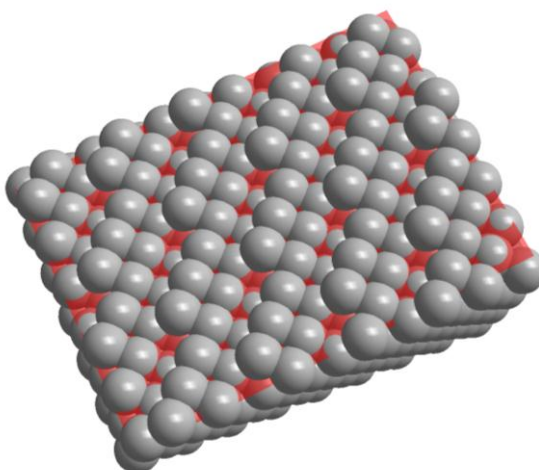
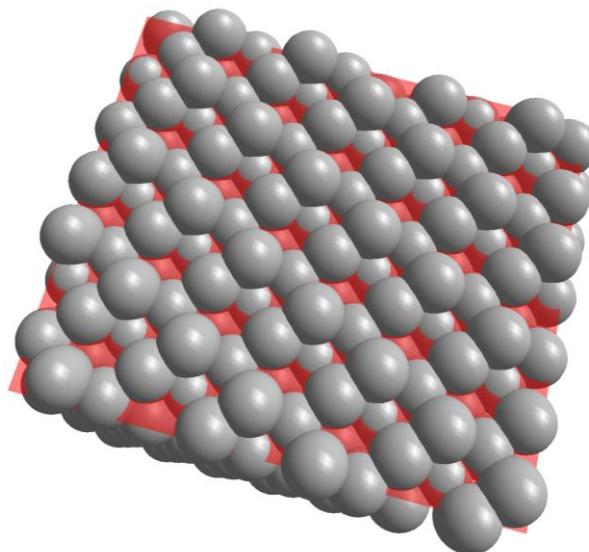
{100}**{721}****{732}**

Figure 6.43. Crystallographic models of orientations near the {100} plane normal: {100} top, {721} middle and {732} bottom. {721} is 17° from the {100} plane normal ($\beta_{\{100\}} = 17.7^\circ$). {732} is 27° from the {111} plane normal.

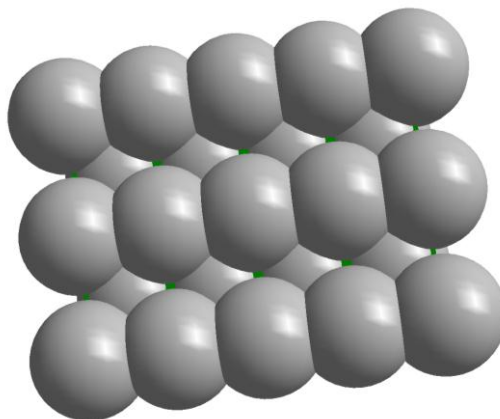
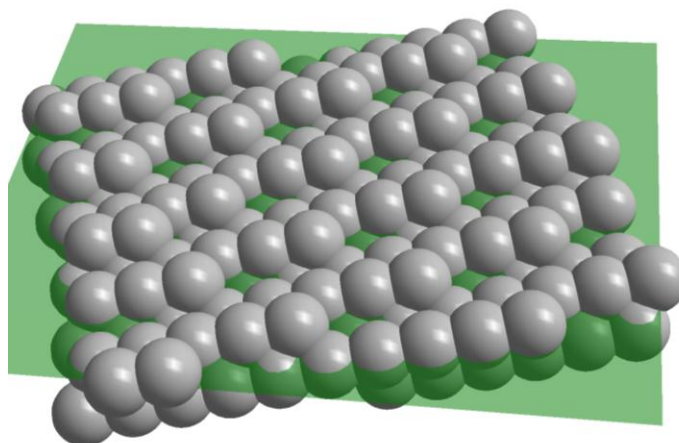
{110}**{431}**

Figure 6.44. Crystallographic models of the orientations near the {110} plane normal. {431} is 14° from the {100} plane normal ($\beta_{\{110\}} = 13.9^\circ$).

6.8 References

1. Ives, M.B., *Localized corrosion*, in *International corrosion conference series*, U.R. Evans, et al., Editors. 1974, National Association of Corrosion Engineers: Houston, Tex. p. 78-103.
2. Inoue, M., Teramoto, I., Takayanagi, S., *Etch pits and polarity in CdTe crystals*. *Journal of Applied Physics*, 1962. **33**(8): p. 2578-2582.
3. Fushimi, K., K. Miyamoto, and H. Konno, *Anisotropic corrosion of iron in pH 1 sulphuric acid*. *Electrochimica Acta*, 2010. **55**(24): p. 7322-7327.
4. Holme, B., N. Ljones, A. Bakken, O. Lunder, J.E. Lein, L. Vines, T. Hauge, O. Banger, and K. Nisancioglu, *Preferential Grain Etching of AlMgSi(Zn) Model Alloys*. *Journal of the Electrochemical Society*, 2010. **157**(12): p. C424-C427.
5. Koroleva, E.V., G.E. Thompson, P. Skeldon, and B. Noble, *Crystallographic dissolution of high purity aluminium*. *Proceedings of the Royal Society a-Mathematical Physical and Engineering Sciences*, 2007. **463**(2083): p. 1729-1748.
6. Lillard, R.S., G.F. Wang, and M.I. Baskes, *The role of metallic bonding in the crystallographic pitting of magnesium*. *Journal of the Electrochemical Society*, 2006. **153**(9): p. B358-B364.

7. Sugiyama, M., S. Harada, and R. Oshima, *Change in Young Modulus of Thermoelastic Martensite Fe-Pd Alloys*. Scripta Metallurgica, 1985. **19**(3): p. 315-317.
8. Davis, B.W., P.J. Moran, and P.M. Natishan, *Metastable pitting behavior of aluminum single crystals*. Corrosion Science, 2000. **42**(12): p. 2187-2192.
9. Schreiber, A., J.W. Schultze, M.M. Lohrengel, F. Karman, and E. Kalman, *Grain dependent electrochemical investigations on pure iron in acetate buffer pH 6.0*. Electrochimica Acta, 2006. **51**(13): p. 2625-2630.
10. Shahryari, A., J.A. Szpunar, and S. Orriánovic, *The influence of crystallographic orientation distribution on 316LVM stainless steel pitting behavior*. Corrosion Science, 2009. **51**(3): p. 677-682.
11. Treacy, G.M. and C.B. Breslin, *Electrochemical studies on single-crystal aluminium surfaces*. Electrochimica Acta, 1998. **43**(12-13): p. 1715-1720.
12. Yasuda, M., F. Weinberg, and D. Tromans, *Pitting Corrosion of Al and Al-Cu Single-Crystals*. Journal of the Electrochemical Society, 1990. **137**(12): p. 3708-3715.
13. Gentile, M., E.V. Koroleva, P. Skeldon, G.E. Thompson, P. Bailey, and T.C.Q. Noakes, *Influence of grain orientation on zinc enrichment and surface morphology of an Al-Zn alloy*. Surface and Interface Analysis, 2010. **42**(4): p. 287-292.
14. König, U. and B. Davepon, *Microstructure of polycrystalline Ti and its microelectrochemical properties by means of electron-backscattering diffraction (EBSD)*. Electrochimica Acta, 2001. **47**(1-2): p. 149-160.
15. Dingley, D.J. and V. Randle, *Microtexture Determination by Electron Back-Scatter Diffraction*. Journal of Materials Science, 1992. **27**(17): p. 4545-4566.
16. Randle, V. and O. Engler, *Introduction to texture analysis : macrotexture, microtexture and orientation mapping*. 2000, Amsterdam, The Netherlands: Gordon & Breach. xx, 388 p.
17. Bunge, H.J., *Texture analysis in materials science : mathematical methods*. English ed. 1982, London ; Boston: Butterworths. xx, 593 p.
18. Malan, D. *Public Domain: Wikimedia Commons*. Available from: <http://commons.wikimedia.org/wiki/File:EulerG.png>.
19. Nicholas, J.F., *An atlas of models of crystal surfaces*. Materials science and engineering program. 1965, New York,: Gordon and Breach. ix, 229 p.
20. Yiping, L., G.C. Hadjipanayis, C.M. Sorensen, and K.J. Klabunde, *Structural and Magnetic-Properties of Ultrafine Fe-Pd Particles*. Journal of Applied Physics, 1994. **75**(10): p. 5885-5887.
21. Ghosh, G., C. Kantner, and G.B. Olson, *Thermodynamic modeling of the Pd-X (X= Ag, Co, Fe, Ni) systems*. Journal of Phase Equilibria, 1999. **20**(3): p. 295-308.
22. Hultgren, R. and C.A. Zappfe, *The Crystal Structures of the Iron-Palladium Superlattices*. Kristallchem, 1938. **99**(509).
23. Puigdomenech, I., *MEDUSA: Make Equilibrium Diagrams Using Sophisticated Algorithms*. 2009: Stockholm, Sweden.
24. Joy, D.C., *Monte Carlo modeling for electron microscopy and microanalysis*. Oxford series in optical and imaging sciences 9. 1995, New York: Oxford University Press. viii, 216 p.

25. Oshima, R. and M. Sugiyama, *Martensite Transformations in Fe-Pd Alloys*. Journal De Physique, 1982. **43**(Nc-4): p. 383-388.
26. Lohrengel, M.M., A. Schreiber, and C. Rosenkranz, *Grain-dependent anodic dissolution of iron*. Electrochimica Acta, 2007. **52**(27): p. 7738-7745.
27. Mackenzie, J.K., A.J.W. Moore, and J.F. Nicholas, *Bonds broken at atomically flat crystal surfaces--I: Face-centred and body-centred cubic crystals*. Journal of Physics and Chemistry of Solids, 1962. **23**(3): p. 185-196.
28. Nicholas, J., *Calculation of Surface Energy as a Function of Orientation for Cubic Crystals*. Australian Journal of Physics, 1968. **21**(1): p. 21-34.
29. Zhang, J.-M., F. Ma, and K.-W. Xu, *Calculation of the surface energy of FCC metals with modified embedded-atom method*. Applied Surface Science, 2004. **229**(1-4): p. 34-42.
30. Grochola, G., S.P. Russo, I. Yarovsky, and I.K. Snook, *"Exact" surface free energies of iron surfaces using a modified embedded atom method potential and lambda integration*. Journal of Chemical Physics, 2004. **120**(7): p. 3425-3430.
31. Sohmura, T., R. Oshima, and F.E. Fujita, *Thermoelastic Fcc-Fct Martensitic-Transformation in Fe-Pd Alloy*. Scripta Metallurgica, 1980. **14**(8): p. 855-856.
32. Hirth, J.P., *Energetics in metallurgical phenomena*, W.M. Mueller, Editor. 1965, Routledge. p. 1.
33. Heyraud, J.C. and J.J. Metois, *Equilibrium Shape and Temperature - Lead on Graphite*. Surface Science, 1983. **128**(2-3): p. 334-342.
34. McLean, M., *Determination of the surface energy of copper as a function of crystallographic orientation and temperature*. Acta Metallurgica, 1971. **19**(4): p. 387-393.
35. Jun, W., Y.L. Fan, D.W. Gong, S.G. Shen, and X.Q. Fan, *Surface relaxation and stress of fcc metals: Cu, Ag, Au, Ni, Pd, Pt, Al and Pb*. Modelling and Simulation in Materials Science and Engineering, 1999. **7**(2): p. 189.
36. Aburada, T., *Effects of Minor Solute on Corrosion*, in *Materials Science and Engineering*. 2011, University of Virginia: Charlottesville, VA.
37. Soffa, W.A., D.E. Laughlin, and N. Singh, *Interplay of ordering and spinodal decomposition in the formation of ordered precipitates in binary fcc alloys: Role of second nearest-neighbor interactions*. Philosophical Magazine, 2010. **90**(1-4): p. 287-304.

7 Conclusions and Future Work

7.1 Conclusions

This dissertation has studied the role of selected nano-structural defects on corrosion properties in two model solid solution alloy systems. The investigation of the amorphous to single phase crystalline transformation in $\text{Cu}_{75}\text{Hf}_{20}\text{Dy}_{05}$ indicated that the disordered amorphous structure is detrimental to the overall corrosion performance, theorized to be due to local atomic clustering of beneficial solute atoms or void-free volume issues. Either one of these is argued to effect the corrosion properties. High-resolution characterization techniques did not completely determine the presence of a clustering layer. Compositional analysis performed using scanning TEM indicated compositional contrast on the order of 10 nm, however atom probe tomography was unable to detect any clustering, likely due to detector efficiency limitations. In the passive/localized breakdown condition the efficacy of passive film formation was reduced in the amorphous state leading to an increase in dissolution transients. During preferential dissolution of Hf from the matrix, the amorphous structure enabled more rapid dissolution of Hf and reconstruction of Cu into fcc polycrystalline Cu. When alloying elements can be retained in solid solution, the amorphous condition is a detrimental effect when considering the corrosion performance in the sense of resistance to degradation. However in cases where rapid formation of the dealloyed layer with nanoscale porosity is sought, using amorphous precursor alloys proves to be a beneficial quality.

In the $\text{Fe}_{50}\text{Pd}_{50}$ model alloy system the role of structural change was studied by comparing a disordered crystalline (fcc) phase to an ordered crystalline (pT) phase of the same composition. A significant difference in behavior between the two structural states

was observed in HCl solution under conditions where both Fe and Pd undergo congruent dissolution. The overall dissolution susceptibility of the ordered case was higher than the crystalline case. It is thought the underlying polytwinned microstructure is the key factor underlying this behavior instead of compositional effects due to the ordered structure.

In the case of the disordered (fcc) Fe₅₀Pd₅₀ phase, the dissolution susceptibility in HCl solution was shown to depend on the crystallographic orientation of the individual grains. Grain orientations showed grain characteristic faceting and the most dissolved orientations (10 - 20° from the {111} plane normal) also showed the highest surface roughness. Orientations near the {111} becoming more dissolution resistant has not been observed in other fcc dissolution studies. These results were compared to surface energy of other fcc metals and similar trends were revealed but an exact correlation was not confirmed.

In both alloy systems, these results make clear that categorical determinations of the 'corrosion resistance' based on single environments is not a very useful metric for determining the properties of new alloys. In particular, amorphous alloys containing a given solid solution are often assumed to be more corrosion resistant than their crystalline counterparts, in part, due to the amorphous structure. In reality, the corrosion behavior of amorphous alloys exhibit electrochemical behavior that is highly dependent on corrosion regime and environment as well as the precise details of the interplay of the constituent species. Factors that should be considered include: 1) Passive layer formation criteria (critical threshold concentration for enrichment of the oxide of the beneficial element and complete surface net coverage), 2) Role of constituent beneficial elements as dissolution

moderators, and 3) Effect on ad/absorption of ions, effect on surface diffusion and other pertinent parameters to a specific corrosion regime.

7.2 Suggested Future Work

7.2.1 Role of the Amorphous Structure on Corrosion Properties in the $\text{Cu}_{75}\text{Hf}_{20}\text{Dy}_{05}$ Alloy

- The conclusions drawn from the electrochemistry experiments on $\text{Cu}_{75}\text{Hf}_{20}\text{Dy}_{05}$ indicated a strong effect theorized to be due to compositional clustering in the amorphous structure. Atom probe tomography work did not indicate any significant clustering, however the detector efficiency makes detecting one for one clustering characterization at the 1st, 2nd, and 3rd nearest neighbor length scales difficult to determine. Improvements to the spatial resolution (counting efficiency) of atom probe tomography could serve to definitively characterize the local atomic clustering. Modeling and scattering experiments similar to cited examples of the Cu-Zr system would be another avenue to determine the existence of clusters.
- In general the effect of local clustering and the effect of 1st, 2nd, 3rd NN arrangements is poorly understood due to limitations in electrochemical and characterization techniques. These variables, including free volume, affect the bonding strength and the ability to form a complete surface net of beneficial solute. One possible route for direct observation of the role of clustering would be corrosion of TEM foils, but high compositional resolution would be required.
- Preferential dissolution of Hf from the alloy matrix and subsequent reorganization to form a nanoporous Cu suggested that the surface diffusion of Cu on the alloy surface showed a strong dependence on the underlying structure. Surface

diffusion on metallic amorphous materials has currently not been studied. Cited studies on amorphous Si indicate a different mechanism of surface diffusion on amorphous compared to crystalline materials due to a 'continuum' of binding energies enabling many short range diffusion steps. Experiments on amorphous metals could determine the mechanism of surface diffusion. This knowledge could prove important in the design of future nanoporous materials which are becoming more prevalent as the need for catalysts and fuel cells becomes more widespread.

7.2.2 Role of the Structure in the Fe₅₀Pd₅₀ Alloys

- The increase in dissolution observed in ordered pT structure over the disordered fcc structure of the same composition is thought to be, in part, due to the underlying polytwinned structure in the ordered pT structure. Specific thermal mechanical processing could be tried to achieve a microstructure free of polytwins. Then the effect of the polytwins could be isolated and investigated.
- The grain orientation dependent dissolution study of the disordered fcc Fe₅₀Pd₅₀ alloy in HCl solution could be enhanced by several additional series of measurements and modeling:
 - The dissolution induced morphology of each grain results in specific characteristic facet formation. The orientation of these facets would prove very informative. One possible procedure for determining facet orientations involves ion milling the surface parallel to the facets. This would enable using standard EBSD to determine the facet orientation. The

work presented within this thesis would serve as an important guide for what orientations should be studied in more detail.

- The orientation dependence of the disordered $\text{Fe}_{50}\text{Pd}_{50}$ dissolution showed somewhat similar trends to the surface energy as a function of orientation determined via modeling and experiment for various fcc metals. Modeling the exact values of surface energy for the binary fcc $\text{Fe}_{50}\text{Pd}_{50}$ alloy could more conclusively determine if the dissolution rate shows a conclusive dependence on surface energy. Additionally other factors such as the electronic structure may prove informative.
- Electrochemically, determining the kinetics of the dissolution reaction on different orientations should be the next step in this research as the reaction rate may have a strong orientation dependence. Larger grains, achieved via long term annealing, would allow isolation of each grain electrically (by masking of other grains or using the electrochemical microprobe technique). Experiments on individual grains could then be used to elucidate the orientation dependence of the dissolution kinetics.